Strong Constraints on New Physics from the IceCube South Pole Neutrino Observatory

by

Grant K. Parker

Submitted in fulfillment of the requirements for the degree of

Doctor of Philosophy in Physics

at the

University of Texas at Arlington

December 2022

Author .....

Grant K. Parker
Department of Physics

Certified by .....

Ben J. P. Jones
Associate Professor of Physics
Thesis Supervisor

Accepted by .....

Alex H. Weiss
Department Chair of Physics

Abstract

Grant K. Parker

Strong Constraints on New Physics from the IceCube South Pole Neutrino Observatory

The IceCube Neutrino Observatory, a gigaton-scale ice Cherenkov detector located deep within the Antarctic glacier, has detected hundreds of thousands of atmospheric neutrinos at energies from a few GeV to 100 TeV. Above 100 GeV, where ordinary oscillation effects become vanishingly small, this data sample is particularly sensitive to a wide range of beyond-standard-model (BSM) neutrino oscillation mechanisms. This thesis presents two searches for such BSM physics: flavor-changing nonstandard neutrino interactions (NSI) and neutrino oscillation decoherence (decoherence).

The first analysis constrains the $\mu - \tau$ flavor-changing NSI parameter $\epsilon_{\mu\tau}$ with eight years of IceCube atmospheric neutrino data ranging from 500 GeV to 1 TeV. No evidence is found for $\epsilon_{\mu\tau}$ NSI with a p-value of 25.2%, and the constraints of this analysis improve on the previous leading constraints by a factor of two.

The second analysis probes for signals of neutrino oscillation decoherence through interactions with spacetime foam. Two models of spacetime foam are tested at four different values of energy power law. No evidence is found for neutrino decoherence, and constraints are improved in comparison with previous leading measurements with the improvement increasing exponentially with the decoherence power law index.

These measurements, taken together, represent new leading results on priority fronts in the search for new physics and demonstrate IceCube's unique sensitivity to high-energy BSM physics through experimental statements on the nature of both sub-dominant neutrino interactions and the quantum behavior of spacetime.

Acknowledgements

One of my favorite parts in writing this thesis is thanking all the people who contributed to my success. As you will find out, I have done it *relentlessly*.

First and foremost, I deeply appreciate the guidance from my advisor, Ben Jones. Being open to my research interests, Ben let me transition between different projects until I found an experiment I have a deep passion for: IceCube. He has sharpened me into an academic that understands the nuances between the big picture and the finest details, and I am eternally grateful to receive that wisdom.

This research would also not have been possible without the Jones-Nygren Neutrino Rare Event Searches Group (νRES). Every undergrad, grad student, and postdoc has contributed to making νRES a strong, exciting, and supportive community that I was able to thrive in. Two particular colleagues I want to thank are Matt Molewksi and Akshima Negi, who made the second analysis of this thesis possible. Special thanks also go to Dave Nygren for being the most supportive of mentors with a critical mind I aspire to model. With regard to postdocs, one of my earliest projects involved a deep fear (electronics), and to my rescue was Katherine Woodruff, who I immensely enjoyed working (and exploding circuits) with. Sadly, I primarily interacted with Krishan Mistry over virtual connections, but still appreciate all the support and kindness he has shared. And Jackie Baeza-Rubio was there for it all, and her enthusiasm for our field is what gives me the most hope for the future.

Having a cohort of grad students to complain to in Texas was a tremendous source of stress relief, so many thanks, hugs, and apologies go to Ben Smithers,

Nick Byrnes, and Karen Navarro. When I first started, Austin McDonald was extremely patient and helped me with practically everything, so I will never stop thanking him. Leslie Rogers handled both my incessant questions and complaints, and as a result became one of my closest friends. You all are amazing and I am endlessly thankful I got to do this with you.

Halfway through my PhD I became a visiting researcher at IceCube's headquarters in Madison, Wisconsin. I want to thank all the members of the Wisconsin IceCube Particle Astrophysics Center (WIPAC) for welcoming me with open arms. Being in the heart of the experiment I got to work on was a life-changing opportunity, and I appreciate everyone in the IceCube Collaboration (both in person and abroad) for offering me their technical knowledge, advice, and community.

While I had my cohort of Texas grad students, I eventually found an additional cohort in the grad students at WIPAC and within IceCube. To my WIPAC circle including Marjon Moulai, Kayla DeHolton, Alex Pizzuto, Sarah Mancina, Manuel Silva: you are all crazy and made my time in IceCube the most fun. You made me feel sane when I needed it the most. Additional collaborators Jeff Lazar, Kareem Farrag, Will Luszczak, Maria Prado, Jessie Thwaites, Abby Bishop: you are all amazing scientists and equally amazing friends, and I am so grateful for the time I had with you.

Particularly, this research would not have been possible without the collaboration of the Conrad MIT and Argüelles Harvard groups. Their feedback was key in conducting the analyses successfully. In particular, I have never had a dull conversation with Janet Conrad, and hope our lively discussions will continue (maybe we'll figure out why CP violation matters... someday...). Carlos Argüelles is the technical mastermind of our group; his software and knowledge of the most complicated details has given life to all of our analyses. I owe many, many thanks (and drinks) to Austin Schneider for making me software-capable and giving me a hand with everything technical. The people in our

combined group are also now dear friends — Alex Diaz, John Hardin, Phillip Weigel, Alfonso Garcia, David Vannerom, Ibrahim Safa, I don't think I'll ever find collaborators that will be as capable as you all.

I also have Dr. Eric Kramer and Dr. Mike Bergman to thank for giving me an excellent, personalized foundation from which to start my physics journey, and Dr. Ramon Lopez for taking a chance on me and bringing me to UTA.

The people in my personal life have been instrumental in keeping me in one piece. Andy Zito, Tony Alexander, André Santana, Saisha Manan, Abby Donnelly, Justin Little, Connor Lehman: thank you for dealing with my persistent hermiting, you have all been so generous with your love and support. I couldn't have done this without you.

My parents Janet and Mark have made all of this possible, I will never understate everything they have given me. More thanks to my sibling Cade, my grandmother Mary, and everyone in my family who has supported me in amounts that are impossible to express. Their love and support has propelled me farther than I ever imagined.

To Amanda, I never imagined meeting someone who could love me so much without asking anything in return. You are the embodiment of grace, and I love you with all my heart.

Contents

Chapter 1

Introduction

Approximately 50 years ago, a fundamental theory of how the elementary matter particles (fermions) and force-carrying particles (bosons) interact solidified into what is now known as the Standard Model of Particle Physics (SM). While the SM has yielded predictions that agree with experimental measurements to an astonishing degree, there remain significant gaps in the theory's ability to model all physical processes. For instance, gravity remains the glaring omission from the set of fundamental forces due to contradictions that arise when attempting to merge general relativity (the theory of gravitation) and quantum mechanics. In addition, at the highest energy scales the SM is incomplete due to the emergence of quadratic corrections to the mass of the Higgs boson (the "hierarchy problem").

Another instance of the SM's incompleteness is the mass of the neutrino. In the original formulation, the SM never predicted the neutrino to have mass. After countless experiments and decades of research, it was found that not only is there a neutrino mass, but that neutrinos have three mass states that interfere and combine to produce what are called *flavor* states, which are the states that neutrinos are produced, interact, and detected in. Neutrinos, with these non-zero masses and unique oscillation behavior, are one of the few direct sources of evidence that there exists physics "beyond" the Standard Model (BSM).

Although the properties of neutrinos now challenge the completeness of the Standard Model, it is through these properties that physicists now have the

strongest opportunities to probe BSM physics. Coupled only to the weak force and gravity, neutrinos rarely interact and thus travel through matter and the Universe with minimal disturbance, hence their nickname as "ghost particles". Because of this limited interaction and their flavor oscillations, neutrinos that travel long baselines are a prime candidate for use in quantum interferometry, where the deviations between the observed and predicted number of neutrinos at detectors is compelling evidence for certain models of new physics that rely on quantum interference effects. Another advantage is that in the language of effective field theory, the masses of the neutrinos can be added to the SM through a new dimension-five term, the *Weinberg operator*, which opens the door to physics of higher dimensions.

This thesis describes two searches for evidence of new physics: dimension-six neutrino nonstandard interactions (NSI), and interactions between neutrinos and a hypothetical spacetime foam. These analyses use neutrino data collected by the IceCube Neutrino Observatory, located within the ice at the geographic South Pole. The following outlines the contents of the document:

Chapter 2 highlights important moments in the formation of neutrino physics, then proceeds to describe the framework of neutrino oscillation both in vacuum and in matter. This chapter also underscores the persistent anomalies that have emerged from neutrino experiments and the implications of such anomalies.

Chapter 3 reviews the design and operation of the IceCube Neutrino Observatory ("IceCube"), the experiment used for the analyses described in this thesis. This includes discussion of the detector's construction history, calibration, and event types.

Chapter 5 introduces the first model of new physics proposed in this thesis, non-standard neutrino interactions (NSI). This chapter walks through the motivation for NSI searches, the mathematical formalism, and previous constraints set by neutrino experiments.

Chapter 6 presents the analysis conducted to constrain $\mu-\tau$ flavor-changing NSI with data from IceCube. Contents include the details of the analysis sample, simulation, procedures, tests, and the results of the fit to the unblinded sample. Results of the analysis fail to reject the SM with a p-value of 25.2%, but set the leading 90% CL constraints on $\epsilon_{\mu\tau}$ NSI parameter with a factor of ~ 2 improvement on the next-leading constraints.

Chapter 7 begins the portion of the thesis dedicated to the second model of new physics constrained by the author, neutrino oscillation decoherence ("decoherence"). In this chapter the common method of parameterizing decoherence is derived, and the latter half is spent motivating a model of neutrino decoherence via virtual black hole interactions from spacetime foam.

Chapter 8 presents the analysis conducted to constrain neutrino oscillation decoherence with data from IceCube. Models constrained are two neutrino-virtual black hole interactions, each for energy power indices $n = 0$, 1, 2, and 3. The results yield no evidence for decoherence but improve on previous results from two to eight orders of magnitude.

Chapter 9 concludes the dissertation with discussion of results from the analyses and their context in the greater picture of current and future neutrino physics activities.

Part I

Neutrino Fundamentals

Chapter 2

The Physics of Massive Neutrinos

2.1 Brief History of the Neutrino

The history of neutrinos arises from the study of the weak force, which first began with the discovery of radioactivity in 1896 by Dr. Henri Becquerel [1, 2]. In the ensuing study of radiation, it was found that, unlike in decays that produce α and γ[1] particles with a narrowly-restricted energy, β particles are produced with a wide spectrum of allowed energies [3]. To account for this observation, only two explanations were viable: the conservation of energy was violated, or a yet-to-be-detected, massless (or very light) neutral particle carries away some of the decay energy, allowing the β particle to have a variable energy spectrum. It was in 1930 that Dr. Wolfgang Pauli supported the latter hypothesis, arguing a new neutral particle would resolve the β-decay mystery in addition to the anomalous spin properties of lithium and nitrogen [4]. Two years later, Dr. James Chadwick indeed discovered a new neutral particle, but this particle only resolved the lithium and nitrogen spin anomalies, as the neutral particle was too massive to be a product of β-decay (this particle came to be known as the *neutron*) [5]. A lighter neutral particle was still required.

With this knowledge, in 1934 Dr. Enrico Fermi was able to form a physical theory of β-decay. From this theory, the still-undiscovered light neutral particle

[1] α particles consist of two protons and two neutrons, which is the equivalent of a Helium-4 nucleus. γ particles are photons emitted through gamma nuclear decays.

dubbed "neutrino", or "little neutral one" by Fermi, would have to be exceedingly small, with an interaction cross-section[2] of $\sim 10^{-44}$ cm^2 [6]. To overcome the very low probability of interaction, a large flux of neutrinos would be required for any attempt at direct observation. Such a large flux can be found at nuclear reactors, and in 1956, "Project Poltergeist" at the Savannah River nuclear reservation in South Carolina directly observed the first neutrinos[3] [7].

With Fermi's theory of a new "weak" force confirmed, physicists were confronted with the challenge of developing novel ways of studying the neutrino. As a result of a new method for developing pure neutrino beams [8, 9], a new type of neutrino, the muon neutrino, was discovered in 1962 [10]. The discovery of a second neutrino type prompted the notion that for each charged lepton[4] there is an associated neutrino. This was confirmed with the discovery of the tau lepton in 1975 [11] and the subsequent discovery of the tau neutrino in 2000 [12]. The neutrinos have since been labeled according to *flavor*, or the charged lepton associated with their production.

The story of neutrino physics does not end with the discovery of the three different flavors; measurements of the solar neutrino flux at the Homestake experiment in the 1960's and 70's made apparent that more than half of the predicted number of neutrinos were missing [13, 14]. One theory, posited in years earlier by Dr. Bruno Pontecorvo, was neutrinos *oscillate* between flavors as they propagate [15, 16]. Following this, in 1978 Dr. Lincoln Wolfenstein would describe how an oscillating neutrino system would be modified in a matter environment[5] [17, 18], and in 1986, Drs. Stanislav Mikheyev and Alexei Smirnov would describe mixing resonances in a continuously changing matter density.

[2] The cross-section is a parameter that quantifies the probability of an interaction taking place.

[3] These were actually electron antineutrinos, observed through inverse β-decay ($\overline{\nu} + p \rightarrow n + e^+$) releasing photons in a liquid scintillator.

[4] A lepton is a fundamental particle with spin $\frac{1}{2}$ that does not participate in strong interactions.

[5] Wolfenstein's particular focus when describing neutrino oscillations in matter was how oscillations were modified within the Sun, as addressing the "solar neutrino problem" was the priority of the decade.

This is called the *MSW effect* after Mikheyev, Smirnov, and Wolfenstein [19, 20].

It would not be until the 1990's that the flavor oscillation theory was confirmed by the Super-Kamiokande, SAGE, and GALLEX experiments through further solar neutrino flux measurements [21–23]. The discovery of neutrino oscillations is a pivotal moment in physics, as neutrino oscillations requires two of the neutrino masses to be non-zero, a beyond-Standard-Model (BSM) phenomenon. To this day, it remains the only direct measurement of BSM physics. Thus, physicists within the last 20 years have studied neutrinos with great interest, as they represent the most promising opportunity for the discovery of new physics. For instance, extensions of the Standard Model that include massive neutrinos also open the door to possible new forces and their corresponding particles, which we explore in Chapter 5. Another frontier in this research is using neutrino oscillations to probe possible models of quantum gravity, described in Chapter 7. This thesis presents work on both of these fronts through the use of tools and data from the IceCube Neutrino Observatory.

2.2 Neutrino Vacuum Oscillations Framework

Neutrinos are produced, absorbed, and interact in the basis of flavor states, whereas neutrinos propagate in their mass states. The mass states are the eigenstates of the neutrino Hamiltonian, and when a neutrino propagates through space in these mass states, their interference produce weak force potential ("weak potential") eigenstates, which have been dubbed "flavor" states.

Having a map between the two bases is critical to developing a formalism for neutrino oscillations, and such mapping is denoted by the PMNS matrix U, named after Drs. Pontecorvo, Maki, Nakagawa, and Sakata, the primary

contributors to the formulation [9, 24, 25]. This matrix is a unitary operator[6] that describes the mixing between the mass and flavor states, which can be used to describe the composition of a neutrino of arbitrary flavor α like so:

$$|\nu_\alpha\rangle = \sum_{i=1,2,3} U_{\alpha i} |\nu_i\rangle \tag{2.1}$$

Expanding this to the full vector form, the equation appears as:

$$\begin{pmatrix} \nu_e \\ \nu_\mu \\ \nu_\tau \end{pmatrix} = \begin{pmatrix} U_{e1} & U_{e2} & U_{e3} \\ U_{\mu 1} & U_{\mu 2} & U_{\mu 3} \\ U_{\tau 1} & U_{\tau 2} & U_{\tau 3} \end{pmatrix} \begin{pmatrix} \nu_1 \\ \nu_2 \\ \nu_3 \end{pmatrix}. \tag{2.2}$$

An intuitive way to view the PMNS matrix is in the expanded form, seen below:

$$U = \begin{pmatrix} 1 & & \\ & c_{23} & s_{23} \\ & -s_{23} & c_{23} \end{pmatrix} \begin{pmatrix} c_{13} & & s_{13}e^{i\delta_{CP}} \\ & 1 & \\ -s_{13}e^{i\delta_{CP}} & & c_{13} \end{pmatrix} \begin{pmatrix} c_{12} & s_{12} & \\ -s_{12} & c_{12} & \\ & & 1 \end{pmatrix} P \tag{2.3}$$

with $c_{ij} = \cos(\theta_{ij})$ and $s_{ij} = \sin(\theta_{ij})$. Parameter δ_{CP} is the angle that quantifies how much neutrino oscillations violates charge-parity symmetry (the "CP-violating" phase). The angles θ_{23}, θ_{13}, and θ_{12} are the mixing angles that have taken on the colloquial names of the atmospheric, reactor, and solar mixing angles, respectively, historically named after the neutrino sources where their impact is most prominent. The above decomposition is organized such that each matrix represents the contribution (a basis rotation) from each form of mixing. Matrix P is either the identity matrix if neutrinos are Dirac particles or the matrix $\text{diag}(e^{i\alpha_1}, e^{i\alpha_2}, 1)$ if neutrinos are Majorana particles[7]

[6] A unitary operator is an operator that changes states without changing the normalization of probability distributions ($U^\dagger U = UU^\dagger = I$, where $U^\dagger$ is the conjugate transpose of matrix U).

[7] Majorana particles are their own antiparticle, which is not true in the case of Dirac particles.

Thus, combining the matrices in Eq. 2.3 yields the values of the matrix in Eq. 2.2:

$$U_{\text{PMNS}} = \begin{pmatrix} c_{12}c_{13} & s_{12}c_{13} & s_{13}e^{i\delta_{\text{CP}}} \\ s_{12} - c_{12}s_{13}s_{23}e^{i\delta_{\text{CP}}} & c_{12} - s_{12}s_{13}s_{23}e^{i\delta_{\text{CP}}} & c_{13}s_{23} \\ s_{12} - c_{12}s_{13}c_{23}e^{i\delta_{\text{CP}}} & c_{12} - s_{12}s_{13}c_{23}e^{i\delta_{\text{CP}}} & c_{13}c_{23} \end{pmatrix} \tag{2.4}$$

While Eq. 2.2 presents the time-dependent relationship between neutrino flavor states and mass states, we have yet to provide a formula to calculate the time evolution of neutrino states, the simplest case being in vacuum. To derive this, let us assume a neutrino is produced at time $t = t_0$. Since the neutrino vacuum Hamiltonian is independent of time, the time evolution for a given mass state $|\nu_j\rangle$ takes the form of a plane wave solution to Schrödinger's equation:

$$|\nu_j(t)\rangle = e^{-ip_\omega x^\omega} |\nu_j(t_0)\rangle \,, \tag{2.5}$$

where $p_\omega x^\omega$ is the four-vector scalar product such that $p_\omega x^\omega = E_j t_j - \vec{p}_j \cdot \vec{x}_j$ for mass state energy E_j and three-vector momentum-position scalar product $\vec{p}_j \cdot \vec{x}_j$ with $\vec{p}_j = (p_x, p_y, p_z)$ and $\vec{x}_j = (x_x, x_y, x_z)$.

The $|\nu_j\rangle$ mass state energy is related to the neutrino mass state mass and momentum by the famous Einstein mass-energy equation $E_j^2 = m_j^2 + |\vec{p}_j|^2$ (in natural units). As all neutrinos are produced relativistically ($m_\nu \ll E_\nu$) as a consequence of energy-limited production mechanisms and the extremely small neutrino mass, the quadratic approximation $E_j \approx |\vec{p}_j| + \frac{m_j^2}{2|\vec{p}_j|}$ is sufficiently accurate. Also in the relativistic limit, with the use of natural units, $|\vec{x}|_j = t_j = L$. Hence, substituting the definition for the energy and $\vec{p}_j \cdot \vec{x}_j$ for $|\vec{p}_j|t$ in $p_\omega x^\omega$, we get $p_\omega x^\omega = (|\vec{p}_j| + \frac{m_j^2}{2|\vec{p}_j|})t - |\vec{p}_j|t = \frac{m_j^2}{2|\vec{p}_j|}t = \frac{m_j^2}{2|\vec{p}_j|}L$. So,

$$|\nu_j(t)\rangle = e^{-i\frac{m_j^2}{2\vec{p}_j}L} |\nu_j(t_0)\rangle \,. \tag{2.6}$$

From the smallness of neutrino masses and the relativistic energies of neutrinos, we may use the approximation $E_j \approx \vec{p}_j$ to get

$$|\nu_j(t)\rangle = e^{-i\frac{m_j^2}{2E}L}\,|\nu_j(t_0)\rangle\,. \tag{2.7}$$

Now, as neutrinos are produced, detected, and annihilated in flavor states, we can use the mapping from Eq. 2.2 to show that the time evolution of a flavor state $|\nu_\alpha\rangle$ is the PMNS-weighted time evolution of the mass states:

$$|\nu_\alpha(t)\rangle = \sum_j U_{\alpha j}\,|\nu_j(t)\rangle = \sum_j U_{\alpha j} e^{-i\frac{m_j^2}{2E}L}\,|\nu_j(t_0)\rangle\,. \tag{2.8}$$

While this is an accurate representation of the flavor state time evolution, since measurements and interactions take place in the flavor state, it is most sensible to do one last conversion of the mass state $|\nu_j(t_0)\rangle$ to the flavor basis:

$$\begin{aligned} |\nu_\alpha(t)\rangle = \sum_j U_{\alpha j} e^{-i\frac{m_j^2}{2E}L}\,|\nu_j(t_0)\rangle &= \sum_j U_{\alpha j} e^{-i\frac{m_j^2}{2E}L}\left(\sum_\gamma U^*_{\gamma j}\,|\nu_\gamma(t_0)\rangle\right) \\ &= \sum_j \sum_\gamma U_{\alpha j} U^*_{\gamma j} e^{-i\frac{m_j^2}{2E}L}\,|\nu_\gamma(t_0)\rangle\,. \end{aligned} \tag{2.9}$$

In this formulation, we may use the tools of quantum mechanics to calculate the probability of a neutrino flavor transition $\nu_\alpha \to \nu_\beta$ with energy E at propagation distance L:

$$\begin{aligned} P(\nu_\alpha \to \nu_\beta; E, L) &= |\langle \nu_\beta(L)|\nu_\alpha(L_0 = 0)\rangle|^2 \\ &= \left|\left(\sum_j \sum_\gamma \left[U_{\beta j} U^*_{\gamma j} e^{-i\frac{m_j^2}{2E}L}\right]^* \langle \nu_\gamma(0)|\right)|\nu_\alpha(0)\rangle\right|^2 \\ &= \left|\sum_j \sum_\gamma U^*_{\beta j} U_{\gamma j} e^{i\frac{m_j^2}{2E}L}\,\langle \nu_\gamma(0)|\nu_\alpha(0)\rangle\right|^2. \end{aligned} \tag{2.10}$$

The basis flavor states are orthogonal, so the product $\langle \nu_\gamma(0)|\nu_\alpha(0)\rangle$ is 1 when $\gamma = \alpha$ and 0 otherwise. This reduces the sum in Eq. 2.10 to

$$
\begin{aligned}
P(\nu_\alpha \to \nu_\beta; E, L) &= \left| \sum_j U^*_{\beta j} U_{\alpha j} e^{i \frac{m_j^2}{2E} L} \right|^2 \\
&= \left(\sum_j U^*_{\beta j} U_{\alpha j} e^{i \frac{m_j^2}{2E} L} \right) \left(\sum_k U^*_{\beta k} U_{\alpha k} e^{i \frac{m_k^2}{2E} L} \right)^* \\
&= \sum_{j,k} U_{\alpha j} U^*_{\alpha k} U^*_{\beta j} U_{\beta k} e^{i \frac{\Delta m^2_{jk}}{2E} L},
\end{aligned}
\tag{2.11}
$$

where $\sum_{j,k} = \sum_j \sum_k$ for mass state indices $j, k = 1, 2, 3$ and $\Delta m^2_{jk} = m^2_j - m^2_k$ (called the "mass square difference").

Eq. 2.11 is the final, compact form of the SM neutrino flavor transition probability. In this form, there are notable features to discuss. For instance, the term $e^{i \frac{\Delta m^2_{jk}}{2E} L}$ indicates the the flavor transition probability *oscillates* as the neutrino travels; this is where the term "neutrino oscillations" originates. Another critical feature is the term Δm^2_{jk}. The implication is that neutrino oscillation measurements are sensitive *only* to the neutrino mass square differences — that the neutrino masses cannot be measured through neutrino oscillations.

To see how the neutrino flavor transition probability changes under a CP transformation, note that the flavor transition probability for antineutrinos follows the transformation $|\nu_\alpha\rangle = \sum_j U_{\alpha j} |\nu_j\rangle \to |\overline{\nu}_\alpha\rangle = \sum_j U^*_{\alpha j} |\overline{\nu}_j\rangle$. Then the measure of CP violation in neutrino oscillations can be quantified through:

$$
\begin{aligned}
\mathcal{A}^{\mathrm{CP}}_{\alpha\beta} &= P(\nu_\alpha \to \nu_\beta) - P(\overline{\nu}_\alpha \to \overline{\nu}_\beta) \\
&= 16 \sin\left(\frac{\Delta m^2_{21} L}{4E} \right) \sin\left(\frac{\Delta m^2_{31} L}{4E} \right) \sin\left(\frac{\Delta m^2_{32} L}{4E} \right) \mathcal{J} \sum_\gamma \varepsilon_{\alpha\beta\gamma},
\end{aligned}
\tag{2.12}
$$

such that $\mathcal{J} = \mathrm{Im}(U_{\alpha j} U^*_{\alpha k} U^*_{\beta j} U_{\beta k}) \sum_{\gamma,l} \varepsilon_{\alpha\beta\gamma} \varepsilon_{jkl}$ is the *Jarlskog invariant* [26] where ε is the Levi-Civita symbol[8]. It is this term $\mathcal{J}$, which incorporates the CP-violating angle from Eq. 2.3, that introduces CP-violation to neutrino oscillations.

[8] The Levi-Civita symbol is defined as $\varepsilon_{ijk} = \begin{cases} +1, & \text{if } (i,j,k) \text{ is } (1,2,3),\ (2,3,1),\ (3,1,2) \\ -1, & \text{if } (i,j,k) \text{ is } (3,2,1),\ (2,1,3),\ (1,3,2) \\ 0, & \text{if } i = j \text{ or } j = k \text{ or } i = k \end{cases}$

2.3 Neutrino Matter Oscillations Framework

Although neutrinos rarely interact with matter, traveling through a large medium with many particles results in multiple forward-scattering interactions. The compounding effect of these interactions ultimately modifies the neutrino oscillation probability such that the contribution can be modeled as an added potential to the vacuum Hamiltonian. This is analogous to the refractive index for light moving in media.

To formulate the matter potential, every contribution to neutrino forward scattering from every matter particle must be considered. As macroscopic matter is composed of electrons, protons, and neutrons, we write the respective contributions from *neutral* weak scattering via Z^0 as

$$V_{\nu_\alpha e}^{Z^0} = -\frac{\sqrt{2}}{2} G_F N_e, \quad V_{\nu_\alpha p}^{Z^0} = \frac{\sqrt{2}}{2} G_F N_p, \quad V_{\nu_\alpha n}^{Z^0} = -\frac{\sqrt{2}}{2} G_F N_n, \tag{2.13}$$

where N are the respective particle number densities and G_F is the Fermi constant. In the case of charged weak interactions via $W^\pm$, there is a single charged forward scattering interaction allowed between ν_e and e, adding a $\sqrt{2} G_F N_e$ term to the total electron neutrino matter potential. The total potentials for each neutrino are thus $V_{\nu_\alpha} = V_{\nu_\alpha e} + V_{\nu_\alpha p} + V_{\nu_\alpha n}$. For stable atomic nuclei with approximately equal numbers of protons and neutrons, the proton and neutron potential contributions cancel such that $V_{\nu_\mu} = V_{\nu_\tau} = -\frac{\sqrt{2}}{2} G_F N_e$ and $V_{\nu_e} = \frac{\sqrt{2}}{2} G_F N_e$. From Sec. 2.2 we know that neutrino oscillations are only sensitive to the relative differences between diagonal values in the mass basis, and with only one unique value of potential difference ($V = V_{\nu_e} - V_{\nu_\mu} = V_{\nu_e} - V_{\nu_\tau} = \sqrt{2} G_F N_e$), the matter potential may hence be written as $H_{\text{mat}} = V(x)\text{diag}(1, 0, 0)$, where $V(x) = \sqrt{2} G_F N_e(x)$ such that x is the neutrino depth in matter and $N_e(x)$ is the electron number density at that depth.

Therefore, the total Hamiltonian may be expressed as sum of the vacuum Hamiltonian with the matter contribution:

$$H_{\text{total}} = \frac{1}{2E_\nu}\left[U\begin{pmatrix} 0 & & \\ & \Delta m^2_{21} & \\ & & \Delta m^2_{31} \end{pmatrix}U^\dagger + V_{CC}(x)\begin{pmatrix} 1 & & \\ & & \\ & & \end{pmatrix}\right]. \tag{2.14}$$

Utilizing this Hamiltonian to analytically develop a flavor transition probability is not trivial. Yet one common approach is to take the total Hamiltonian and diagonalize it:

$$H_{\text{total}} = \tilde{U}\text{diag}(\tilde{m}_1^2, \tilde{m}_2^2, \tilde{m}_3^2)\tilde{U}^\dagger, \tag{2.15}$$

where $\tilde{U}$ can be viewed as a matter-enhanced PMNS mixing matrix and $\tilde{m}$ are the mass eigenstates in this new matter environment. Then obtaining the flavor transition probability in matter is a matter of substituting these new terms into the probability from Sec. 2.2:

$$P(\nu_\alpha \to \nu_\beta; L) = \left|\sum_{j=1}^{3} \tilde{U}_{\alpha j}\tilde{U}^*_{\beta j} e^{-i\frac{\tilde{m}_j^2 L}{2E}}\right|^2. \tag{2.16}$$

What this derivation indicates is that the matter potential alters the effective neutrino masses in materials.

The last feature that arises from neutrino matter oscillations is the MSW ("Mikheyev, Smirnov, and Wolfenstein") effect, which is illustrated from the approximate, two-flavor oscillation form of Eq. 2.14:

$$H^{\text{eff}}_{\text{tot}} = \frac{\Delta m^2}{4E}\begin{pmatrix} \cos 2\theta + \xi & \sin 2\theta \\ -\sin 2\theta & \cos 2\theta - \xi \end{pmatrix}, \tag{2.17}$$

such that $\xi = \frac{2\sqrt{2}VG_F N_e E}{\Delta m^2}$ is the modification to the two-flavor mixing matrix with mixing angle θ. This ξ component can be folded in to rewrite Eq. 2.17 in terms of effective parameters:

$$H^{\text{eff}}_{\text{tot}} = \frac{\Delta \tilde{m}^2}{4E}\begin{pmatrix} \cos 2\theta_m & \sin 2\theta_m \\ -\sin 2\theta_m & \cos 2\theta_m \end{pmatrix}, \tag{2.18}$$

where

$$\sin^2 2\theta_m = \frac{\sin^2 2\theta}{\sin^2 2\theta + (\cos 2\theta - \xi)^2} \quad , \quad \Delta\tilde{m}^2 = \Delta m^2 \sqrt{\sin^2 2\theta + (\cos 2\theta - \xi)^2}. \tag{2.19}$$

When treating these terms as functions of ξ, which is proportional to V and E, a *resonance* in the neutrino mixing occurs when $\xi = \cos 2\theta$ such that the mixing term $\sin^2 2\theta$ is maximal. This effect is what ultimately resolved the "solar neutrino problem", where solar neutrino experiments were missing a significant amount of the predicted flux [13, 14, 19, 20, 22, 23, 27–29].

2.4 Unresolved Experimental Anomalies

While the three-neutrino formalism has been experimentally verified to be robust, several measurements have turned into unresolved anomalies that may indicate additional physics with subleading effects to the three-neutrino model.

The first such anomaly to emerge was the excess of $\overline{\nu}_e$ events seen by the LSND detector in 1996. LSND is the Liquid Scintillator Neutrino Detector, which produces a beam of neutrinos from a decay-at-rest source that are detected through scintillation light from interactions within the 167-tons of mineral oil at the end of the 30-m beam baseline. After six years of data collection, the detector observed a $\sim 3.8\sigma$ excess of ν_e events [30].

Following the LSND anomaly was a confirmation of the excess at the MiniBooNE experiment. MiniBooNE, the Mini Booster Neutrino Experiment, is located at the Fermi National Accelerator Laboratory ("Fermilab") and scales the principle design of the LSND experiment with a larger baseline and beam energy, yet similar L/E. The detector employs a decay-in-flight neutrino beam incident on a 818-ton mineral oil volume with a baseline of 541 m. The added feature of MiniBooNE is the ability to alter the relative concentration of beam

neutrinos to antineutrinos, switching between a neutrino "mode" and antineutrino "mode". After 17 years of run time, the MiniBooNE Collaboration published an excess of neutrino and antineutrino events at a combined significance of $\sim 4.7\sigma$, supporting the observed LSND excess [31, 32].

A followup of the MiniBooNE excess was recently released with the first published results of the MicroBooNE experiment, a larger-scale version of MiniBooNE. MicroBooNE observed no excess of $\overline{\nu}_e$ events, yet MicroBooNE is not sufficiently sensitive to rule out the excess anomaly at this time [33].

Detector measurements of nuclear reactor antineutrinos were also found to be in significant tension with predictions when subdominant fission effects were integrated into the event rate calculation (the "reactor anomalies"). Counts $\overline{\nu}_e$ of across multiple reactors were found to be below the updated prediction at a significance of $\sim 3\sigma$ [34, 35]. While reactor neutrino fluxes present a similar range of the ratio of neutrino baseline over energy (L/E), the sources of measurement error are considerably different and understood at various levels of accuracy, making predictions of reactor neutrino fluxes somewhat tenuous. Therefore, further research is underway to continue refining the models of reactor neutrino production to determine the significance of the reactor measurement anomalies.

Lastly, anomalous measurements emerged from experiments that count solar neutrinos from neutrino-Gallium interactions (the "Gallium anomalies"). Gallium experiments count neutrinos by calculating the concentration of Germanium-71 within the detector after a specified period of time, as Ge^{71} is the byproduct of inverse beta decay between solar ν_e and Ga^{71}. The SAGE (Soviet-American Gallium Experiment) [27] and GALLEX ("GALLium EXperiment") [29] detectors recorded a deficit of predicted events that have a combined significance of 2.7σ. A followup to this anomaly was the BEST detector, or Baksan Experiment on Sterile Transitions, which upgraded the SAGE detector to monitor a steady source of ν_e from Chromium-51 decay. Recent measurements from BEST also record a deficit of ν_e at a $\sim 3\sigma$ level of significance [36, 37].

These anomalies support one overarching conclusion: that neutrino physics in its current form is incomplete. The work in this thesis seeks to illuminate the nature of subleading neutrino interactions and add to the overall neutrino picture; the neutrino nonstandard interactions of Part III can alleviate certain experimental tensions yet add a new layer of complication to current parameter measurements, while Part IV of the thesis explores and constrains a possible coupling between neutrinos and spacetime at the quantum scale.

Part II

Detector And Simulation

Chapter 3

The IceCube Neutrino Observatory

3.1 History at a Glance

In 1988, Dr. Francis Halzen and Dr. John Learned first proposed an experimental approach to detecting neutrinos using deep natural ice formations as a detection medium [38] after the first suggestion of using liquid water was made in 1960 [39]. Such a detector has many advantages when attempting to collect light from neutrino interactions, including the optical purity and abundance of glacial ice. With an active volume of $\sim$ 1 km^3, ice-based neutrino detectors would be sensitive to neutrinos from several sources, such as neutrinos from high-energy cosmic events taking place outside our galaxy and atmospheric neutrinos.

Three years after this initial proposal, sites for the first sensor deployment for an experiment prototype were scouted at the center of the geographic South Pole on the continent of Antarctica. By 1994 the first prototype, AMANDA (Antarctic Muon And Neutrino Detector Array) version A was deployed, which at glacial maximum depth of 1 km found the optical scattering from frozen bubbles to be too high for a practical application. Therefore, two years later, AMANDA-B was deployed with four sensor columns drilled down via hot water drill to a maximum sensor depth of 2 km, and found the light scattering from ice impurities to be two orders of magnitude less than that measured by AMANDA-A [39]. From 1995-2000, AMANDA was upgraded to a full 19-string

array of 667 sensors dubbed AMANDA-II, the last proof-of-concept stage that would increase the number of sensors by an order of magnitude before the main IceCube array (first proposed in 1999) would go on to increase the number of sensors by another order of magnitude. [40–42].

IceCube construction began in 2005, which incorporated the already-deployed AMANDA array, and concluded by the end of December 2010, making the detector fully operational in January 2011. Collecting data since the earliest stages of construction, IceCube has yielded world-leading results on multiple fronts of particle physics and astronomy, such as the first detection of extragalactic neutrinos, the first confirmed multi-messenger astronomical signal, precision oscillation parameter measurements, and foremost limits on multiple BSM models [43–46]. In particular, the IceCube Collaboration, with the full array surpassing 10 years of detector livetime, now has a large sample of atmospheric neutrinos within a range of energies and matter baselines unique to IceCube, making the detector highly sensitive to BSM oscillation effects including the NSI and neutrino decoherence phenomena discussed in this thesis.

3.2 Experiment Design and Operations

IceCube occupies a cubic-kilometer of South Pole glacial ice with 4860 digital optical modules (DOMs) evenly divided amongst 78 sensor cables (or "strings") spaced 125 m apart within a hexagonal grid [47, 48]. An additional set of eight specialized strings with high-quantum-efficiency (HQE) DOMs deployed at the center of the configuration compose the DeepCore array [49], making the total count of IceCube DOMs to 5160. The array occupies glacial depths of 1450 m to 2450 m below the surface, where DOMs in the main array are spaced 17 m apart while DeepCore DOMs are 7 m apart.

The subterranean array is accompanied by a surface array called IceTop, which is 81 stations containing two tanks, with one DOM inside each, that

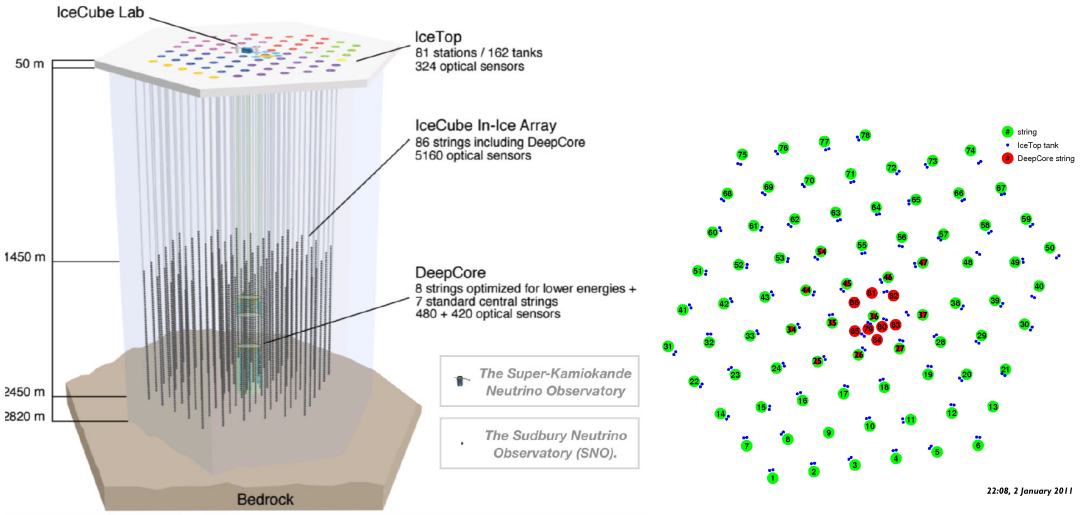

FIGURE 3.1: (Left) A schematic of the IceCube Neutrino Observatory, including the DeepCore array and the SNO and Super-Kamiokande detector volumes for comparison [50]. (Right) The surface distribution of IceCube strings (green), IceTop tanks (blue), and DeepCore strings (red) [51].

are filled with water that eventually freezes after deployment. This surface array, more than 1 km away from the detector active volume, acts both as an independent cosmic ray detector and a veto mechanism for very high energy cosmic ray air shower products incident upon the detector.

3.3 Digital Optical Module Design

The following reviews the design and operation of the detector light sensors, the digital optical modules (DOMs). DOMs are composed of two major components: the light-sensing apparatus called the *photomultiplier tube*, discussed in Section 3.3.1, and the onboard computer called the *main board*, reviewed in Subsection 3.3.2. The schematic of the DOM and the full DOM-cable assembly is displayed in Fig. 3.2.

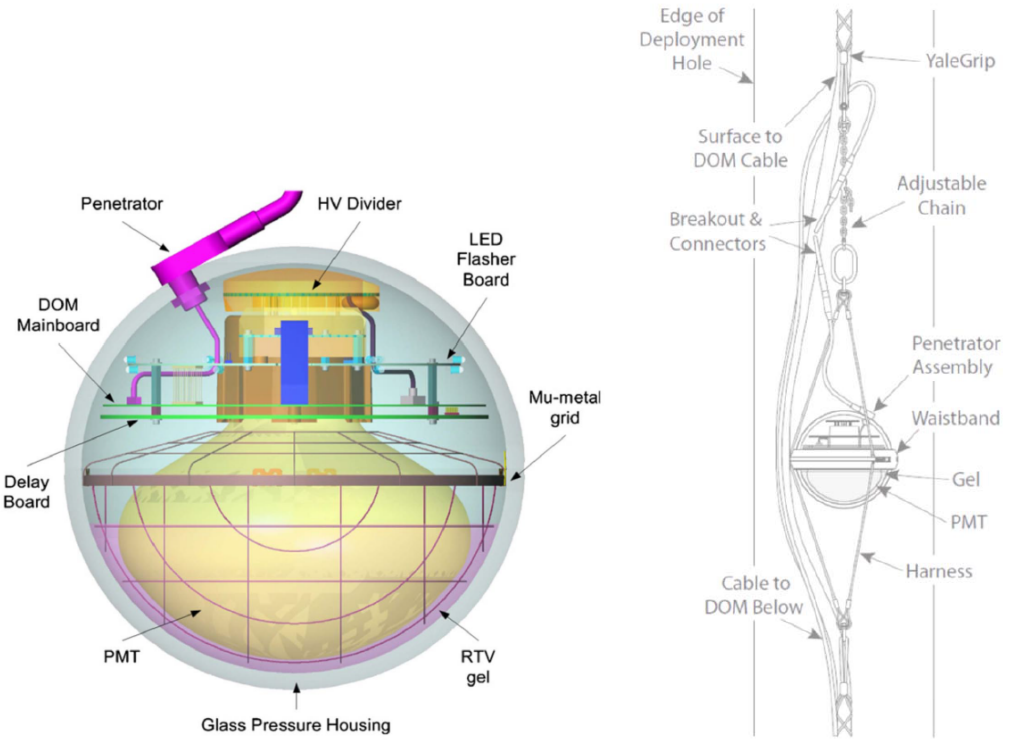

FIGURE 3.2: (Left) The schematic for the IceCube DOM [51]. (Right) The assembly for a single DOM mounted on an IceCube string [50].

3.3.1 Photomultiplier Tubes

The light-detecting component within each DOM is a down-facing 10" R7081-02 Hamamatsu Photonics photomultiplier tube (PMT) housed within the 0.5"-thick spherical borosilicate glass pressure vessel approximately 12" in diameter that also contains the remaining electronics of the DOM [52]. The PMT is able to detect photons with wavelengths inside the 300-650 nm range, with a peak quantum efficiency of 25% at 390 nm [53]. To avoid photon loss and maximize the desired yield of short-wavelength photons, the PMT sensor end is sealed against the glass housing with an optical gel and is protected from the ambient planetary magnetic field with a surrounding mu-metal wire mesh (Fig. 3.2 left). Among the 5160 PMTs, the average effective photocathode area is 550 cm^2.

The HQE DOMs within DeepCore employ a different model of PMT, the Hamamatsu R7081-02MOD, which have a maximum quantum of efficiency of 34%, a 36% improvement to the main array DOM efficiency.

3.3.2 Main Board

The hardware that determines the trigger conditions for sending a signal from a DOM up the DOM cable (Fig. 3.2, right) to the surface data acquisition system, or *DAQ*, is the DOM main board. It is a circular motherboard with a central hole that allows the board to fit on the neck of the PMT, resting above the photocathode bubble (Fig. 3.2, left).

When the PMT detects at least one photon with enough charge to trigger the board discriminator, the signal collection process is initiated. Two comparator circuits, one at high resolution and the other at low resolution, are used to determine if a charge signal is from either a single photon or multi-photon capture by the PMT [54].

The high-resolution comparator, with a resolution of 1 photoelectron[1] (PE) per $\sim$ 417 DAQ counts, triggers at single-photon, or single-*photoelectron* (SPE) events that have a peak voltage greater than 1.28 mV (0.2325 PE), enough to avoid triggering from electronic/thermal noise. The low-resolution comparator, with a resolution of 1 PE per $\sim$ 42 DAQ counts, is designed to trigger for multi-photoelectron (MPE) events [55].

When a comparator is triggered, the signal is directed to four input channels, where three of the channels pass the signal through a loop that delays by 75 ns to reconstruct the earliest component of the signal. These three channels each then direct the signal to distinct wide-band amplifiers with gains of separate orders of magnitude (0.1, 1.0, 10.0). The various gains allow a custom 10-bit Analog Transient Waveform Digitizer (ATWD) to take the amplified signals and discriminate between a wide range of photon counts. To avoid keeping the DOM from detecting further signals, a second ATWD is integrated parallel to the first, such that any signals received when the first ATWD is processing are passed to the second. The fourth channel from the comparator sends signals

[1]The photoelectron is a unit of detected charge from the detection of a single photon in the DOM.

through an express amplification circuit that is then digitized and sent up the cable while the other three channels are processed [55]. A schematic of the trigger layout is displayed in Fig. 3.3.

3.4 Signal Classification and Transmission

Additional signal processing takes place on-site after the individual DOM triggering by way of coincidence thresholds. At the surface, the IceCube Lab (ICL) compares every DOM's triggered discriminator signal to that of the DOM's first- and second-degree neighbors, and if any of the neighbors have had their discriminator triggered within a 1μs window, the total signal between those DOMs is labelled a "hard local coincidence" (HLC). The case of a DOM triggering with no coincident neighbor triggers is a "soft local coincidence" (SLC). When either an SLC or HLC takes place, the array registers a *hit*, or fundamental unit of recorded information, that is sent to the ICL. Each hit is composed of the signal trigger timing and waveform information. In the case of an SLC, only the highest fast Analog-to-Digital converter value is sent and the two adjacent bin counts are transmitted, whereas the full waveform information is sent when a HLC is triggered. Every DOM stores data for intervals of 1 second before transmitting hits, but are capable of storing 10 seconds of data with onboard RAM in the event of failed initial transmission [55, 56].

3.4.1 Triggers and Filters

Hit information is collected and processed within the ICL's computer array. Events, or coincident collections of hits, are categorized by two forms of processing: *triggers* (not to be confused with DOM triggers) and *filters*. Triggers use the software package pDAQ to examine hit waveform data and determine if an event is likely a particle signal. There are many triggers applied to hit collections, and should an event pass a given trigger, the now-particle event is

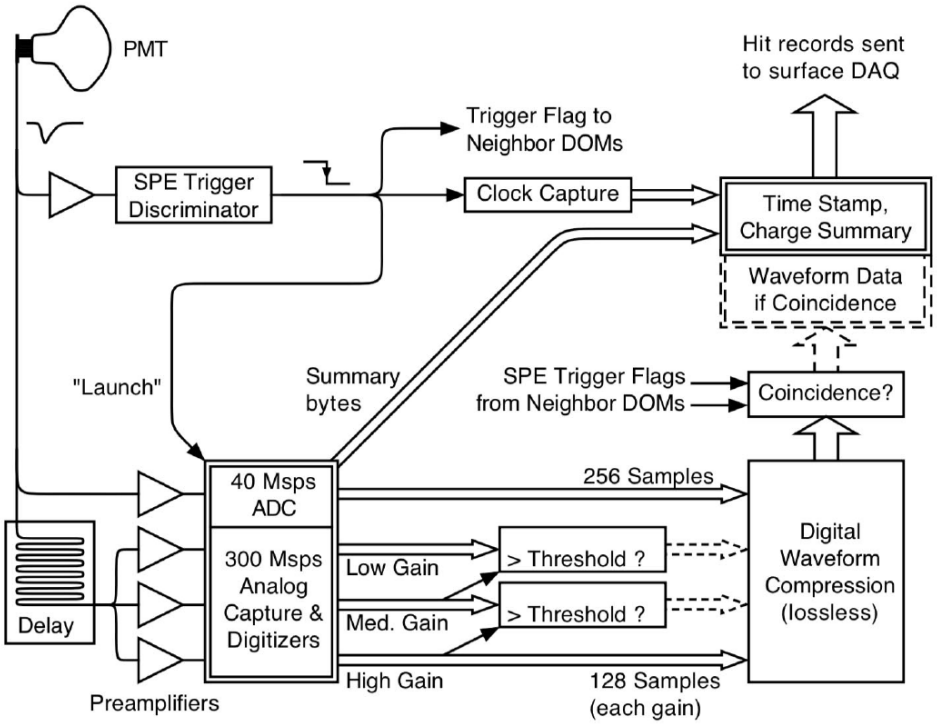

FIGURE 3.3: The PMT data triggering and filtering architecture enacted by each individual DOM main board [53].

categorized according to the filters. Filters are applied through the Processing and Filtering (PnF) system and account for various particle event searches. A filter will do a simplified reconstruction of the event and determine if the event merits further examination as a particle event candidate [55, 56].

3.4.2 Exporting Data

Events that have been collected by their respective filters are transmitted via satellite from the ICL to IceCube Data Warehouse in Madison, Wisconsin, to a limited rate of 100 GB per day. Due to the bulk of information collected and the limited bandwidth for satellite transmission, filters at the ICL have "prescales" that determine what fraction of the bulk data will actually be passed through that filter. This provides filtered data for immediate use offsite while the non-filtered data, stored on magnetic tape at the ICL, is physically retrieved and brought to the mainland for use and archival every austral summer. Data that has reached IceCube's data storage facilities is further processed by *offline* filters

that examine candidate events with higher computational sophistication and is then made available to collaborators for sample construction and analysis work [56].

3.5 Detector Calibration

IceCube collects raw data in the form of charge and timing information, and thus calibration of (photon) charge and timing measurements across all steps of data collection is necessary.

With regard to timing measurements, the Reciprocal Active Pulsing Calibration (RAPCal) software implements a synchronization protocol between all DOM main boards and the ICL timing circuits such that events are labeled within nanosecond precision. The ICL further adds to the each event time stamp by adding the corresponding Coordinated Universal Time (UTC). To measure the timing offsets between individual DOMs and the ICL, the ICL master clock sends 20 MHz bipolar square wave pulses to each string's DOM hub, or computer regulating that string of DOMs, and the hub relays the pulse to the individual DOMs. DOMs time stamp the instance of receiving the pulse according to their main board clocks, then return a 20 MHz bipolar square wave pulse back up the cable to the ICL. The ICL marks the receipt time and compares this value to the initial pulse launch time to measure the individual DOM clock offsets [56].

Calibration of charge measurements is done by sending pulses of light between DOMs using "flasher" light-emitting diodes (LEDs) built into the DOM main boards (Fig. 3.2). Each main board contains 6 pairs of LEDs equidistantly spaced, with one LED per pair angled 48° up from the main board and the other angled radially outwards from the DOM central axis. These LED arrays are used for multiple purposes, such as event simulation and glacial ice studies, but for calibration the LED arrays are instructed to emit nanosecond-scale pulses

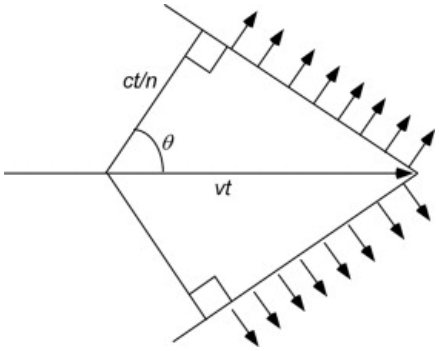

FIGURE 3.4: A 2D schematic of a Cherenkov cone, adapted from Ref. [57]. The center horizontal arrow is the charged particle trajectory, with velocity v, and the outwardly-radiating arrows represent the coherent Cherenkov wavefront. The index of refraction for the medium is n and the cone opening angle is given by θ.

of photons that are received by other DOMs across the detector to measure the DOM responses, which in turn lets the experiment calibrate each DOM's charge response [56].

3.6 Cherenkov Radiation

While neutral atoms have net-zero charge, individual nucleons and electrons can interact electromagnetically. When a charge comes into the vicinity of the neutral atom, the atom's like-charges will be repelled away within the bounds of the atom and the unlike-charges will be attracted to the source. This process is called *polarization*. Water is a dipolar molecule, meaning that the interaction between the constituent atoms forms a natural polarization between the electrons and nucleons without external charges, despite the molecule being electrically neutral in total charge. When water is frozen into ice, these molecules are still dipolar, and can experience further polarization by electric fields. For instance, when a charged particle travels through ice, the charge will increase the polarization of nearby water molecules. As the particle distances from the polarized water molecules, the molecules release photon (light) radiation as they return to their original polarization.

A unique form of this phenomenon is when the charged particle moves

through the ice faster than the *speed of light in water*[2], as transparent media electromagnetically interacts with light such that the velocity of light decreases. This high-energy particle example is shown in Fig. 3.4, where at this scale of energy, the light released from the electromagnetic disturbance constructively interferes to form a cone (outward arrows) in the charged particle's direction (horizontal arrow). A common analogy for this phenomenon is a sonic boom for a supersonic plane. This is *Cherenkov* radiation, named after Pavel Cherenkov, who first detected the phenomenon in 1934 [58].

In general, for any dielectric material, Cherenkov photons will be emitted if a charged particle satisfies the velocity condition $v_{\text{particle}} > c/n$, where c is the speed of light in vacuum and n is the index of refraction for the material, which quantifies how much a material electromagnetically interferes with the propagation of vaccum light. The opening angle θ of the subsequent cone of Cherenkov photons ("Cherenkov cone") is then $\theta = \cos^{-1}(1/n\beta)$, where $\beta = v_{\text{particle}}/c$. For IceCube, where the detector medium is ice (n = 1.31, or $c_{\text{water}} = 0.75c_{\text{vacuum}}$), relativistic particles ($v_{\text{particle}} \approx c$) from neutrino-matter interactions produce cones with 41° opening angles. The wavelength range of these photons mostly overlaps with that of the visible spectrum, from 300 nm to 600 nm.

3.7 Characteristics of Deep Antarctic Glacial Ice

As neutrino signals are derived from Cherenkov light emission within the detector, effects on the transmission of signal light are a primary concern. The main effect on light propagation within the South Pole glacier is the optical properties of the ice itself, with their treatment described in this section.

[2]Matter can still not move faster than the speed of light in *vacuum*.

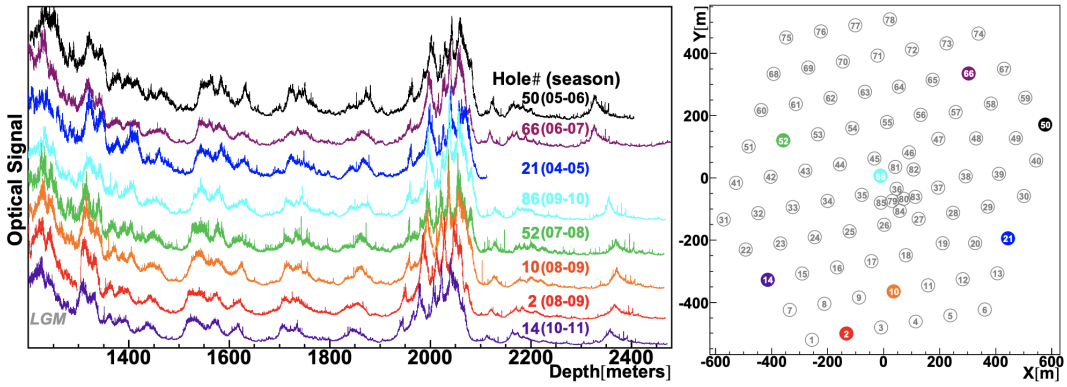

FIGURE 3.5: The results of the IceCube dust logging. Left: optical response as a function of depth for each logged borehole, denoted by different colors. Hole 21 has an abrupt stop in the profile at $\sim$ 2000 m after a logger malfunction. Right: the aerial map of the IceCube array, with numbered markers representing the locations of boreholes. Colored markers correspond to the holes that have been dust logged in the left plot. Figure adapted from Ref. [59].

3.7.1 Bulk Ice

Effects on the propagation of light within ice are measured in light *absorption* and *scattering*, which are wavelength-dependent. The largest sources of absorption and scattering within the bulk glacial ice ("bulk ice") are air bubbles and atmospheric impurities (dust) that have been trapped within the ice after fallen snow has been compressed for thousands of years. During the AMANDA phase of construction, it was found that scattering on air bubbles was the predominant source of error for light measurements in ice above 1400 m of depth. Below 1400 m, the weight of the above ice was sufficient to collapse trapped air bubbles, making *clathrate*, a form of ice with diffuse air molecules embedded in the ice but no bubbles. Thus, the IceCube array was deployed below 1400 m; specifically, from 1450 to 2450 m, where the primary effect on light propagation is interactions with dust.

To accurately account for the effects of the dust within the glacier, devices called *dust loggers* were engineered to travel through drilled sensor boreholes, fire light beams laterally across the ice to pre-stationed opaque baffles, and record the back-scattered light from interactions with dust to determine the scattering and absorption for the corresponding ice depth. These devices were

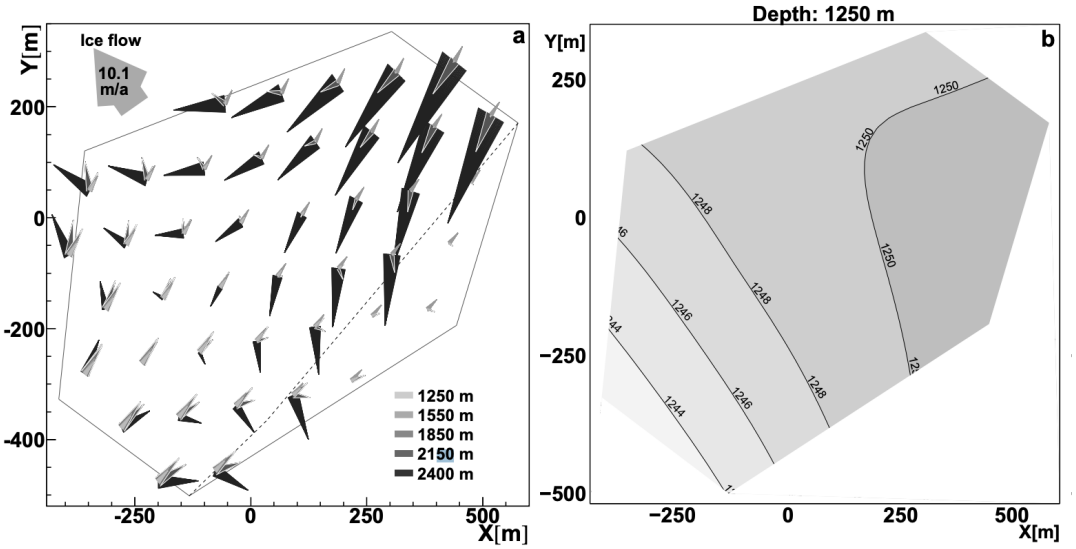

FIGURE 3.6: Left: an above view of the relative tilt between isochrons according to arrow size. Ice flow velocity is denoted by the top left arrow. Right: the cross-section of the tilt map at 1250 m, which shaded regions representing distinct isochrons. Figure adapted from Ref. [59].

deployed during both the AMANDA and IceCube constructions phases for three and six boreholes, respectively. The results of the logging are shown in Fig. 3.5, where a notable feature is the region of high dust density at 2000 m, corresponding to the midway instrumentation depth of IceCube (the IceCube "dust layer") [59]. When comparing the dust profiles for various boreholes, similar peaks in the concentration would be seen at different depths, implying the layers of ice are not necessarily parallel but have "tilt". Hence, tilt maps have been developed to display the depth variation for specified layers of optical properties corresponding to a particular age of ice ("isochrons"). The source of this tilt can be attributed to the slow shear and flow of the ice layers.

Further, it was found that the flow of ice has produced an optical anisotropy due to the birefringent nature of ice crystals [60]. Birefringence is the property of a material having an index of refraction that depends on the polarization and incident direction of light. This results in the double refraction of light, where the light is split by polarization and travels along different trajectories (Fig. 3.7 left).

Flow of the glacier ice induces shear between ice crystal grains that forces the

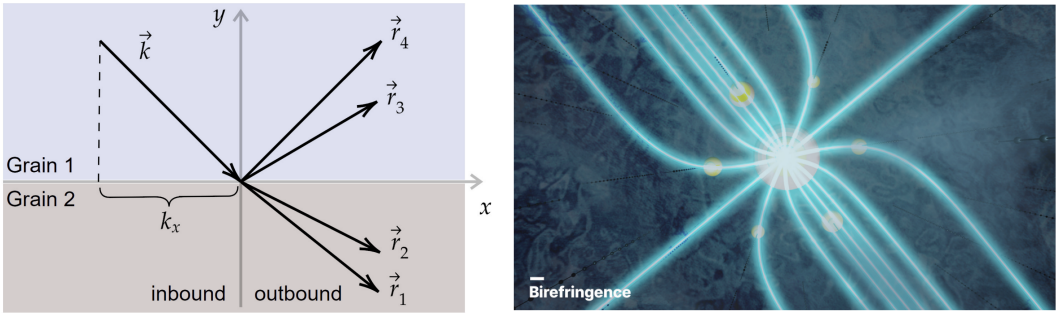

FIGURE 3.7: Left: a diagram of the double refraction and reflection effect of a birefringent grain boundary, where $\vec{k}$ is the incident ray of light. Right: an illustration of the optical anisotropy effect on a radial light source from ice birefringence in the South Pole glacial. Figure adapted from Ref. [60].

crystal (long) axis to reorient orthogonal to the flow. Ice crystals deep within the Antarctic glacier are birefringent, and light transitioning between orthogonal grains undergoes double refraction. The compounded double refraction of light moving through the bulk ice thus results in light diffusion that is greatest along the flow axis and a small amount of deflection towards the flow axis (Fig. 3.7 right). This is the latest effect to be included in IceCube optical model of the ice, discussed in Subsection 3.7.3.

3.7.2 Borehole Ice Optical Properties

To install the DOM strings within the glacier, a hot water drill bores columns ("boreholes") that the DOM cables are lowered into. These boreholes are filled with water, which eventually freezes inward from the hole wall. In that time, the contact between liquid water and glacial ice releases the embedded air within the clathrate to produce bubbles that are trapped during the refreezing. The result is a column of bubbles in the borehole that scatter incident light ("hole ice") [61–64]. From camera studies of the boreholes it was determined that bubbles do not fill the entire column but are concentrated to a central $\sim 5-10$ cm radius. The current model of the effect from hole ice is described in the review of analysis nuisance parameter treatments in Section 6.6.7.

3.7.3 Models of Instrumented Ice

To incorporate the optical properties of the south pole ice in simulation, models are required. The collection of IceCube ice model are the South Pole ice (SPICE) models, the first being SPICE1.

SPICE1 measures scattering through the effective scattering length $\lambda_e = \lambda_s/(1 - \langle\cos\theta\rangle)$, where λ_s is the average length between scatters and $\langle\cos\theta\rangle$ is the average scattering angle for large numbers of scattering events. The effective scattering parameter is thus $b_e = 1/\lambda_e$. As a function of ice depth z and light wavelength λ, in nm, the parameter is $b_e(\lambda, z) = (\lambda/400)^{-\alpha} b_e(400, z)$, where α is the power law index for calculating the scattering from the value of scattering for 400 nm light at depth z $[b_e(400, z)]$. Similarly, the absorption is measured through the parameter $a = 1/\lambda_a$, where λ_a is the length at which the survival probability for light is $1/e$. Converted to a function of z and λ, $a(\lambda, z) = (\lambda/400)^{-\kappa} a_{\text{dust}}(400, z) + Ae^{B/\lambda}(1+0.01\delta\tau)$, where the first term follows the form of $b_e(\lambda, z)$ with power law index κ and $a_{\text{dust}}(400, z) \approx 400^{-\kappa}[D \cdot b_e(400, z) + E]$ is the absorption measured for 400 nm light at depth z and correlation parameters D and E. The second term, $Ae^{B/\lambda}(1 + 0.01\delta\tau)$, incorporates the exponential increase in absorption for the red to infrared wavelengths as a consequence of the dynamics for molecular water, scaled by the relative temperature difference $\delta\tau$ between the layer temperature and the temperature at depth 1730 m. Hence, SPICE1 models absorption and scattering through the six free parameters α, κ, A, B, D, and E [65]. The model divides instrumented ice into 10 m layers (170 total) and assigns each layer a value for each free parameter. SPICE1 also assumed each DOM had the same angular sensitivity and incorporated this effect into the model values of the free parameters, in turn folding in the effect of hole ice [66].

The next generation of SPICE models, SPICE2, would go on to incorporate

the dust logger data, tilt maps, and more string flasher data to further calibrate the six parameter values of the SPICE1 model [67]. SPICEMie improved this generation by fitting the absorption and scattering parameters to a Mie scattering treatment [65], while SPICELea includes the anisotropy discovered during the creation of SPICEMie through redefining the scattering parameter such that it has a directional dependence.

The subsequent SPICE generation, SPICE3, made improvements through a full-detector flasher fit, modeling the variation in LED emission, introducing a new relative DOM efficiency (RDE) parameter, and adding corrections to the layer scattering. SPICE3.2.1 is the last model of this generation, and was the latest stable model available for use in the analyses of this thesis. The new generation of ice models, SPICE-BFR, integrates the birefringence effect on light scattering and absorption [60], with SPICE-BFRv1 now the most current model in use.

3.8 Event Topologies

Neutrino event topologies come in two basic forms: "tracks" and "cascades".

Tracks are so named because the event will appear as a linear trajectory of light seen within the detector (Fig. 3.8). This is the result of a muon neutrino charged current interaction ($\nu_\mu CC$), where an incident muon neutrino interacts with an ice nucleon and produces a muon that carries 50% - 80% of the neutrino's energy in the same direction as the neutrino, to an excellent approximation. Being charged and supplied with the relativistic energy of the neutrino, the muon produces Cherenkov light along its trajectory, forming a track event. Relativistic muons have the capacity to travel significant distances ($\mathcal{O}$[10 km]), so IceCube most often does not contain the full track of the muon, which implies that track events have better directional resolution (1°) than energy resolution

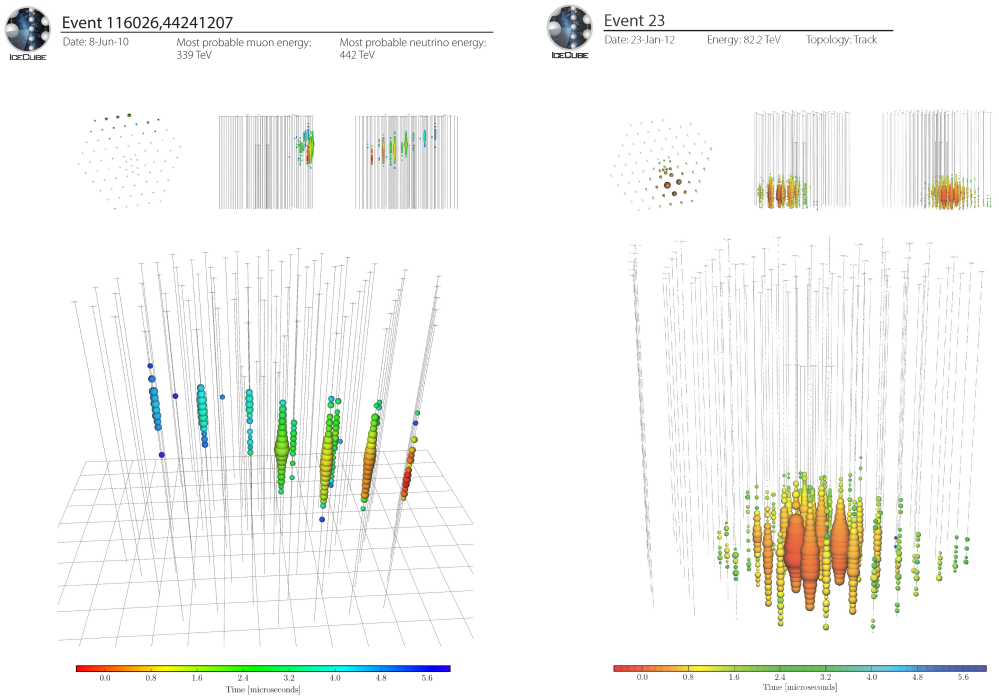

FIGURE 3.8: (Left) An example of a muon track event. (Right) An example of a neutrino cascade event. In both examples, time from the event start to end is read from red to blue following the bottom color spectrum [51].

($\sigma_{\log(E)} \sim 0.5$, where $\sigma_{\log(E)}$ is the standard deviation in the predicted difference between the muon reconstructed energy and true energy).

Cascades are events that take on a spherical topology with minor asymmetry correlated with the direction of the incident neutrino, and are the result of neutral current interactions between all neutrino flavors (νNC) and electron neutrino and tau neutrino charged current interactions ($\nu_e CC$, $\nu_\tau CC$). These events are divided according to their source mechanism: hadronic cascades and electromagnetic cascades. νNC interactions take place when a neutrino interacts with an ice nucleon and the result is a near-isotropic ejection of hadrons, which are relativistic and produce a spherical emission of photons. In $\nu_e CC$ interactions, the resulting electron has such high energy, it quickly emits gamma photons that decay into position-electron pairs that further emit photons, erupting into a cascade of photons and beta particles that emit light in a spherical

topology. $\nu_\tau CC$ interactions induce a cascade topology through a similar electromagnetic process.

Chapter 4

Monte Carlo Simulation Chain

Every aspect of a neutrino event in IceCube is simulated through the Monte Carlo method, including the initial neutrino-matter interaction, the propagation of Cherenkov photons, and the full detector response. This chapter reviews each of these steps, which ultimately results in Monte Carlo simulation ("MC") that is used for both of the analyses in this thesis. A schematic view of the MC generation, event selection, and final analysis fitting is given in Fig. 4.1.

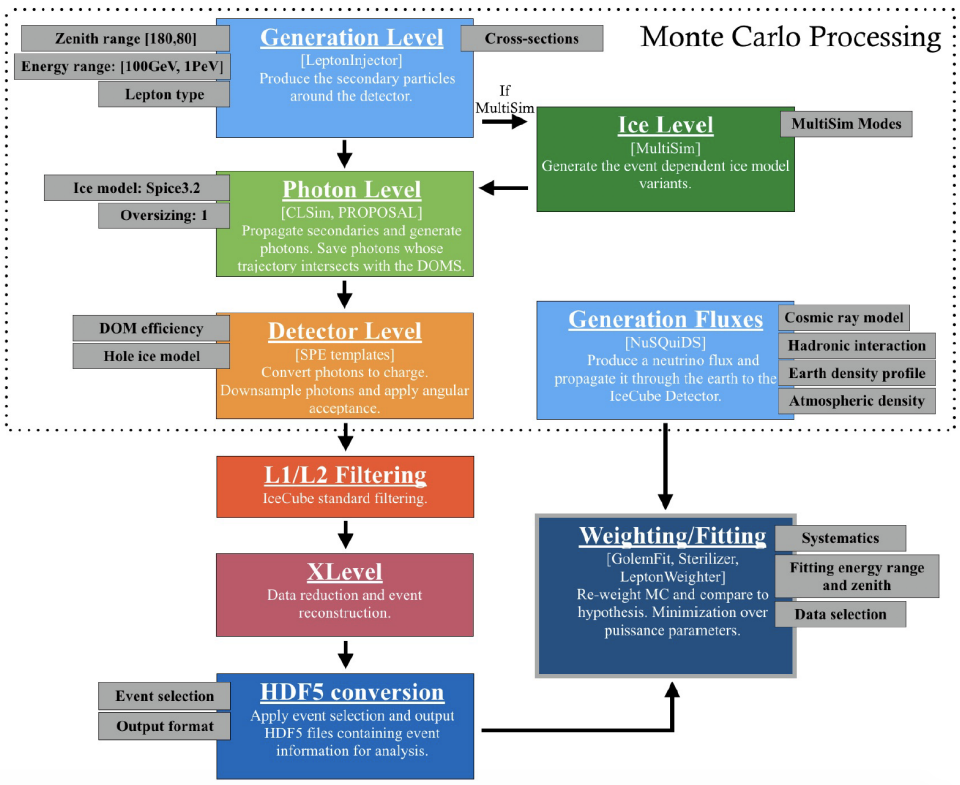

FIGURE 4.1: The organizational flow from simulation to test statistic calculation for the analyses in this thesis. Adapted from Ref. [50].

4.1 Detector Event Generation

The processing of simulation for analyses in this thesis follows Refs. [50, 68, 69] and is designed to be computationally efficient. Notice from the scheme in Fig. 4.1 that, rather than start the simulation process with neutrino production and follow the simulation chronologically, which is computationally expensive when incorporating BSM physics that may only step in at an interstitial step, simulation production starts with the neutrino interactions at the detector. Running many neutrino interaction events produces secondary particle distributions that are then associated with the relevant physics hypotheses at the reweighting stage of the simulation chain, bypassing the need to run multiple neutrino production models.

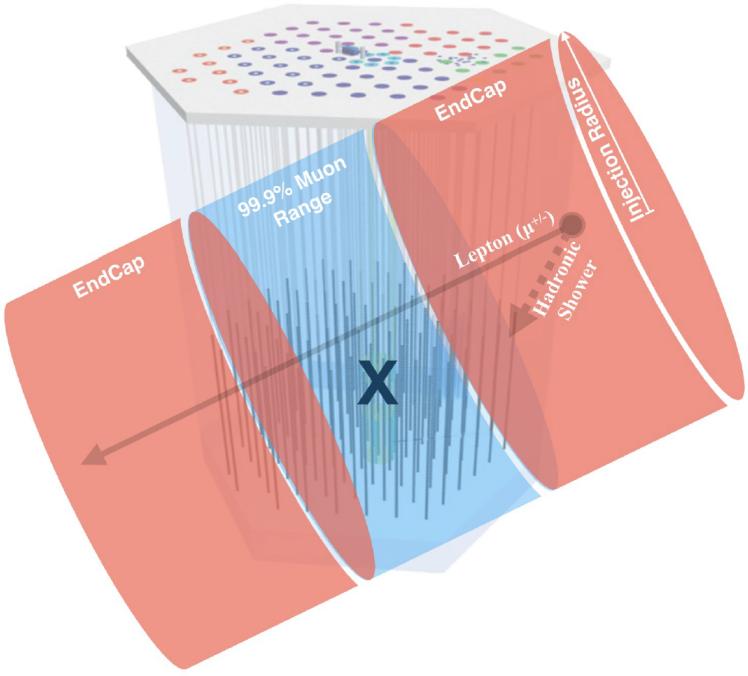

FIGURE 4.2: Example of an injected cylinder for a muon from LeptonInjector (not to scale). Adapted from Ref. [50].

The software that performs this secondary particle injection is LeptonInjector [70], which inserts final lepton state particle distributions in a volume that envelops a large swath of the volume in and around the detector, sampling primary ν_μ properties of 100 GeV - 1 PeV and $\cos\theta = 0.2$ to $\cos\theta = 1$. Energy

sampling follows a E^{-2} power law and the sampling for zenith and azimuth is isotropic. The injection volume is a cylinder with a long axis in the direction of the injected lepton[1], centered on the detector (Fig. 4.2). The cylinder length is approximately the lepton maximal ice range plus two 1200 m endcaps. Every event logs the primary neutrino energy, the lepton final energy and zenith, the Bjorken x and y components, the inelasticity probability, final column depth, and impact parameter. The simulation of the analyses in this thesis is comprised of $2 \cdot 10^9$ events that amount to an effective live time of ~ 500 years [50, 70].

4.2 Lepton/Photon Propagation

Once LeptonInjector selects the site of a neutrino interaction and produces the secondary particle distribution, the secondary particles are propagated through the ice via trajectories determined by the PROPOSAL software package [71]. The Cherenkov radiation that forms the track and cascade topologies from Section 3.8 is calculated along the particle trajectories from CLSim [72]. CLSim propagates the individual photons through the ice either until the photon is absorbed or collected by a detector DOM. It is at this step that the ice model of Section 3.7.3 is utilized to dictate the photon scattering.

The average muon from a track event produces more than 10^7 photons, which for $2 \cdot 10^9$ events, is considerably expensive for a computer CPU. A novel workaround of this obstacle is the use of specialized GPU cores to run thousands of photon propagations in parallel, making the Cherenkov light simulation for this amount of live time feasible. By this method, we are able to produce a 30% excess of photons per event for later "down-sampling" (random rejection) when producing the uncertainty templates for DOM efficiency.

[1] The leptons injected are primarily muons, as these are the predominant secondary particle of ν_μ interactions relevant to the analysis sample.

From the photon propagation, only the photons that reach a DOM are recorded in the output, including their incident angle, position, and detection time logged to form a photon series map that is employed in the next simulation step.

4.2.1 SnowStorm

A consequence of employing glacial bulk ice models with 340 parameters[2] is that extensive computational resources are required to accurately determine the effect of ice model uncertainty on high-statistics analyses. A traditional method is to create entire MC sets for uniform shifts in the absorption and scattering parameters across the entire detector depth, yet this method is guaranteed to miss any depth-dependent features in the uncertainty. Hence, a new method is required.

The SnowStorm software package [73] is generalized method of accomplishing this task through the perturbation of a single central MC. This central MC is unique in that rather than generating events at a fixed set of nuisance parameter values, each event is generated with it's own unique set of values. It is through this variation in parameter values that we answer two necessary questions in the error calculation: 1) How do observable distributions vary changes to the individual nuisance parameters? and 2) What is the systematic uncertainty on an analysis distribution from the uncertainty on nuisance vector $\vec{\eta}$?

To answer these questions, a few definitions are required — For a predicted distribution of events $\Psi_{\vec{\rho}}$ on a measurement $\vec{\rho}$, the uncertainty on the distribution is described by the covariance matrix $\Sigma_{\vec{\rho}}$. If $\psi_{\vec{\rho},\vec{\eta}}$ is the predicted event distribution assuming measurement $\vec{\rho}$ and nuisance (systematic uncertainty) parameter values $\vec{\eta}$, then we set $\vec{\eta} = \vec{0}$ such that $\Psi_{\vec{\rho}} = \psi_{\vec{\rho},\vec{0}}$ is the "central" model. If the effects of systematic uncertainties are sufficiently small, the distribution $\psi_{\vec{\rho},\vec{\eta}}$ may be Taylor-expanded with respect to the central model:

[2] 170 layers $\times$ 2 optical parameters, see Section 3.7.3

$$\psi_{\vec{\rho},\vec{\eta}} = \Psi_{\vec{\rho}} + \vec{\eta} \cdot \nabla_{\vec{\eta}} \left[\psi_{\vec{\rho},\vec{\eta}}\right]_{\vec{\eta}=\vec{0}} + \mathcal{O}(\eta^2), \tag{4.1}$$

where $\mathcal{O}(\eta^2)$ are the higher-order terms that may be treated as negligible.

To calculate the systematic uncertainties, SnowStorm first determines how $\psi_{\vec{\rho},\vec{\eta}}$ varies as a function of $\vec{\rho}$. In other words, the gradients $\vec{G}_{\vec{\rho}} = \nabla_{\vec{\eta}} \left[\psi_{\vec{\rho},\vec{\eta}}\right]_{\vec{\eta}=\vec{0}}$ are extracted. Assuming the nuisance parameters have symmetric, normalized distributions, one may write the $\vec{\eta}$ distribution as

$$P(\vec{\eta}) = \prod_i \frac{1}{\sigma\sqrt{2\pi}} e^{-\eta_i^2/2\sigma}, \tag{4.2}$$

where for simplicity we assume the product of nuisance parameters distributions is Gaussian. From here, the method of determining the nuisance parameter gradients with the best statistical performance is a "cutting" method, described as follows: first, the SnowStorm ensemble is divided ("cut") along one direction in η space. For simplicity, we choose a cut along $\eta_i = 0$ for an arbitrary i. The ensemble is then represented by two sets of distributions,

$$\psi_{\vec{\rho}}^{+i} = \int_0^\infty d\eta_i \int_{-\infty}^\infty d^{N-1} P(\vec{\eta}) \left(\Psi_{\vec{\rho}} + \vec{\eta} \cdot \vec{G}_{\vec{\rho}}\right) \tag{4.3}$$

$$\psi_{\vec{\rho}}^{-i} = \int_{-\infty}^0 d\eta_i \int_{-\infty}^\infty d^{N-1} P(\vec{\eta}) \left(\Psi_{\vec{\rho}} + \vec{\eta} \cdot \vec{G}_{\vec{\rho}}\right). \tag{4.4}$$

The integrals $\int_{-\infty}^{\infty} d^{N-1}$ are 0 except for η_i by symmetry, so the distribution sets reduce after evaluating the η_i integral:

$$\psi_{\vec{\rho}}^{\pm i} = \frac{1}{2}\Psi_{\vec{\rho}} \pm \frac{\sigma}{\sqrt{2\pi}} \vec{G}_{\vec{\rho},i}, \tag{4.5}$$

where $\vec{G}_{\vec{\rho},i}$ is the gradient along the η_i direction. Solving for $\vec{G}_{\vec{\rho},i}$,

$$\vec{G}_{\vec{\rho},i} = \frac{\sqrt{\pi}}{\sqrt{2}\sigma} \left(\psi_{\vec{\rho}}^{+i} - \psi_{\vec{\rho}}^{-i}\right). \tag{4.6}$$

Therefore, the full gradient vector $\vec{G}_{\vec{\rho}}$ is found by cutting the SnowStorm ensemble along every η_i for the N nuisance parameters. This answers the first

question regarding how distributions change with different values of each nuisance parameter.

The final uncertainty on distribution $\Psi_{\vec{\rho}}$ is then encapsulated through a covariance matrix in the analysis binning. Tecall that the gradient functions are dependent on the distribution variables, i.e. $G_i(E_\alpha) = G_{i;\alpha}$. Then the binned analysis space covariance matrix is represented by

$$\Sigma_{\alpha,\beta} = G_{i;\alpha} \Xi G_{j;\beta}, \tag{4.7}$$

where Ξ is an analysis-dependent covariance matrix of constrains on $e\vec{t}a$ that can be derived from calibration data.

This method is employed in determining the bulk ice uncertainties through a fast Fourier transform (FFT) method on the scattering and absorption coefficients in a technique described in Section 6.6.6.

4.3 Detector Response

The last step in the event simulation is the detector response, which begins with the DOMs. After specifying a desired DOM efficiency, which for the central MC of this thesis is 0.97, the photons that are not rejected have a DOM-acceptance probability corresponding to their incident direction and the DOM angular acceptance curve. Accepted photons generate Monte Carlo photoelectrons (MCPEs) at the DOM PMT. Single photoelectron (SPE) charge templates for each DOM were developed by Ref. [50] from in-situ PMT measurements to sample the MCPE's PMT anode charge response. This stage also includes charge contributions from thermal, signal, and PMT noise. The photoelectron pulses are then fit to waveforms in the WaveDeform software [74] to create the DOM hits defined in Section 3.4. Output from this stage is what constitutes "mature" MC that can be used in event reconstruction like actual data.

4.4 Neutrino Production and Propagation

With the full detector event generation and response prepared, physics hypothesis related to neutrino production and propagation can now be produced which will later be used to reweight the final detector MC. Here, we review neutrino production and propagation for SM physics.

The leptons produced at the event generation stage must correspond to a neutrino flux. We start with the atmospheric neutrino flux: cosmic ray (CR), hadronic interaction, and atmospheric temperature models are fed to the MCEq software [75, 76] to calculate the air shower characteristics of a CR-atmosphere interaction, with a month-averaged atmospheric neutrino flux ultimately extracted. The neutrinos are then propagated through Earth via the neutrino Simple Quantum Integro-Differential Solver (nuSQuIDS) [77], which is built off the basic infrastructure of SQuIDS and accounts for coherent and non-coherent interactions, as well as tau neutrino regeneration. The result is the neutrino flux at the detector, and these fluxes are what delineate physics hypotheses in an analysis that are later translated to reweighted event distributions from the detector response stage. A separate propagation run is performed to calculate the prompt neutrino flux from charmed meson decay in air showers, which is separate from the "conventional" atmospheric neutrino flux from pion and kaon decays. Hence, generating hypothesis simulation for physics such as NSI and decoherence only requires the neutrino propagation stage and not the sum of computations described up to now.

Similar to the atmospheric flux, the astrophysical component is produced from an initial energy power law with normalization Φ_{astro} and spectral index γ_{astro}: $\Phi(\nu_\mu + \overline{\nu}_\mu) = \Phi_{\text{astro}}(E/100\,\text{TeV})^{\gamma_{\text{astro}}}$.

4.4.1 nuSQuIDS

The software program nuSQuIDS dictates the neutrino propagation step in the simulation chain, and since the new physics models of this thesis alter the propagation of neutrinos, here we discuss the operation principles of the program. This review follows the details and documentation in Refs. [77, 78].

nuSQuIDS propagates neutrino ensembles in the open quantum system formalism, where a flux-weighted ensemble is described by the state density matrix

$$\rho(E,x) = \sum_{\alpha} \phi_{\alpha}(E,x) \left|\nu_{\alpha}\right\rangle \left\langle\nu_{\alpha}\right|, \tag{4.8}$$

where $|\nu_\alpha\rangle$ is the flavor α eigenstate and ϕ_α is the flux of flavor α at neutrino energy E and propagation distance x. Note that nuSQuIDS can accommodate additional neutrino flavor/mass states beyond the conventional three-neutrino model. More on the open quantum system formalism is discussed in Section 7.1.

From here, the evolution of the system is described by the von Neumann equation:

$$\frac{\partial\rho(E,x)}{\partial x} = -i[H(E,x), \rho(E,x)], \tag{4.9}$$

such that H is the total system Hamiltonian. H can be divided into two components— the vacuum oscillations term H_0 and the matter interaction term H_1:

$$H(E,x) = H_0(E) + H_1(E,x), \tag{4.10}$$

with

$$H_0(E) = \frac{1}{2E}\text{diag}(0, \Delta m_2 1^2, \Delta m_3 1^2) \tag{4.11}$$

$$H_1(E,x) = \sqrt{2} G_F N_e(x) U^{\dagger} \text{diag}(1,0,0) U, \tag{4.12}$$

where U is the PMNS neutrino mixing matrix, G_F is the Fermi constant, and

Δm^2 are the neutrino square mass splittings. In the case of antineutrinos, $H_1 \to -H_1^*$. Solutions to the evolution of the H_0 component can be found analytically, so a convenient basis from which to do the full evolution calculation is to transform to the *interaction basis*, where such a transformation on $\rho(E, x)$ follows

$$\rho_I(E, x) = e^{-iH_0 x} \rho(E, x) e^{iH_0 x}. \tag{4.13}$$

Hence, with analytic solutions available for H_0, we shift our focus to solutions for the evolution of the matter interaction term in the interaction picture:

$$\frac{\partial \rho_I(E, x)}{\partial x} = -i[H_{I,1}(E, x), \rho_I(E, x)]. \tag{4.14}$$

With this framework, we may now assume that operators are implicitly in the interaction picture (dropping the I) write the full expressions for neutrino ensembles that will experience additional effects including noncoherent scattering and Glashow resonances.

These expressions for neutrinos (ρ) and antineutrinos ($\overline{\rho}$) are

$$\frac{\partial \rho(E, x)}{\partial x} = -i[H_1(E, x), \rho(E, x)] - \{\Gamma(E, x), \rho(E, x)\} - F\left[\rho, \overline{\rho}; E, x\right] \tag{4.15}$$

$$\frac{\partial \overline{\rho}(E, x)}{\partial x} = i[H_1^*(E, x), \overline{\rho}(E, x)] - \{\overline{\Gamma}(E, x), \overline{\rho}(E, x)\} - \overline{F}\left[\rho, \overline{\rho}; E, x\right], \tag{4.16}$$

where Γ, $\overline{\Gamma}$ are the attenuation contributions from noncoherent scattering and F, $\overline{F}$ are functionals that account for tau regeneration (Section 8.3.1), Glashow resonance, neutrino-antineutrino coupling, and low-energy neutrino re-injection from neutral current interactions.

Attenuation terms Γ and $\overline{\Gamma}$ have the form

$$\Gamma(E, x) = \frac{1}{2} \sum_\alpha \frac{\Pi_\alpha(E, x)}{\lambda^\alpha_{\rm NC}(E, x) + \lambda^\alpha_{\rm CC}(E, x)} \tag{4.17}$$

$$\overline{\Gamma}(E, x) = \frac{1}{2} \sum_\alpha \frac{\overline{\Pi}_\alpha(E, x)}{\overline{\lambda}^\alpha_{\rm NC}(E, x) + \overline{\lambda}^\alpha_{\rm CC}(E, x) + \overline{\lambda}^\alpha_{\rm GR}(E, x)}, \tag{4.18}$$

with Π_α the neutrino projection operator onto flavor α, the neutral (charged) current interaction length for matter nucleon density $N_{\rm nuc}$ and the Glashow resonance mean free path for electron number density N_e given by

$$\lambda_{\rm NC,(CC)} = \frac{1}{N_{\rm nuc}(x)\sigma^{\alpha}_{\rm NC,(CC)}(E)} \tag{4.19}$$

$$\overline{\lambda}_{\rm GR} = \frac{1}{N_{\rm e}(x)\sigma^{\alpha}_{\rm (GR)}(E)}. \tag{4.20}$$

The functionals F and $\overline{F}$ are

$$\begin{aligned} F\left[\rho,\overline{\rho};E,x\right] = &\sum_{\alpha}\Pi_\alpha(E,x)\int_E^\infty \frac{\mathrm{Tr}[\Pi(E_{\nu_\alpha},x)\rho(E_{\nu_\alpha},x)]}{\lambda^{\alpha}_{\rm NC}(E_{\nu_\alpha},x)}\frac{\partial N^{\alpha}_{\rm NC}(E_{\nu_\alpha},E)}{\partial E}dE_{\nu_\alpha} \\ &+\Pi_\tau(E,x)\int_E^\infty\int_{E_\tau}^\infty \frac{\mathrm{Tr}[\Pi(E_{\nu_\tau},x)\rho(E_{\nu_\tau},x)]}{\lambda^{\tau}_{\rm NC}(E_{\nu_\tau},x)}\frac{\partial N^{\tau}_{\rm NC}(E_{\nu_\tau},E)}{\partial E} \\ &\times\frac{\partial N^{\rm all}_{\rm dec}(E_\tau,E)}{\partial E}dE_{\nu_\tau}dE_\tau \\ &+\left[\mathrm{Br}_e\Pi_e(E,x)+\mathrm{Br}_\mu\Pi_\mu(E,x)\right]\int_E^\infty\int_{E_\tau}^\infty \frac{\mathrm{Tr}\left[\overline{\Pi}(E_{\nu_\tau},x)\overline{\rho}(E_{\nu_\tau},x)\right]}{\overline{\lambda}^{\tau}_{\rm NC}(E_{\overline{\nu}_\tau},x)} \\ &\times\frac{\partial\overline{N}^{\tau}_{\rm CC}(E_{\overline{\nu}_\tau},E)}{\partial E}\frac{\partial\overline{N}^{\rm lep}_{\rm dec}(E_\tau,E)}{\partial E}dE_{\overline{\nu}_\tau}dE_\tau, \end{aligned} \tag{4.21}$$

$$\begin{aligned} \overline{F}\left[\rho,\overline{\rho};E,x\right] = &\sum_{\alpha}\overline{\Pi}_\alpha(E,x)\int_E^\infty \frac{\mathrm{Tr}\left[\overline{\Pi}(E_{\overline{\nu}_\alpha},x)\overline{\rho}(E_{\overline{\nu}_\alpha},x)\right]}{\overline{\lambda}^{\alpha}_{\rm NC}(E_{\overline{\nu}_\alpha},x)}\frac{\partial\overline{N}^{\alpha}_{\rm NC}(E_{\overline{\nu}_\alpha},E)}{\partial E}dE_{\overline{\nu}_\alpha} \\ &+\overline{\Pi}_\tau(E,x)\int_E^\infty\int_{E_\tau}^\infty \frac{\mathrm{Tr}\left[\overline{\Pi}(E_{\overline{\nu}_\tau},x)\overline{\rho}(E_{\overline{\nu}_\tau},x)\right]}{\overline{\lambda}^{\tau}_{\rm NC}(E_{\overline{\nu}_\tau},x)}\frac{\partial\overline{N}^{\tau}_{\rm NC}(E_{\overline{\nu}_\tau},E)}{\partial E} \\ &\times\frac{\partial\overline{N}^{\rm all}_{\rm dec}(E_\tau,E)}{\partial E}dE_{\overline{\nu}_\tau}dE_\tau \\ &+\left[\mathrm{Br}_e\overline{\Pi}_e(E,x)+\mathrm{Br}_\mu\overline{\Pi}_\mu(E,x)\right]\int_E^\infty\int_{E_\tau}^\infty \frac{\mathrm{Tr}[\Pi(E_{\nu_\tau},x)\rho(E_{\nu_\tau},x)]}{\lambda^{\tau}_{\rm NC}(E_{\nu_\tau},x)} \\ &\times\frac{\partial N^{\tau}_{\rm CC}(E_{\nu_\tau},E)}{\partial E}\frac{\partial N^{\rm lep}_{\rm dec}(E_\tau,E)}{\partial E}dE_{\nu_\tau}dE_\tau \\ &+\left(\sum_{\alpha}\overline{\Pi}_\alpha(E,x)\right)\int_E^\infty \frac{\mathrm{Tr}\left[\overline{\Pi}_e(E_{\overline{\nu}_e},x)\overline{\rho}(E_{\overline{\nu}_e},x)\right]}{\overline{\lambda}^{e}_{\rm GR}(E_{\overline{\nu}_e},x)} \\ &\times\frac{\partial\overline{N}^{e}_{\rm GR}(E_{\overline{\nu}_e},E)}{\partial E}dE_{\overline{\nu}_e}, \end{aligned} \tag{4.22}$$

where NC, CC, and Glashow interactions are given by

$$\frac{\partial N^{\tau}_{\mathrm{NC(CC))}}(E_{\nu_\tau}, E)}{\partial E} = \frac{1}{\sigma^{\alpha}_{\mathrm{NC(CC)}}(E_{\nu_\alpha})} \frac{\partial \sigma^{\alpha}_{\mathrm{NC(CC)}}(E_{\nu_\alpha}, E_\alpha)}{\partial E_\alpha} \tag{4.23}$$

$$\frac{\partial \overline{N}^{e}_{\mathrm{GR}}(E_{\overline{\nu}_e}, E)}{\partial E} = \frac{1}{\overline{\sigma}^{e}_{\mathrm{GR}}(E_{\overline{\nu}_e})} \frac{\partial \overline{\sigma}^{e}_{\mathrm{GR}}(E_{\overline{\nu}_e}, E_e)}{\partial E_e}, \tag{4.24}$$

and Br_α is the $\tau \to \nu_\alpha$ branching ratio. The τ decay distributions from all modes ($N^{\mathrm{all}}_{\mathrm{dec}}$) and leptonic-only modes ($N^{\mathrm{lep}}_{\mathrm{dec}}$) are represented by

$$\frac{\partial N^{\mathrm{lep}}_{\mathrm{dec}}(E_\tau, E)}{\partial E} = \frac{1}{\tilde{\Gamma}^{\tau}_{\mathrm{lep}}(E_\tau)} \frac{\partial \tilde{\Gamma}^{\tau}_{\mathrm{lep}}(E_\tau, E)}{\partial E} \tag{4.25}$$

$$\frac{\partial N^{\mathrm{all}}_{\mathrm{dec}}(E_\tau, E)}{\partial E} = \frac{1}{\tilde{\Gamma}^{\tau}_{\mathrm{all}}(E_\tau)} \frac{\partial \tilde{\Gamma}^{\tau}_{\mathrm{all}}(E_\tau, E)}{\partial E}, \tag{4.26}$$

where $\tilde{\Gamma}^{\tau}(E_\tau) = E_\tau \tau_\tau / m_t$ such that τ_τ is the tau-lepton decay lifetime and E_τ and m_τ are the tau energy and mass, respectively.

To solve Eqs. 4.15 and 4.16, nuSQuIDS uses a C++ framework to perform a numeric calculation with parameters set by the user. The user specifies the number of discrete propagation steps are to be calculated, and in the multi-energy mode, also specifies the binning in energy. Any mixing parameter can be modified, and the Body and Track objects are customizable such that neutrinos may be propagated through any user-specified material. Output files are serialized such that information and format allow for a file to be used as an initial flux that can be fed to nuSQuIDS for further propagation. Lastly, a feature of nuSQuIDS is the ability to add models of new physics through the construction of new inherited classes that may also be folded into the nuSQuIDS flux serialization. Examples of such new physics used in nuSQuIDS can be seen in Sections 6.2.2 and 8.2.

Part III

Neutrino Nonstandard Interactions

Chapter 5

Theory of Nonstandard Interactions

The origin of neutrino nonstandard interactions, or NSI[1], is in two papers released by Dr. Lincoln Wolfenstein in 1978-1979. Neutrino flavor oscillations had yet been discovered and there was no resolution to the mystery of missing SM-predicted electron neutrinos from the Sun (the "solar neutrino problem") [13, 14]. Oscillation to other neutrino flavors had been previously suggested by Dr. Bruno Pontecorvo [15, 25], and from that notion Wolfenstein derived a formalism that posited flavor-changing interactions for neutrinos exiting the Sun and travelling through Earth [79, 80]. This established the Mikheyev-Smirnov-Wolfenstein (MSW) effect, in which the potential from the matter a neutrino travels through can generate oscillation resonances [28, 81].

While the final model of neutrino vacuum and matter oscillations is different than what Wolfenstein first proposed, the formalism in Refs. [28, 81] is a general method for adding new matter effects to standard neutrino oscillations. It is through this formalism that neutrino-matter interactions not described by the SM (NSI) are introduced.

For detailed reviews of the formalism, motivations, and latest constraints on NSI, see Refs. [82–84].

[1] Specifically, NSI refers to neutrino-matter nonstandard interactions, excluding models of nonstandard neutrino *self* interactions (NSSI).

5.1 Motivation for NSI

NSI are of significant interest to the particle physics community due to three core implications for neutrino physics:

First, NSI would be a direct indicator of new physics beyond the Standard Model (BSM). Such models include new massive particle interaction mediators, i.e. new fundamental force(s) [85–93] and NSI as a probe/source of dark matter [94–96]. More importantly, NSI would lend significant insight to physics at the highest energy scales (Section 5.2) and are inherently connected to origin of neutrino masses (Section 5.3).

Second, the presence of NSI would have serious repercussions for the interpretation of oscillation parameter measurements. Examples would be the degenerate measurement of the solar neutrino effective mixing angle [97–99], the mixing angle θ_{13} [100, 101], the CP-violating angle δ_{CP} [102, 103], the neutrino mass hierarchy [103, 104], and the octant of θ_{23} [103, 105].

Third, NSI are an appealing route to resolving tensions between experiments while possibly improving the precision of certain neutrino mixing parameter measurements. For instance, the measurements of the neutrino mass hierarchy at JUNO and RENO-50 could have enhanced precision in the event NSI are well-constrained [106, 107]. On the other hand, tension in the measurement of Δm_{21} between solar neutrino experiments and the KamLAND reactor experiment are relieved when NSI are introduced [97–99].

It is these primary drivers that neutrino physicists seek to constrain NSI in current and future experiments.

5.2 Effective Field Theory

The formalism of NSI is written in the language of quantum field theory (QFT), where particles are treated as excitations of fields that permeate all of spacetime.

The mechanics of physical systems are dictated in QFT by the Lagrangian density $\mathcal{L}$, which is an extension of the Lagrangian treatment of classical systems to quantum fields. For the remainder of this work, we colloquially refer to the Lagrangian density as the *Lagrangian*. The SM Lagrangian is comprised of terms that describe all known interactions between matter and force-carrying particles, yet elaborating on the entire model is beyond the scope of this work.

Terms in the SM Lagrangian are constructed from particle field *operators*, which are objects that operate on particle states to produce other particle states. It is important to note that any given term in the Lagrangian will be a product of operators that can be rewritten and referred-to as a single operator. In the standard convention of natural units, where $\hbar$ (the reduced Planck constant) and c (speed of light in vacuum) are set to 1, each operator is in units of energy[2]. The total exponent of unit energy for an operator is the operator's *dimension*, a term of significant relevance in discussions of EFTs.

Each term in the SM Lagrangian is dimension-4 as the action of a system, which dictates the probability amplitudes, is a unitless quantity defined as the integral of the Lagrangian over four-dimensional spacetime: $\mathcal{S} = \int \mathcal{L} dx^4$. The exception to this statement is the dimension-2 Higgs mass term. If new physics exists as high-energy scalars, the Standard Model can be considered an *effective* field theory (EFT), in which the particles and interactions described by the model are those visible at the current energy density of the Universe. Other possible interactions, which may have occurred more frequently when the Universe was in a younger, higher-energy state, would now only have subleading contributions. Therefore, operators representing new physics can have a dimensionality higher than four and be incorporated through the EFT extension of the SM Lagrangian:

[2]Other authors keep terms in units of mass rather than energy, the two are proportional and treated as equivalent.

$$\mathcal{L} = \mathcal{L}^{(4)}_{\text{SM}} + \frac{1}{\Lambda}\sum_k C^{(5)}_k Q^{(5)}_k + \frac{1}{\Lambda^2}\sum_k C^{(6)}_k Q^{(6)}_k + \dots, \tag{5.1}$$

where $\mathcal{L}^{(4)}_{\text{SM}}$ represents the SM Lagrangian terms, $Q^{(n)}_k$ are the nth-order operators, and $C^{(n)}_k$ are the corresponding coupling coefficients known as *Wilson* coefficients. As the operators increase in dimension, they are scaled by increasing orders of Λ, the energy scale of the mass for the new interaction's mediator. It is important to note that operators with $n > 4$ are nonrenormalizable, but renormazibility is not a requirement within an EFT. The operators are also not inherently Hermitian, so the values $C^{(n)}_k$ can be complex-valued. Note that many UV-complete models can generate the same Wilson coefficients, so effective parameters may be defined to represent the new physics modes. Another last note is that the EFT interpretation of the SM excludes other forms of new physics. For instance, *nonstandard* Lagrangian terms such as multiplicative Lagrangians [108] are a viable method of introducing higher-order operators at energy scales lower than those proposed by the EFT-SM. The remainder of this thesis solely discusses operators from the EFT-SM expansion.

In the EFT-SM picture, NSI are a class of these possible interactions that would display as subleading effects in modern particle physics experiments.

5.3 The Dimension-5 Operator

Before entering discussion of dimension-6 operators, of which NSI are a subset, it is important to examine why the dimension-5 operators are bypassed.

Any new physically-realizable interactions must be Lorentz[3] invariant (Special Relativity cannot be locally violated) and must be invariant under transformations of the $SU(3)_c \otimes SU(2)_L \otimes U(1)_Y$ symmetry of the low-energy $\mathcal{L}^{(4)}_{\text{SM}}$

[3]Specifically, the interactions must be Poincaré invariant, which is a stronger condition that is invariance under Lorentz transformations in addition to reference frame transformations ("translations").

interactions, as this symmetry is required to emerge from any physics at higher energy scales. In the case of dimension-6 operators, these gauge invariances are satisfied in a number of operator models, many of which are reviewed in Ref. [82].

The only dimension-5 operator that satisfies these conditions and is constructed with known SM fields is:

$$\mathcal{L}^(5) = \frac{C^{(5)}_{ll'}}{\Lambda}\left[H \cdot \overline{L}^C_l\right]\left[L_{l'} \cdot H\right] + \text{h.c.} \tag{5.2}$$

where $C^{(5)}_{ll'}$ is the operator's Wilson coefficient, L is the left-handed lepton doublet (ν_l, l), H is the Higgs doublet, and h.c. is the Hermitian conjugate of the first term. This singular dimension-5 operator is referred-to as the *Weinberg* operator, and happens to violate lepton number conservation [109, 110].

The Weinberg operator has the unique property of introducing neutrino (*Majorana*[4]) masses to the Standard Model after electroweak symmetry breaking through any of what are called the "seesaw" mechanisms [111–113]. It is why the dimension-5 operator only exists for neutrinos– there are no other electrically-neutral leptons in the SM. Therefore, neutrinos are the sole probe of the Weinberg operator. Yet, signals of a non-zero Weinberg operator are restricted, as the operator does not contribute any effect to forward scattering, and other contributions would be highly suppressed by the measured smallness of the neutrino masses (directly proportional to the Wilson coefficient).

The most-promising experimental probe of the Weinberg operator is neutrinoless double-beta decay ($0\nu\beta\beta$), which would be direct evidence of dimension-5 physics and physics beyond the Standard Model. As limiting as this one channel is, the Weinberg operator is the leading contender as the neutrino mass-generating mechanism, and is thus the focus of much work to find evidence for

[4]Majorana particles are fermions that are their own antiparticle. This requires that only electrically neutral particles can be Majorana particles. Particles with a distinct antiparticle partner are *Dirac* particles. All particles in the SM are Dirac particles except for the neutrinos, whose type is yet to be determined.

or against [114, 115].

Beyond the dimension-5 operator is the opportunity to constrain possible new physics from higher-dimensional operators that is motivated by the reasoning in Sec. 5.1. Therefore, it is of great interest to explore the dimension-6 operators, which have the next-smallest energy scale suppression.

5.4 Dimension-6 Operators

A considerable number of dimension-6 operators pass the constraints listed in Sec. 5.3. Of interest to neutrino physicists are neutrino-fermion interactions (except self interactions), which have the dimension-6 operators:

$$\begin{aligned}\mathcal{L}_{\text{NSI}}^{NC} &= -2\sqrt{2}G_F\epsilon_{\alpha\beta}^{fC}(\overline{\nu}_\alpha\gamma^\mu P_L\nu_\beta)(\overline{f}\gamma_\mu P_C f)\\ \mathcal{L}_{\text{NSI}}^{CC} &= -2\sqrt{2}G_F\epsilon_{\alpha\beta}^{ff'C}(\overline{\nu}_\alpha\gamma^\mu P_L l_\beta)(\overline{f}\gamma_\mu P_C f')\end{aligned} \tag{5.3}$$

where G_F is the Fermi constant, ν are the neutrino spinors, $f \neq f'$ are the common matter fermion (e, u, d) spinors, l is a lepton spinor, $P_C = P_L, P_R$ are the left and right chiral projection operators, and ϵ are the Wilson coefficients that now are referred-to as the NSI parameters. This set of operators emerges from most models of NSI in the literature [82].

This contribution to the Lagrangian is actually a *sum* of terms (Einstein notation), in which it is implied that a term exists for each combination of α, β, f, and f' values, where the Greek indices range across the 3 observed neutrino flavors (e, μ, τ) and the f-spinors are the first-generation leptons (e, u, d). The collection of interactions where the outgoing lepton is the same as the incoming lepton ($f = f'$) are the *neutral-current* (NC) NSI. When this is not the case, the terms are *charged-current* (CC) interactions. These definitions assume that NSI preserve lepton number.

5.5 Source, Detector, and Propagation NSI

The Wilson coefficients of the NSI dimension-6 operators are not inherently measurable by neutrino experiments. What instead is needed is a physically-motivated parameterization of new effects on neutrino production (ϵ^s, "source" NSI), neutrino propagation (ϵ^m, "matter" NSI), and the neutrino detection (ϵ^d, "detector" NSI). The purpose of this section is to demonstrate how the Eq. 5.3 CC-NSI terms relate to measurable source-detector NSI parameters and how the NC-NSI terms relate to measurable propagation NSI parameters.

5.5.1 Source and Detector NSI

As neutrinos are produced and detected in flavor states, NSI modifications to neutrino production/detection can be introduced through adding the NSI flavor contribution to the produced and detected neutrino flavor states:

$$|\nu_\alpha^s\rangle = |\nu_\alpha\rangle + \sum_{\beta=e,\mu,\tau} \epsilon_{\alpha\beta}^s |\nu_\beta\rangle \tag{5.4}$$

$$\langle\nu_\alpha^d| = \langle\nu_\alpha| + \sum_{\beta=e,\mu,\tau} \epsilon_{\alpha\beta}^d \langle\nu_\beta| . \tag{5.5}$$

Converting the right side of Eq. 5.4 to the mass state basis, we get

$$|\nu_\alpha^s\rangle = (1+\epsilon^s)U |\nu_m\rangle \tag{5.6}$$

$$\langle\nu_\alpha^d| = \langle\nu_m| U^\dagger \left[1 + (\epsilon^d)^\dagger\right] , \tag{5.7}$$

such that ϵ^s and ϵ^d are the matrices of source and detector NSI parameters, respectively, and U is the vacuum PMNS matrix. From this conversion, it can be seen that source and detector NSI can be added to neutrino vacuum oscillations as a reweighting of the PMNS matrix elements:

$$P_{CC}(\nu_\alpha^s \to \nu_\beta^d; L) = \left| \sum_{\gamma,\delta,i} (1+\epsilon^d)_{\gamma\beta}(1+\epsilon^s)_{\alpha\delta} U_{\delta i} U_{\gamma i}^* e^{-i\frac{m_i^2 L}{2E}} \right|^2 . \tag{5.8}$$

This probability can be re-written in terms of a modified Jarlskog invariant similar to the invariant defined in Sec. 2.2:

$$P_{CC}(\nu_\alpha^s \to \nu_\beta^d; L) = \sum_{i,j} \hat{\mathcal{J}}_{\alpha\beta}^{i,CC} \hat{\mathcal{J}}_{\alpha\beta}^{j,CC*} - \sum_{i>j} \mathrm{Re}\left\{\hat{\mathcal{J}}_{\alpha\beta}^{i,CC} \hat{\mathcal{J}}_{\alpha\beta}^{j,CC*}\right\} \sin^2\left(\frac{\Delta m_{ij}^2 L}{4E}\right) + \sum_{i>j} \mathrm{Im}\left\{\hat{\mathcal{J}}_{\alpha\beta}^{i,CC} \hat{\mathcal{J}}_{\alpha\beta}^{j,CC*}\right\} \sin\left(\frac{\Delta m_{ij}^2 L}{2E}\right), \tag{5.9}$$

such that

$$\hat{\mathcal{J}}_{\alpha\beta}^{i,CC} = U_{\alpha i}^* U_{\beta i} + \sum_\gamma \epsilon_{\alpha\gamma}^s U_{\gamma i}^* U_{\beta i} + \sum_\gamma \epsilon_{\gamma\beta}^d U_{\alpha i}^* U_{\gamma i} + \sum_{\gamma,\delta} \epsilon_{\gamma\alpha}^s \epsilon_{\delta\beta}^d U_{\gamma i}^* U_{\delta i}. \tag{5.10}$$

The definition in Eq. 5.10 spotlights the independent and correlated contributions from source and detector NSI parameters. Importantly, the probability form in Eq. 5.9 reflects that even if the produced neutrino is immediately annihilated (propagation distance $L = 0$), the oscillation probability still relies on values of the source and detection NSI:

$$P_{CC}(\nu_\alpha^s \to \nu_\beta^d; L = 0) = \sum_{i,j} \hat{\mathcal{J}}_{\alpha\beta}^{i,CC} \hat{\mathcal{J}}_{\alpha\beta}^{j,CC*}. \tag{5.11}$$

This is called the "zero-distance" effect.

In the case of no-NSI, the probability of flavor transition at $L = 0$ reduces to the SM prediction:

$$\begin{aligned} P_{CC}(\nu_\alpha^s \to \nu_\beta^d; L = 0; \epsilon_{\alpha\gamma}^s = \epsilon_{\beta\delta}^d = 0) &= \sum_{i,j} \hat{\mathcal{J}}_{\alpha\beta}^{i,SM} \hat{\mathcal{J}}_{\alpha\beta}^{j,SM*} \\ &= \sum_{i,j} U_{\alpha i}^* U_{\beta i} U_{\alpha j} U_{\beta j}^* \\ &= \delta_{\alpha\beta}. \end{aligned} \tag{5.12}$$

The relationship between $\epsilon_{\alpha\beta}^{s/d}$ and $\epsilon_{\alpha\beta}^{ff'C}$ relies on the methods of neutrino production and detection. One convention, examining neutrinos that are sourced from meson decays, derives the relationship [84]

$$\epsilon_{\alpha\beta}^{s/d} = \frac{\epsilon_{\alpha\beta}^{ff'C}}{\sqrt{(\epsilon_{\alpha e}^{ff'C})^2 + (\epsilon_{\alpha\mu}^{ff'C})^2 + (\epsilon_{\alpha\tau}^{ff'C})^2}}. \tag{5.13}$$

It is important to note that IceCube is not particularly sensitive to this form of NSI. As neutrinos are identified in detectors by the presence of their SM charged-lepton partner, introducing source/detector CC NSI to measurement predictions for flavor-sensitive detectors is ill-defined [116]. Limits on CC NSI are also found to be consistently tighter than limits on NC NSI [117]. And while both NC and CC NSI modify the neutrino inelastic scattering cross section, only NC NSI also modify coherent forward scattering, which IceCube is sensitive to through access to neutrinos from a large range of baselines.

5.5.2 Propagation NSI

NSI as an effect on the propagation of neutrinos can be parameterized as an addition to the matter potential [79, 80]:

$$H_{\text{mat+NSI}} = V_{CC}(x) \begin{pmatrix} 1+\epsilon_{ee} & \epsilon_{e\mu} & \epsilon_{e\tau} \\ \epsilon_{e\mu}^* & \epsilon_{\mu\mu} & \epsilon_{\mu\tau} \\ \epsilon_{e\tau}^* & \epsilon_{\mu\tau}^* & \epsilon_{\tau\tau} \end{pmatrix} \tag{5.14}$$

such that ϵ^* is the complex conjugate of ϵ and $V_{CC}(x) = \sqrt{2} G_F N_e(x)$ is the normal matter charged-current weak potential. Diagonal parameters are real-valued and represent flavor-conserving interactions while the off-diagonal parameters can be complex and represent flavor-violating interactions.

The "1" in the ee position represents the CC SM weak interaction between electron neutrinos and left-handed electrons, with the remaining contributions normalized relative to this value.

When incorporating vacuum oscillations, we get the full neutrino Hamiltonian,

$$H_{\text{total}} = \frac{1}{2E_\nu} \left[U \begin{pmatrix} 0 & & \\ & \Delta m_{21}^2 & \\ & & \Delta m_{31}^2 \end{pmatrix} U^\dagger + V_{CC}(x) \begin{pmatrix} 1+\epsilon_{ee} & \epsilon_{e\mu} & \epsilon_{e\tau} \\ \epsilon_{e\mu}^* & \epsilon_{\mu\mu} & \epsilon_{\mu\tau} \\ \epsilon_{e\tau}^* & \epsilon_{\mu\tau}^* & \epsilon_{\tau\tau} \end{pmatrix} \right], \tag{5.15}$$

where U is the vacuum PMNS matrix, E_ν is the neutrino energy, and Δm^2_{ij} are the neutrino mass squared differences. Using the total Hamiltonian, the NSI-modified oscillation probability can be derived by first diagonalizing the Hamiltonian under a unitary transformation:

$$H_{\text{total}} = \tilde{U}\text{diag}(\tilde{m}^2_1, \tilde{m}^2_2, \tilde{m}^2_3)\tilde{U}^\dagger. \tag{5.16}$$

In this form, the diagonalized vacuum+matter+NSI Hamiltonian yields modified neutrino mass eigenstates $\tilde{m}_i$ and a modified PMNS mixing matrix $\tilde{U}$, which is now dependent on $\epsilon_{\alpha\beta}$ and the matter density. From here, the modified parameters can be substituted in to the SM probability of Sec. 2.2 to get the NSI oscillation probability,

$$P_{NC}(\nu_\alpha \to \nu_\beta; L) = \left| \sum_{i=1}^{3} \tilde{U}_{\alpha i}\tilde{U}^*_{\beta i} e^{-i\frac{\tilde{m}^2_i L}{2E}} \right|^2. \tag{5.17}$$

5.6 Previous NSI Results

As a topic of interest, many neutrino experiments publish NSI constraints that improve over time as more data is collected. Here, we report recent results that are illustrative of the order of magnitude to which NSI are currently constrained.

5.6.1 Source-Detector Bounds

In a review by Ref. [118], the most concise, direct bounds on source-detector NSI were

$$\begin{pmatrix} |\epsilon^{\mu e}_{ee}|<0.025 & |\epsilon^{\mu e}_{e\mu}|<0.03 & |\epsilon^{\mu e}_{e\tau}|<0.03 \\ |\epsilon^{\mu e}_{\mu e}|<0.025 & |\epsilon^{\mu e}_{\mu\mu}|<0.03 & |\epsilon^{\mu e}_{\mu\tau}|<0.03 \\ |\epsilon^{\mu e}_{\tau e}|<0.025 & |\epsilon^{\mu e}_{\mu}|<0.03 & |\epsilon^{\mu e}_{\tau\tau}|<0.03 \end{pmatrix}, \tag{5.18}$$

$$\begin{pmatrix} \left|\epsilon^{ud}_{ee}\right| < 0.041 & \left|\epsilon^{ud}_{e\mu}\right| < 0.025 & \left|\epsilon^{ud}_{e\tau}\right| < 0.041 \\ \left|\epsilon^{ud}_{\mu e}\right| < \begin{cases} 1.8 \cdot 10^{-6} \\ 0.026 \end{cases} & \left|\epsilon^{ud}_{\mu\mu}\right| < 0.078 & \left|\epsilon^{ud}_{\mu\tau}\right| < 0.013 \\ \left|\epsilon^{ud}_{\tau e}\right| < \begin{cases} 0.087 \\ 0.12 \end{cases} & \left|\epsilon^{ud}_{\mu}\right| < \begin{cases} 0.013 \\ 0.018 \end{cases} & \left|\epsilon^{ud}_{\tau\tau}\right| < 0.13 \end{pmatrix}, \tag{5.19}$$

where the entries with two values are presenting the NSI left-handed component $\epsilon^{ud,L}_{\alpha\beta}$ bound (upper) and the NSI right-handed component $\epsilon^{ud,R}_{\alpha\beta}$bound (lower).

5.6.2 Propagation Bounds

As an example of recent matter NSI bounds, here we present the results from the global oscillations survey presented in Ref. [119]. Tab. 5.1 displays the allowed values of each NSI propagation parameter, where LMA refers to the "Large Mixing Angle" model and LMA-D is the "LMA-Dark" model [120].

5.6.3 Previous IceCube Results

The latest IceCube analysis to constrain NSI was the 2021 all-parameter analysis of Ref. [121]. This analysis used three years of IceCube data including data from the DeepCore array, which allowed for a sample energy range of $\sim 5-100$ GeV. At this low of energy, the sample is well-suited to an all-parameter fit, as the non-$\epsilon_{\mu\tau}$ off-diagonal parameters have the most prominent effects on the oscillation probability in this regime. Fig. 5.1 displays the results of this analysis in comparison to the precursor IceCube measurements and other leading measurements.

With previous IceCube analyses constraining NSI with three years of neutrino data below 100 GeV [121, 122], one can imagine that constraining NSI with the 8-year, 500 GeV - 10 TeV sample of Refs. [50, 68, 69] could yield a

significant improvement on the constraints of NSI parameters sensitive to the higher energy. Such an analysis is described in the next chapter.

OSC			+COHERENT		
	LMA	LMA ⊕ LMA-D		LMA	LMA ⊕ LMA-D
$\varepsilon^u_{ee} - \varepsilon^u_{\mu\mu}$	$[-0.020, +0.456]$	$\oplus[-1.192, -0.802]$	ε^u_{ee}	$[-0.008, +0.618]$	$[-0.008, +0.618]$
$\varepsilon^u_{\tau\tau} - \varepsilon^u_{\mu\mu}$	$[-0.005, +0.130]$	$[-0.152, +0.130]$	$\varepsilon^u_{\mu\mu}$	$[-0.111, +0.402]$	$[-0.111, +0.402]$
			$\varepsilon^u_{\tau\tau}$	$[-0.110, +0.404]$	$[-0.110, +0.404]$
$\varepsilon^u_{e\mu}$	$[-0.060, +0.049]$	$[-0.060, +0.067]$	$\varepsilon^u_{e\mu}$	$[-0.060, +0.049]$	$[-0.060, +0.049]$
$\varepsilon^u_{e\tau}$	$[-0.292, +0.119]$	$[-0.292, +0.336]$	$\varepsilon^u_{e\tau}$	$[-0.248, +0.116]$	$[-0.248, +0.116]$
$\varepsilon^u_{\mu\tau}$	$[-0.013, +0.010]$	$[-0.013, +0.014]$	$\varepsilon^u_{\mu\tau}$	$[-0.012, +0.009]$	$[-0.012, +0.009]$
$\varepsilon^d_{ee} - \varepsilon^d_{\mu\mu}$	$[-0.027, +0.474]$	$\oplus[-1.232, -1.111]$	ε^d_{ee}	$[-0.012, +0.565]$	$[-0.012, +0.565]$
$\varepsilon^d_{\tau\tau} - \varepsilon^d_{\mu\mu}$	$[-0.005, +0.095]$	$[-0.013, +0.095]$	$\varepsilon^d_{\mu\mu}$	$[-0.103, +0.361]$	$[-0.103, +0.361]$
			$\varepsilon^d_{\tau\tau}$	$[-0.102, +0.361]$	$[-0.102, +0.361]$
$\varepsilon^d_{e\mu}$	$[-0.061, +0.049]$	$[-0.061, +0.073]$	$\varepsilon^d_{e\mu}$	$[-0.058, +0.049]$	$[-0.058, +0.049]$
$\varepsilon^d_{e\tau}$	$[-0.247, +0.119]$	$[-0.247, +0.119]$	$\varepsilon^d_{e\tau}$	$[-0.206, +0.110]$	$[-0.206, +0.110]$
$\varepsilon^d_{\mu\tau}$	$[-0.012, +0.009]$	$[-0.012, +0.009]$	$\varepsilon^d_{\mu\tau}$	$[-0.011, +0.009]$	$[-0.011, +0.009]$
$\varepsilon^p_{ee} - \varepsilon^p_{\mu\mu}$	$[-0.041, +1.312]$	$\oplus[-3.327, -1.958]$	ε^p_{ee}	$[-0.010, +2.039]$	$[-0.010, +2.039]$
$\varepsilon^p_{\tau\tau} - \varepsilon^p_{\mu\mu}$	$[-0.015, +0.426]$	$[-0.424, +0.426]$	$\varepsilon^p_{\mu\mu}$	$[-0.364, +1.387]$	$[-0.364, +1.387]$
			$\varepsilon^p_{\tau\tau}$	$[-0.350, +1.400]$	$[-0.350, +1.400]$
$\varepsilon^p_{e\mu}$	$[-0.178, +0.147]$	$[-0.178, +0.178]$	$\varepsilon^p_{e\mu}$	$[-0.179, +0.146]$	$[-0.179, +0.146]$
$\varepsilon^p_{e\tau}$	$[-0.954, +0.356]$	$[-0.954, +0.949]$	$\varepsilon^p_{e\tau}$	$[-0.860, +0.350]$	$[-0.860, +0.350]$
$\varepsilon^p_{\mu\tau}$	$[-0.035, +0.027]$	$[-0.035, +0.035]$	$\varepsilon^p_{\mu\tau}$	$[-0.035, +0.028]$	$[-0.035, +0.028]$

TABLE 5.1: The 2σ allowed intervals for NSI parameters constrained in the global oscillations analysis from Ref. [119]. Parameters ϵ^d, ϵ^u, and ϵ^p are the parameters representing NSI between neutrinos and d-quarks, u-quarks, and protons, respectively ($\epsilon^p_{\alpha\beta} = 2\epsilon^u_{\alpha\beta} + \epsilon^d_{\alpha\beta}$). OSC refers to the global oscillations analysis while +COHERENT refers to the global oscillations analysis with COHERENT data included. Table from Ref. [119].

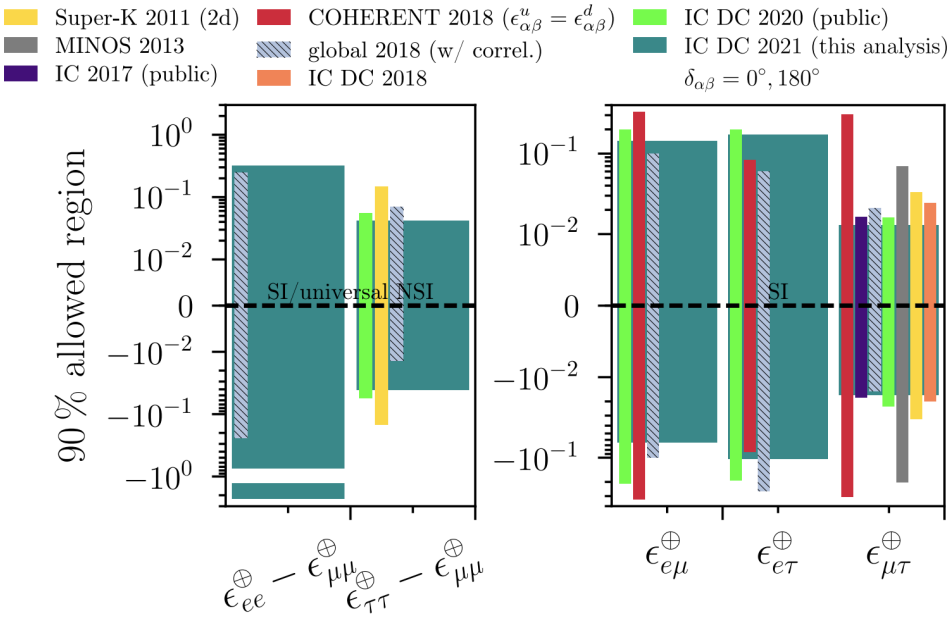

FIGURE 5.1: Comparison of previous IceCube NSI constraints from Refs. [116, 119, 121–126]. Adapted from Ref. [121].

Chapter 6

NSI Analysis Description

We perform an analysis to search for signals of complex-valued $\epsilon_{\mu\tau}$ in IceCube atmospheric neutrino data from 500 GeV - 10 TeV. The remaining NSI parameters are fixed to a value of 0. Section 6.2 describes how this choice of fixed parameter values leads to a conservative result. All contributing SM 3-neutrino mixing parameters are set to the global best-fit values found by Ref. [127]. This analysis fits to both the normal neutrino mass ordering (NMO) and the inverted mass ordering (IMO) [128]. Note that this analysis constrains an effective NSI parameter that is model-independent with regard to the underlying interaction mediator.

6.1 Sample Event Selection

The sample of 500 GeV - 10 TeV neutrino events used for both analyses in this thesis is produced from a series of filters and cuts that are referred collectively as the *event selection*, which is briefly described in this section following the procedure in Refs. [50, 68, 69].

As events in this particular sample are muon tracks from neutrino interactions, a series of precuts and low-level filters eliminate a large bulk of data:

1. Remove events with $\cos\theta \geq 0.2$.

2. Only keep an event with $\cos\theta \geq 0.0$ if event total charge $Q_{\text{tot}} > 100$ PE (photoelectrons) and the Average Charge Weighted Distance (ACWD) > 200 m/PE.

3. Minimum 15 triggered DOMs (NChan) with 6+ DOMs triggered on direct (minimally-scattered) light (DirNDOMs).

4. The track length from direct light (DirL) ≥ 200 m and the track smoothness (DirS) ≤ 0.6.

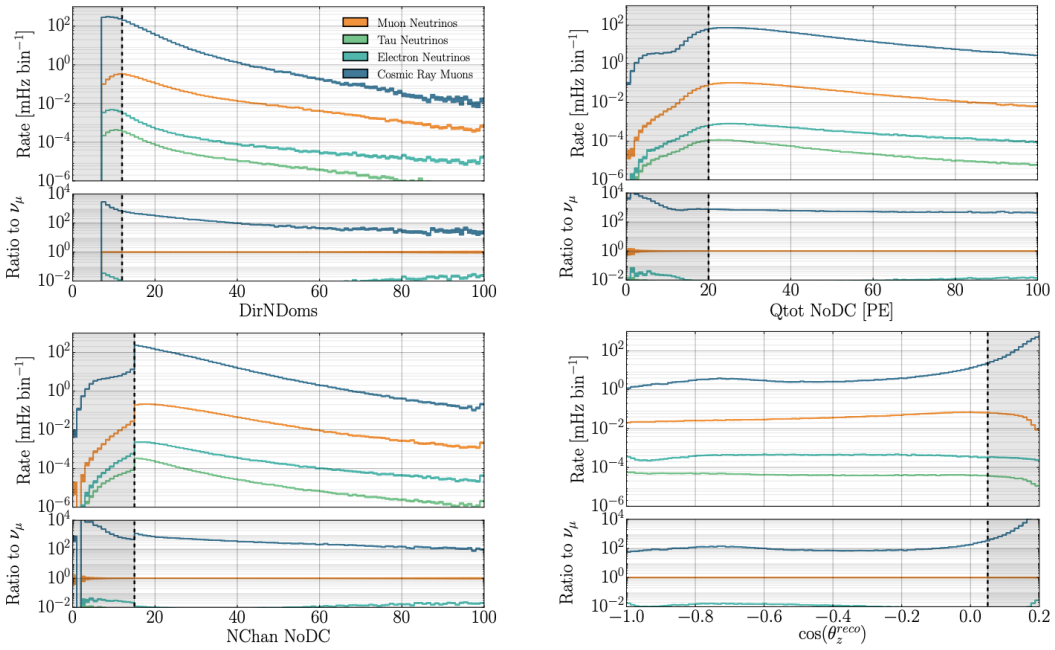

FIGURE 6.1: Distributions of reconstruction parameters after application of the Diamond Filter.

The first analysis-level selection is the "Golden Filter", with full details included in Ref. [129]. While a complete description is beyond the scope of this section, the Gold Filter can be summarized as a successive number of cuts that aim to maximally reduce the amount of background muon data. The result is a ν_μ sample purity of $> 99\%$.

The second selection step, the Diamond Filter, attempts to increase the sample statistics while preserving the purity of the Gold Filter by doing the following:

1. $Q_{\text{tot}} > 20$ PE outside the DeepCore array.
2. NChan > 15 outside the DeepCore array.
3. DirNDOMs ≥ 12.
4. $\cos\theta \leq 0.05$.

These two filters comprise the majority of the analysis-level event selection filters, resulting in the parameter distributions of Fig. 6.1 and an averaged event rate of 20 mHz.

6.2 Parameterization

With a sample of atmospheric neutrinos that have propagated various distances through Earth to reach IceCube, this analysis constrains neutral-current (NC) propagation NSI. The coupling strength of a given interaction is defined by the population-weighted sum of NSI contributions to the weak potential from the matter particles within the environment the neutrino travels through (electrons, protons, and neutrons): $\epsilon_{\alpha\beta} \approx \epsilon^e_{\alpha\beta} + \epsilon^p_{\alpha\beta} + Y_n^{\oplus}\epsilon^n_{\alpha\beta}$, where $Y_n^{\oplus} \equiv \langle N_n(x)/N_e(x)\rangle$ is the average neutron fraction per electron, $N_e(x)$ and $N_n(x)$ are the electron and neutron particle number densities, respectively, at trajectory position x. These generalized NSI parameters are assumed constant, as $Y_n^{\oplus} \approx 1.051$ within Earth [130].

The combined matter+NSI weak Hamiltonian is represented by

$$H_{\text{mat+NSI}} = V_{CC}(x) \begin{pmatrix} 1+\epsilon_{ee} & \epsilon_{e\mu} & \epsilon_{e\tau} \\ \epsilon^*_{e\mu} & \epsilon_{\mu\mu} & \epsilon_{\mu\tau} \\ \epsilon^*_{e\tau} & \epsilon^*_{\mu\tau} & \epsilon_{\tau\tau} \end{pmatrix}, \tag{6.1}$$

such that ϵ^* is the complex conjugate of ϵ and $V_{CC}(x) = \sqrt{2}G_F N_e(x)$ is the normal matter charged-current weak potential. Diagonal parameters are real-valued and represent flavor-conserving interactions while the off-diagonal

parameters can be complex and represent flavor-violating interactions. For a thorough derivation of this parameterization, see Sec. 5.

As atmospheric neutrinos primarily oscillate between the μ and τ flavors in the sample energy range, this analysis constrains the real and imaginary components of $\epsilon_{\mu\tau}$ while accounting for contributions[1] from $\epsilon_{\mu\mu} - \epsilon_{\tau\tau}$.

6.2.1 Degeneracies

In the process of developing sensitivities for this analysis, it was found that between the assumed two degrees of freedom [Re($\epsilon_{\mu\tau}$),Im($\epsilon_{\mu\tau}$)], there are two forms of degeneracy that arise from the two-flavor nature of the oscillation channel and the high-energy content of the sample. It will be shown that these degeneracies (also referred to as symmetries) reduce the effective degrees of freedom to one.

The first degeneracy is the equivalence of LLH values between positive and negative values of Im($\epsilon_{\mu\tau}$) with the same magnitude. This can be seen through the 2-flavor oscillation approximation posed by Ref. [116]: for values of $\epsilon_{\mu\tau}$ and $\epsilon_{\tau\tau}$ at the upper limits from the previous IceCube NSI analysis [121] and the analysis sample energies, we can determine the range of values for the NSI+matter contribution to the oscillation phase (ϕ_{mat}) and the ratio of the NSI+matter to vacuum oscillation phase contributions (R_0). A compact representation of these definitions is:

$$R_0 = \frac{\phi_{\text{mat}}}{\phi_{\text{vac}}} = \frac{V_{\text{NSI}} L/2}{\Delta m^2_{31} L/4E_\nu}, \tag{6.2}$$

where $V_{\text{NSI}} = V_d\sqrt{\epsilon^2_{\mu\tau} + \epsilon^2_{\tau\tau}}$ is the NSI potential with respect to the down-quark potential. The Ref. [121] upper bound NSI values and the maximum propagation baseline for this analysis sample (1 Earth diameter) were used to

[1] Diagonal parameters in the NSI matrix are measured in oscillation experiments relative to each other, so the $\tau\tau$ element is relative to the $\mu\mu$ value, written as $\epsilon_{\mu\mu} - \epsilon_{\tau\tau}$. For the remainder of the text, we simply write this as $\epsilon_{\tau\tau}$.

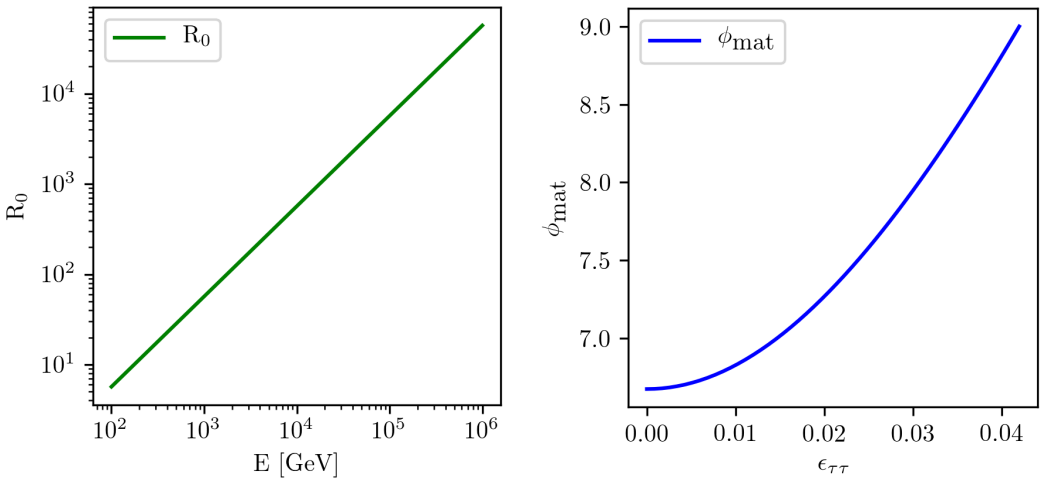

FIGURE 6.2: (Left) Values of R_0 for the analysis energies at the Ref. [121] upper 90% CL limit values of $\epsilon_{\mu\tau}$ and $\epsilon_{\tau\tau}$. (Right) Values of ϕ_{mat} for baseline L = 12,742 km (1 Earth diameter) and upper 90% CL limit values of $\epsilon_{\mu\tau}$ and $\epsilon_{\tau\tau}$ from Ref. [121] where $\epsilon_{\tau\tau}$ is sampled from 0 to the upper limit.

determine through Fig. 6.2 (left) that R_0 is $\gg \mathcal{O}(1)$ and through Fig. 6.2 (right) that ϕ_{mat} is $\gg 1$ for the entire sample energy range. This reduces the flavor transition probability to a particular approximation from Ref. [116]:

$$P(\nu_\mu \to \nu_\tau) \approx \sin^2(2\xi)\sin^2(\phi_{\mathrm{mat}}), \tag{6.3}$$

such that $\sin(2\xi) = \frac{2\epsilon_{\mu\tau}}{\sqrt{\epsilon_{\mu\tau}^2+\epsilon_{\tau\tau}^2}}$. In this formulation, $\epsilon_{\mu\tau}^2$ is the the *modulus square* if $\epsilon_{\mu\tau}$ is complex, and thus for every complex $\epsilon_{\mu\tau} = a + bi$, it can be seen that $P(a+bi) = P(a-bi)$.

The second degeneracy is the radial symmetry of all LLH contours in $\mathrm{Re}(\epsilon_{\mu\tau})-\mathrm{Im}(\epsilon_{\mu\tau})$ space. At lower energies, there is significant asymmetry between $\pm\mathrm{Re}(\epsilon_{\mu\tau})$ (although the $\pm\mathrm{Im}(\epsilon_{\mu\tau})$ symmetry remains preserved). With this high-energy sample, this asymmetry is suppressed to form circular LLH profiles in the 2D space. The circular form emerges when examining the form the oscillation probability takes at sample energies. We start with the general form of the oscillation probability given in Eq. 6.3 from Ref. [116]:

$$P(\nu_\mu \to \nu_\tau) = \left[\frac{(\sin 2\theta_{23} + R_0 \sin 2\xi)^2}{R^2}\right] \sin^2\left(\frac{\Delta m_{31}^2 L}{4E_\nu} R\right), \tag{6.4}$$

where $R = 1 + R_0^2 + 2R_0 \cos 2(\theta_{23} - \xi)$. Since the analysis sample has neutrino energies of $E_\nu > 100$ GeV and baselines at or less than the Earth diameter, then $\frac{\Delta m^2_{31} L}{4E_\nu} << 1$. Hence, the small-angle approximation $\sin x = x$ can be employed:

$$\begin{aligned} P(\nu_\mu \to \nu_\tau) &= \left[\frac{(\sin 2\theta_{23} + R_0 \sin 2\xi)^2}{R^2}\right]\left(\frac{\Delta m^2_{31} L}{4E_\nu} R\right)^2 \\ &= L^2 \left(\sin 2\theta_{23} \frac{\Delta m^2_{31}}{4E_\nu} + \epsilon_{\mu\tau} V_d\right)^2. \end{aligned} \tag{6.5}$$

With a median sample energy of $E_\nu = 1$ TeV, we see that $\frac{\Delta m^2_{31}}{4E_\nu} \sim 10^{-25}$ GeV. Note that $\sin 2\theta_{23} \approx 1$ and $V_d \approx 10^{-21}$ GeV. Given previous IceCube constrains [121] of $\epsilon_{\mu\tau}$, $\mathcal{O}(\epsilon_{\mu\tau})$ is maximally $\sim 10^{-2}$. Therefore, in the case of maximal NSI for the energies of this sample, $\sin 2\theta_{23} \frac{\Delta m^2_{31}}{4E_\nu}$ is at least one order of magnitude less than $\epsilon_{\mu\tau} V_d$, and thus the test statistic (LLH), which is proportional to $P(\nu_\mu \to \nu_\tau)$, can take the approximate form:

$$LLH \sim P(\nu_\mu \to \nu_\tau) \approx (|\epsilon_{\mu\tau}| L V_d)^2. \tag{6.6}$$

Rewriting as an equation for $\epsilon_{\mu\tau}$:

$$|\epsilon_{\mu\tau}| \approx \frac{\sqrt{P}}{L V_d}, \tag{6.7}$$

which is radially symmetric in the $\mathrm{Re}(\epsilon_{\mu\tau}) - \mathrm{Im}(\epsilon_{\mu\tau})$ plane, resulting in circular CL contours.

From these two degeneracies, only the LLH values along the $\mathrm{Re}(\epsilon_{\mu\tau})$ axis $[\mathrm{Im}(\epsilon_{\mu\tau}) = 0]$ are needed to fit circles that interpolate the full 2D LLH space. The circular projection of LLH values against tested 2D LLH calculations are found to match within excellent precision ($< 0.0001\%$ relative difference, see Sec. 6.10, Fig. 6.34). Thus, this analysis determines confidence levels for 1 degrees of freedom (DoF) and verifies the correct DoF with the Feldman-Cousins "spot-check" method in Sec. 6.11.

Notably, while the contours from fits in this analysis are circular, they are not centered about $\mathrm{Re}(\epsilon_{\mu\tau}) = \mathrm{Im}(\epsilon_{\mu\tau}) = 0$, but are offset along the $\mathrm{Re}(\epsilon_{\mu\tau})$ axis.

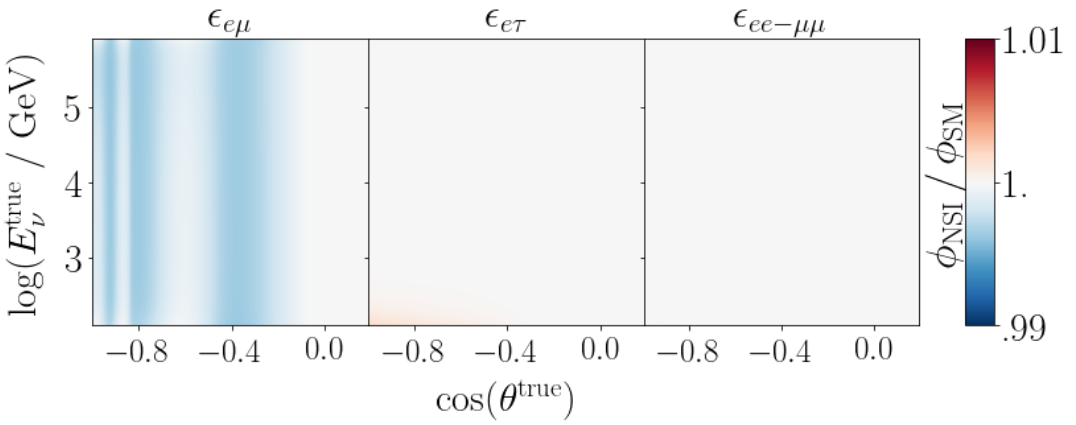

FIGURE 6.3: Ratio of the predicted SM to NSI $\nu_\mu + \overline{\nu}_\mu$ flux in true neutrino energy E_ν and true neutrino incident direction (zenith, $\cos\theta$) space for e-flavor NSI parameters at values in Ref. [121]. Blue represents where the NSI suppresses the SM flux while red represents NSI-induced increases in flux.

From Eq. 6.5, it can be seen that the oscillation probability (proportional to the test statistic) is a function of $\epsilon_{\mu\tau}$ that is offset towards negative $\text{Re}(\epsilon_{\mu\tau})$ by the term $\sin 2\theta_{23} \frac{\Delta m^2_{31}}{4E_\nu}$.

6.2.2 $\epsilon_{\mu\tau} - \epsilon_{\tau\tau}$ Correlation

From the inaugural measurement in Ref. [123] to recent measurements [122, 131], limits on $\epsilon_{\mu\tau}$ have frequently been coupled with $\epsilon_{\tau\tau}$ as the $\mu - \tau$ oscillation of atmospheric neutrinos makes the outcomes of flavor-conserving and flavor-violating interactions paired phenomena.

Simulated within nuSQuIDS (see Sec. 4.4), the upper limit non-$\epsilon_{\mu\tau}$, non-$\epsilon_{\tau\tau}$ NSI values from Ref. [121] induce $< 0.2\%$ less muon neutrino flux (Fig. 6.3) from the SM prediction (muon neutrino "disappearance", a measure of the NSI effect employed by this analysis). Note that plots of the kind in Fig. 6.3 are called *oscillograms*, which represent oscillation probability and flux calculations in the space of event observables for IceCube.

In contrast, $\epsilon_{\mu\tau}$ at the 90% CL sensitivity for this analysis induces $\sim 3.2\%$ disappearance (Fig. 6.4). Since the non-$\epsilon_{\mu\tau}$ NSI upper limits are significantly

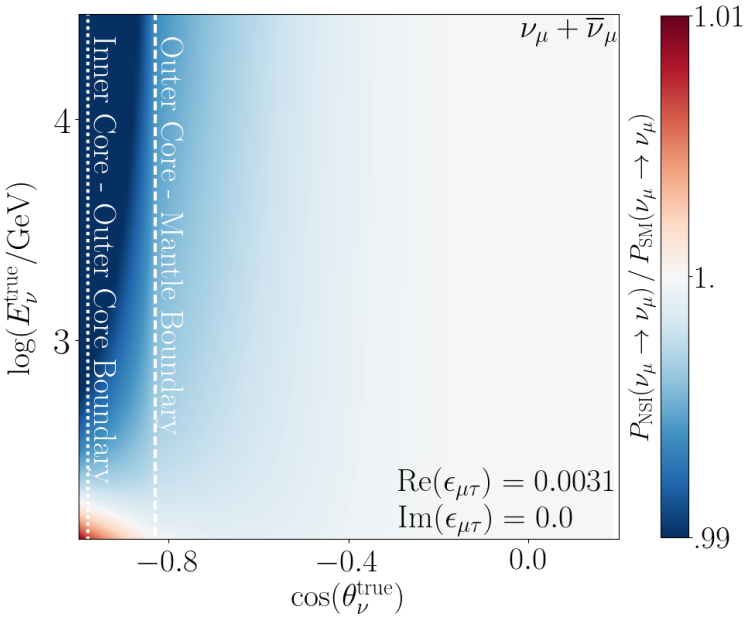

FIGURE 6.4: Oscillogram of nuSQuIDS-simulated ν_μ and $\overline{\nu}_\mu$ flux. Blue represents where the NSI suppresses the SM flux while red represents NSI-induced increased flux.

higher values than that of the analysis sensitivity upper limit, we tested uniformly lowering the values of non-$\epsilon_{\mu\tau}$ and $\epsilon_{\mu\tau}$ parameters for any resonances and find that as the NSI parameter values lower, the amount of induced disappearance lowers with the exception of $\epsilon_{\mu\tau}$, which maintains $\sim 3\%$ disappearance.

The parameter $\epsilon_{\tau\tau}$ also has a large effect on the predicted flux at IceCube. Simulating the flux at IceCube using the latest IceCube upper bound (DeepCore 3-year analysis, Ref. [121]) value of $\epsilon_{\tau\tau}$, Fig. 6.5 exhibits the strong appearance induced by $\epsilon_{\tau\tau}$ at the low energies and large baselines. When a sensitivity is generated for the sample of this analysis to both $\epsilon_{\mu\tau}$ and $\epsilon_{\tau\tau}$, it is seen in Fig. 6.6 that values within the Ref. [121] $\epsilon_{\tau\tau}$ limits can move the upper (lower) bound of the $\epsilon_{\mu\tau}$ sensitivity by up to +(-)30% of the original value. Yet, when the single-parameter $\epsilon_{\tau\tau}$ LLH data profile from Ref. [121] is overlapped with the $\epsilon_{\mu\tau}$-$\epsilon_{\tau\tau}$ sensitivity for this analysis, we see that the analysis sensitivity (and result) bounds on $\epsilon_{\mu\tau}$ are ultimately conservative for non-zero values of $\epsilon_{\tau\tau}$ (Fig. 6.7).

Hence, this analysis proceeds to constrain $\epsilon_{\mu\tau}$ as an independent parameter.

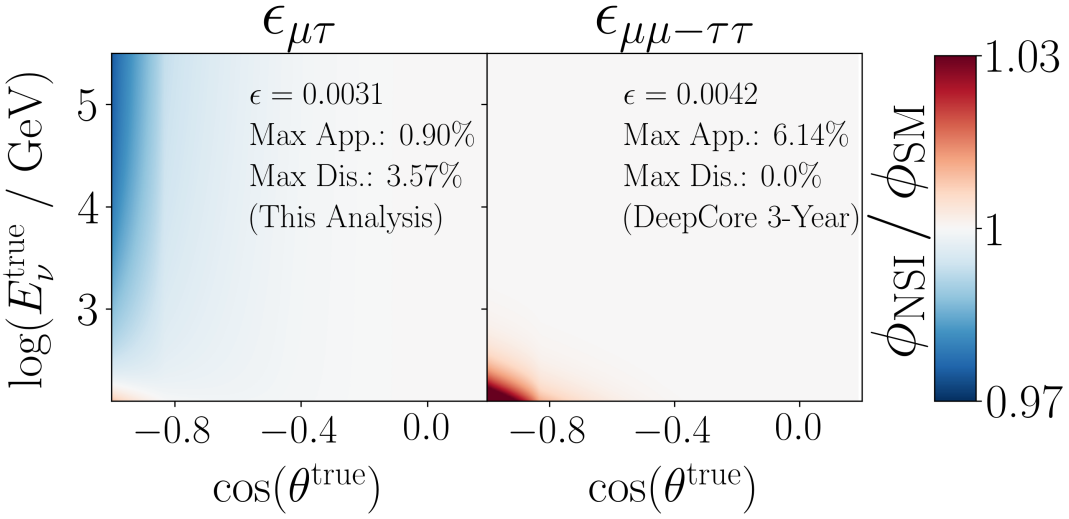

FIGURE 6.5: Oscillograms of the predicted SM to NSI $\nu_\mu + \overline{\nu}_\mu$ flux for the NSI parameters with only μ- and τ-flavor components.

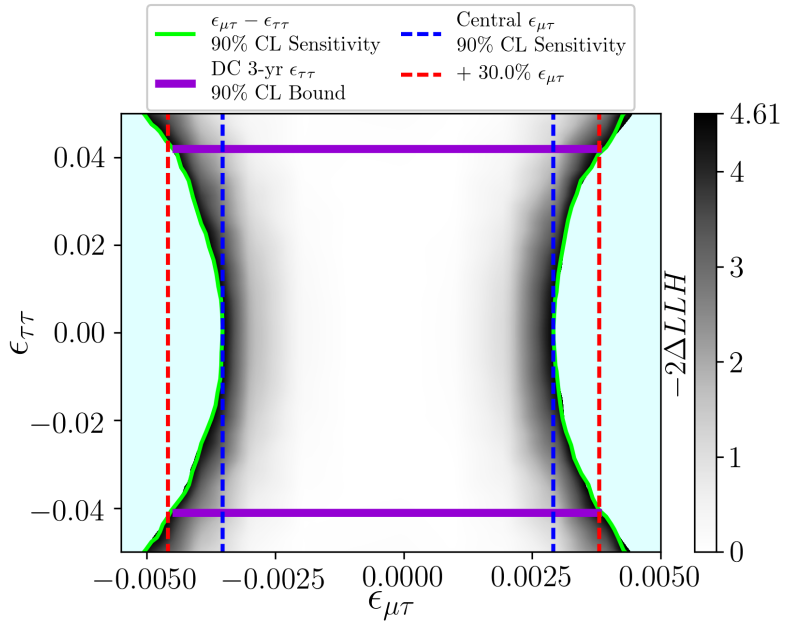

FIGURE 6.6: Sensitivity with 2 DoF in $\epsilon_{\mu\tau} - \epsilon_{\tau\tau}$ space. Limits on $\epsilon_{\tau\tau}$ from the IceCube DeepCore 3-yr analysis are shown in purple [121].

6.3 Analysis Overview

The parameter space of hypotheses tested is 201 points within $\text{Re}(\epsilon_{\mu\tau}) \in [-0.01, 0.01]$ such that the radial and real-complex degeneracies described in Sec. 6.2.1 are utilized to produce the full complex parameter constraints. For each point in the hypothesis space, the neutrino flux at IceCube is simulated.

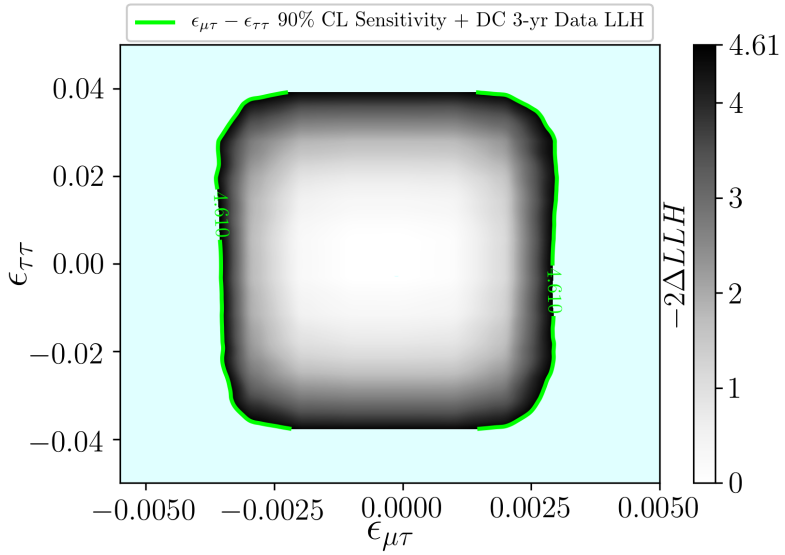

FIGURE 6.7: Sensitivity with 2 DoF in $\epsilon_{\mu\tau} - \epsilon_{\tau\tau}$ space with the sensitivity LLH added to the data LLH profile of $\epsilon_{\tau\tau}$ from Ref. [121].

The total neutrino flux IceCube detects has components from multiple sources. Overwhelmingly, the flux consists of neutrinos from atmospheric and astrophysical sources. The conventional component of the atmospheric flux is simulated with the Hillas-Gaisser 2012 H3a cosmic ray model [132] while the subsequent air showers from high-energy CR interactions is modeled by Sibyll, version 2.3c [133]. The simulated prompt component of the atmospheric flux follows the BERSS model [134]. For the astrophysical component, the flux is modeled as an isotropic, single power energy law [68, 69].

The atmospheric density, a factor in the hadronic processes that eject atmospheric neutrinos, relies on atmospheric temperature. Global temperatures are modeled with the livetime-averaged data from the AIRS satellite [135]. For the actual simulation of neutrino production in the atmosphere, MCEq performs the calculation [75]. nuSQuIDS then propagates the simulated flux that that reaches the surface of Earth through the planet, incorporating the NSI effects for a given hypothesis [77]. The CSMS model of the neutrino-nucleon cross section is employed for both neutrino propagation and interaction within the volume

surrounding and including the detector [136]. Contributing to the propagation calculation is the PREM Earth density model, which assumes spherically-symmetric shells of different matter densities [137]. For simulated neutrinos that have reached the vicinity of the detector, the neutrino interaction kinematics are passed on to the LeptonInjector software [70]. Should the detector respond to this event, the signal is weighted based on the hypothesis-modified flux and the cross section model using the LeptonWeighter software [70]. When it comes to the detector response, the glacial ice forming the detector medium is divided into 170 layers, each with it's own measured light scattering and absorbing properties, along with an overall measurement of that layer's optical anisotropy. Photons from events have simulated propagation to the DOMs via CLSim [72]. The DOM response to various photon of different incident angles and energies is described by the SPE (single-photoelectron) charge templates outlined in Refs. [138, 139].

Simulated and actual data are partitioned by 13 logarithmically-spaced bins [500 GeV - 9976 GeV] in reconstructed muon energy, E^{μ}_{reco}, and 20 linearly-spaced bins [-1.0 - 0.0] in reconstructed muon cosine of the zenith angle, the angle between the horizon and the direction of the muon, $\cos(z^{\mu}_{\text{reco}})$. Thus, the 2D reconstruction space consists of 260 bins. These reconstructed muon quantities are calculated within IceCube's proprietary software, MuEX and MPEFIT [140, 141].

The effect of NSI itself is simulated through adding the NSI potential of Section 5.5.2 to the Hamiltonian in the nuSQuIDS evolution equations. With constant matrix values for the duration of propagation, incorporating NSI takes advantage of functionality built into the nuSQuIDS main branch.

In addition to the physics parameters, the analysis includes 18 nuisance parameters that model the systematic uncertainties at each stage of the neutrino's existence, which are further described in Sec. 6.6. The code managing the likelihood calculation with re-weighting and systematic uncertainties included is

GolemFit [142].

6.4 Signal Prediction

As a "disappearance-appearance" analysis, we search for NSI effects on the expected flux at IceCube (also known as flux *shape* effects). To simulate how NSI signals would manifest in IceCube, we first look at the physics prediction of the NSI-affected flux that would reach IceCube, no detector response included.

With the nuSQuIDS [77] software package, we propagate an initial half-ν_μ, half-$\overline{\nu}_\mu$ flux from the atmosphere to IceCube through zenith angles within the analysis sample range as an illustration of how NSI affect the IceCube neutrino flux. This propagation fully incorporates SM matter effects and standard oscillations, which are small in this E_ν range, in addition to the NSI effects for a given value of $\epsilon_{\mu\tau}$. From simulations of fluxes for values of $\epsilon_{\mu\tau}$ across the analysis scanning range, we find that the effect of $\epsilon_{\mu\tau}$ differs significantly for certain conditions.

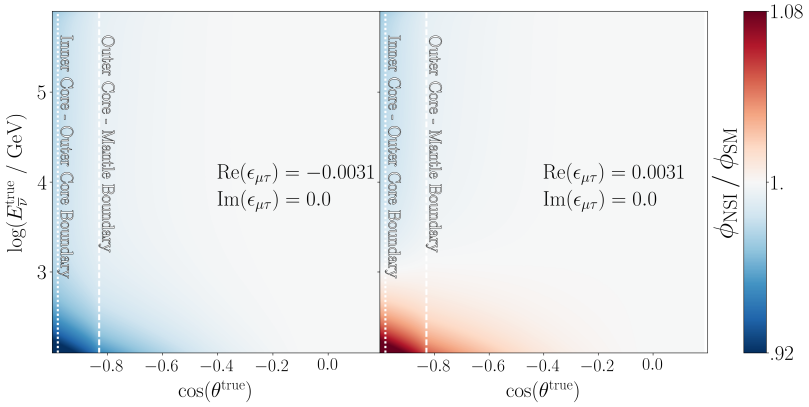

FIGURE 6.8: Oscillogram of ν_μ-only flux for $\epsilon_{\mu\tau} = -0.0031$ (left) and $\epsilon_{\mu\tau} = 0.0031$ right.

Specifically, the ν_μ flux is strongly enhanced at low energies [$\mathcal{O}$(100 GeV)] and large baselines ($\cos\theta \sim$ -1) when Re($\epsilon_{\mu\tau}$) is negative. Conversely, the ν_μ flux is proportionately suppressed when Re($\epsilon_{\mu\tau}$) is positive (Fig.6.8). This trend is reversed in the case of $\overline{\nu}_\mu$ oscillation (Fig.6.9) and in the case of the inverted

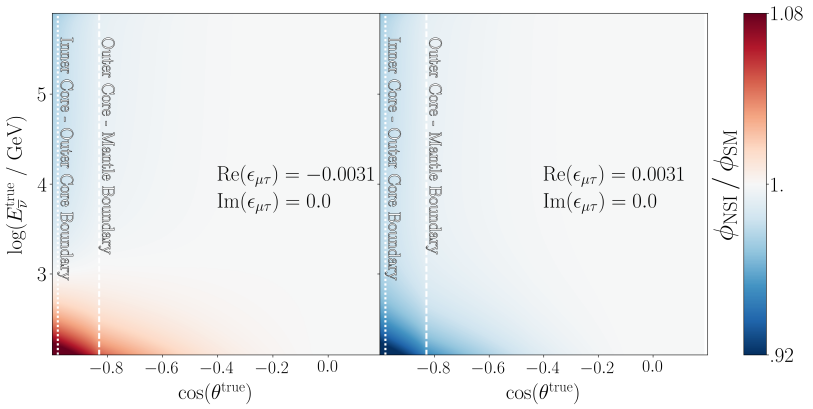

FIGURE 6.9: Oscillogram of $\overline{\nu}_\mu$-only flux for $\epsilon_{\mu\tau} = -0.0031$ (left) and $\epsilon_{\mu\tau} = 0.0031$ right.

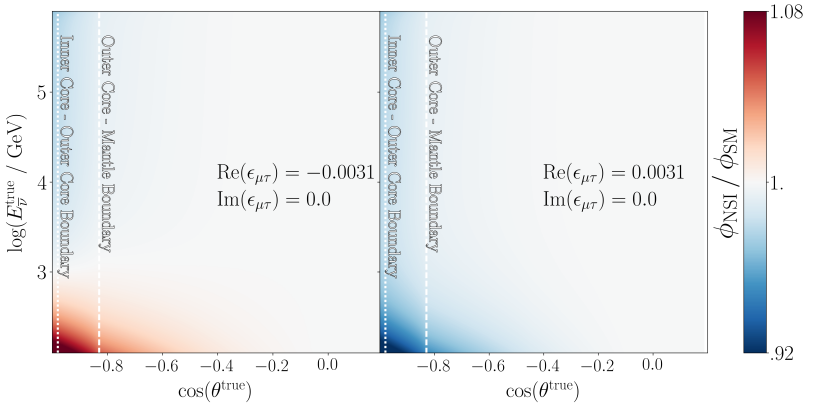

FIGURE 6.10: Oscillogram of ν_μ-only flux for $\epsilon_{\mu\tau} = -0.0031$ (left) and $\epsilon_{\mu\tau} = 0.0031$ (right) in the IMO scenario.

mass ordering (IMO) (Fig.6.10). The mechanisms behind these patterns are explained accordingly:

First, the $\pm\text{Re}(\epsilon_{\mu\tau})$ contribution asymmetry can be explained through investigation of the oscillation probability in Eq. 6.4:

$$P(\nu_\mu \to \nu_\tau) = \sin^2(\Theta)\sin^2\left(\frac{\Delta m^2_{31} L}{4E_\nu} R\right), \tag{6.8}$$

where $\sin^2(\Theta) = \left[\frac{(\sin 2\theta_{23} + R_0 \sin 2\xi)^2}{R^2}\right]$. As the major flux modification happens at the lowest energies, let us examine the case of $E_\nu = 100$ GeV. The second term, $\sin^2\left(\frac{\Delta m^2_{31} L}{4E_\nu} R\right)$ is a function of L that varies slowly with $\epsilon_{\mu\tau}$ and defines the spread of the oscillation, so the first term $\sin^2(\Theta)$ acts as an amplitude. With $\sin 2\theta_{23} \approx 1$, we can see $\sin^2(\Theta) \approx \frac{(1+R_0 \sin 2\xi)^2}{R^2}$ for positive NSI $+\epsilon_{\mu\tau}$ and

$\sin^2(\Theta) \approx \frac{(1-R_0 \sin 2\xi)^2}{R^2}$ for negative NSI $-\epsilon_{\mu\tau}$. For the Standard Model case ($\epsilon_{\mu\tau} = 0$), $\sin^2(\Theta) \approx 1$.

$$\frac{P^{(+\epsilon_{\mu\tau})}_{\nu_\mu \to \nu_\tau}}{P^{\mathrm{SM}}_{\nu_\mu \to \nu_\tau}} \approx \frac{(1 + R_0 \sin 2\xi)^2}{R^2} \quad , \quad \frac{P^{(-\epsilon_{\mu\tau})}_{\nu_\mu \to \nu_\tau}}{P^{\mathrm{SM}}_{\nu_\mu \to \nu_\tau}} \approx \frac{(1 - R_0 \sin 2\xi)^2}{R^2}, \tag{6.9}$$

For $E_\nu = 100$ GeV, $P^{(+\epsilon_{\mu\tau})}/P^{\mathrm{SM}} > 1$ and $P^{(-\epsilon_{\mu\tau})}/P^{\mathrm{SM}} < 1$ for all L in the sample (Fig. 6.11). Hence, through ratios of the oscillation probabilities, we see that $+\epsilon_{\mu\tau}$ induces appearance and $-\epsilon_{\mu\tau}$ induces disappearance at the low energies.

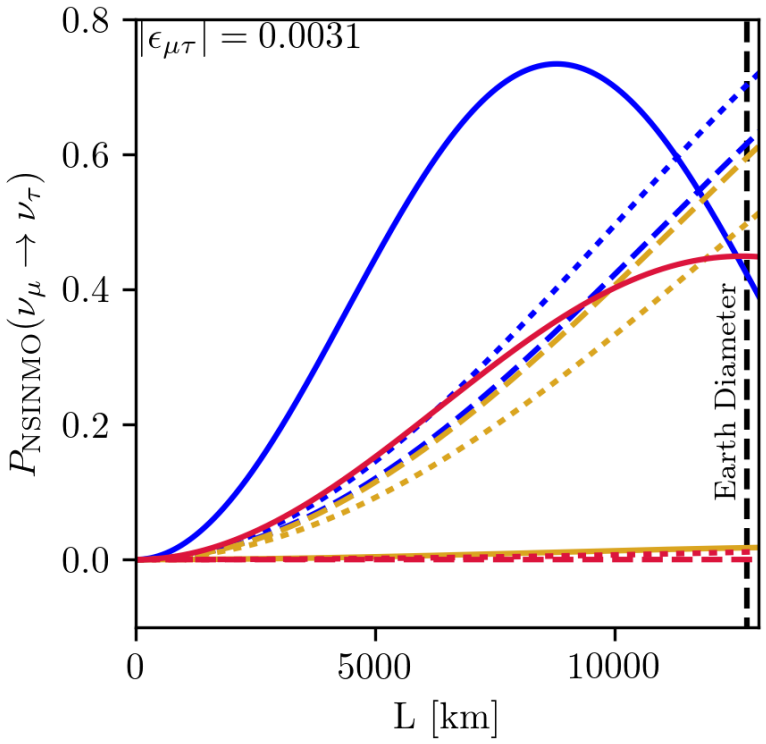

FIGURE 6.11: Oscillation probabilities for NSI values in Fig. 6.4. Solid lines have $E_\nu = 100$ GeV, dashed have $E_\nu = 1$ TeV, and dotted have $E_\nu = 10$ TeV. Blue is for ν_μ oscillation with NSI, gold for $\overline{\nu}_\mu$ with NSI, red for the Standard Model ($\epsilon_{\mu\tau} = 0$). The contours for $\overline{\nu}_\mu$ gold are the equivalent of the ν_μ calculation with $\epsilon_{\mu\tau} = -0.0031$.

Fig. 6.11, which performs the full probability calculation of Eq. 6.4, shows how the the ratios (appearance and disappearance) diminish as the probabilities change with increasing energy (dotted and dashed lines), and that the effect of $-\epsilon_{\mu\tau}$ goes from disappearance to appearance for $E_\nu > \mathcal{O}(100\mathrm{GeV})$.

The mathematics of $\pm\text{Re}(\epsilon_{\mu\tau})$ argument also account for the behavior-swapping between ν_μ and $\overline{\nu}_\mu$, as the transformation from calculating the neutrino oscillation probability to the antineutrino oscillation probability follows $H \to -H$, which implies the probability transforms as $\epsilon_{\mu\tau} \to -\epsilon_{\mu\tau}$. This is confirmed empirically by the independent flux ratio calculation in Fig. 6.9.

To understand the interchange of appearance-disappearance between the NMO and IMO scenarios for ν_μ, we start again with Eq. 6.4 and assume $E_\nu = 100$ GeV. The transformation from NMO to IMO approximately follows, to good precision, $\Delta m^2_{31} \to -\Delta m^2_{31}$. In terms of the probability components for Eq. 6.4, this transformation is the equivalent of $R_0 \to -R_0$ and subsequently $R^2_+ = 1 + R^2_0 + 2R_0 \cos 2(\theta_{23} - \xi) \to R^2_- = 1 + R^2_0 - 2R_0 \cos 2(\theta_{23} - \xi)$. R^2_0 is sufficiently small that $R_+ \approx R_-$, and employing $\sin 2\theta_{23} \approx 1$, we see that

$$\frac{P^{\text{NMO}}_{\nu_\mu \to \nu_\tau}}{P^{\text{SM}}_{\nu_\mu \to \nu_\tau}} \approx \frac{(1 + R_0 \sin 2\xi)^2}{R^2} \quad , \quad \frac{P^{\text{IMO}}_{\nu_\mu \to \nu_\tau}}{P^{\text{SM}}_{\nu_\mu \to \nu_\tau}} \approx \frac{(1 - R_0 \sin 2\xi)^2}{R^2} \tag{6.10}$$

As suggested from Figs.6.9 and 6.10, these are the same approximate probability equations as those in Eq. 6.9. This is verified with the independent probability calculation in Fig.6.12. Overall, this demonstrates what is shown in Figs. 6.8 - 6.10; an approximate equivalence between interchanging $\pm\epsilon_{\mu\tau}$, ν_μ and $\overline{\nu}_\mu$, and NMO with IMO.

IceCube cannot discriminate between ν_μ and $\overline{\nu}_\mu$ signals, so the combination of the $\nu_\mu - \overline{\nu}_\mu$ NSI effects on the total flux significantly weakens the strength of potential signals. The result of the full $\nu_\mu - \overline{\nu}_\mu$ flux propagation is a mostly-disappearance signal along the sample energy range for $\cos(z) < -0.8$, with only a small amount of appearance at the low energy offering weak discrimination between $\pm\text{Re}(\epsilon_{\mu\tau})$. An example of this full flux calculation was shown in Fig. 6.4. When the same NSI parameter values of Fig. 6.4 are applied to the full simulation of the detector response, we get the 2D histogram in Fig. 6.13. Note that the overall normalization change in Fig. 6.13 negligible compared to the flux normalization uncertainty, as shall be shown in Sec. 6.6.

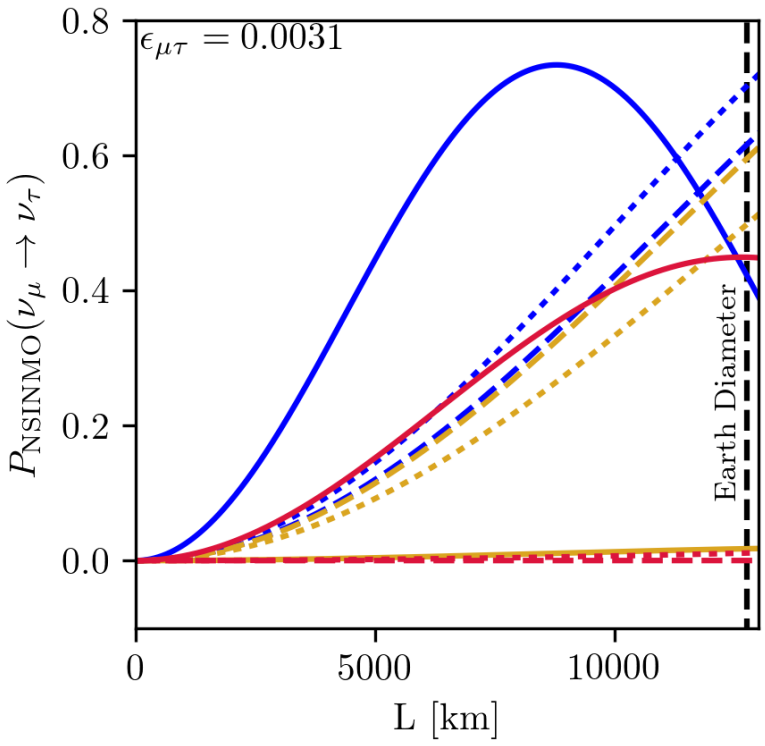

FIGURE 6.12: Oscillation probabilities for NSI values in Fig. 6.4. Solid lines have $E_\nu = 100$ GeV, dashed have $E_\nu = 1$ TeV, and dotted have $E_\nu = 10$ TeV. Blue is for the NMO scenario, gold for the IMO scenario, red for the Standard Model ($\epsilon_{\mu\tau} = 0$, NMO-IMO invariant).

6.5 Fit and Sensitivity Procedures

To search for NSI effects on the shape of atmospheric neutrino fluxes, we compared Monte Carlo simulation to data and calculated the binned likelihood for each NSI hypothesis in reconstructed energy-zenith space. Events are binned uniformly[2] in muon reconstructed log-energy, $\log(E^\mu_{\text{reco}})$, and cosine of the incident zenith angle, $\cos(\theta^\mu_{\text{reco}})$. The tested hypotheses are 201 points uniformly distributed in $\text{Re}(\epsilon_{\mu\tau}) \in [-0.01, 0.01]$, from which the hypotheses with non-zero $\text{Re}(\epsilon_{\mu\tau})$ can have their likelihoods interpolated. Among the tested hypotheses is the null (no-NSI) hypothesis, $\epsilon_{\mu\tau} = 0$.

This analysis utilizes a maximum-likelihood technique that is described as follows: the likelihood, or the probability of observing the given data after

[2]There are 13 energy bins, $E^\mu_{\text{reco}} \in [500\text{ GeV}, 9976\text{ GeV}]$, and 20 zenith bins, $\cos(\theta^\mu_{\text{reco}}) \in [-1.0, 0.0]$.

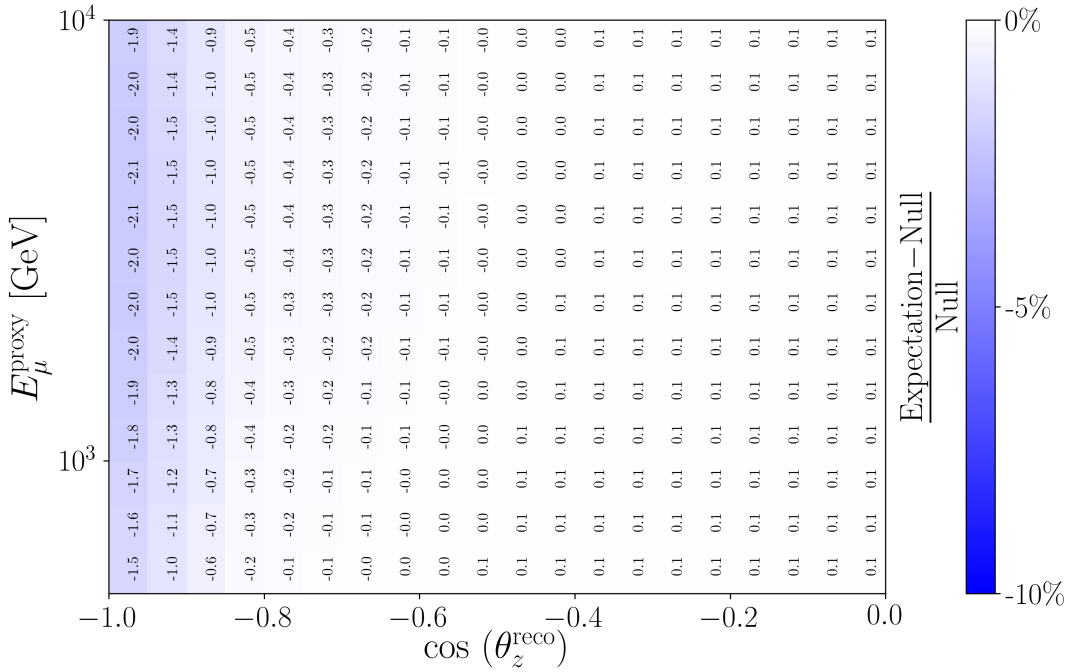

FIGURE 6.13: Percent relative difference between the MC signal expectation for the NSI values in Fig. 6.4 and the null (SM) hypothesis MC expectation.

specifying a hypothesis, is defined in this analysis as

$$\mathcal{L}(\vec{\Theta},\vec{\eta}) = \prod_{i=1}^{\text{N}_{\text{bins}}} \mathcal{L}_{\text{Eff}}\left[\,\mu_i(\vec{\Theta},\vec{\eta})\,,\sigma_i(\vec{\Theta},\vec{\eta})\,;\,x_i\,\right], \tag{6.11}$$

where $\vec{\Theta}$ is the physics hypothesis, $\vec{\eta}$ is the set of systematic nuisance parameters, x_i is the observed event bin count, and $\mu_i(\vec{\Theta},\vec{\eta})$ and $\sigma_i(\vec{\Theta},\vec{\eta})$ are the expected bin count and bin MC statistical uncertainty, respectively, for the given hypothesis and nuisance parameter values. $\mathcal{L}_{\text{Eff}}$ is the effective likelihood that replaces the Poisson likelihood to account for the aforementioned MC statistical uncertainty, and is defined as

$$\mathcal{L}_{\text{Eff}}(\vec{\Theta}|x_i) = \left(\frac{\mu_i}{\sigma_i^2}\right)^{\frac{\mu_i^2}{\sigma_i^2}+1}\Gamma\left(x_i+\frac{\mu_i^2}{\sigma_i^2}+1\right)\left[x_i!\left(\frac{\mu_i}{\sigma_i^2}+1\right)^{x_i+\frac{\mu_i^2}{\sigma_i^2}+1}\Gamma\left(\frac{\mu_i^2}{\sigma_i^2}+1\right)\right]^{-1}. \tag{6.12}$$

To incorporate known constraints on the systematic parameters, we weight the likelihood with the collected Gaussian[3] nuisance parameter prior probability

[3]While most parameters have Gaussian prior, "ice gradient 0" and "ice gradient 1" from the bulk ice FFT parameterization have correlated (bivariate) Gaussian priors (see Sec. 6.6).

distributions ("priors"). These weighted likelihoods are maximized across the constraint values to form a *profile* likelihood, defined as

$$\mathcal{L}_{\text{profile}}(\vec{\Theta}) = \max_{\vec{\eta}}[\,\mathcal{L}(\vec{\Theta},\vec{\eta})\,\Pi(\vec{\eta})\,], \tag{6.13}$$

where

$$\Pi(\vec{\eta}) = \prod_{j=1}^{\text{N}_{\text{syst.}}} \Pi(\eta_j), \tag{6.14}$$

is the product of Gaussian priors $\Pi(\eta_j)$ for the systematic nuisance parameters.

With these components, the analysis test statistic (TS) for producing confidence regions can be defined:

$$\begin{aligned} \text{TS}(\vec{\Theta}) &= -2\left[\log\mathcal{L}_{\text{profile}}(\vec{\Theta}) - \log\mathcal{L}_{\text{profile}}(\hat{\vec{\Theta}})\right] \\ &= -2\,\Delta\log\mathcal{L}_{\text{profile}}(\vec{\Theta}) \\ &= -2\Delta\text{LLH}, \end{aligned} \tag{6.15}$$

where $\hat{\vec{\Theta}}$ is the hypothesis that minimizes $\mathcal{L}(\vec{\Theta})$, or, in other words, the hypothesis that best matches the data (best-fit point). Hence, discussion of the test statistic refers to the LLH (specifically, -2ΔLLH). Frequentist confidence regions are built with the Neyman method in the Feldman-Cousins ordering. From tests of multiple hypothesis points with MC pseudoexperiment ensembles (see Sec. 6.11), the test statistic reliably conforms to Wilks' theorem [143, 144], and thus Wilks' theorem is assumed throughout the analysis when drawing contours.

6.6 Sensitivity and Systematic Uncertainties

To include systematic uncertainties in the LLH calculation, a collection of nuisance parameters that reweight MC event sets through continuous parameterizations are employed. The predominant sources of uncertainty originate from the shape and normalization of both the atmospheric and astrophysical neutrino fluxes, optical impurities of continental South Pole glacier ice, the optical properties of encasing the DOMs, and the neutrino interaction cross-sections. In the 8-year sterile neutrino search from which this analysis sample is obtained, other forms of systematic uncertainty were investigated and found quantitatively inconsequential to the total statistical uncertainty [68, 69]. The following subsections describe the nuisance parameters applied to this analysis.

6.6.1 Conventional Flux Normalization

The total conventional[4] atmospheric ν_μ and $\overline{\nu}$ flux has an overall normalization uncertainty [75] quantified by the Φ_{conv} parameter. As $\epsilon_{\mu\tau}$ affects both the rate and shape of the atmospheric neutrino flux, the analysis seeks to only constrain $\epsilon_{\mu\tau}$ with flux shape information. Hence, we have the conventional atmospheric flux normalization nuisance parameter, with major uncertainty from further effects (see Secs. 6.6.2, 6.6.3, and 6.6.4), float freely with a Gaussian prior.

Further, an investigation by Ref. [145] found that an informed choice of this prior can reflect flux *rate* information, which allows for hypotheses that induce minimal shape changes but significant oscillation effects[5] to be identified and properly weighted in likelihood calculations. The first factor in choosing the prior is the normalization uncertainty from model variation effects calculated by Ref. [147] (Fig.6.14, left), which found a $\pm 30 - 40\%$ uncertainty for the

[4] The conventional atmospheric flux refers to neutrinos ejected from π and K meson decays in the atmosphere. This terminology is meant to differentiate the conventional component from the prompt atmospheric flux component, where the term "prompt" refers to neutrinos produced from atmospheric charmed meson decays.

[5] This occurs when neutrino oscillations are so rapid, they "average-out".

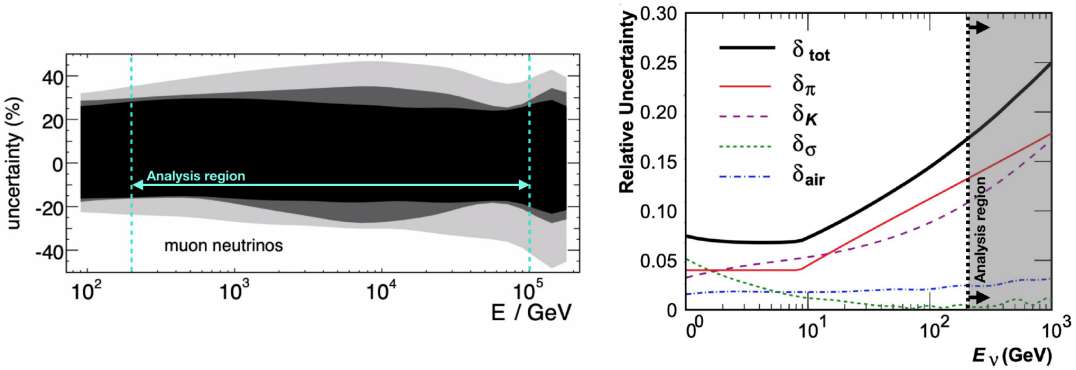

FIGURE 6.14: Left: Uncertainty band determined from perturbations of the atmospheric interaction model (inner band) and the bands from combined models of both the atmospheric interaction model and different cosmic ray models (outer bands), modified from Ref. [145]. Right: Component and total (black) neutrino production uncertainties. δ_π and δ_K are uncertainties pertaining to pion and kaon production, respectively. δ_σ is the uncertainty contribution from hadronic production and δ_{air} from the uncertainty in the atmospheric density. Modified from Ref. [146].

relevant ν_μ energies. Second was the agreement of the analysis uncertainty calculation and that of Ref. [146] (the "HKKM calculation"), shown in Fig.6.14, right. The uncertainty at the energy maximum of the HKKM calculation is $\pm 25\%$ and is projected to increase with energy. Between these two factors, a choice of a $\pm 40\%$ prior was determined for Φ_{conv}.

6.6.2 Cosmic Ray Spectral Index

The various spectra of CR primary particles relevant to this particular neutrino flux follows an approximate energy power law of $E^{-2.65}$. The implementation of this power law, and $\Delta\gamma$, the uncertainty in the spectral power, relies on a pivot energy E_0 through

$$\phi(E) = \phi(E)_0 \frac{E}{E_0}^{-\Delta\gamma}, \tag{6.16}$$

such that E_0 is 2.2 TeV to approximately preserve the flux normalization. From an analysis performed by Refs. [50, 68, 69] of multiple CR experimental measurements [148–151], a $\Delta\gamma$ prior width of 0.03 was selected.

6.6.3 Meson Production

Uncertainties from the meson production due to CR-atmosphere and subsequent interactions are incorporated through reweighting fluxes by gradients calculated for values near the nominal production uncertainty parameter values [50, 68, 69]. These parameters are calculated as functions of incident parent particle energy E_i and the ratio of the secondary particle energy to the incident particle energy, $x_{\text{lab}} = E_s/E_i$.

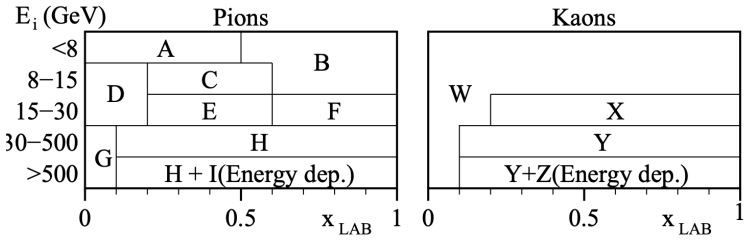

FIGURE 6.15: Pion and kaon uncertainty parameterization as a function of E_i and x_{lab}. Table from Ref. [152].

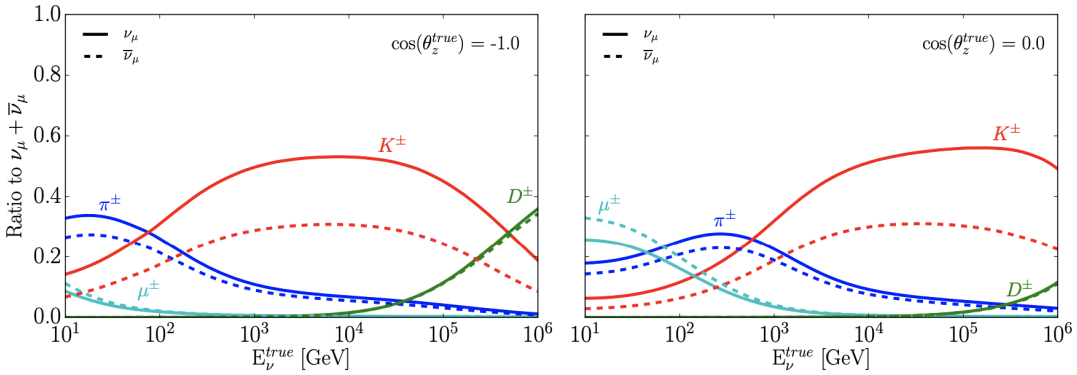

FIGURE 6.16: The neutrino flux contribution from each parent particle to the total flux at IceCube. The left panel is the upgoing neutrino flux while the right panel is the flux at the horizon. Figure from Ref. [68].

This model follows the model defined in Ref. [152] (the "Barr parameterization", Fig. 6.15). Refs. [50, 68, 69] found that for the energy range of this

analysis ($\geq$ 500 GeV), parameters pertaining to pion decay were negligible (parameters $A^{\pm}$-$I^{\pm}$) while those relevant to kaon decay ($W^{\pm}$,$Y^{\pm}$,$Z^{\pm}$) were dominant[6], as kaon decay is the predominant source of atmospheric neutrino production above 30 GeV (Fig. 6.16). The prior 1σ widths on these six nuisance parameters are listed in Table 6.1.

Parameter	Central Value	Uncertainty
W+	0	±40%
W−	0	±40%
Y+	0	±30%
Y−	0	±30%
Z+	0	±12.2%
Z−	0	±12.2%

TABLE 6.1: The priors for the Barr parameters employed in this analysis. Adapted from Ref. [50].

It is sufficient to only employ nuisance parameters for kaon neutrino production, as variations of the kaon uncertainty parameters sufficiently cover the possible contributions to the flux from pions.

6.6.4 Atmospheric Density

From the decay of pions and kaons ejected from CR-atmosphere interactions, the conventional atmospheric neutrino flux is produced. It is known from Ref. [153] that the rates of neutrino production due to CR shower pion and kaon decay are affected by the density of atmospheric particles. This is because density of air surrounding the meson affects the likelihood of the meson interacting and not producing a decay neutrino (the more air near a meson, the more likely it will interact with an air particle). As density is proportional to temperature, we can quantify this neutrino production dependence on density through a characteristic energy ε_i:

[6]The positive and negative signs denote the separate parameters for each positively and negatively charged meson

$$\varepsilon_i = T(X) \cdot \frac{Rcm_i}{Mg\tau_i}, \tag{6.17}$$

where i is the index for the K or π mesons, $T(X)$ is the temperature at atmospheric slant depth X, R is the ideal gas constant, M is the molar mass, g is the acceleration due to gravity, c the vacuum speed of light, and m_i and τ_i are the mass and decay time, respectively, of the meson.

When $E_\nu \cdot \cos\theta_\nu < \varepsilon_i$, the meson is favored to decay and the flux of neutrinos is density-independent. Yet for $E_\nu \cdot \cos\theta_\nu > \varepsilon_i$, decay is suppressed and the neutrino flux is now correlated with density. Therefore, the density is a determining factor in the atmospheric neutrino flux and with uncertainty that must be accounted for.

The atmospheric density nuisance parameter, *Atm. Density*, has a prior determined from analysis by Refs. [50, 68, 69] of atmospheric temperature data from the AIRS satellite [135] by simulating CR air showers in stochastically-perturbed atmospheric density profiles within predetermined uncertainty ranges.

6.6.5 Astrophysical Neutrino Flux

The astrophysical neutrino flux is assumed to have a $\nu_\mu : \overline{\nu}$ ratio of 1 : 1, an isotropic distribution, and an energy power dependence. Similar to the conventional atmospheric neutrino flux, the astrophysical flux relies on a normalization parameter Φ_{astro}, with a central value defined at pivot energy 100 TeV of $0.787 \times \text{GeV}^{-1}\text{sr}^{-1}\text{s}^{-1}\text{cm}^{-2}$, and a spectral index of -2.5 with an added value that quantifies the uncertainty ($\Delta\gamma_{\text{astro}}$). $\Delta\gamma_{\text{astro}}$ has a central value of 0.0:

$$\frac{dE_\nu}{dE} = \Phi_{\text{astro}} \frac{E_\nu}{100\text{TeV}}^{-2.5+\Delta\gamma_{\text{astro}}}. \tag{6.18}$$

The priors on Φ_{astro} and $\Delta\gamma_{\text{astro}}$ are correlated Gaussian distributions determined from the confidence region encompassing (Fig. 6.17) IceCube astrophysical flux measurements [154–159], modeled with a $\nu_\mu : \overline{\nu}$ ratio of 1 : 1 assuming

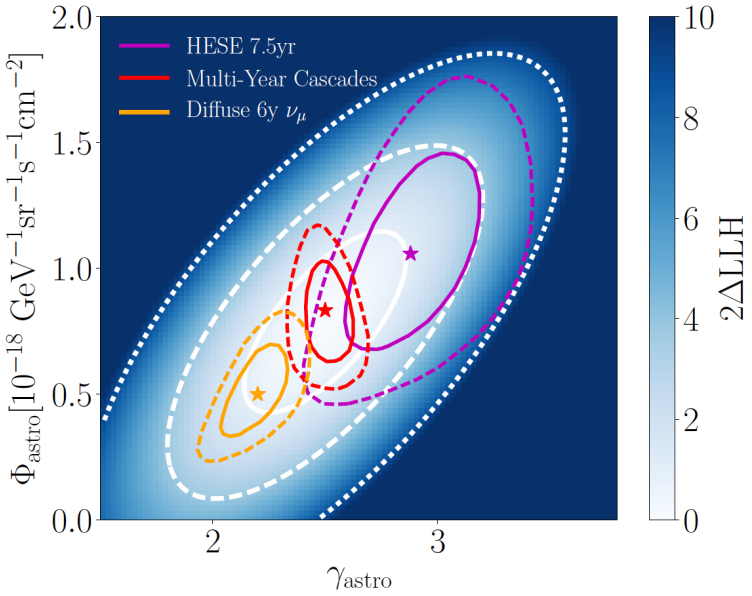

FIGURE 6.17: From Refs. [50, 68, 69, 154]: Comparison of global and independent IceCube astrophysical flux measurements from Refs. [154–159]. Stars denote independent best-fit parameters while the dotted lines mark 99.7% CL regions, dashed lines represent 95.4% CL regions, and solid lines represent 68.3% CL regions. White lines highlight the analysis correlated Gaussian prior CL regions from the global fit to data.

a single-power energy law [50, 68, 69]. Widths for the priors are 36% for both.

6.6.6 Glacial Ice Optical Purity

The ice sheet that is up to 3 km thick covering Antarctica, referred-to as the bulk glacial ice, is optically impure due to depth-dependent dust concentrations. To efficiently model the optical properties of the bulk ice and the corresponding uncertainties, the absorption and scattering coefficients measured for each 10 m slice of glacier depth are transformed into a Fourier series via a "Fast Fourier Transform" (FFT) method up to a finite cutoff, with modes ordered from the largest to smallest effects on the propagation of light in the ice [73]:

$$\frac{1}{2}\log(\text{Abs}\times\text{Sca}) = \frac{A_0}{2} + \sum_{n=1}^{N} A_n \sin\left(\frac{2\pi n x}{L} + \phi_n\right), \tag{6.19}$$

where Abs and Sca are the original optical parameters for the ice layer of depth x and L is the range of depth layers. Each amplitude and phase of the FFT is

now an effective nuisance parameter, but only the first few modes (9) occupy the majority of the uncertainty contribution.

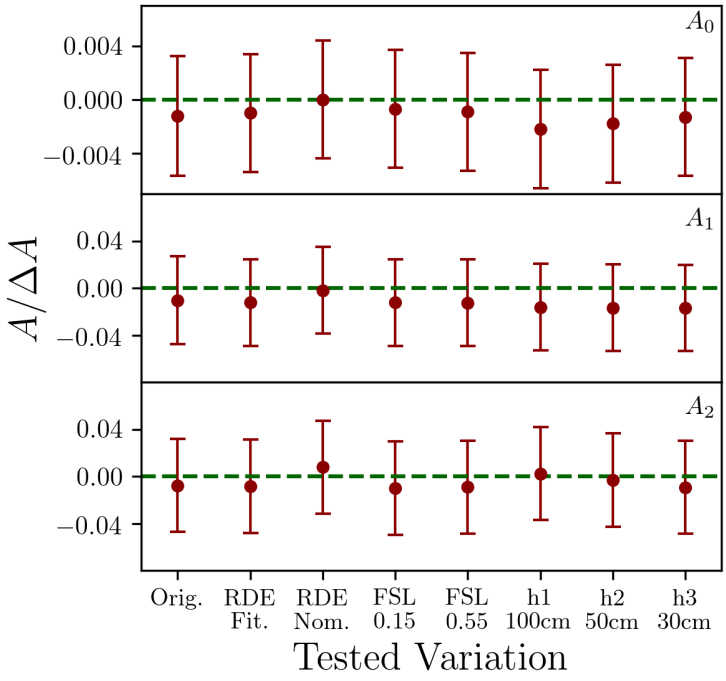

FIGURE 6.18: A comparison of the original Refs. [50, 68, 69] (Orig.) Gaussian prior width of the FFT amplitudes to the widths recovered from the tested variations. Widths shown are calculated for SREP = 10.

To derive priors on each parameter, the amplitudes and phases are perturbed and the corresponding likelihood values are compared to the profile derived from DOM calibration flasher data. Yet, rather than remain burdened with 18 parameters (reduced from 170 pairs of layer optical parameters), another technique allows us to further reduce the number of effective nuisance parameters.

The SnowStorm software suite [73] implements a method of sampling the Fourier parameter space through perturbing a single central MC set rather than generating more MC sets within the parameter space. Two energy-dependent basis functions emerge from correlations between the perturbed modes, and the amplitudes (Ice Gradient 0 and Ice Gradient 1) of the functions ultimately serve as the nuisance parameters for the bulk glacial ice uncertainties. These nuisance parameters, like the astrophysical nuisance parameters, have bivariate (correlated) Gaussian priors.

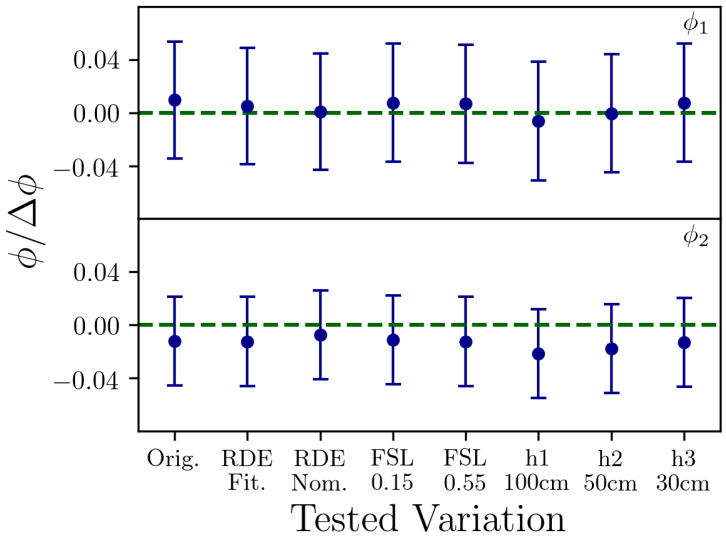

FIGURE 6.19: A comparison of the original Refs. [50, 68, 69] (Orig.) Gaussian prior width of the FFT phases to the widths recovered from the tested variations. Widths shown are calculated for SREP = 10.

Since the original analysis framework developed by Refs. [50, 68, 69] was first used, advancements have continued within the IceCube Collaboration. One such advancement has been the improvements in models of the bulk ice optical properties. This analysis has adopted SPice3.2.1 Refs. [67, 160], the successor to the model used in Refs. [50, 68, 69]. A portion of the NSI analysis was spent determining if the updated ice model returns Gaussian prior widths of the FFT amplitudes and phases with comparable sizes to those in Refs. [50, 68, 69]. Should the sizes return approximately the same, the bulk ice uncertainties from Refs. [50, 68, 69] would not require adjustment for use in the NSI analysis.

To determine if the SPice3.2.1 widths change negligibly and that the bulk ice uncertainty is robust under variations in leading effects from the ice or detector, each FFT parameter width is calculated for multiple configurations of the photon propagation simulator and likelihood calculator, PPC (Photon Propagation Code) [66]. The calculation was performed for the first three amplitudes (Fig.6.18) and first two phases[7] (Fig.6.19) as these are the leading-order effects

[7]Mode 0 sets the absolute scale of the ice model and is depth-independent, having no phase as can be seen in Eq. 6.19.

on the bulk ice uncertainty.

Configurations tested are the FSL [66] (forward scattering length) parameter, the relative DOM efficiency (RDE), and the borehole radius. The FSL determines the shape of the in-ice light scattering function, and values tested are 0.15 and 0.55. The RDE is defined as RDE = individual DOM efficiency / average DOM efficiency, with values tested at the nominal RDE value (RDE Nom.) and the fitted value (RDE Fit.). Lastly, the tested values of the borehole radius are h1 = 100 cm, h2 = 50 cm, and h3 = 30 cm. As a last test, each variation was also tested at multiple values of SREP (Simulated photon event REPitions): SREP = 1, 10, and 50.

Results of the width calculations for SPice3.2.1 with variations at SREP = 10 are shown in Fig. 6.18 (amplitudes) and Fig. 6.19 (phases). The original Refs. [50, 68, 69] widths for SPice3.2 are listed as "Orig.". Comparing the new widths to the original, the relative change in size is $< 2\%$. This is also true for SREP = 1 and 50. Hence, the bulk ice uncertainties from Refs. [50, 68, 69] are sufficient to cover variations in the new ice model.

6.6.7 Refrozen Borehole Ice Optical Characteristics

After deployment of the cables containing the optical modules, the melted water in the drilled borehole refreezes around the sensors with bubbles and dust inhomogeneously distributed, creating a new source of uncertainty from a region termed "hole ice" [61–64]. The impurities in this type of ice modify the trajectories of photons that travel to DOMs through the bulk ice, and thus changes the effective DOM angular efficiency such the efficiency must be determined empirically after deployment. After such studies were conducted, two new parameters, p_1 and p_2, emerged as the degrees of freedom of the angular efficiency function:

$$A(\eta) = 0.34(1 + 1.5\eta^3/2) + p_1\eta(\eta^2 - 1)^3 + p_2 e^{10(\eta - 1.2)}, \tag{6.20}$$

where η is the incident photon angle.

Refs. [50, 68, 69] found that only p_2 contributes significantly to the uncertainty from the hole ice such that perturbations in p_2 cover all effects from perturbations of p_1. Henceforth, the p_2 parameter has been referred-to as the "Forward Hole Ice" parameter.

6.6.8 Optical Module Efficiency

The DOM has an overall effective sensitivity to photons with a corresponding uncertainty and nuisance parameter. The contributions to DOM efficiency include elements internal to the DOM, such as the photocathode efficiency and wavelength acceptance, and aspects external to the DOM, including the surrounding hole ice and shadow from the sensor cable [50, 68, 69]. Due to the contributions from other forms of systematic uncertainty, the prior on the DOM efficiency was determined through simulations events and their corresponding photons reaching the DOMs with different sets of perturbed nuisance parameter values. The final DOM efficiency prior width was determined to be 10%.

6.6.9 Cross-Sections

Three distinct cross-sections contribute to the uncertainty: the kaon energy loss cross-section, and the neutrino/antineutrino interaction cross-sections.

As charged kaons are predominantly responsible for the neutrino flux that composes the analysis sample, the kaon-nuclei cross-section in-atmosphere hence becomes a source of uncertainty. Since the total kaon cross-section is only known for $E_\nu < 310$ GeV (below the analysis energy range), Refs.[50, 68, 69] proceeded to carry out a theoretical projection of σ_K at the relevant energies. Ultimately, it was determined that the prior width would conservatively be $\pm 7.5\%$

The $\nu/\overline{\nu}$ cross-sections determine the rate of neutrino absorption as fluxes propagate through Earth [161, 162], which in turn affects the rate of interactions within the detector [163, 164]. Uncertainty contributions from neutrino interactions at the detector were found by Refs. [145, 165] to be inconsequential while the uncertainties of the neutrino cross-sections on in-Earth absorption could be parameterized in a scheme of linearly-scaling cross-sections (σ_{ν_μ} and $\sigma_{\overline{\nu}}$). From there, the priors have been fixed at the maximum uncertainties found within the analysis sample energy range [164].

6.6.10 Uncertainty Impact on Sensitivity

To find the impact of systematic uncertainties on the analysis fit, the Wilks 90% CL sensitivity has been calculated in each instance of fixing the value of a selected nuisance parameter while the others were left free. These tests employ the "Asimov" [166] method, followed by validation against the true median sensitivity from 1,000 pseudoexperiment trials. The most concise treatment of these tests for this analysis is to use categories of parameters organized into three types: hadronic[8], cosmic[9], and detector[10].

From these tests, it was found that fixed cosmic nuisance parameter values resulted in a $\sim -0.82\%$ relative change in the $|\epsilon_{\mu\tau}|$ sensitivity, while fixed hadronic parameters have a relative change of $\sim -1.63\%$. Lastly, the most significant uncertainty contribution is from the collection of detector parameters, which have a $\sim -9.80\%$ relative change from the central sensitivity radius. These systematic impact contours, in addition to the central 90% CL sensitivity, are displayed in Fig. 6.20.

[8] W/Y/Z parameters, atmospheric density, Φ_{conv}, $\Delta\gamma_{\text{conv}}$
[9] Φ_{astro}, $\Delta\gamma_{\text{astro}}$
[10] DOM efficiency, Ice Gradient 0 and Ice Gradient 1 (SnowStorm), p_2 (column ice)

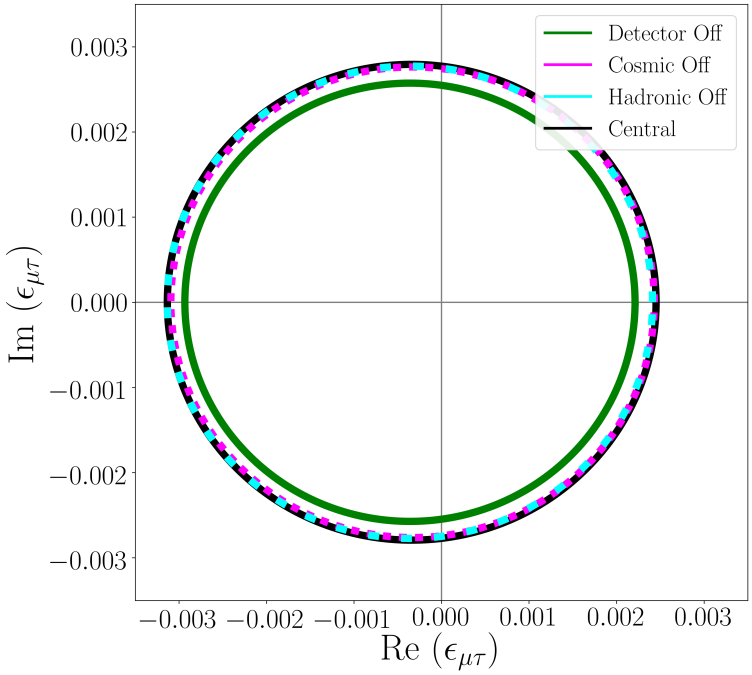

FIGURE 6.20: The central 90% CL sensitivity (black) and the 90% CL sensitivity contours when one of the three categories of systematic uncertainties is fixed to the nuisance parameter central values.

6.7 Inject-Recover (Roundtrip) Tests

Inject-recover (IR) tests measure the capability of the statistics minimizer (GolemFit) to correctly recover artificially injected NSI signals, which establishes confidence that the best-fit NSI parameters recovered from the data are accurate. To perform the IR test, an Asimov dataset [166] is generated for a chosen set of NSI parameters. The dataset is then compared against the entire hypothesis space to generate a LLH profile, from which the best-fit parameters are determined.

This analysis tested 19 points across the parameter space to demonstrate that the correct best-fit will be recovered in any data scenario (examples of these tests are shown in Fig. 6.21).

Out of the 19 tests, 18 recovered the injected signal. The test that did not recover the parameters exactly found the best-fit point to be adjacent to the injection at 10^{-4} $\epsilon_{\mu\tau}$ units away with a $-2\Delta LLH$ difference of $2 \cdot 10^{-4}$ (see Fig. 6.22), which is qualitatively extremely small. Due to the proximity of the recovered point to the injection and the smallness of the $-2\Delta LLH$ value, the

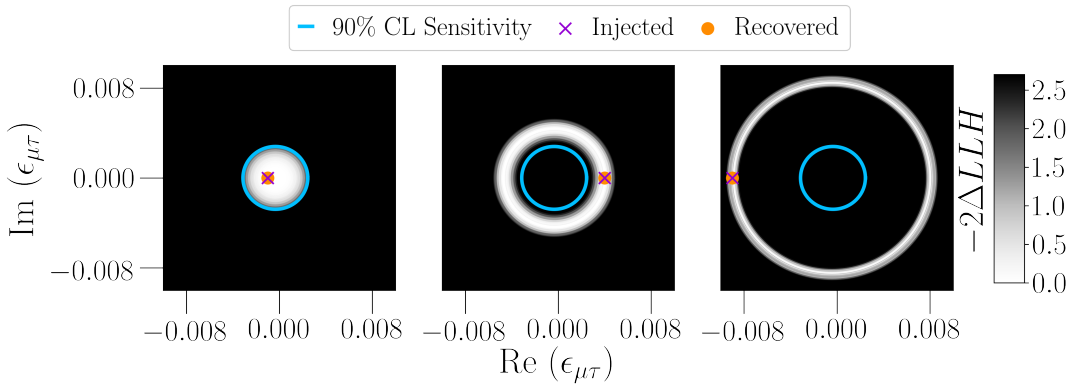

FIGURE 6.21: Examples of IR tests performed within, near, and outside the central 90% CL sensitivity in the NSI parameter space.

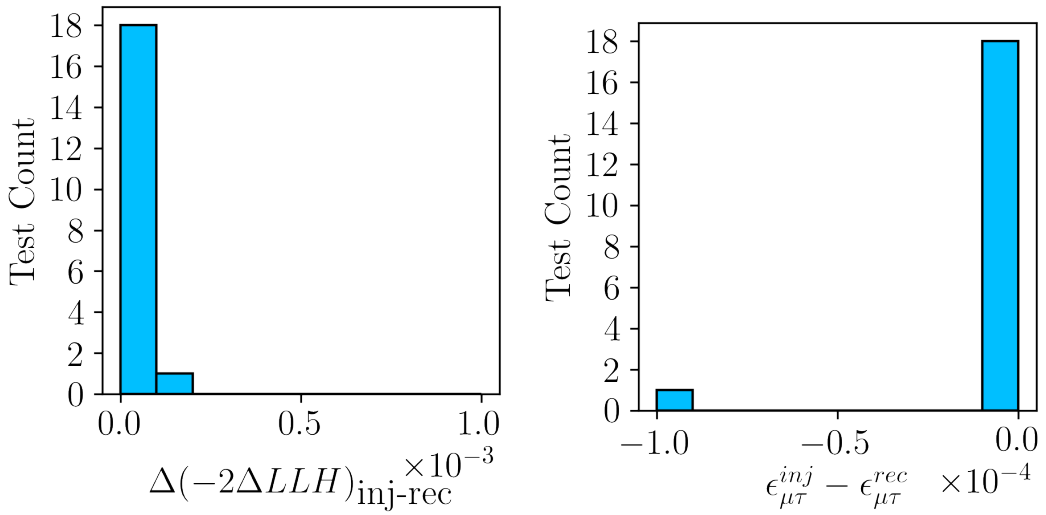

FIGURE 6.22: (Left) LLH mismodelling between injected and recovered NSI hypotheses. (Right) mismodelling between injected and recovered NSI hypotheses.

failed test is inconsequential when compared to the number of successful tests, especially when considering the hypotheses surrounding each injection have similar likelihood values often within the precision of the minimizer. Therefore, we confirm that the minimizer is capable of accurately recovering the best-fit NSI signal.

6.8 Frequentist Regions (Brazil Bands)

The sensitivity in Sec. 6.6 is an estimation of what CL contour the unblinded data would yield assuming every step in the modeling is a perfect representation

of the physical world. As this is inherently not possible, a further illustrative calculation is determining the *frequentist regions*, or "Brazil bands"[11]. Frequentist regions denote the areas of the hypothesis space where a specified percentage of pseudoexperiment trials ("realizations") at the null hypothesis have their CL contour. The Asimov sensitivity is calculated with an Asimov realization, which is the expected distribution for a given hypothesis without statistical fluctuations and is a representative average of what the hypothesis signal would appear as. In contrast, to reflect the variation in real-world data, the frequentist region realizations have Poisson-fluctuated[12] expected distributions at the null hypothesis, with the nuisance parameters kept at the prior central values. These fluctuated realizations result in CL contours that deviate from that of the Asimov realization, and a large number of realizations will have CL contours that converge to produce the frequentist regions. For this procedure, 1000 realizations at the NSI null hypothesis ($\epsilon_{\mu\tau} = 0$) were generated and had their respective LLH profiles calculated, after which the CL contours were produced. Fig. 6.23 exhibits the regions where 68% (green) and 95% (yellow) of the realizations have their CL contour. The median value of the bands, which converges to the Asimov sensitivity, is shown in the dotted line. This calculation is beneficial in discussions of a result's significance. Result contours that lie outside the frequentist regions are notable, and the farther the result distances from the regions, the more significant the result is, meriting further investigation.

6.9 Pre-Unblinding Checks and Data Sample

To verify that no issues existed within the fitting software or the data sample, a series of pre-unblinding checks were devised to act as stopping triggers in the event an unreasonable divergence between the MC and data arose. First, all

[11] Named after the resemblance to the flag colors of the Federative Republic of Brazil

[12] The Poisson distribution is a statistical distribution that represents the probability of a given number of events will occur over a specified time.

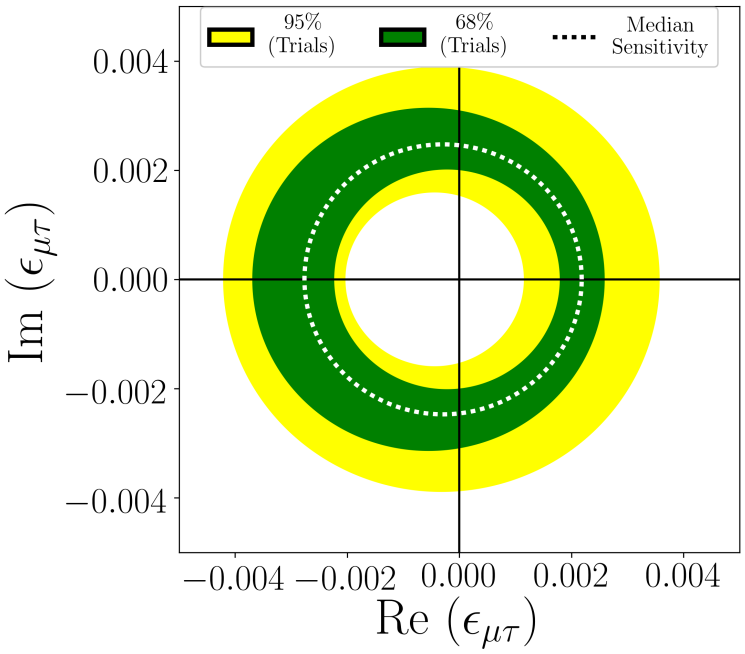

FIGURE 6.23: Frequentist regions: regions where 95% (yellow) and 68% (green) of 1000 pseudoexperiment trials have their 90% CL sensitivity contours. The analysis 90% CL median sensitivity is shown with the dotted line.

tests were applied to a random 5% selection of the total data sample. Should the initial 5% sample tests pass, the tests would then be applied to the full sample.

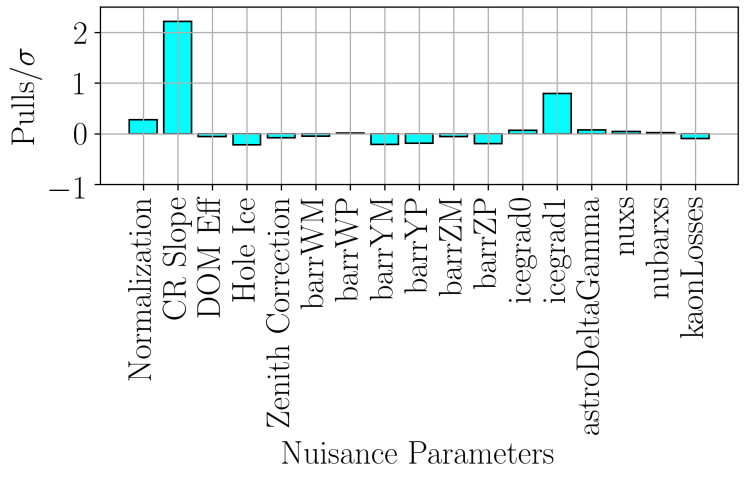

FIGURE 6.24: Pulls of nuisance parameters at the NSI best-fit point using 100% of data.

After minimizing across the profile likelihood of the data and storing a blind best-fit point, the first test was to calculate the statistical pulls of the systematic

nuisance parameter values at the blind best-fit point. If any pull exceeded 3σ, the procedure is halted. The resulting pulls of the 100% data test are displayed in Fig. 6.24. Both the 5% and 100% data selections pass the nuisance parameter pull test.

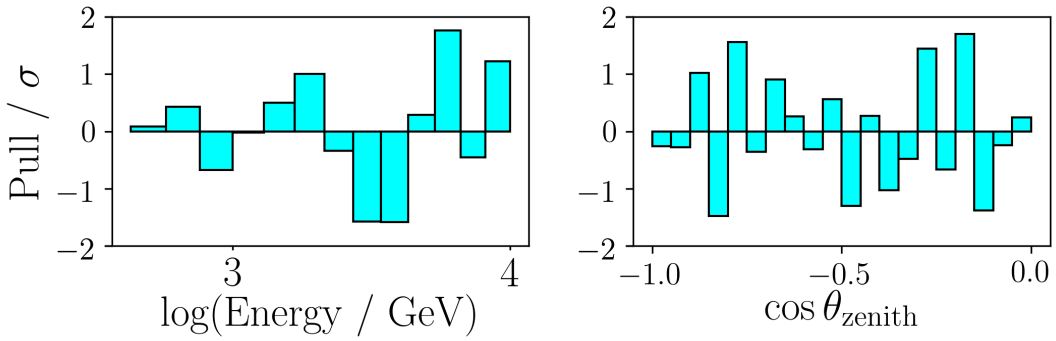

FIGURE 6.25: 1D data/MC pull distributions at NSI best-fit in event energy bins (left) and zenith bins (right) for 100% of data.

Next, the best-fit MC-data pulls in the one-dimensional zenith and energy distributions are calculated, in which the stopping threshold is if three or more bins pull greater than 3σ. The "1D pulls" for the 100% data test are displayed in Fig. 6.25. Both the 5% and 100% data selections pass the 1D distribution pull test.

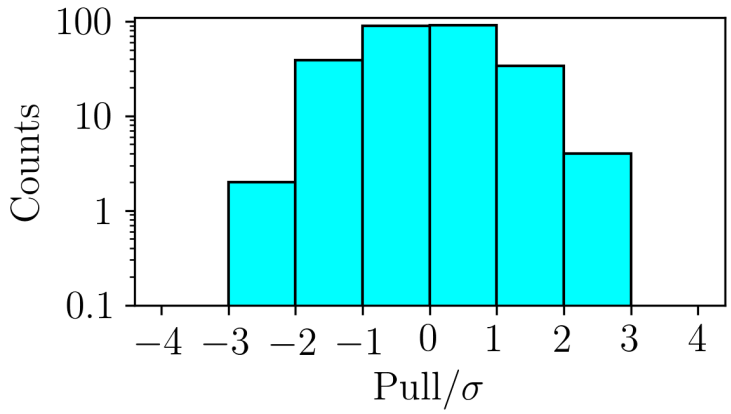

FIGURE 6.26: Histogram of 2D data/MC bin pulls at NSI best-fit for 100% of data.

In the complete two-dimensional event binning, the MC-data pulls are calculated, and the stop trigger activates if six or more bins pull greater than 3σ.

The 2D pull distribution is shown in Fig. 6.26. Both the 5% and 100% data selections pass the 2D distribution pull test.

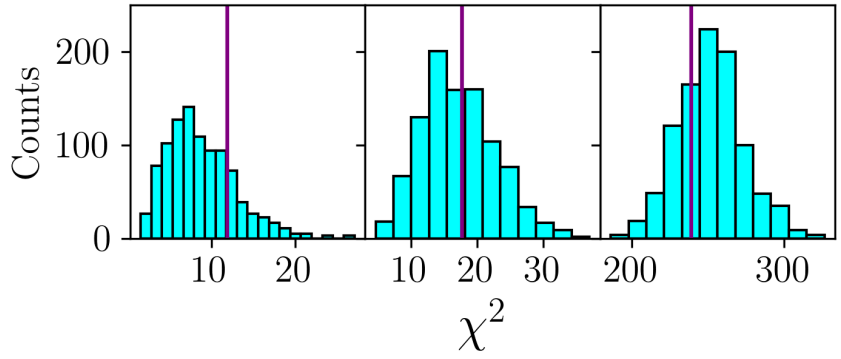

FIGURE 6.27: Histogram of χ^2 values from 1000 pseudoexperiment trials for the 1D energy distributions (left), 1D zenith distributions (middle), and 2D data distributions (right). Purple lines denote the χ^2 value from the respective data best-fit distribution.

Lastly, the 1D and 2D binned χ^2 distributions are calculated with the p-values are extracted, all from generating 1,000 pseudoexperiments ("realizations") injected with the blind best-fit NSI value. Should any p-value be less than 5% (0.05), the procedure is stopped. The full data χ^2 distributions are shown in Figs. **??** and **??**. Both the 5% and 100% data selections pass the p-value test.

6.10 Results

The following sections present the NSI analysis results on unblinded data, a post-unblinding verification of the proper degrees of freedom, and discussion on how the analysis limits on $\epsilon_{\mu\tau}$ compare to leading other leading $\epsilon_{\mu\tau}$ measurements. These results were published in Ref. [167].

6.10.1 Best-Fit Points and CL Contours

The IceCube 8-year high energy muon track dataset was fully unblinded for the NSI analysis in August of 2021.

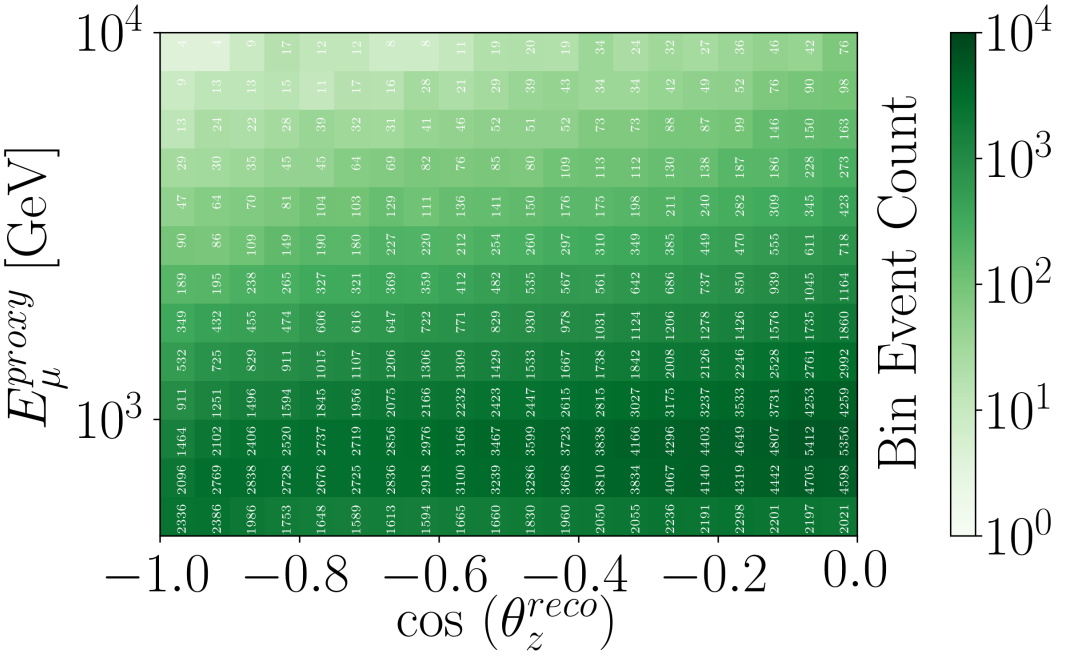

FIGURE 6.28: The number of observed IceCube neutrino events in the NSI analysis binning.

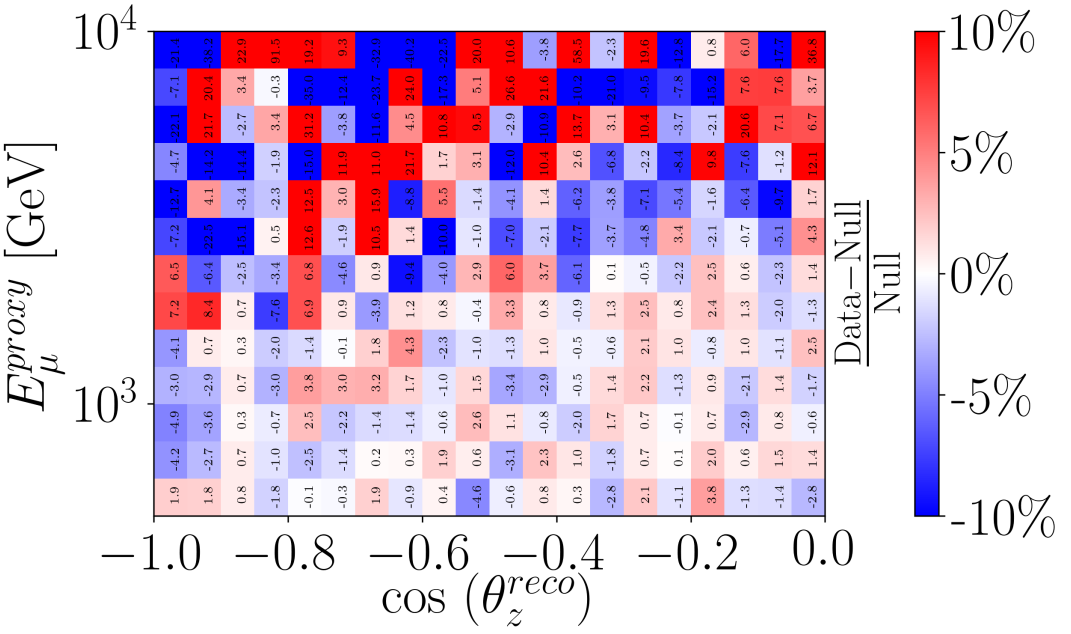

FIGURE 6.29: Difference of values between data distribution and null hypothesis MC expectation at the NSI best-fit nuisance parameter values.

A display of the binned event counts for the unblinded data is shown in Fig. 6.28. To quantify the tension between the analysis MC and the unblinded data, Fig. 6.29 displays the differences between the binned data counts and the MC null hypothesis prediction.

Results of the analysis are presented as 68%, 90%, and 95% CL regions in Fig. 6.30, with the 68% CL region excluding the null hypothesis.

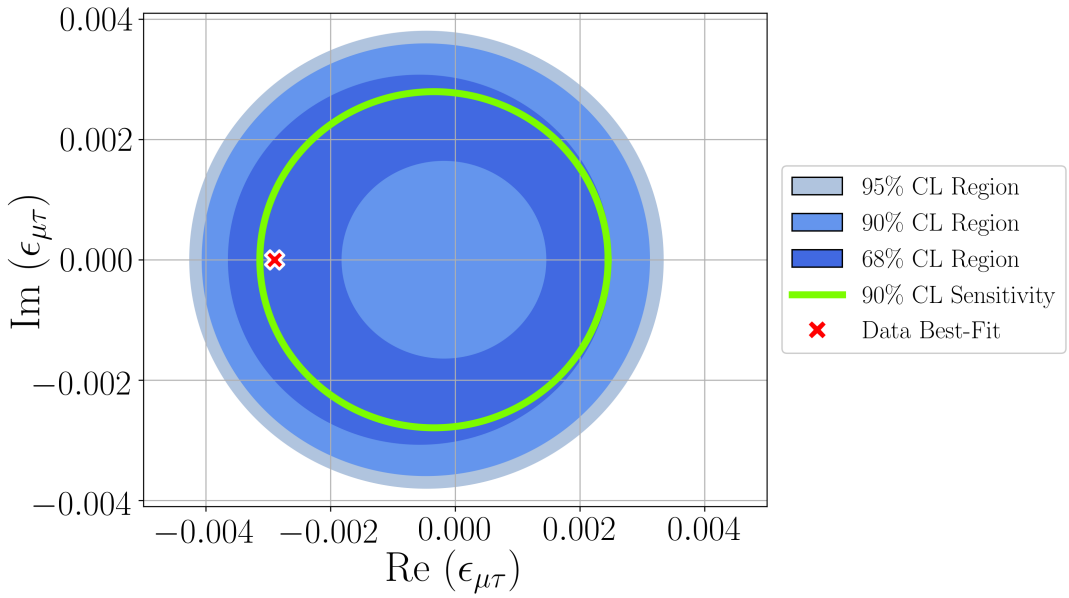

FIGURE 6.30: Results of the $\mathrm{Re}(\epsilon_{\mu\tau}) - \mathrm{Im}(\epsilon_{\mu\tau})$ fit to data. The blue-shaded regions mark the CL regions. The green line is the analysis 90% CL sensitivity.

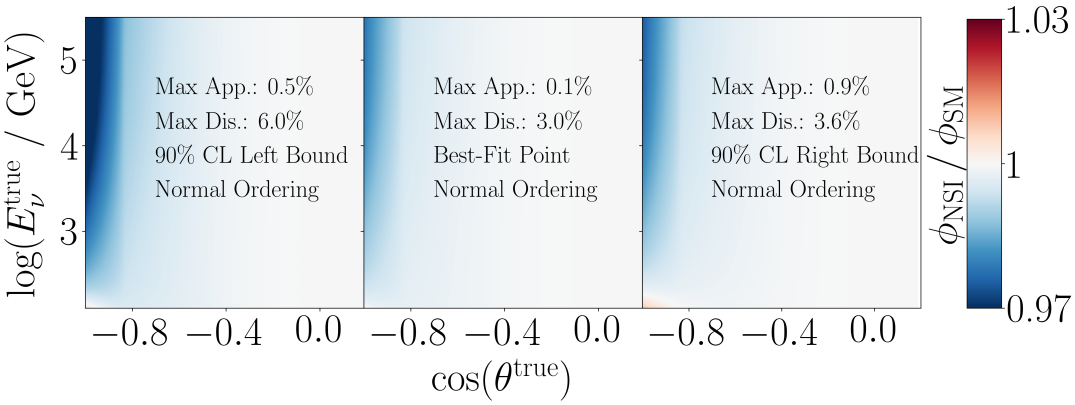

FIGURE 6.31: Flux prediction for 90% CL bounds (left, right) and best-fit value (middle) of NO scenario $\epsilon_{\mu\tau}$ fit.

No evidence for $\epsilon_{\mu\tau}$ NSI was observed. The measured best-fit value in the NO (IO) scenario was found to be $\epsilon_{\mu\tau} = -0.0029$ (0.0030). The test statistic difference in values between the NO (IO) best-fit point and the null hypothesis is $2\Delta\mathrm{LLH} = 2.23$ (2.49). The 90% CL limits for $\epsilon_{\mu\tau}$ in the normal (inverted) mass ordering are -0.0041 $< \epsilon_{\mu\tau} <$ 0.0031 (-0.0031 $< \epsilon_{\mu\tau} <$ 0.0041). Fig. 6.31 shows the impact of the NO 90% CL bound $\epsilon_{\mu\tau}$ values and best-fit $\epsilon_{\mu\tau}$ value on

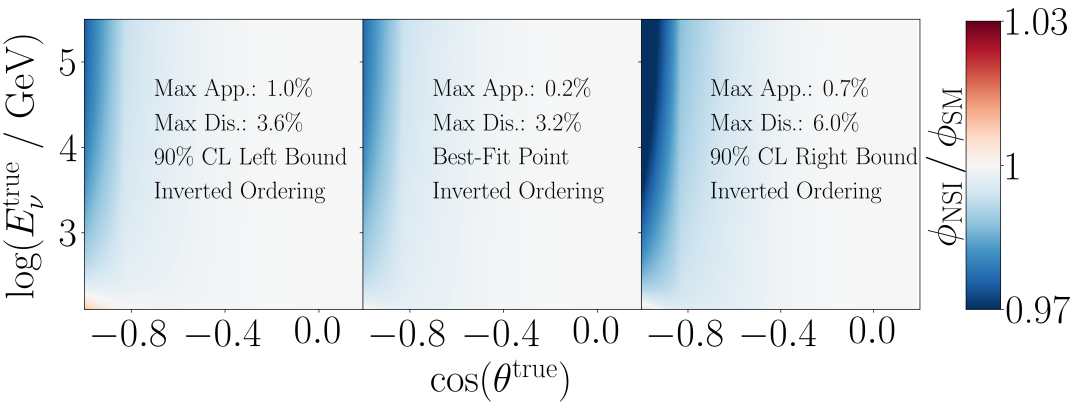

FIGURE 6.32: Flux prediction for 90% CL bounds (left, right) and best-fit value (middle) of IO scenario $\epsilon_{\mu\tau}$ fit.

the predicted flux while Fig. 6.32 shows the impact of the IO 90% CL bound $\epsilon_{\mu\tau}$ values and best-fit $\epsilon_{\mu\tau}$ value on the predicted flux.

The best-fit NO p-value was determined empirically from comparing the data best-fit LLH to the minimized LLH of 1000 pseudoexperiment trials simulated at the null hypothesis but with the data best-fit nuisance parameter values. This yields a value of $p = 0.252$ (25.2%).

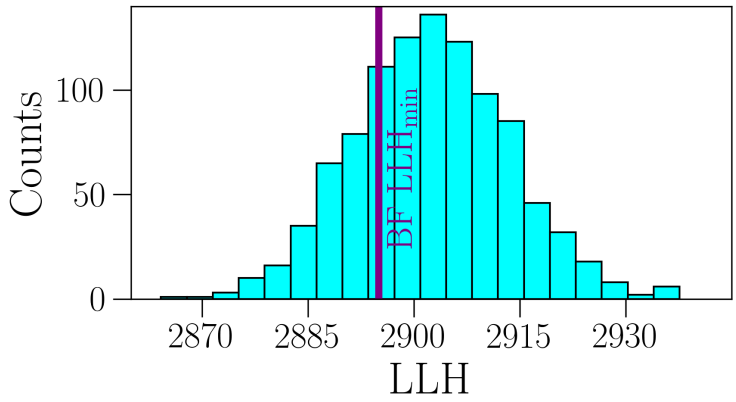

FIGURE 6.33: Histogram of LLH profile minima from 1000 pseudoexperiment trials at the null hypothesis with the NSI best-fit nuisance parameter values. The purple line denotes the LLH profile minimum for the NSI best-fit hypothesis.

As a verification of the 1 DoF fit utilizing the symmetries described in Sec. 6.2.1, a 2 DoF fit done in the full $\text{Re}(\epsilon_{\mu\tau}) - \text{Im}(\epsilon_{\mu\tau})$ hypothesis space was conducted (Fig. 6.34). Fig.6.34 demonstrates that both the 1 DoF and 2

DoF fits recover the same $\epsilon_{\mu\tau}$ best-fit point and 90% CL contour to excellent precision.

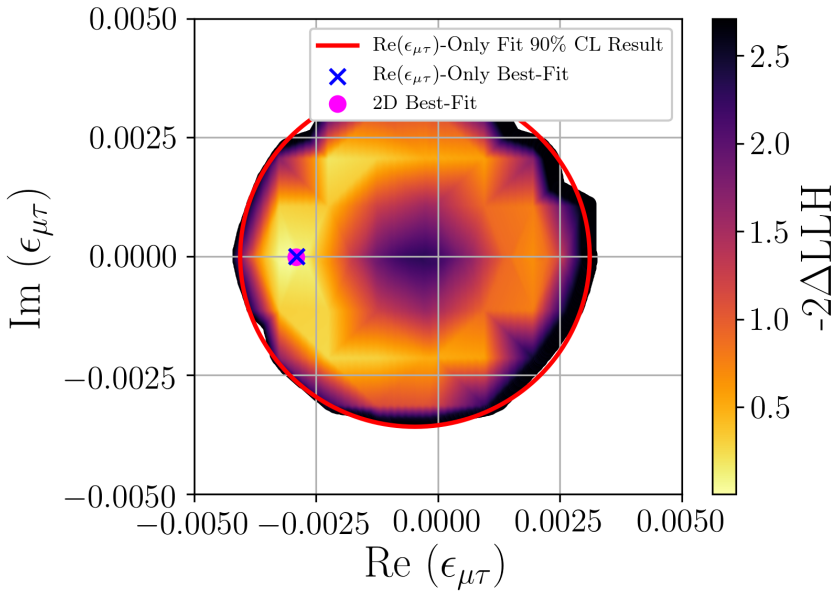

FIGURE 6.34: Comparison of the 1D circular fit result (red line) to the full 2D $\mathrm{Re}(\epsilon_{\mu\tau}) - \mathrm{Im}(\epsilon_{\mu\tau})$ scan of 601 points (color bar) in $\mathrm{Im}(\epsilon_{\mu\tau}) \in [-0.01, 0.01]$ and $\mathrm{Re}(\epsilon_{\mu\tau}) \in [-0.01, 0.01]$. The 1D scan best-fit is represented by the blue "x" while the 2D scan best fit is represented by the pink circle.

6.10.2 Comparison to Previous Results

IceCube has previously placed leading constraints on complex $\epsilon_{\mu\tau}$ in Ref. [121] that we present here to give context to the results of this analysis.

The IceCube DeepCore 2021 NSI analysis was an all-NSI, complex-valued parameter fit to 3 years of 5.6 - 100 GeV atmospheric neutrino data from IceCube and its low-energy extension, DeepCore. This analysis set leading constraints $|\epsilon_{\mu\tau}|$ when compared to limits set by oscillation, accelerator, and scattering experiments [121].

In Fig. 6.35, the top panel is a cross-section of the $\mathrm{Re}(\epsilon_{\mu\tau}) - \mathrm{Im}(\epsilon_{\mu\tau})$ result from Fig. 6.30 along $\mathrm{Im}(\epsilon_{\mu\tau}) = 0$. This is a representation of $\mathrm{Re}(\epsilon_{\mu\tau})$-only constraints, which is valid in this scenario as the analysis $\epsilon_{\mu\tau}$ best-fit point has $\mathrm{Im}(\epsilon_{\mu\tau}) = 0$ and the constraints on $\mathrm{Im}(\epsilon_{\mu\tau})$ are symmetric for a given value

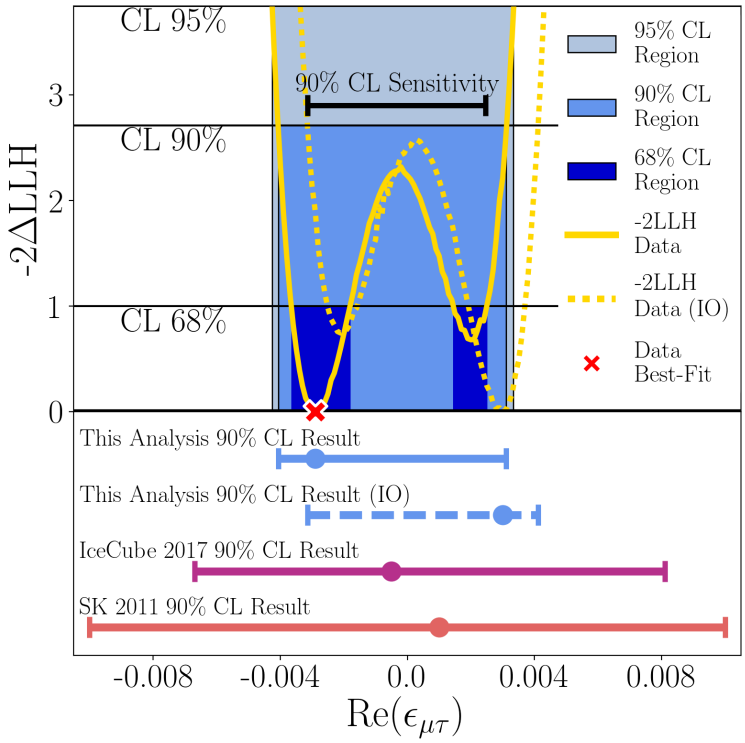

FIGURE 6.35: (Top) Results of the Re($\epsilon_{\mu\tau}$)-only fit to data. Solid yellow line is LLH profile for NO scenario, dashed yellow line is LLH profile for IO scenario. The blue-shaded regions mark the CL regions. (Bottom) Comparison of Re($\epsilon_{\mu\tau}$)-only results to results from Refs. [121, 123].

of Re($\epsilon_{\mu\tau}$) (see Sec. 6.2.1). The below panel displays the 1D 90% CL constraints and compares these limits to the limits from the DeepCore 2021 results (Ref. [121]) and to the inaugural $\epsilon_{\mu\tau}$ 2011 limits set by the Super-Kamiokande[13] experiment.

Hence, from this comparison, it is clear that the results of this analysis improve the constrains on $\epsilon_{\mu\tau}$ by an order of magnitude, and are the global leading constraints on $\epsilon_{\mu\tau}$.

While not many analyses constrain Im($\epsilon_{\mu\tau}$), there remains fruitful comparison to the Ref. [121] results. Fig. 6.36 is the full 2D comparison of results between Ref. [121] and this analysis. As with the Re($\epsilon_{\mu\tau}$)-only case, the results of this analysis set an order-of-magnitude improvement in constraints on Im($\epsilon_{\mu\tau}$). Note that the contour of Ref. [121] is symmetric in $\pm$Im($\epsilon_{\mu\tau}$), which

[13]Super-Kamiokande is an underground neutrino observatory located at Mount Ikeno, Japan [123].

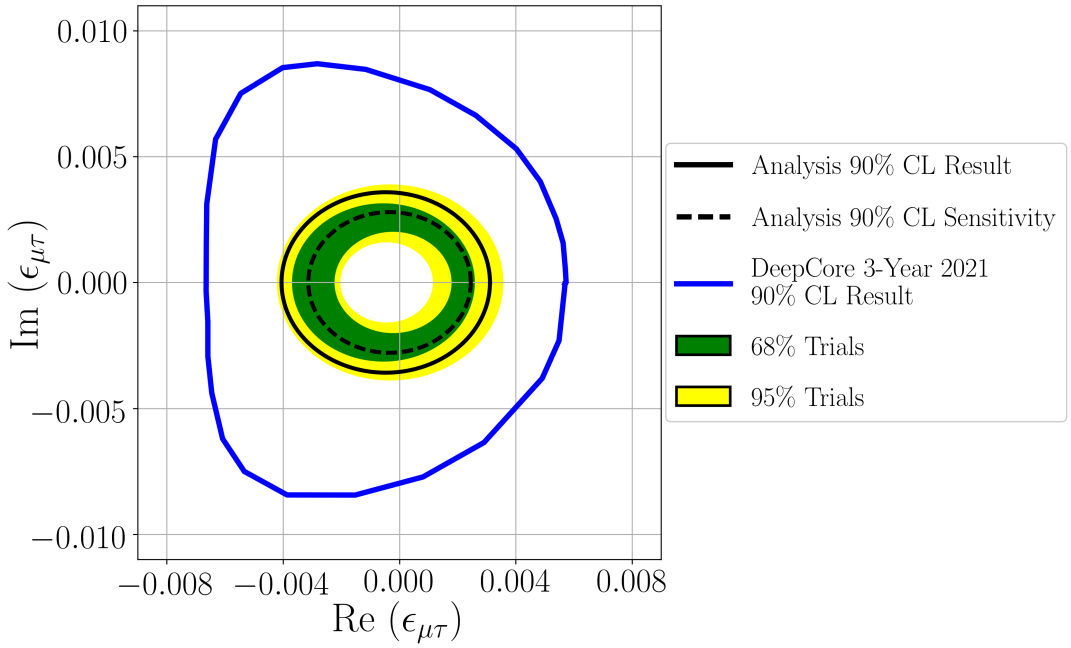

FIGURE 6.36: Comparison of previous IceCube $\mathrm{Re}(\epsilon_{\mu\tau}) - \mathrm{Im}(\epsilon_{\mu\tau})$ results [121] to analysis results. Green and yellow regions denote the interval of 1σ and 2σ limits, respectively, for 1000 pseudoexperiment trials (see Sec. 6.8).

can be explained by Eq. 6.3 in Sec. 6.2.1, yet is not radially-symmetric like the results of this analysis. The like of a circle-like contour for Ref. [121] is on account of the sample energies being < 100 GeV, which implies the energy condition for the radial symmetry of Eq. 6.7 (Sec. 6.2.1) are not satisfied.

6.11 Statistical Coverage (Feldman-Cousins) Check

To verify that Wilks' theorem is sufficiently valid within this analysis space (that the CL limits cover the correct range of parameter values), multiple points across the range of $\epsilon_{\mu\tau}$ hypotheses were tested. Wilks' theorem states that the analysis test statistic, $-2\Delta LLH$, has a distribution equivalent to a χ^2 with the same degrees of freedom as the $-2\Delta LLH$ distribution in the limit that the analysis sample size approaches infinity. Given that this analysis utilizes degeneracies that reduce the number of effective degrees of freedom, it is critical to ensure that Wilks theorem holds in our statistical treatment. Note that this check was performed only for the normal mass ordering (NO).

A statistical coverage check requires the Feldman-Cousins [168] prescription, which is a frequentist analysis of the test statistic to determine the actual CL thresholds as opposed to assuming the Wilks' CL thresholds are true for this analysis.

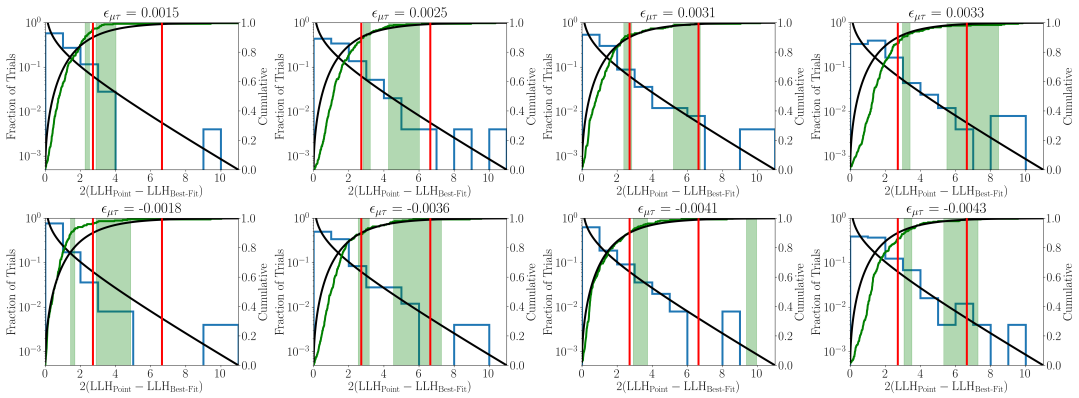

FIGURE 6.37: Statistical coverage (Feldman-Cousins tests for eight points that span the range of $\epsilon_{\mu\tau}$ hypotheses. Green bands denote the ranges of recovered 90% and 99% CL thresholds, red lines the corresponding Wilks thresholds. The blue histograms denote the density distribution of recovered of -2ΔLLH best-fit values, the sloping-down black line the χ^2 for two DoF. The green line is the cumulative distribution of best-fit -2ΔLLH values, the sloping-up black line the cumulative distribution for the 2DoF χ^2.

To perform a single Feldman-Cousins (FC) "spot check", a value of $\epsilon_{\mu\tau}$ is selected and a statistically large number (1000) of detector pseudoexperiments (realizations) are generated for that value of $\epsilon_{\mu\tau}$. For each pseudoexperiment, the -2ΔLLH profile is calculated and the best-fit point, along with the -2ΔLLH are retrieved. From there, a probability density of best-fit -2ΔLLH values (relative to the analysis best-fit -2ΔLLH value) is formed, and the actual CL threshold is determined according to the below equation:

$$\int_0^{-2\Delta LLH} P(x)dx = CL \tag{6.21}$$

where $P(x)$ is the probability density (normalized distribution) of best-fit -2ΔLLH values. To use this analysis as an example, determining the 95% CL for a given set of 1000 pseudoexperiments is to find the 950th largest -2ΔLLH value for

a given histogram of Fig. 6.37. In Fig. 6.37 the recovered FC CL values, representing the 1 σ uncertainty regions (green bands,) are compared to the Wilks CL values (red lines).

So long as the Wilks CL value is reasonably close to the FC uncertainty band, Wilks theorem is sufficient for use in the analysis. Should the FC uncertainty band cover a range of values smaller than the Wilks value, using Wilks would be a conservative choice that requires no correction for that hypothesis.

From tests across the $\epsilon_{\mu\tau}$ space, particularly at the values marking the analysis 90% Wilks CL $\epsilon_{\mu\tau}$ result limits, the Wilks and FC CL threshholds match sufficiently such that the analysis CL intervals provide the correct coverage, and confirm that the reduction from two to one effective degrees of freedom is correct.

6.12 Supplementary Material: Nuisance Parameter Effects on Simulated Analysis Distributions

The following tables of histograms, adapted from Refs. [50, 68], present the individual effect each nuisance parameter has on the final MC analysis event distribution when the parameter is deviated by the specified amount.

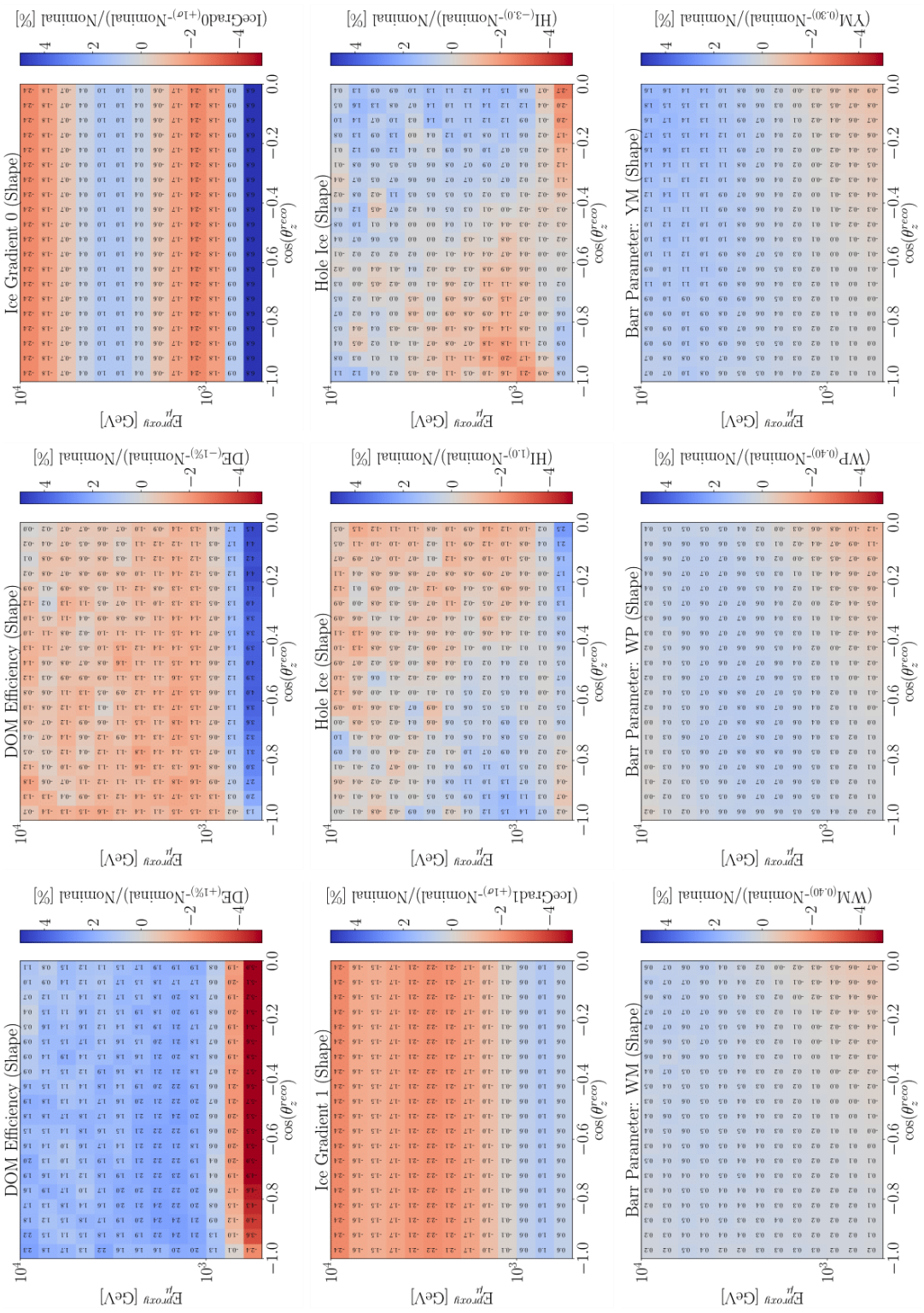

FIGURE 6.38: Individual impacts of nuisance parameters on simulated neutrino event distributions. Adapted from Refs. [50, 68].

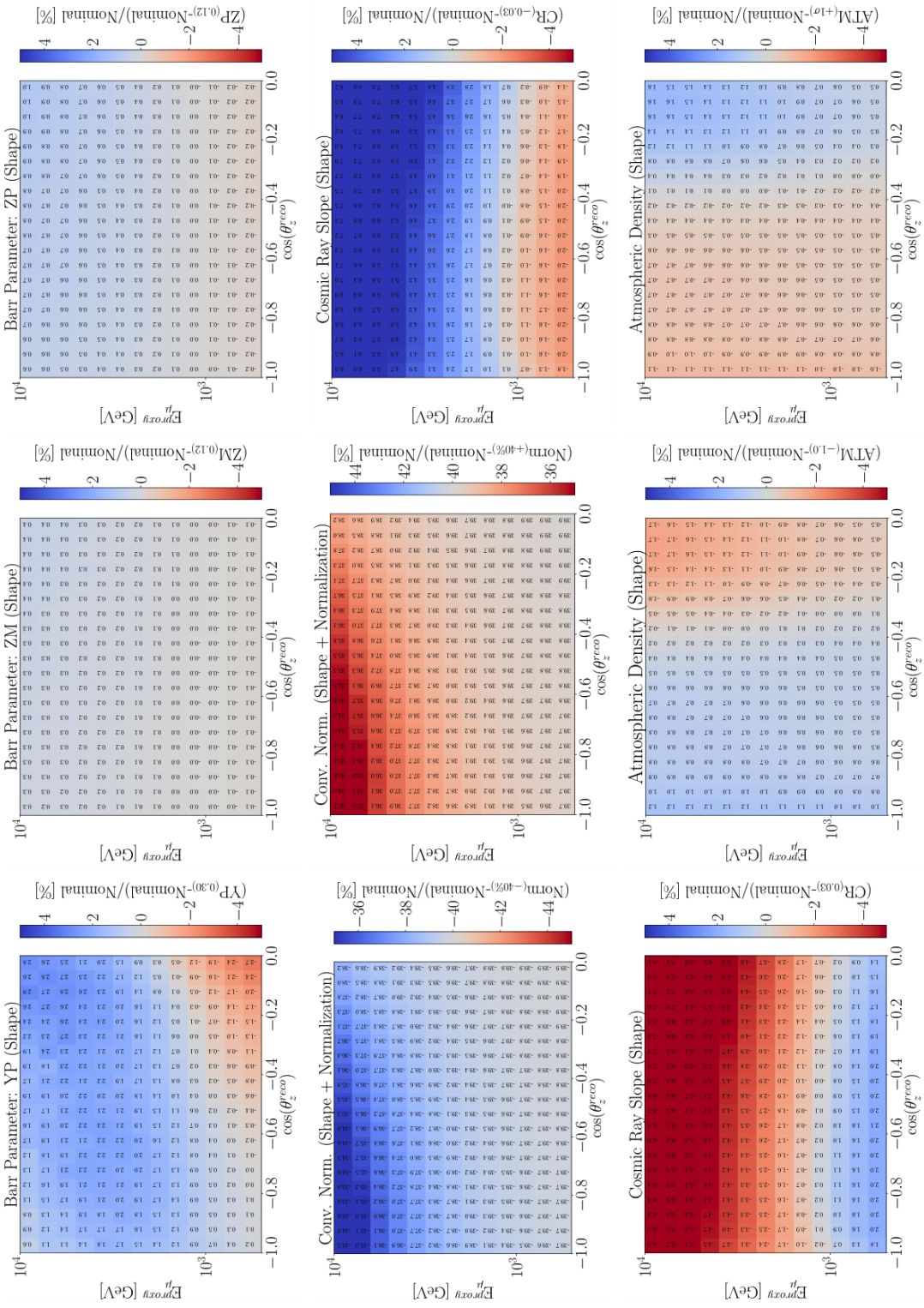

FIGURE 6.39: Individual impacts of nuisance parameters on simulated neutrino event distributions. Adapted from Refs. [50, 68].

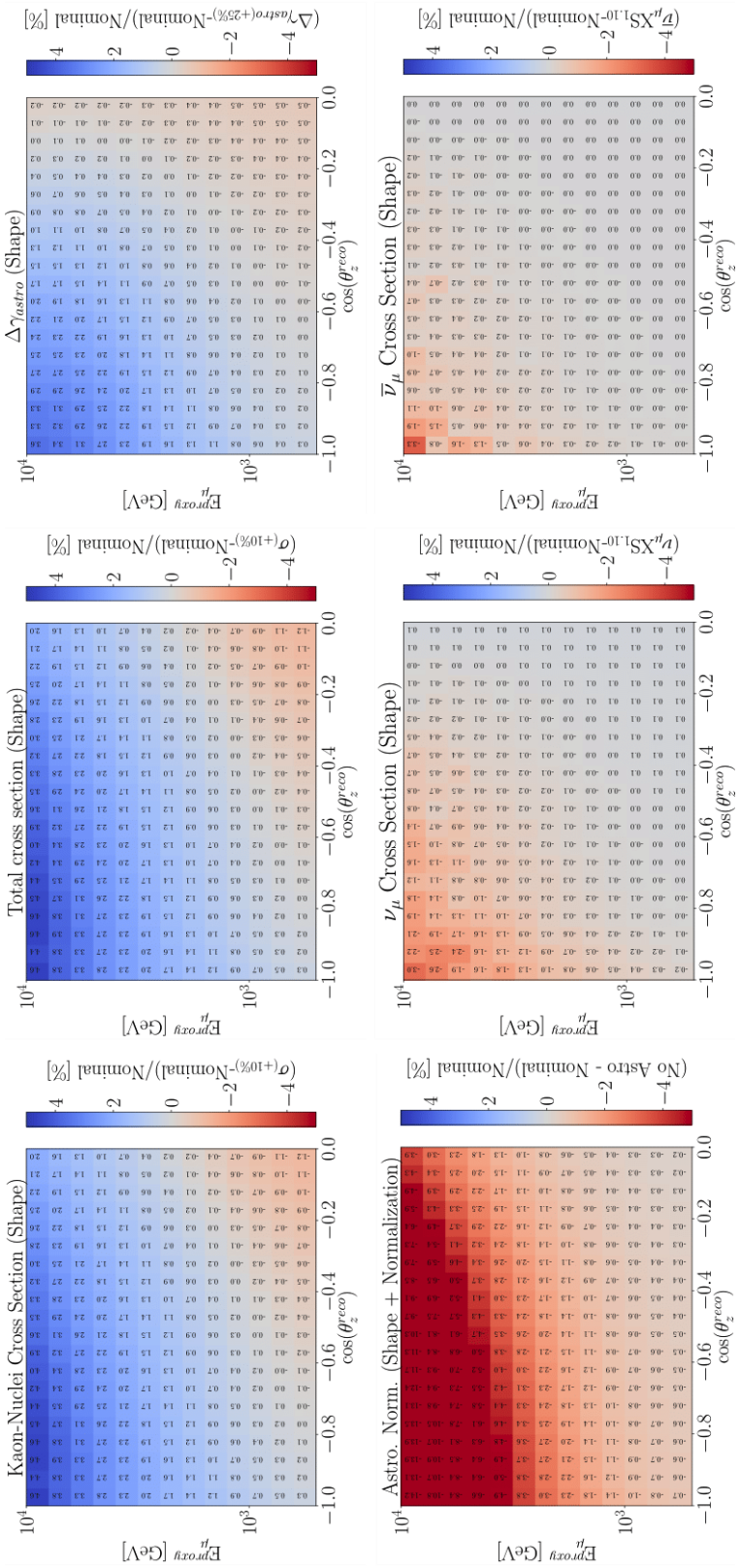

FIGURE 6.40: Individual impacts of nuisance parameters on simulated neutrino event distributions. Adapted from Refs. [50, 68].

Part IV

Decoherence of Neutrino Oscillations

Chapter 7

Theory of Neutrino Decoherence

Early in the development of quantum theory, Dr. Werner Heisenberg proposed what is now known as the "Heisenberg uncertainty principle". This principle describes how the position and momentum of a particle (or any system) are coupled, and that decreasing the uncertainty in one of these observables will increase the uncertainty in the other [169]. This is not due to the limitations of technology but a consequence of the wave-like nature of matter: to have ill-defined physical properties at quantum scales. Shortly after Heisenberg's publication, Drs. Erwin Schrödinger and Howard Robertson developed a generalized uncertainty principle for any two quantum mechanical operators [170, 171].

Since the formulation of the generalized principle, many authors have explored the implications of a "fundamental length": a distance scale below which particles cannot have definite properties [172–183]. This scale is most often postulated to be the *Planck scale*, the selection of constants that emerge when the fundamental constant of quantum mechanics, $\hbar$, meets the fundamental constants of general relativity, G and c, to introduce the limits of where quantum effects and gravitational effects are comparable. In the case of the fundamental distance scale, the resulting quantity is the Planck length $L_{\text{Planck}} = \sqrt{\hbar G/c^3} \approx 10^{-33}$ cm.

General relativity models gravity as an effect of the geometry of spacetime. Should gravity obey quantum mechanics, there would be an inherent uncertainty

in the spacetime metric at the Planck distance scale. This introduces a major implication: that spacetime fluctuates at the Planck distance scale to create a stochastic "foam" [184, 185].

These spacetime fluctuations are a frequent prediction of quantum gravity models [184, 185], yet take place at a physical scale that is outside the reach of direct detection experiments. A novel approach to probe spacetime fluctuations is to test quantum systems over long distances or times. An example of such a system is neutrino oscillations over large distances. Should neutrinos have a weak coupling to spacetime foam, the cumulative effect of the oscillation *decoherence* would be apparent to a neutrino oscillations experiment for large samples and large propagation baselines.

The following chapter describes the formalism of neutrino decoherence via environmental coupling (Sec. 7.1), how virtual black holes are a possible consequence of quantum foam (Sec. 7.2), and a rudimentary model of neutrino-virtual black hole interactions with testable predictions (Sec. 7.3). Lastly, we spend Sec. 7.4 discussing what expectations can be imposed on the neutrino-foam models in the limit of Planck-scale physics.

7.1 General Decoherence Formalism

In quantum mechanics, the state of a physical system can be described by a *density matrix* ρ. This matrix is constructed from a basis of the system's pure states $|\psi_i\rangle$ (states that are not a probabilistic mixture of other states), each with a weight p_i corresponding to the probability of finding the system in state $|\psi_i\rangle$:

$$\rho = \sum_i p_i \left|\psi_i\right\rangle \left\langle\psi_i\right| . \tag{7.1}$$

States that are not pure are *mixed*; i.e. mixed states are probabilistic mixtures of pure states. Mixed states arise either when the observer's knowledge

of the system is limited and there is an ensemble of possible states the system could be in, or when the system is exchanging information such that it becomes *entangled* with another system. The physics of this chapter will work with mixed states of the former description.

With this construction, called the *open quantum system formalism*, measuring system observable F from operator $\hat{F}$ is easy to accomplish; one just takes the trace of the product of density with the operator:

$$\langle F \rangle = \mathrm{Tr}[\rho F] \tag{7.2}$$

where $\mathrm{Tr}[A]$ is the trace operation on matrix A.

In this scenario, the transition probability of neutrino ν_α at initial time t_0 with state density ρ_α to neutrino ν_β at time t with state density ρ_β can be calculated through

$$P(\nu_\alpha \to \nu_\beta) = \mathrm{Tr}[\rho_\alpha(t_0)\rho_\beta(t)], \tag{7.3}$$

The time evolution of state $\rho(t_0)$ to $\rho(t)$ is described by the von Neumann equation[1] [186],

$$\dot{\rho} = -i[H, \rho], \tag{7.4}$$

where H is the Hamiltonian of the system, the same as from Section 2.3.

This concludes how standard neutrino oscillations are treated in the open quantum system formalism. Now, we seek to include a mechanism that includes the environmentally-induced decoherence of these standard neutrino oscillations.

Neutrino oscillation decoherence, by definition, is the loss of an oscillating flavor transition probability into a statistical ensemble of possible flavor transition probabilities. Hence, in the language of the open quantum systems,

[1] Also called the Liouville-von Neumann equation.

decoherence is the effect of pure state dissipation into mixed states. As this is a gradual effect, introducing a decoherence effect requires modifying the time evolution of the neutrino system.

The generalized technique for adding dissipative effects to the open quantum system formalism was conceived by Dr. Göran Lindblad [187] during his studies of semigroup dynamics. This technique introduces the term $\mathcal{D}[\rho]$ to the time evolution equation, now called the Lindblad equation:

$$\dot{\rho} = -i[H, \rho] - \mathcal{D}[\rho]. \tag{7.5}$$

This $\mathcal{D}[\rho]$ term[2] is a linear map of density matrices to density matrices, and is required to meet certain conditions. First, $\mathcal{D}[\rho]$ must be a completely positive map, meaning state density matrix values must be positive and only be mapped to positive matrices, following the earlier probabilistic definition of the density matrix. Second, $\mathcal{D}[\rho]$ must preserve the trace of ρ, as $\mathrm{Tr}[\rho] = 1$ defines the conservation of probability for the system.

These conditions form a completely positive, trace-preserving semigroup[3] of maps that have the general form [187, 189, 190]

$$\mathcal{D}[\rho] = \frac{1}{2}\sum_{k}^{N^2-1}\Big([\rho V_k^\dagger, V_k] + [\rho V_k, V_k^\dagger]\Big), \tag{7.6}$$

such that N is the SU(N) Hilbert space dimension of the quantum system ($N = 3$ in this instance, given the three-mass/flavor state neutrino model), and V_k are $N \times N$ complex matrix operators that couple the system to the environment that induces the decoherence effect.

To satisfy the second law of thermodynamics, that entropy must increase with time, V_k must be Hermitian [190]. Defining entropy in the open quantum

[2] This term is also called a "Lindblad generator" [188].

[3] A semigroup is an algebraic structure composed of a set of elements and a single binary operation between elements that returns elements within the groups. For a semigroup, the operation is required to be associative, but the existence of an identity element or element inverses is not required.

system formalism is accomplished through the von Neumann entropy, $S = -\operatorname{Tr}[\rho \ln \rho]$.

The general map form in Eq. 7.6 can be converted to a form that reflects the specific system at hand: three-neutrino oscillation. Conveniently, with $N = 3$ established, the special unitary (Lie) group of 3×3 matrices with determinant 1 [SU(3)] offers a well-understood basis to generate the operators V_k. These generators are the *Gell-Mann* matrices:

$$b^0 = \begin{pmatrix} 1 & & \\ & 1 & \\ & & 1 \end{pmatrix} \quad b^1 = \begin{pmatrix} & 1 & \\ 1 & & \\ & & \end{pmatrix} \quad b^2 = \begin{pmatrix} & -i & \\ i & & \\ & & \end{pmatrix} \tag{7.7}$$

$$b^3 = \begin{pmatrix} 1 & & \\ & -1 & \\ & & \end{pmatrix} \quad b^4 = \begin{pmatrix} & & 1 \\ & & \\ 1 & & \end{pmatrix} \quad b^5 = \begin{pmatrix} & & -i \\ & & \\ i & & \end{pmatrix} \tag{7.8}$$

$$b^6 = \begin{pmatrix} & & \\ & & 1 \\ & 1 & \end{pmatrix} \quad b^7 = \begin{pmatrix} & & \\ & & -i \\ & i & \end{pmatrix} \quad b^8 = \frac{1}{\sqrt{3}}\begin{pmatrix} 1 & & \\ & 1 & \\ & & -2 \end{pmatrix}. \tag{7.9}$$

With this basis, we can rewrite $\mathcal{D}[\rho]$ as a linear combination of the basis matrices:

$$\mathcal{D}(\rho) = c_\mu b^\mu, \tag{7.10}$$

where $\mu = 0, ..., 8$.

In this form, the density matrix ρ is incorporated into the matrix coefficient c_μ and can be returned through the ρ decomposition in SU(3):

$$\mathcal{D}(\rho) = (D_{\mu\nu}\rho^\nu)b^\mu, \tag{7.11}$$

such that $\rho = \sum_{\mu=0}^{8} \rho^\mu b^\mu$.

Now, a new 9×9 matrix $D_{\mu\nu}$ quantifies the decoherence effect, yet it is tremendously difficult to gain physical insight from 91 free parameters. Further constraints on the physics of the environment-neutrino coupling reduce the degrees of freedom— elements $D_{0\nu}$ and $D_{\mu 0}$ must be zero to conserve oscillation probability (unitarity of ρ), as non-zero $D_{0\nu}$ acts on the Gell-Mann identity b^0 and non-zero $D_{\mu 0}$ modifies the density identity component ρ^0. This is further reinforced in the density matrix component-wise time evolution:

$$\dot{\rho}_\mu = \sum_{i,j} h_i \rho_j f_{ij\mu} + \sum_\nu D_{\mu\nu}\rho_\nu. \tag{7.12}$$

where $i, j = 1, ..., 8$, μ and $\nu = 0, ..., 8$, h_i is the SU(3) component of the Hamiltonian and f_{ijk} is the SU(3) structure constant for ordered indices i, j, k. Any structure constant f_{ijk} with $k = 0$ is zero[4], so for the initial state at $t = 0$, the time derivative of the ρ identity component is:

$$\dot{\rho}_0(t=0) = \sum_\nu D_{0\nu}\rho_\nu. \tag{7.13}$$

Therefore, to have a initial state preserved from decoherence effects, $D_{0\nu}$ and $D_{\mu 0}$ must be zero.

From the extensive derivations by Benatti and B on Markov evolution equations and quantum dynamical semigroups [190–192], imposing a weak coupling between the neutrino system and the environment allows the matrix $D_{\mu\nu}$ to be reduced further into a diagonal matrix,

$$D_{\mu\nu} = \text{diag}(0, \gamma_1, \gamma_2, \gamma_3, \gamma_4, \gamma_5, \gamma_6, \gamma_7, \gamma_8). \tag{7.14}$$

Eight free parameters is much more manageable than 91, and a diagonal mapping is intuitive— $D_{\mu\nu}$ dissipates the pure state ρ by damping component ρ^μ by γ_μ. This is final form of $D_{\mu\nu}$ that most authors use when parameterizing decoherence [189, 193–195], with publications studying various forms of dissipation by equating certain combinations of the γ_μ parameters.

The mapping from the matrix D in Eq. 7.14 to the linear map $\mathcal{D}[\rho]$, we employ Eq. 7.11 to get [193]

$$\mathcal{D}[\rho] = \begin{pmatrix} \Omega_3+\Omega_8 & \gamma_1\text{Re}(\rho_{01})-i\gamma_2\text{Im}(\rho_{10}) & \gamma_4\text{Re}(\rho_{02})-i\gamma_5\text{Im}(\rho_{20}) \\ \gamma_1\text{Re}(\rho_{01})+i\gamma_2\text{Im}(\rho_{10}) & -\Omega_3+\Omega_8 & \gamma_6\text{Re}(\rho_{12})-i\gamma_7\text{Im}(\rho_{21}) \\ \gamma_4\text{Re}(\rho_{02})+i\gamma_5\text{Im}(\rho_{20}) & \gamma_6\text{Re}(\rho_{12})+i\gamma_7\text{Im}(\rho_{21}) & \Omega_3+\Omega_8 \end{pmatrix}, \tag{7.15}$$

where $\Omega_3 = \frac{\gamma_3}{2}(\rho_{00} - \rho_{11})$ and $\Omega_8 = \frac{\gamma_8}{6}(\rho_{00} + \rho_{11} - 2\rho_{22})$.

[4]The SU(3) structure constants are defined as $f^{147} = f^{246} = f^{257} = f^{345} = -f^{156} = -f^{367} = \frac{1}{2}$, $f^{458} = f^{678} = \frac{\sqrt{3}}{2}$, and $f^{123} = 1$, with all other constants equal to zero.

7.2 Virtual Black Hole Spacetime Foam

Quantum fluctuations in spacetime were introduced in the opening discussion of this chapter, yet the form of these fluctuations was not specified. As there are many models of quantum gravity that result in the appearance of a quantum foam, there are a variety of forms that the foam takes [184, 185, 196–209]. A popular contender is a model assuming spacetime fluctuations are comprised of *virtual black holes*.

A particle is "virtual" when it has an existence limited by quantum uncertainty, often decaying within the scale of time that measurements of the particle are not possible. This decay time is the *Planck* time ($\mathcal{O}[10^{-44}]$ s), alluding to the aforementioned Planck scale. Virtual particles are what mediate particle interactions in QFT and can briefly violate the conservation of energy for the duration of their existence (be "off-shell"[5]). This is not a contradiction to energy conservation, as the total interaction process conserves energy and the particle exists only within the Planck time scale.

Virtual black holes are thus objects that do not bear much resemblance to macroscopic black holes. They are only so named due to the momentary formation of a singularity from the quantum spacetime fluctuation— otherwise, they are chargeless, spinless, and do not interact with macroscopic systems.

There are several approximate formulations in the literature that describe how singularities emerge from uncertainty principles at the quantum scale [180, 184, 196, 210]. For instance, following the argument of Ref. [180], if one started from the position-momentum uncertainty principle and imagined a particle of extremely large energy, then $\sigma_p \sim c\sigma_E$ and

$$\sigma_x \sigma_E \geq \frac{\hbar c}{2}. \tag{7.16}$$

[5]Being "off-shell" refers to a particle not having a mass-energy (or momentum) satisfying the equation $E^2 = p^2 + m^2$, which forms an ellipsoid "shell" in mass-momentum space.

From this expression, the uncertainty on E is $\sigma_E = \hbar c/2\sigma_x$. Therefore, small σx allows for a large range in E for that region of spacetime. Recall that the radius at which an event horizon for a Schwarzschild black hole forms[6] is given by

$$R_g = \frac{2GE}{c^4}, \tag{7.17}$$

such that G is the gravitational constant. As σ_x decreases, σ_E grows and in turn increases R_g to the point that $R_g = \sigma_x$. At this critical value, an observer cannot make a measurement on a region smaller than σ_x, as it would require increasing the energy and extending the gravitational radius beyond the region to be measured. Therefore, this condition $R_g = \sigma_x$ is when a microscopic black hole has formed. Combining Eq. 7.16 with Eq. 7.17, we see that for the minimal uncertainty condition $\sigma_x\sigma_E = \hbar c/2$,

$$\sigma_{R_g} = \frac{2G\sigma_E}{c^4} = \frac{\hbar G}{\sigma_x c^3} = \frac{L^2_{\text{Planck}}}{\sigma_x}. \tag{7.18}$$

Therefore, $\sigma_{R_g}\sigma_x \geq L^2_{\text{Planck}}$, implying L_{Planck} is the critical scale at which microscopic black hole formation takes place.

Hence, virtual black holes are a natural medium for spacetime foam, and the remaining chapter discusses a basic model of neutrino-VBH (ν-VBH) interactions.

7.3 Neutrino-VBH Interaction Model

The following discussion constructs a model of weak neutrino coupling to a virtual black hole foam based on minimal assumptions for a neutrino-VBH interaction. As there is no presently accepted model of quantum gravity, the underlying ν-VBH interaction is viewed purely from a phenomenological perspective, following the construction from Ref. [193].

[6] This is called the Schwarzschild/gravitational radius.

As neutrinos propagate in their mass states, the time evolution of a mass state can be written as[7]

$$|\nu(L)_j\rangle = e^{\frac{-im_j^2 L}{2E}} |\nu_j(0)\rangle \,, \tag{7.19}$$

for mass state j where m_j is the mass, E is the neutrino energy, L is the propagation distance, and $|\nu_j(0)\rangle$ is the initial state.

Inserting spacetime fluctuations can be represented by a modified phase of the neutrino state: one can picture neutrino scattering with a VBH at some point in the propagation such that the interaction perturbs any number of the neutrino mass state phases. The outgoing neutrino mass state for a given state j can thus be written as

$$|\nu(L)_j\rangle = e^{-i\left(\frac{m_j^2 L}{2E} - \delta\phi_j\right)} |\nu_j(0)\rangle \,, \tag{7.20}$$

where $\delta\phi_j$ is the phase perturbation for that mass state induced from the ν-VBH interaction. Note that this is not a unitary effect through the following: the probability transforms with random perturbations as:

$$P_{\text{SM}}^{\nu_\alpha \to \nu_\beta} = \sum_{j,k} \mathcal{U} e^{i\frac{\Delta m_{jk}^2}{2E} L} \longrightarrow P_{\text{Deco}}^{\nu_\alpha \to \nu_\beta} = \sum_{j,k} \mathcal{U} e^{i\frac{\Delta m_{jk}^2 - \delta\phi_k}{2E} L}, \tag{7.21}$$

where $\mathcal{U} = U_{\alpha j} U_{\alpha k}^* U_{\beta j}^* U_{\beta k}$. Given that $\delta\phi$ is a stochastic perturbation for any an arbitrary interaction, the transition probability for a neutrino at a given L and E is not longer fixed, violating unitarity.

What remains unspecified is if a ν-VBH interaction results in *specific* outgoing pure neutrino flavor/mass states or if the interaction indiscriminately modifies the mass state phases according to the selected model of quantum gravity. Therefore these interaction scenarios must be given equal consideration and testing.

[7] Assuming relativistic neutrinos, $t = L$.

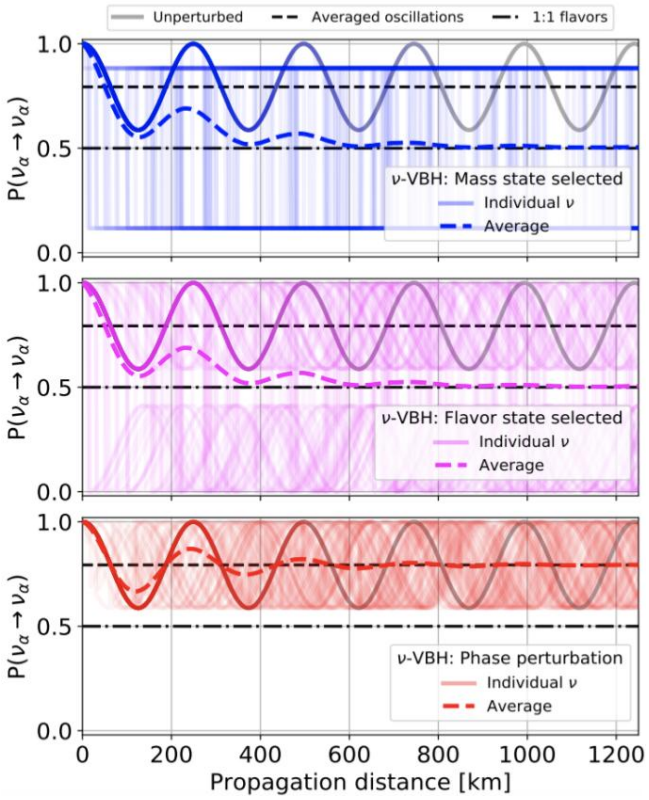

FIGURE 7.1: Oscillation probabilities for ensembles of 1000 identical neutrinos in a toy model simulation of the mass state selection (top), flavor state selection (middle), and phase perturbation (bottom) scenarios. Adapted from Ref. [193].

To test the cumulative effect of these possible interactions on a neutrino flux, simulation is required. Ref. [193] used the nuSQuIDS neutrino oscillation software to propagate an ensemble of identical neutrinos with ν-VBH interactions taking place stochastically along the trajectory. The averaged rate at which the interactions take place is specified through an interaction mean-free path, which is the product of the VBH foam density and the interaction cross-section. From a large ensemble and large propagation range, the effect of ν-VBH interactions can be measured through how the ensemble-averaged oscillation probability changes.

The following discussions of ν-VBH models and their effects references Fig. 7.1, which displays survival probabilities as a function of propagation distance when oscillating an ensemble of 1000 identical neutrinos through a toy model of each interaction case. The model employs two-flavor (α, β) neutrino oscillation with

a mixing angle of $\theta = 20^o$, initial flavor state ν_α, initial neutrino energy of 1 GeV, masses $m_1 = 0.1$ eV and $m_2 = \sqrt{2}m_1$, and an interaction mean free path of 250 km.

Least complicated of the possible interaction scenarios is indiscriminate mass state phase perturbations ("phase perturbation" scenario). Following the simulation in Fig. 7.1 (bottom panel), as neutrinos oscillate, they begin to interact with the foam. An interaction with a VBH can distinctly perturb between one and two mass state phases of the neutrino[8] by any amount, and as the neutrino flavor states are superpositions of the mass states, the changes in phase change the overall nature of the neutrino oscillation, both perturbing the width of the oscillation and the phase of the oscillation relative to the standard case. This is shown for the individual neutrinos in Fig. 7.1, bottom panel, as the transparent solid red lines. The effect on the ensemble-averaged oscillation probability is shown in the dashed red line: as more neutrinos interact with the foam, the average oscillation probability dampens until the entire ensemble has decohered and the probability has converged to a fixed value. This implies that while the measurement of flavor states ν_α and ν_β is still probabilistic, the probabilities are fixed after long propagation distances rather than exhibiting the oscillation behavior of the Standard Model case (solid red line). Note that the dampened oscillation converges to a value based on the neutrino mixing angle θ. In this simulation, $\theta - 20^o$, so mixing prefers the α flavor in measurement. However, as the mixing evens ($\theta \to 45^o$), the probability of measuring either flavor equalizes.

The next scenario to consider is random neutrino flavor state selection (democratic "flavor state selection"). In this scenario, ν-VBH interactions require the mass state phase perturbations to only result in pure flavor states for the outgoing neutrino without preference to which flavor is selected. The effect of this scenario is shown in Fig. 7.1, middle panel. Such interactions produce a

[8]This is because neutrino oscillations are invariant to global changes in phase, meaning perturbing each mass state phase by the same amount results in no change in neutrino oscillation.

similar individual neutrino effect (transparent pink lines) to the phase perturbation case, where the oscillation phases overall shift from the standard case (solid pink line). Yet this interaction bypasses the flavor preference induced by the mixing angle in the phase perturbation example by evenly producing neutrinos of both flavors after significant exposure to the foam. The result is two populations of $\nu - VBH$ outgoing neutrinos: outgoing ν_α that mix preferably to ν_α and outgoing ν_β that mix preferably to ν_β. Consequently, the average oscillation probability dampens with propagation distance until the ensemble has completely decohered. With equal populations of interaction product neutrinos, the damping converges to an equal transition probability between the flavors.

Lastly, there is the random neutrino mass state selection (democratic "mass state selection"). This interaction produces a random outgoing neutrino mass state. Recall that neutrinos oscillate as superpositions of three mass states in the Standard Model, so an outgoing single mass state would exhibit no oscillation. Given that mass states are fixed mixtures of the flavor states, a flavor measurement on the mass state would yield a flavor state that is probabilistically determined according to the flavor mixture of the mass state; the probability of finding the neutrino in a given flavor state is fixed. The impact of this interaction is presented in Fig. 7.1, top panel. With individual neutrinos interacting and shifting from oscillating transition probability to fixed transition probability (transparent blue lines), once again two populations of neutrinos emerge. Given that the mass states are not equal mixtures of the flavors, each mass state will induce a greater probability of measuring one flavor over the other. As a result, the ensemble-averaged probability dampens and converges to equal transition probability once the entire ensemble has decohered.

Several important consequences emerge from the simple toy model of Fig. 7.1. First, the interactions from mass and flavor state selection produce equal results that are independent from the neutrino mixing parameters. Hence, these

physics are indiscernible in the limit of a large neutrino flux with prolonged exposure to the VBH foam, and thus we combine these scenarios into the *state selection* model.

Further, the choice of mixing angle affects how distinguishable the phase perturbation scenario is from the state selection scenario. As mixing angle θ approaches 45^o, the two models become identical, becoming a single degenerate model of neutrino decoherence in spacetime foam. This is quite relevant when studying neutrino fluxes that approximately oscillate between two flavors, such as atmospheric neutrino oscillations. See Sec. **??** for continued discussion on using various neutrino fluxes to constrain neutrino decoherence effects.

With these insights on how VBH foam can potentially interact with large numbers of neutrinos, we can translate the physics described here to the formalism outlined in Sec. 7.1.

As seen from the toy model in Fig. 7.1, the averaged oscillation probability dampens as a function of propagation distance L. From the time evolution equation Eq. 7.5, this damping can take the form of $\mathcal{D}[\rho] \sim \alpha\rho$, where α is the unknown damping coefficient. This is because in the mass basis, SM neutrino oscillations are driven by Hamiltonian H diagonal terns, and these oscillations terms translate to the off-diagonal terms of $i[H, \rho]$ in Eq. 7.5 [193]. So damping oscillations through $\mathcal{D}$ can take place through non-zero off-diagonal terms.

We know from the discussion of the weak coupling limit that the term $\mathcal{D}[\rho]$ will quantify the decoherence effects through the diagonal matrix $D = \text{diag}(0, \gamma_1, \gamma_2, \gamma_3, \gamma_4, \gamma_5, \gamma_6, \gamma_7, \gamma_8)$ (Eq. 7.14). Therefore, a constant damping coefficient α can define the γ parameters. The toy model in Fig. 7.1 only required one free parameter to change the average rate of ν-VBH interactions, the ν-VBH mean free path. Thus, only one parameter is needed to quantify the damping from the foam, and the gamma parameters can all be set equal to a common value, Γ. What is left to determine is which parameters distinguish the D matrices between the state selection ($D_{\text{state selection}}$) and phase perturbation

($D_{\text{phase perturbation}}$) scenarios.

From Eq. 7.15 it is evident that the diagonal terms of $\mathcal{D}[\rho]$, which dampen the diagonal terms in ρ associated with the pure neutrino states, are determined from the γ_3 and γ_8 parameters of Eq. 7.14. Phase perturbation always produces an outgoing neutrino that continues to oscillate; the system does not dampen the pure state coefficients in the density, but the uncertainty in the outgoing states introduces off-diagonal mixed state terms. Therefore, the γ_3 and γ_8 terms in $D_{\text{phase perturbation}}$ are 0. On the other hand, state selection democratically selects the outgoing neutrino mass/flavor state, resulting in a portion of the outgoing neutrinos being mass states that do not oscillate, which is an interaction inducing loss of pure state information. Ergo, the γ_3 and γ_8 parameters in $D_{\text{state selection}}$, which dampen the pure states, are allowed to be nonzero and thus are set to Γ [193, 211].

With this simple construction of a weak coupling to a virtual black hole spacetime foam, we now have a parameterized form of the two interaction models in the open quantum system formalism:

$$D_{\text{phase perturbation}} = \text{diag}(0, \Gamma, \Gamma, 0, \Gamma, \Gamma, \Gamma, \Gamma, 0), \tag{7.22}$$

and

$$D_{\text{state selection}} = \text{diag}(0, \Gamma, \Gamma, \Gamma, \Gamma, \Gamma, \Gamma, \Gamma, \Gamma). \tag{7.23}$$

We now turn our attention to the damping parameter Γ. As there are still few restrictions to the nature of quantum gravity, the energy dependence of a ν-VBH interaction is unknown. To include an energy dependence, authors often reformulate Γ as $\Gamma(E_\nu) = \Gamma(E_0)(E_\nu/E_0)^n$, where E_0 is an arbitrary reference energy that keeps the scaling unitless, E_ν is the neutrino energy, and n is the unknown energy power scaling [189, 193, 194]. This form of energy dependence lends to the prediction that the strength of interactions with quantum gravity

will scale with energy, with $n < 0$ having degenerate physics with other unique forms of decoherence. Consequently, any experiment adopting this generalization would need to constrain the free parameters $\Gamma(E_0)$ (also called Γ_0) and n.

This is the complete formulation for a minimal model of ν-VBH interactions. Note that the damping parameter Γ is in units of energy and causes damping proportional to $e^{-\Gamma L}$. From another perspective, one may define a coherence length of an ensemble $L_{\text{coh}} = 1/\Gamma$ such that L_{coh} is the distance at which the damping factor has reached e^{-1}.

The next section discusses how experimental limits placed on the ν-VBH models translate to further insight on physics at the Planck scale.

7.4 Interactions and the Planck Scale

Parameter $\Gamma(E)$ has units of energy, which allows for the $\Gamma(E)$ definition to be modified to include the Planck mass-energy M_{Planck} ($\approx \mathcal{O}[10^{19}\,\text{GeV}]$) [212]:

$$\Gamma(E_\nu) = \xi_{\text{Planck}} \frac{E^n}{M_{\text{Planck}}^{n-1}}, \tag{7.24}$$

where ξ_{Planck} is the dimensionless parameter that quantifies the amount of damping. This in turn reformulates the definition of L_{coh} as

$$L_{\text{coh}} = \frac{L_{\text{Planck}}}{\xi_{\text{Planck}}} \left(\frac{M_{\text{Planck}}}{E_\nu} \right)^n, \tag{7.25}$$

where L_{Planck} is the Planck length. From Eq. 7.25 it is apparent that the term $(M_{\text{Planck}}/E_\nu)^n$ quantifies the suppression of decoherence physics at neutrino energies below the Planck scale.

In this formulation, neutrinos with a Planck energy M_{Planck} would have a coherence length of L_{Planck} should $\xi_{\text{Planck}} \sim 1$. Hence, $\xi_{\text{Planck}} = \mathcal{O}(1)$ is considered a "natural" theory of decoherence, as neutrinos with Planck energy

in the $\xi_{\text{Planck}} = \mathcal{O}(1)$ scenario would couple to the quantum foam at the scale of Standard Model couplings.

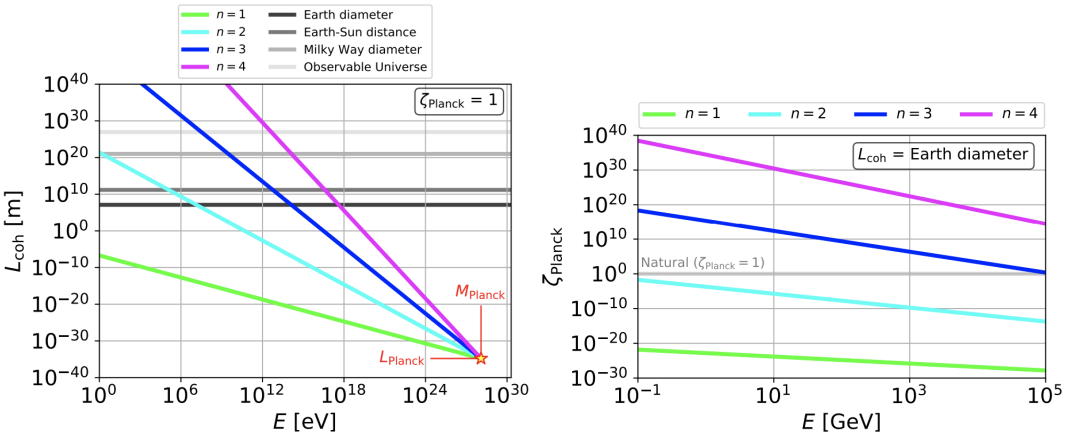

FIGURE 7.2: Left: The coherence length for $n = 1, 2, 3, 4$ as a function of neutrino energy in case of $\xi = 1$. Common baselines are shown in greyscale horizontal lines. Right: ξ_{Planck} as a function of energy when L_{coh} is fixed to the Earth diameter. The natural theory is given by the grey line. Adapted from Ref. [193].

Fig. 7.2, left, displays how the neutrino coherence length scales with neutrino energy in the natural theory ($\xi_{\text{Planck}} = 1$). Note that most constructions of quantum gravity predict suppressed foam effects at low energy scales, so this discussion is limited to $n > 0$.

Fig. 7.2, right, reverses the conditions of the left panel such that the neutrino coherence length is fixed to be the length of Earth's diameter and ξ_{Planck} shown as a function of neutrino energy. By converting experimental limits placed on Γ_0 for a given n to limits on ξ_{Planck}, we may compare the limits to the predictions from Fig. 7.2 and determine how well the data supports the natural theory.

With a derived formulation of decoherence effects on neutrino oscillations, we have discussed and quantified the effect of a potential coupling between neutrinos and the environment through virtual black hole production. In the next chapter, we test this model against eight years of IceCube atmospheric neutrino data to constrain the parameter Γ_0 for several values of n.

Chapter 8

Decoherence Analysis Description

We perform an analysis to search for signals of a real-valued decoherence parameter Γ_0 in IceCube atmospheric neutrino flux data for multiple values of energy power index n, following the neutrino-virtual black hole interaction model presented in Chapter 7. Section 8.1 briefly reviews the parameterization while Sections 8.2 - 8.7 provide a comprehensive review of the analysis. To conclude, Section 8.8 presents and discusses the results of the unblinded fit to data. All contributing SM 3-neutrino mixing parameters are set to the global best-fit values found by Ref. [127] just as in the NSI analysis of Chapter 6. Additionally, the analysis follows the same procedures, sample, and nuisance parameter treatments as the NSI analysis of Chapter 6. Data is fit solely to the neutrino normal mass ordering (NMO).

8.1 Parameterization

Parameterizing neutrino[1] oscillation decoherence (not to be confused with wavepacket interference) requires the open quantum system formalism, where ρ is the density matrix of the neutrino system describing the system's quantum state in terms of probability-weighted basis states:

[1]Important to note is that the ν-VBH models outlined in this analysis to not assume different effects between neutrinos and antineutrinos.

$$\rho = \sum_i p_i \left|\psi_i\right\rangle \left\langle\psi_i\right| . \tag{8.1}$$

The evolution of this system is then described by the Lindblad Master Equation for system Hamiltonian H, which at the end includes the operator $\mathcal{D}$ that parameterizes the state-dependent decoherence effect:

$$\dot{\rho} = -i[H, \rho] - \mathcal{D}(\rho). \tag{8.2}$$

Solutions to this equation allow for the calculation of the neutrino oscillation probability from flavor α to flavor β as a function of time t, as shown here:

$$P(\nu_\alpha \to \nu_\beta) = \mathrm{Tr}[\rho_\alpha(t_0)\rho_\beta(t)]. \tag{8.3}$$

A common generalization of this operator is the form

$$\mathcal{D}(\rho) = (D_{\mu\nu}\rho^\nu)b^\mu, \tag{8.4}$$

where b^μ are the SU(3) basis matrices, ρ^ν are the SU(3) expansion coefficients of the density matrix, and $D_{\mu\nu}$ is a 9×9 matrix of real scalars [given the nine independent SU(3) generators] that are the free parameters of the decoherence model [189, 190, 194]. To organize the parameters, the matrix is written below,

$$D = \begin{pmatrix} \Gamma_0 & \beta_{01} & \beta_{02} & \beta_{03} & \beta_{04} & \beta_{05} & \beta_{06} & \beta_{07} & \beta_{08} \\ \beta_{01} & \Gamma_1 & \beta_{12} & \beta_{13} & \beta_{14} & \beta_{15} & \beta_{16} & \beta_{17} & \beta_{18} \\ \beta_{02} & \beta_{12} & \Gamma_2 & \beta_{23} & \beta_{24} & \beta_{25} & \beta_{26} & \beta_{27} & \beta_{28} \\ \beta_{03} & \beta_{13} & \beta_{23} & \Gamma_3 & \beta_{34} & \beta_{35} & \beta_{36} & \beta_{37} & \beta_{38} \\ \beta_{04} & \beta_{14} & \beta_{24} & \beta_{34} & \Gamma_4 & \beta_{45} & \beta_{46} & \beta_{47} & \beta_{48} \\ \beta_{05} & \beta_{15} & \beta_{25} & \beta_{35} & \beta_{45} & \Gamma_5 & \beta_{56} & \beta_{57} & \beta_{58} \\ \beta_{06} & \beta_{16} & \beta_{26} & \beta_{36} & \beta_{46} & \beta_{56} & \Gamma_6 & \beta_{67} & \beta_{68} \\ \beta_{07} & \beta_{17} & \beta_{27} & \beta_{37} & \beta_{47} & \beta_{57} & \beta_{67} & \Gamma_7 & \beta_{78} \\ \beta_{08} & \beta_{18} & \beta_{28} & \beta_{38} & \beta_{48} & \beta_{58} & \beta_{68} & \beta_{78} & \Gamma_8 \end{pmatrix}, \tag{8.5}$$

such that the diagonal parameters are labeled in Γ and the off-diagonal in β. While there are 81 free parameters in this construction, model assumptions and physical constraints outlined in Chp. 7 have the number of free parameters be reduced significantly such that D can take a diagonal form.

For the two ν-VBH scenarios constrained in this analysis, D becomes

$$D_{\text{State Selected}} = \begin{pmatrix} 0 & & & & & & \\ & \Gamma & & & & & \\ & & \Gamma & & & & \\ & & & \Gamma & & & \\ & & & & \Gamma & & \\ & & & & & \Gamma & \\ & & & & & & \Gamma \end{pmatrix}, \tag{8.6}$$

$$D_{\text{Phase Perturbation}} = \begin{pmatrix} 0 & & & & & & \\ & \Gamma & & & & & \\ & & \Gamma & & & & \\ & & & 0 & & & \\ & & & & \Gamma & & \\ & & & & & \Gamma & \\ & & & & & & 0 \end{pmatrix}. \tag{8.7}$$

Notably, each matrix is parameterized by a single variable Γ. The mappings of these D matrices back to $\mathcal{D}[\rho]$ are shown below:

$$\mathcal{D}(\rho) = \begin{pmatrix} \Omega_0+\Omega_3+\Omega_8 & \Gamma_1\,\mathrm{Re}\{\rho_{01}\}-i\Gamma_2\,\mathrm{Im}\{\rho_{10}\} & \Gamma_4\,\mathrm{Re}\{\rho_{02}\}-i\Gamma_5\,\mathrm{Im}\{\rho_{20}\} \\ \Gamma_1\,\mathrm{Re}\{\rho_{01}\}+i\Gamma_2\,\mathrm{Im}\{\rho_{10}\} & \Omega_0-\Omega_3+\Omega_8 & \Gamma_6\,\mathrm{Re}\{\rho_{12}\}-i\Gamma_7\,\mathrm{Im}\{\rho_{21}\} \\ \Gamma_4\,\mathrm{Re}\{\rho_{02}\}+i\Gamma_5\,\mathrm{Im}\{\rho_{20}\} & \Gamma_6\,\mathrm{Re}\{\rho_{12}\}+i\Gamma_7\,\mathrm{Im}\{\rho_{21}\} & \Omega_0-2\Omega_8 \end{pmatrix}, \tag{8.8}$$

where

$$\begin{aligned} \Omega_0 &= \frac{\Gamma_0}{3}(\rho_{00}+\rho_{11}+\rho_{22}) \\ \Omega_3 &= \frac{\Gamma_3}{2}(\rho_{00}-\rho_{11}) \\ \Omega_8 &= \frac{\Gamma_8}{6}(\rho_{00}+\rho_{11}-2\rho_{22}) \end{aligned}, \tag{8.9}$$

and the ρ_{ij} are the entries in the original 3×3 density matrix.

To include any possible dependence of decoherence effects on the neutrino energy, we further define gamma as

$$\Gamma(E_\nu) = \Gamma(E_0)\left(\frac{E_\nu}{E_0}\right)^n = \Gamma_0\left(\frac{E_\nu}{E_0}\right)^n, \tag{8.10}$$

such that E_0 is an arbitrarily-chosen "pivot/reference energy" that indicates when decoherence dampening pivots from subdominant to dominant relative to normal oscillations, and n is the power law index. It is Γ_0 that is constrained in the analysis for the two ν-VBH scenarios and for $n = 0, 1, 2, 3$.

To incorporate these definitions, the full form of $\mathcal{D}[\rho]$ from Eq. 8.2 for each ν-VBH scenario is thus

$$\mathcal{D}_{\text{State Selection}}(\rho) = \Gamma_0\left(\frac{E}{E_0}\right)^n \begin{pmatrix} \Sigma_{11} & \rho_{21} & \rho_{31} \\ \rho_{21} & \Sigma_{22} & \rho_{32} \\ \rho_{31} & \rho_{32} & \Sigma_{33} \end{pmatrix} \tag{8.11}$$

$$\mathcal{D}_{\text{Phase Perturbation}}(\rho) = \Gamma_0 \left(\frac{E}{E_0}\right)^n \begin{pmatrix} 0 & \rho_{21} & \rho_{31} \\ \rho_{21} & 0 & \rho_{32} \\ \rho_{31} & \rho_{32} & 0 \end{pmatrix}, \tag{8.12}$$

such that $\Sigma_{11} = \frac{1}{3}(2\rho_{11} - \rho_{22} - \rho_{33})$, $\Sigma_{22} = \frac{1}{3}(\rho_{11} + 2\rho_{22} - \rho_{33})$, and $\Sigma_{33} = \frac{1}{3}(\rho_{11} - \rho_{22} + 2\rho_{33})$.

We define a coherence length,

$$L_{\text{coh}} = 1/\Gamma_0, \tag{8.13}$$

as the distance (in natural units) for which the damping factor is e^{-1} at the pivot energy E_0. This analysis reports results both in Γ_0 and L_{coh} for a pivot energy of $E_0 = 1$ TeV, as the majority of neutrino energies in the analysis sample are at this order of magnitude.

8.2 Analysis Overview

The parameter space of hypotheses tested for each model is given in Table 8.1. For each point in the hypothesis space, each relevant neutrino flux that reaches IceCube is simulated. The details of each simulation model are outlined in the corresponding NSI analysis section, Sec. 6.3. Decoherence is implemented within SQuIDS and nuSQuIDS (Section 4.4) through introducing the $\mathcal{D}$ term to the evolution equations with the ability to specify E_0 and n [213, 214]. Dependent on the neutrino energy and state density, $\mathcal{D}$ is recalculated at each node in the propagation, which is why a modified version of SQuIDS was required.

Hypothesis Ranges	
n	Γ_0 [eV]
0	$[0, 10^{-19}, 10^{-21}] + [10^{-17} - 10^{-14}$ (20 points, log-spaced)]
1	$[0, 10^{-19}, 10^{-21}] + [10^{-17} - 10^{-14}$ (20 points, log-spaced)]
2	$[0, 10^{-21}] + [10^{-19} - 10^{-15}$ (20 points, log-spaced)]
3	$[0] + [10^{-21} - 10^{-17}$ (20 points, log-spaced)]

TABLE 8.1: Hypothesis points tested for both ν-VBH models at each n.

8.3 Signal Prediction

As with the NSI analysis, this analysis searches for "disappearance-appearance" effects (in this instance, from decoherence) on the expected flux at IceCube. To simulate how decoherence signals would appear in IceCube, we present oscillograms, or plots of in the space of IceCube event observables, of neutrino fluxes for multiple configurations of decoherence. An example of the effects each ν-VBH interaction model has on an atmospheric neutrino flux are shown in Fig.8.1.

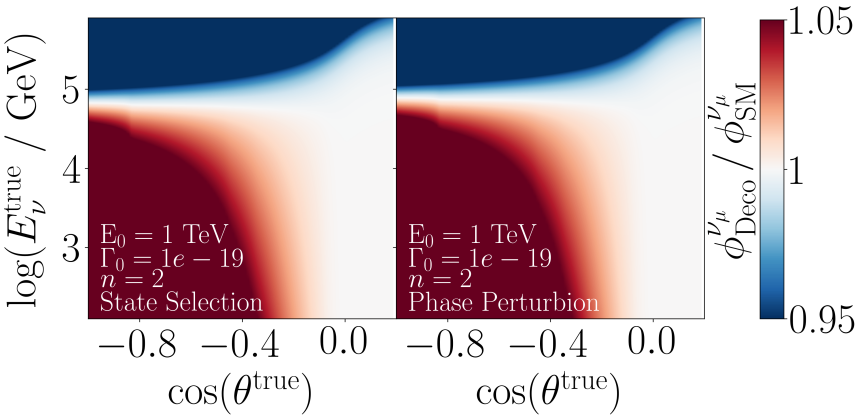

FIGURE 8.1: Oscillogram of nuSQuIDS-simulated $\nu_\mu + \overline{\nu}_\mu$ flux for the state selection model. This oscillogram plots the ratio of the decoherence flux to the SM flux.

We use the nuSQuIDS [77] software package to propagate a 1:1 ν_μ-$\overline{\nu}_\mu$ flux from the atmosphere to the South Pole through zenith angles in the analysis sample range. This propagation includes SM matter effects in addition to the decoherence effects for supplied values of Γ_0 and n. Fig. 8.1 presents the ratio of the $\nu_\mu + \overline{\nu}_\mu$ flux from decoherence+SM to the SM flux for the state selection and phase perturbation models, respectively. From these examples, it can be seen that at the highest sample energies, the neutrino flux is dampened across all zeniths (blue), as this is where the energy-dependent dampening of the model becomes dominant.

To verify the dampening effect at the high energy, we look to the approximate ensemble-averaged oscillation probability [194]:

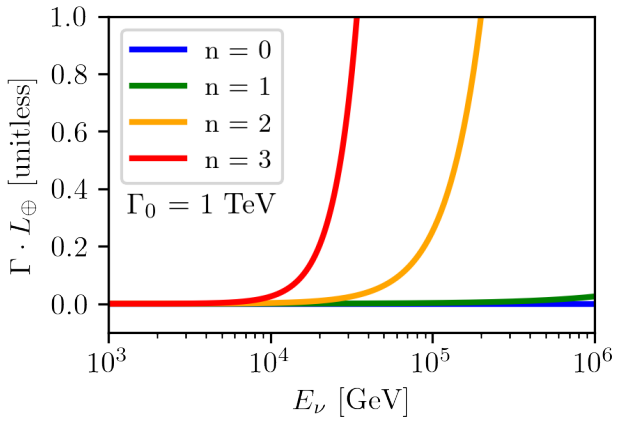

FIGURE 8.2: Values of $\Gamma \cdot L_\oplus$ for all n such that $(L = L_\oplus)$ is equivalent to $\cos(\theta) = -1$ for IceCube events. Γ_0 assumes the value from Fig. 8.1.

$$P_{\text{deco}}(\nu_\mu \to \nu_\mu) = 1 - \frac{1}{2}\sin^2(2\theta)\left[1 - e^{\Gamma L}\cos\left(\frac{\Delta m^2 L}{2E_\nu}\right)\right], \tag{8.14}$$

where θ and Δm^2 are the effective mixing parameters. Using the Γ_0 and n values from Fig. 8.1, we see in Fig. 8.2 that the disappearance becomes significant at the same neutrino energies for the disappearance in Fig.8.1, $1 - 2 \cdot 10^5$ GeV.

On the other hand, what is not predicted by the probability approximation is the flux *enhancement* (red) in Fig. 8.1 at the lower energies, restricted to zeniths below the Earth's horizon.

8.3.1 Tau Regeneration Effect

The enhancement seen in Fig. 8.1 is a result of *tau regeneration*, which is the process of ν_τ interactions producing τ-leptons that further decay into ν_τ's [215].

Fig. 8.4 is a diagram of this process: ν_τ's easily pass through Earth, yet at sufficient energies can interact with Earth nucleons (Fig. 8.3). The result is an outgoing τ-lepton with a short lifetime, subsequently decaying into a ν_τ and for $\sim 35\%$ of decays, either a ν_e or ν_μ with their corresponding charged-lepton partner (Fig. 8.5). The outgoing ν_τ can continue this process of producing a τ that decays to another ν_τ so long as the ν_τ has enough energy to produce the τ.

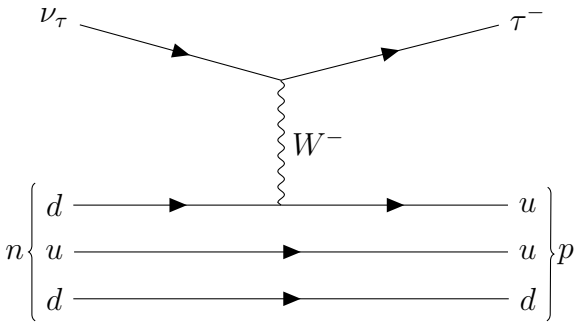

FIGURE 8.3: The Feynman diagram for a CC τ-producing interaction between a ν_τ and a nucleon.

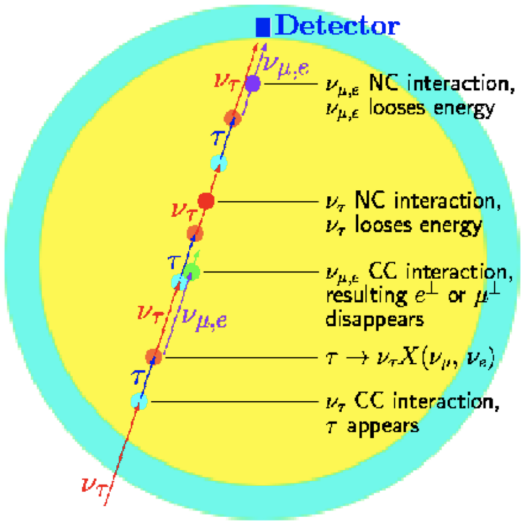

FIGURE 8.4: An illustration of the tau regeneration chain for a ν_τ traveling through Earth. Figure from Ref. [215]

.

In the context of decoherence, our model assumes a VBH foam uniformly permeating all of spacetime, including within Earth. At the beginning of the tau regeneration chain, where the least baseline has been traversed, a ν_τ could interact with a VBH and subsequently exit as any of the three neutrino flavors[2]. In the case of decays that produce secondary ν_e or ν_μ, the ν_μ and ν_e average survival distances increase with energy, but these neutrinos are more opaque to Earth than ν_τ, and ν_μ/ν_e CC interactions with matter result in electrons and muons are quickly reabsorbed at large baselines, preventing regeneration. However, in the case of decoherence, the secondary ν_e's and ν_μ's can interact with the foam, modifying the outgoing neutrino flavor populations such that

[2]In addition to the mass states, for the state selection case.

there is more democratization in the large-sample limit. Outgoing ν_μ from ν-VBH can survive full propagation of the baseline and eventually appear as track events in IceCube, which is what produces the ν_μ signal boost seen at low energies and below the horizon.

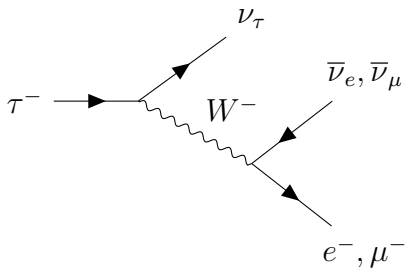

FIGURE 8.5: The Feynman diagram for the decay of a τ into a ν_τ and either a ν_e or ν_μ.

Identifying tau regeneration as the source of the appearance in Fig. 8.1 was confirmed empirically; with independent software from Ref. [216], a ν_μ flux was propagated at the same baselines of the earlier example through a constant matter density that approximates the average matter density of Earth (Fig. 8.6 left). The software DMOS (Decoherence Oscillation Matrix Solver) does not include tau regeneration in the calculation, and replicates to an excellent degree the high-energy disappearance from the earlier example, as can be seen from Fig. 8.6.

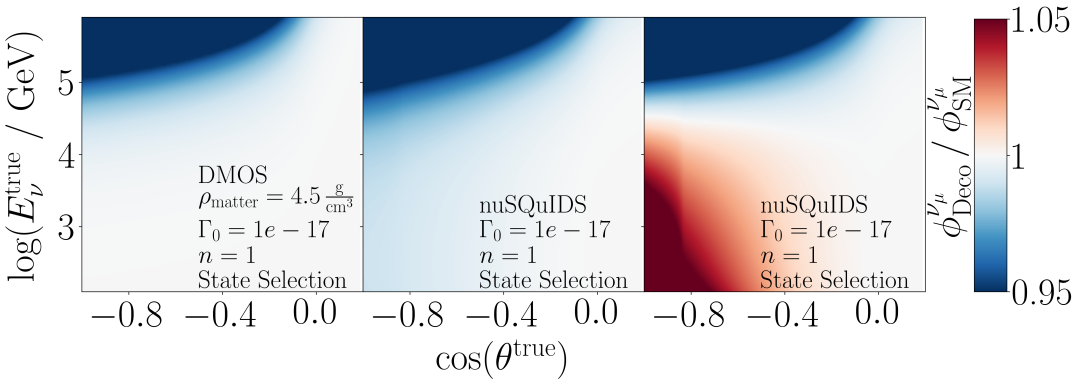

FIGURE 8.6: Comparison of $\nu_\mu + \overline{\nu}_\mu$ SM to decoherence oscillograms for various software configurations. Left: DMOS-simulated flux in a constant matter density. Middle: nuSQuIDS-simulated flux in the PREM variable density with no non-coherent scattering, no tau regeneration. Right: nuSQuIDS-simulated flux with tau regeneration included but no non-coherent scattering.

A next test was to deactivate the only other feature nuSQuIDS includes: non-coherent scattering. The middle panel of Fig. 8.6 displays the result of the calculation for the same parameters as the left panel with no tau regeneration nor non-coherent scattering included, and the result is near-identical disappearance at the high energy and no appearance at the low energy[3]. When tau regeneration is included in the calculation but non-coherent scattering is left deactivated, the appearance from the earlier example returns, as shown in the right panel of Fig. 8.6.

8.3.2 Tau Monte Carlo Considerations

With the added contribution to the decoherence-modified flux from tau regeneration, there is a relevant concern as to how τ-leptons are simulated. This analysis uses the Monte Carlo (MC) from Refs. [68, 69], which later was found to have incorrect/insufficient treatment of the tau simulation. However, this has negligible impact to the results of those analyses given the predicted fraction of ν_τ in the sample ($\sim 0.00007\%$) and that ν_τ do not noticeably contribute to the analysis signals.

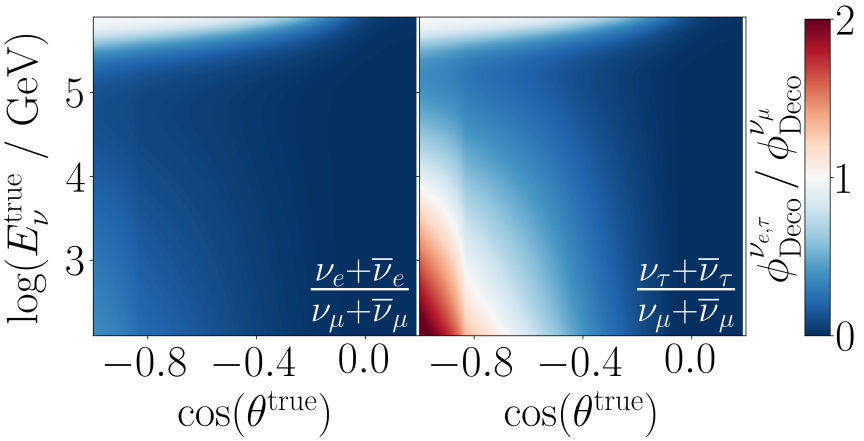

FIGURE 8.7: Oscillograms of the decoherence flux ratios $\nu_e + \overline{\nu}_e \;/\; \nu_\mu + \overline{\nu}_\mu$ (left) and $\nu_\tau + \overline{\nu}_\tau \;/\; \nu_\mu + \overline{\nu}_\mu$ (right).

[3]There is some spread of disappearance to the lower energies due to the layered Earth density of the nuSQuIDS PREM model

In contrast, this analysis demonstrably has a component of the signal from the ν_μ produced in ν_τ interactions. The left panel of Fig. 8.7 verifies that the ν_e population remains negligible while the right panel of Fig. 8.7 confirms the increased population of ν_τ that reach the detector at the low energies and high baselines.

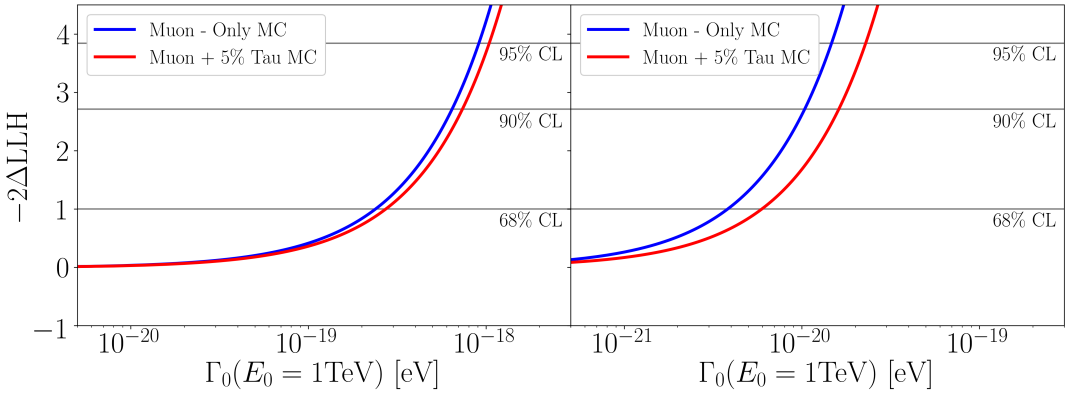

FIGURE 8.8: Oscillogram of nuSQuIDS-simulated $\nu_\mu + \overline{\nu}_\mu$ flux for the phase perturbation model. This oscillogram plots the ratio of the decoherence flux to the SM flux.

Therefore, to test the impact of MC with the correct tau physics against the original MC, we calculated the sensitivities for each simulation set. It is important to note that that although MC with the correct tau physics has been generated, it is 1/100th the size of the original MC and thus is only appropriate to use for comparison purposes, not for use in producing results.

For $n = 0$ - 3 there is negligible change in the sensitivities between the MC with no tau contribution included and the correct tau contribution (Fig. 8.8 left). Yet at $n = 4$, we see that the sensitivity significantly deviates between the two MC (Fig. 8.8 right). Hence, the analysis is restricted must be restricted to $n < 4$ to use the MC from Refs. [50, 68, 69].

Another concern is if the original MC recovers decoherence signals generated with the more accurate physics from the muon + tau MC. To test this, a pseudoexperiment trial was generated for a non-zero decoherence value with the muon + tau MC, resulting in a trial event distribution. Then the likelihood

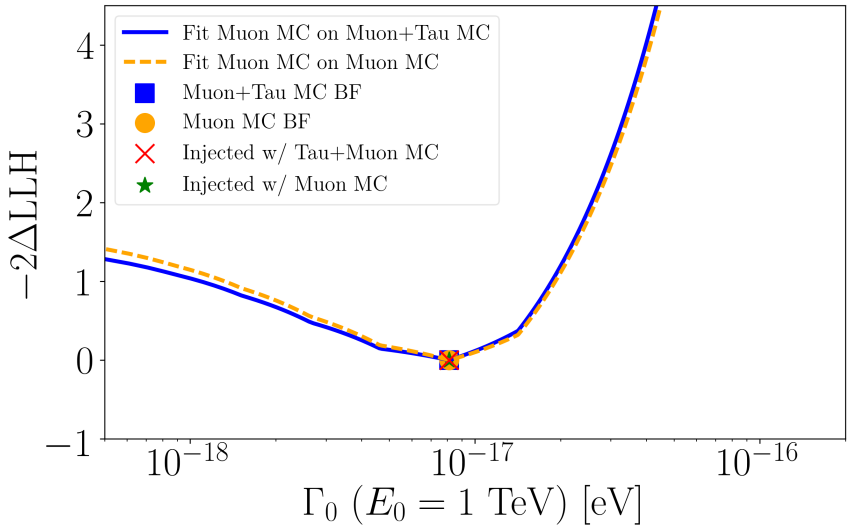

FIGURE 8.9: Test of signal recovery from original muon MC when injecting decoherence with muon + tau MC. The corresponding contour the blue line with the red cross marking the best fit. Also shown is the LLH profile from scanning with the original MC (orange contour) for comparison.

profile of the trial distribution was calculated against the muon MC. The result, shown in Fig. 8.9, is that signals generated with the muon + tau MC are recovered to excellent precision when calculating the likelihood with the muon MC, negligibly changing the LLH profile.

With satisfactory outcomes from these tests, it was deemed appropriate for the decoherence analysis to proceed with the original MC of Refs. [50, 68, 69].

8.4 Fit and Sensitivity Procedures

We search for decoherence effects through the shape of atmospheric neutrino fluxes by comparing Monte Carlo simulation to data and calculating the binned likelihood for each decoherence hypothesis in reconstructed energy-zenith space. Events are binned uniformly[4] in muon reconstructed log-energy, $\log(E^{\mu}_{\text{reco}})$, and cosine of the incident zenith angle, $\cos(\theta^{\mu}_{\text{reco}})$.

This analysis utilizes a maximum-likelihood technique that is described in the correspond NSI analysis section, Sec. 6.5. The Wilks sensitivity calculation

[4]There are 13 energy bins, $E^{\mu}_{\text{reco}} \in [500\text{ GeV}, 9976\text{ GeV}]$, and 20 zenith bins, $\cos(\theta^{\mu}_{\text{reco}}) \in [-1.0, 0.0]$.

employs the “Asimov” [166] method of determining the LLH of a hypothesis against an “ideal" (no statistical fluctuations) dataset for the null hypothesis. These sensitivities are shown with the nuisance parameter impacts in the next section and with the results in Sec. 8.8.

8.5 Uncertainty Impact on Sensitivity

To find the impact of systematic uncertainties on the analysis fit, the Wilks 90% CL sensitivity has been calculated in each instance of fixing the value of a selected nuisance parameter while the others were left free. The most concise treatment of these tests for this analysis is to use categories of parameters organized into three types: hadronic[5], cosmic[6], and detector[7].

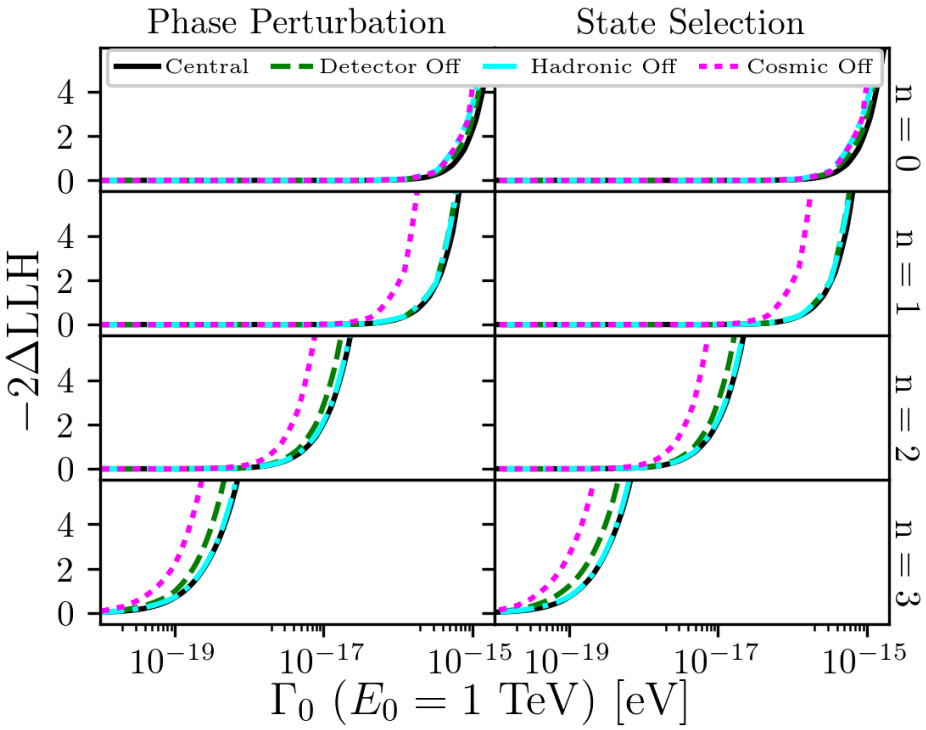

FIGURE 8.10: The central 90% CL sensitivity (black) and the 90% CL sensitivity contours when one of the three categories of systematic uncertainties is fixed to the nuisance parameter central values.

[5] W/Y/Z parameters, atmospheric density, Φ_{conv}, $\Delta\gamma_{\text{conv}}$
[6] Φ_{astro}, $\Delta\gamma_{\text{astro}}$
[7] DOM efficiency, Ice Gradient 0 and Ice Gradient 1 (SnowStorm), p_2 (column ice)

From these tests, it was found that fixed cosmic nuisance parameter values resulted in the greatest improvement in sensitivity. The systematic impact contours, in addition to the central 90% CL sensitivity, are displayed in Fig. 8.10.

8.6 Inject-Recover (Roundtrip) Tests

Inject-recover (IR) tests measure the capability of the statistics minimizer (GolemFit) to correctly recover artificially injected NSI signals, which establishes confidence that the best-fit decoherence parameters recovered from the data are accurate. To perform the IR test, an Asimov dataset [166] is generated for a chosen set of decoherence parameters. The dataset is then compared against the entire hypothesis space to generate a LLH profile, from which the best-fit parameters are determined.

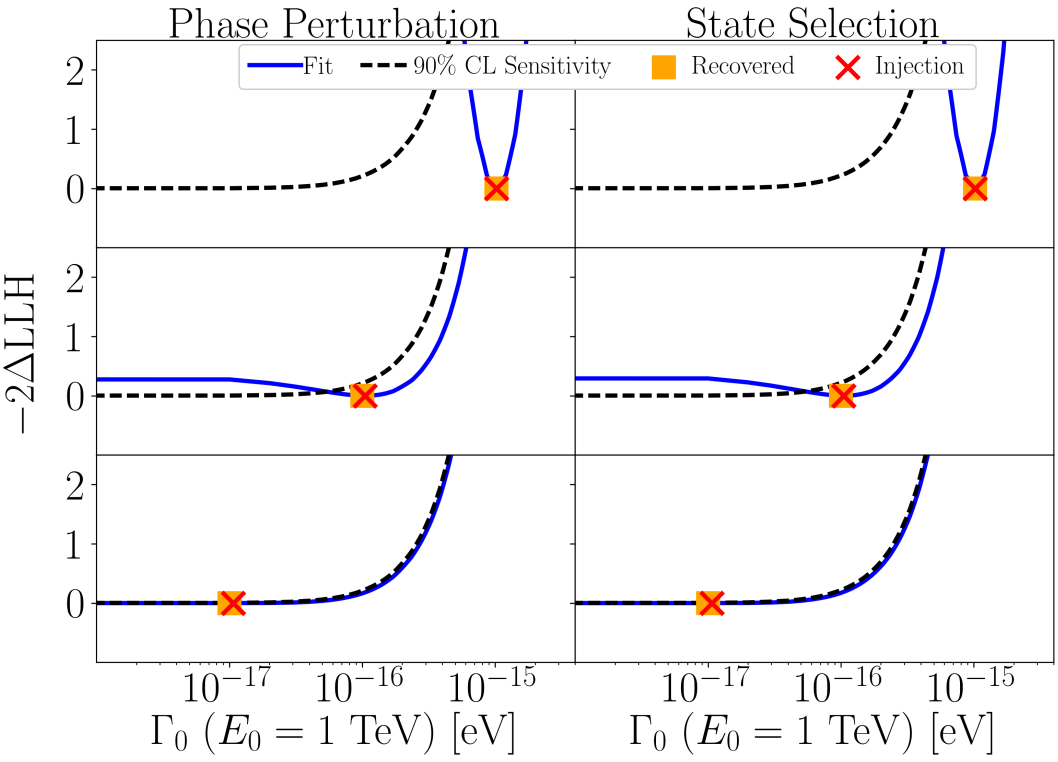

FIGURE 8.11: Examples of IR tests performed within and outside the central 90% CL sensitivity in the decoherence parameter space.

This analysis tested points inside and outside the sensitivity contour for that model and n to demonstrate the correct best-fit will be recovered in any data scenario. All tests recovered the injected values.

Alternatively, inject-recover tests were performed on realizations that were not statistically idealized (included binned fluctuations) and with randomized nuisance parameter values to test a more realistic scenario of fitting against noisy data (examples of these tests are shown in Fig. 8.11). As with the no-fluctuations (Asimov) tests, these tests recovered the inject values of Γ_0. Therefore, we confirm that the minimizer is capable of accurately recovering the best-fit Γ_0 signal.

8.7 Pre-Unblinding Checks and Data Sample

To verify correct and full functionality of the statistics software and consistency within the data sample, a series of pre-unblinding checks were devised to act as stopping triggers in the event an unreasonable divergence between the MC and data. First, the procedure was applied to a random 5% of the data sample, then the full sample.

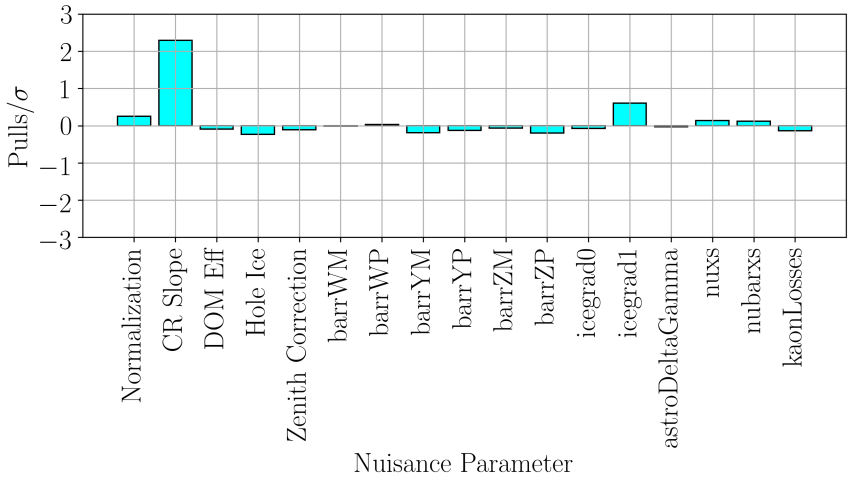

FIGURE 8.12: The pulls of nuisance parameters at the best-fit Γ_0 against the prior central values.

While the following checks were performed for all eight n-interaction combinations of the analysis, only the checks for $n = 0$ with state selection are shown in this section.

After minimizing across the profile likelihood and storing a blind best-fit point, the first test was to calculate the statistical pulls of the systematic nuisance parameter values at the best-fit point. If any pull exceeded 3σ, the procedure is halted. These pulls are displayed in Fig. 8.12.

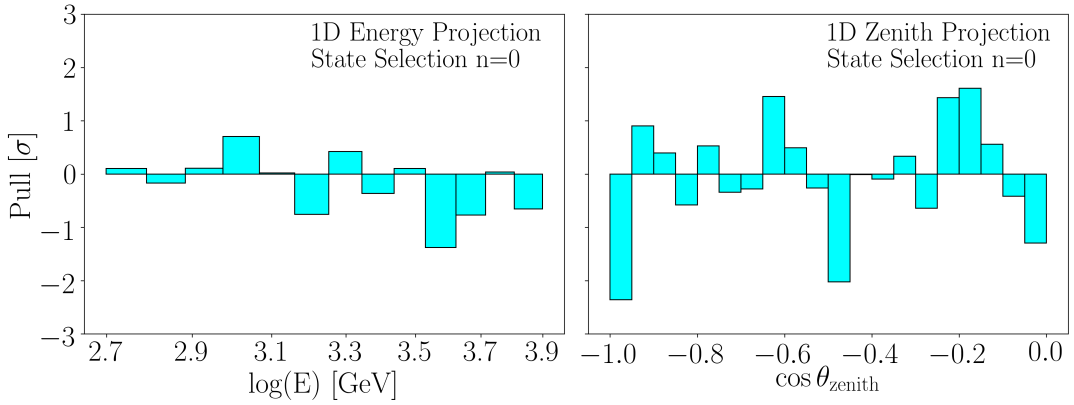

FIGURE 8.13: The pulls of nuisance parameters at the best-fit Γ_0 against the prior central values.

Next, the best-fit MC-data pulls in the one-dimensional zenith and energy distributions are calculated, in which the stopping threshold is if three or more bins pull greater than 3σ. The pulls are displayed in Fig. 8.13 top left and right.

In the complete two-dimensional event binning, the MC-data pulls are calculated, and the stop trigger activates if six or more bins pull greater than 3σ. The 2D pull distribution is shown in Fig. 8.14, bottom right.

Lastly, the 1D and 2D binned χ^2 distributions are calculated with the p-values are extracted, all from generating 1,000 pseudoexperiments ("realizations") injected with the blind best-fit Γ_0 value for the given n and interaction model. Should any p-value be less than 5% (0.05), the procedure is stopped. The full data χ^2 distributions are shown in Fig. 8.14, top left and right, bottom left.

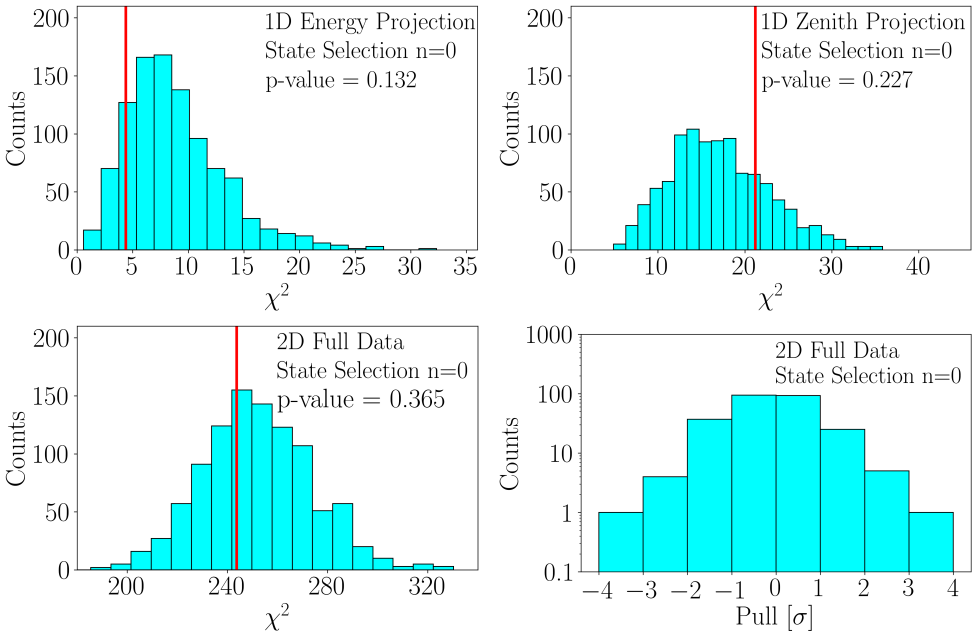

FIGURE 8.14: Top left: 1D energy χ^2 distribution from 1000 realizations at blind best-fit. Top right: 1D zenith χ^2 distribution from 1000 realizations at blind best-fit. Bottom left: 2D data χ^2 distribution from 1000 realizations at blind best-fit. Bottom right: 2D data data distribution pulls.

8.8 Results

The IceCube 8-year high energy muon track dataset was fully unblinded for the decoherence analysis in October of 2022.

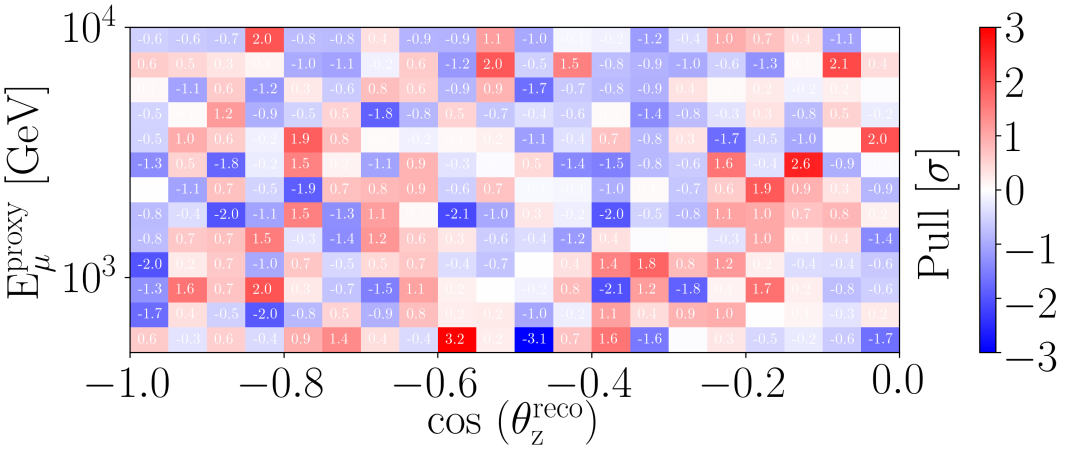

FIGURE 8.15: The pulls of each bin count between the best-fit distribution for $n = 0$, state selection against the null hypothesis.

An example of the difference in event counts per bin from the null (no decoherence) hypothesis after the nuisance parameter fit are shown for $n = 0$,

state selection in Fig. 8.15.

The fit to data presented no significant evidence for decoherence. The 95%, 90%, and 68% confidence level upper limits are shown in Fig. 8.16. To contrast the results against the sensitivities and the sensitivities from 100 pseudoexperiment trials with fluctuated statistics, the frequentist bands are included in the figure.

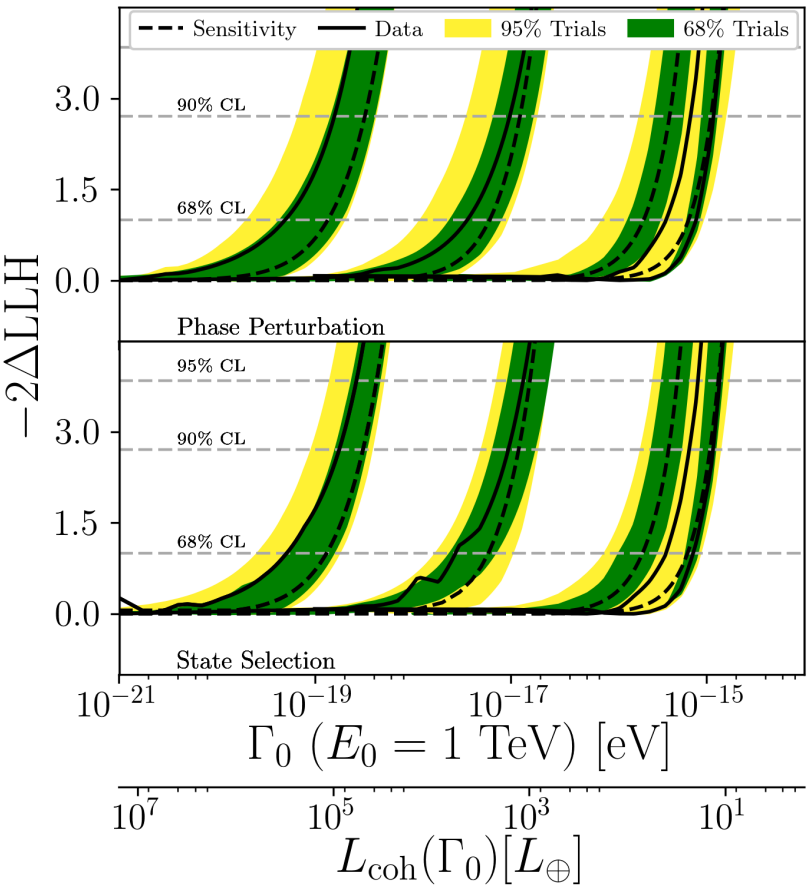

FIGURE 8.16: (Top) The frequentist bands from 100 trials for each scenario, plotted against the corresponding sensitivity and result.

To determine how well the analysis results perform, a comparison of the 90% confidence level limits against previously-published results are shown in Fig. 8.17.

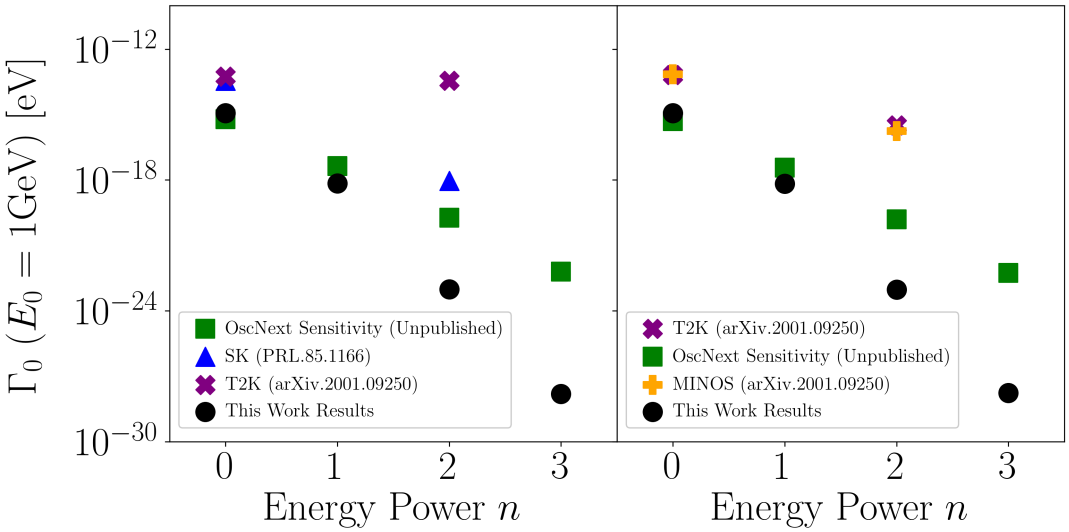

FIGURE 8.17: (Top) The frequentist bands from 100 trials for each scenario, plotted against the corresponding sensitivity and result.

In Tables 8.2 and 8.3, we list the complete set of 90% CL upper limits for all n for the phase perturbation and state selection scenarios, respectively. Included are the parameter conversions to the coherence length parameter L_{coh} and unitless decoherence strength parameter ξ_{Planck}.

Power Index n	Γ_0 90% CL Upper Limit [eV]	L_{coh} 90% CL Lower Limit [km]	ξ_{Planck} 90% CL Upper Limit [unitless]
0	$1.184 \cdot 10^{-15}$	$1.310 \cdot 10^{1}$	$9.694 \cdot 10^{-45}$
1	$6.895 \cdot 10^{-16}$	$2.250 \cdot 10^{1}$	$6.895 \cdot 10^{-19}$
2	$9.800 \cdot 10^{-18}$	$1.583 \cdot 10^{3}$	$1.197 \cdot 10^{6}$
3	$1.588 \cdot 10^{-19}$	$9.766 \cdot 10^{4}$	$2.368 \cdot 10^{30}$

TABLE 8.2: The 90% CL upper limits for each n in the phase perturbation scenario.

Power Index n	Γ_0 90% CL Upper Limit [eV]	L_{coh} 90% CL Lower Limit [km]	ξ_{Planck} 90% CL Upper Limit [unitless]
0	$1.171 \cdot 10^{-15}$	$1.325 \cdot 10^{1}$	$9.588 \cdot 10^{-45}$
1	$6.678 \cdot 10^{-16}$	$2.323 \cdot 10^{1}$	$6.678 \cdot 10^{-19}$
2	$9.485 \cdot 10^{-18}$	$1.635 \cdot 10^{3}$	$1.158 \cdot 10^{6}$
3	$1.776 \cdot 10^{-19}$	$8.733 \cdot 10^{4}$	$2.648 \cdot 10^{30}$

TABLE 8.3: The 90% CL upper limits for each n in the state selection scenario.

These results yield some notable features. From Tables 8.2 and 8.3, it can be seen that the natural theory, where $\xi_{\text{Planck}} \sim \mathcal{O}(1)$, is excluded for $n \leq 1$.

In addition, Fig. 8.17 displays that the results of this analysis are the strongest limits for all scenarios and n, with the improvement on previous limits scaling exponentially with n. It is worth noting that these results agree with measurements from cosmological analyses, which also find no significant evidence for quantum decoherence [217, 218]. Further commentary on these results is presented in Chapter 9.

Part V

Conclusion

Chapter 9

Conclusion

With a new generation of experiments in preparation and current experiments accumulating larger samples, neutrino physics is entering the era of high-precision measurements. Access to this level of precision opens the door to the physics yet described by the Standard Model that takes the form of secondary effects. This thesis reports two searches for such subdominant effects through a high-statistics atmospheric neutrino sample collected by the IceCube Neutrino Observatory.

The first was a search for flavor-changing $\mu-\tau$ nonstandard neutrino interactions, which found a best-fit value in the normal mass ordering of $\epsilon_{\mu\tau} = -0.0029$ at a p-value of 25.2%, hence not rejecting the no-NSI hypothesis. The 90% confidence level limits were found to be $-0.0041 < \epsilon_{\mu\tau} < 0.0031$, an improvement on the next-leading measurement (IceCube 2017) by a factor of two and representing the strongest constraints on any NSI parameter from an oscillations experiment to-date. This has opened up the regime of $\mathcal{O}(0.001)$ matter NSI to the neutrino oscillations community, and is an early suggestion that further oscillations measurements may not disfavor the SM for $\epsilon \sim \mathcal{O}(0.001)$. In turn, this constrains the space of possible NSI models that may assume new light or heavy mediator masses, and is the latest step in determining the nature of subleading effects from higher-energy interactions.

The second analysis constrained possible neutrino oscillation decoherence from coupling to spacetime quantum foam in a model of neutrino-virtual black hole interactions. Upper limits at the 90% confidence level were found to be

$\Gamma_0(n=0) \lesssim 1.2 \cdot 10^{-15}$ eV, $\Gamma_0(n=1) \lesssim 6.9 \cdot 10^{-16}$ eV, $\Gamma_0(n=2) \lesssim 9.8 \cdot 10^{-18}$ eV, and $\Gamma_0(n=3) \lesssim 1.8 \cdot 10^{-19}$ eV at a reference energy of $E_0 = 1$ TeV. These limits correspond to lower limits of the neutrino coherence length, which were found at the 90% confidence level to be $L_{\text{coh}}(n=0) \gtrsim 1.4 \cdot 10^{1}\ L_{\oplus}$, $L_{\text{coh}}(n=1) \gtrsim 2.4 \cdot 10^{1}\ L_{\oplus}$, $L_{\text{coh}}(n=2) \gtrsim 1.7 \cdot 10^{3}\ L_{\oplus}$, and $L_{\text{coh}}(n=3) \gtrsim 9.4 \cdot 10^{4}\ L_{\oplus}$, where $L_{\oplus}$ is the Earth diameter. Insufficient evidence was found to reject the no-decoherence hypothesis. In comparison to previous measurements, the limits on the Γ_0 parameter are an improvement by several orders of magnitude for $n \geq 1$, with the improvement scaling with the power n. Such results place the best experimental constraints on the neutrino dissipation channel, with the strength of the constraint scaling with power n. This implies that should neutrino-virtual black hole interactions take place, the scale of the interaction would occur below the "natural" scale of $\xi_{\text{Planck}} \sim 1$. With a dramatic improvement on previous results, the outcome of this analysis showcases the resolving power of neutrinos in studies of physics at the smallest scales.

Here we presented some of the first leading beyond-Standard Model constraints from this new high-precision era of TeV-scale neutrino physics with data collected at the IceCube Neutrino Observatory. Once considered illusive, neutrinos are now measured with such resolution that the subleading effects governing neutrino interactions are now increasingly available to offer a window into the highest-energy physics we have been able to probe. Similarly, the ability to test models of quantum gravity was long considered impossible. Yet with the novel use of unique neutrino properties, experiments have begun illuminating this space in the hope of discovering physics that may point us towards a unified theory of quantum mechanics and gravity. Larger and more powerful neutrino experiments are already well into development, and current experiments continue to collect invaluable data for use in further studies. It is not inconceivable to imagine that within the next decade, significant milestones in understanding the high-energy interactions and quantum gravity will

be accomplished, and that we may yet be on the cusp of a revolution in physics thanks to discoveries in the neutrino sector.

Bibliography

[1] H. Becquerel. “Sur les radiations émises par phosphorescence”. In: *C. R.* 122 (Jan. 1896), pp. 420–421. URL: https://gallica.bnf.fr/ark:/12148/bpt6k30780/f422.chemindefer.

[2] H. Becquerel. “Sur les radiations invisibles émises par les corps phosphorescents”. In: *C. R.* 122 (Jan. 1896), pp. 501–503. URL: https://gallica.bnf.fr/ark:/12148/bpt6k30780/f503.item.

[3] J. Chadwick. “The intensity distribution in the magnetic spectrum of beta particles from radium (B + C)”. In: *Verh. Phys. Gesell.* 16 (1914), pp. 383–391.

[4] W. Pauli. “Letter to gauverein wien meeting in tubingen”. In: ().

[5] J. Chadwick. “Possible Existence of a Neutron”. In: *Nature* 129.3252 (Feb. 1932), pp. 312–312. ISSN: 1476-4687. DOI: 10.1038/129312a0. URL: https://doi.org/10.1038/129312a0.

[6] H. Bethe and R. Peierls. “The “Neutrino””. In: *Nature* 133.3362 (Apr. 1934), pp. 532–532. ISSN: 1476-4687. DOI: 10.1038/133532a0. URL: https://doi.org/10.1038/133532a0.

[7] C. L. Cowan, F. Reines, et al. “Detection of the Free Neutrino: a Confirmation”. In: *Science* 124.3212 (1956), pp. 103–104. DOI: 10.1126/science.124.3212.103. URL: https://www.science.org/doi/abs/10.1126/science.124.3212.103.

[8] M. Schwartz. "Feasibility of Using High-Energy Neutrinos to Study the Weak Interactions". In: *Phys. Rev. Lett.* 4 (6 Mar. 1960), pp. 306–307. DOI: 10.1103/PhysRevLett.4.306. URL: https://link.aps.org/doi/10.1103/PhysRevLett.4.306.

[9] B. Pontecorvo. "Electron and Muon Neutrinos". In: *Zh. Eksp. Teor. Fiz.* 37 (1959), pp. 1751–1757.

[10] G. T. Danby et al. "Observation of High-Energy Neutrino Reactions and the Existence of Two Kinds of Neutrinos". In: *Phys. Rev. Lett.* 9 (1962), pp. 36–44.

[11] M. L. Perl et al. "Evidence for anomalous lepton production in e+-e- annihilation". In: *Phys. Rev. Lett.* 35.22 (1975), pp. 1489–1492. ISSN: 0031-9007. DOI: 10.1103/PhysRevLett.35.1489.

[12] K. Kodama et al. "Observation of tau neutrino interactions". In: *Phys. Lett. B* 504.3 (Apr. 2001), 218–224. ISSN: 0370-2693. DOI: 10.1016/s0370-2693(01)00307-0. URL: http://dx.doi.org/10.1016/S0370-2693(01)00307-0.

[13] Raymond Davis. "Solar Neutrinos. II. Experimental". In: *Phys. Rev. Lett.* 12 (11 Mar. 1964), pp. 303–305. DOI: 10.1103/PhysRevLett.12.303. URL: https://link.aps.org/doi/10.1103/PhysRevLett.12.303.

[14] John N. Bahcall. "Solar Neutrinos. I. Theoretical". In: *Phys. Rev. Lett.* 12 (11 Mar. 1964), pp. 300–302. DOI: 10.1103/PhysRevLett.12.300. URL: https://link.aps.org/doi/10.1103/PhysRevLett.12.300.

[15] B. Pontecorvo. "Mesonium and anti-mesonium". In: *Sov. Phys. JETP* 6 (1957), p. 429.

[16] B. Pontecorvo. "Inverse beta processes and nonconservation of lepton charge". In: *Zh. Eksp. Teor. Fiz.* 34 (1957), p. 247.

[17] L. Wolfenstein. "Neutrino oscillations in matter". In: *Phys. Rev. D* 17 (9 May 1978), pp. 2369–2374. DOI: 10.1103/PhysRevD.17.2369. URL: https://link.aps.org/doi/10.1103/PhysRevD.17.2369.

[18] L. Wolfenstein. "Neutrino oscillations and stellar collapse". In: *Phys. Rev. D* 20 (10 Nov. 1979), pp. 2634–2635. DOI: 10.1103/PhysRevD.20.2634. URL: https://link.aps.org/doi/10.1103/PhysRevD.20.2634.

[19] S. P. Mikheyev and A. Yu. Smirnov. "Resonance Amplification of Oscillations in Matter and Spectroscopy of Solar Neutrinos". In: *Sov. J. Nucl. Phys.* 42 (1985), pp. 913–917.

[20] S. P. Mikheev and A. Yu. Smirnov. "Neutrino Oscillations in a Variable Density Medium and Neutrino Bursts Due to the Gravitational Collapse of Stars". In: *Sov. Phys. JETP* 64 (1986), pp. 4–7. arXiv: 0706.0454 [hep-ph].

[21] Y. Fukuda et al. "Evidence for Oscillation of Atmospheric Neutrinos". In: *Phys. Rev. Lett.* 81.8 (Aug. 1998), 1562–1567. ISSN: 1079-7114. DOI: 10.1103/physrevlett.81.1562. arXiv: 9807003 [hep-ex]. URL: http://dx.doi.org/10.1103/PhysRevLett.81.1562.

[22] J. N. Abdurashitov et al. "Solar neutrino flux measurements by the Soviet-American Gallium Experiment (SAGE) for half the 22 year solar cycle". In: *J. Exp. Theor. Phys.* 95 (2002), pp. 181–193. DOI: 10.1134/1.1506424. arXiv: 0204245 [astro-ph].

[23] W. Hampel et al. "GALLEX solar neutrino observations: results for GALLEX IV". In: *Phys. Lett. B* 447.1 (1999), pp. 127–133. ISSN: 0370-2693. DOI: https://doi.org/10.1016/S0370-2693(98)01579-2. URL: https://www.sciencedirect.com/science/article/pii/S0370269398015792.

[24] Ziro Maki, Masami Nakagawa, and Shoichi Sakata. "Remarks on the Unified Model of Elementary Particles". In: *Prog. Theor. Phys.* 28.5 (Nov. 1962), pp. 870–880. ISSN: 0033-068X. DOI: 10.1143/PTP.28.870. eprint: https://academic.oup.com/ptp/article-pdf/28/5/870/5258750/28-5-870.pdf. URL: https://doi.org/10.1143/PTP.28.870.

[25] B. Pontecorvo. "Neutrino Experiments and the Problem of Conservation of Leptonic Charge". In: *Zh. Eksp. Teor. Fiz.* 53 (1967), pp. 1717–1725.

[26] C. Jarlskog. "Commutator of the Quark Mass Matrices in the Standard Electroweak Model and a Measure of Maximal CP Nonconservation". In: *Phys. Rev. Lett.* 55 (10 Sept. 1985), pp. 1039–1042. DOI: 10.1103/PhysRevLett.55.1039. URL: https://link.aps.org/doi/10.1103/PhysRevLett.55.1039.

[27] J. N. Abdurashitov et al. "Measurement of the solar neutrino capture rate with gallium metal. III: Results for the 2002–2007 data-taking period". In: *Phys. Rev. C* 80 (2009), p. 015807. DOI: 10.1103/PhysRevC.80.015807. arXiv: 0901.2200 [nucl-ex].

[28] S. P. Mikheyev and A. Yu. Smirnov. "Resonance Amplification of Oscillations in Matter and Spectroscopy of Solar Neutrinos". In: *Sov. J. Nucl. Phys.* 42 (1985), pp. 913–917.

[29] F. Kaether et al. "Reanalysis of the GALLEX solar neutrino flux and source experiments". In: *Phys. Lett. B* 685 (2010), pp. 47–54. DOI: 10.1016/j.physletb.2010.01.030. arXiv: 1001.2731 [hep-ex].

[30] A. Aguilar-Arevalo et al. "Evidence for neutrino oscillations from the observation of $\bar{\nu}_e$ appearance in a $\bar{\nu}_\mu$ beam". In: *Phys. Rev. D* 64 (2001), p. 112007. DOI: 10.1103/PhysRevD.64.112007. arXiv: hep-ex/0104049.

[31] A. A. Aguilar-Arevalo et al. "Updated MiniBooNE neutrino oscillation results with increased data and new background studies". In: *Phys. Rev. D* 103.5 (2021), p. 052002. DOI: 10.1103/PhysRevD.103.052002. arXiv: 2006.16883 [hep-ex].

[32] A. A. Aguilar-Arevalo et al. "Improved Search for $\bar{\nu}_\mu \to \bar{\nu}_e$ Oscillations in the MiniBooNE Experiment". In: *Phys. Rev. Lett.* 110 (2013), p. 161801. DOI: 10.1103/PhysRevLett.110.161801. arXiv: 1303.2588 [hep-ex].

[33] P. Abratenko et al. "Search for an Excess of Electron Neutrino Interactions in MicroBooNE Using Multiple Final-State Topologies". In: *Phys. Rev. Lett.* 128.24 (2022), p. 241801. DOI: 10.1103/PhysRevLett.128.241801. arXiv: 2110.14054 [hep-ex].

[34] Patrick Huber. "Determination of antineutrino spectra from nuclear reactors". In: *Phys. Rev. C* 84 (2 Aug. 2011), p. 024617. DOI: 10.1103/PhysRevC.84.024617. URL: https://link.aps.org/doi/10.1103/PhysRevC.84.024617.

[35] Th. A. Mueller et al. "Improved Predictions of Reactor Antineutrino Spectra". In: *Phys. Rev. C* 83 (2011), p. 054615. DOI: 10.1103/PhysRevC.83.054615. arXiv: 1101.2663 [hep-ex].

[36] V. V. Barinov et al. "Results from the Baksan Experiment on Sterile Transitions (BEST)". In: *Phys. Rev. Lett.* 128.23 (2022), p. 232501. DOI: 10.1103/PhysRevLett.128.232501. arXiv: 2109.11482 [nucl-ex].

[37] V. V. Barinov et al. "Search for electron-neutrino transitions to sterile states in the BEST experiment". In: *Phys. Rev. C* 105.6 (2022), p. 065502. DOI: 10.1103/PhysRevC.105.065502. arXiv: 2201.07364 [nucl-ex].

[38] Francis Halzen and John G. Learned. "HIGH-ENERGY NEUTRINO DETECTION IN DEEP POLAR ICE". In: (June 1988).

[39] Ch. Spiering. "Status of the projects BAIKAL and AMANDA". In: *31st Rencontres de Moriond: Dark Matter and Cosmology, Quantum Measurements and Experimental Gravitation*. 1996, pp. 109–116.

[40] T. Miller et al. "From AMANDA to IceCube: Current and future high energy neutrino telescopes at the South Pole". In: *23rd Johns Hopkins Workshop on Current Problems in Particle Theory: Neutrinos in the New Millennium*. June 1999, pp. 47–61.

[41] E. Andres et al. "Observation of atmospheric neutrino events with the AMANDA experiment". In: *17th International Workshop on Weak Interactions and Neutrinos*. Jan. 1999, pp. 258–262. arXiv: astro-ph/9904379.

[42] Francis Halzen. "Status of the AMANDA South Pole neutrino detector". In: *1st International Heidelberg Conference on Dark Matter in Astro and Particle Physics*. Sept. 1996, pp. 718–728. arXiv: hep-ex/9611014.

[43] M. G. Aartsen et al. "Multimessenger observations of a flaring blazar coincident with high-energy neutrino IceCube-170922A". In: *Science* 361.6398 (2018), eaat1378. DOI: 10.1126/science.aat1378. URL: https://www.science.org/doi/abs/10.1126/science.aat1378.

[44] C. A. Argüelles et al. "New opportunities at the next-generation neutrino experiments I: BSM neutrino physics and dark matter". In: *Rept. Prog. Phys.* 83.12 (2020), p. 124201. DOI: 10.1088/1361-6633/ab9d12. arXiv: 1907.08311 [hep-ph].

[45] M. G. Aartsen et al. "Evidence for High-Energy Extraterrestrial Neutrinos at the IceCube Detector". In: *Science* 342 (2013), p. 1242856. DOI: 10.1126/science.1242856. arXiv: 1311.5238 [astro-ph.HE].

[46] M. G. Aartsen et al. "Measurement of Atmospheric Neutrino Oscillations at 6–56 GeV with IceCube DeepCore". In: *Phys. Rev. Lett.* 120 (7 Feb.

2018), p. 071801. DOI: 10.1103/PhysRevLett.120.071801. URL: https://link.aps.org/doi/10.1103/PhysRevLett.120.071801.

[47] A. Achterberg et al. "First Year Performance of The IceCube Neutrino Telescope". In: *Astropart. Phys.* 26 (2006), pp. 155–173. DOI: 10.1016/j.astropartphys.2006.06.007. arXiv: astro-ph/0604450.

[48] J. Ahrens et al. *IceCube preliminary design document*. http://www.icecube.wisc.edu/science/publications/pdd.

[49] R. Abbasi et al. "The Design and Performance of IceCube DeepCore". In: *Astropart. Phys.* 35 (2012), pp. 615–624. DOI: 10.1016/j.astropartphys.2012.01.004. arXiv: 1109.6096 [astro-ph.IM].

[50] S. Axani. "Sterile Neutrino Searches at the IceCube Neutrino Observatory". PhD dissertation. Massachusetts Institute of Technology, 2020. arXiv: 2003.02796 [hep-ph].

[51] IceCube Collaboration. *IceCube Public Gallery*. https://icecube.wisc.edu/gallery/.

[52] Hamamatsu Photonics KK. *R7081 datasheet*. 2003.

[53] R. Abbasi et al. "Calibration and characterization of the IceCube photomultiplier tube". In: *Nuclear Instruments and Methods in Physics Research Section A: Accelerators, Spectrometers, Detectors and Associated Equipment* 618.1 (2010), pp. 139–152. ISSN: 0168-9002. DOI: https://doi.org/10.1016/j.nima.2010.03.102. URL: https://www.sciencedirect.com/science/article/pii/S0168900210006662.

[54] R. Abbasi et al. "The IceCube Data Acquisition System: Signal Capture, Digitization, and Timestamping". In: *Nucl. Instrum. Meth. A* 601 (2009), pp. 294–316. DOI: 10.1016/j.nima.2009.01.001. arXiv: 0810.4930 [physics.ins-det].

[55] M.G. Aartsen et al. "The IceCube Neutrino Observatory: instrumentation and online systems". In: *Journal of Instrumentation* 12.03 (Mar. 2017), P03012–P03012. DOI: 10.1088/1748-0221/12/03/p03012. URL: https://doi.org/10.1088/1748-0221/12/03/p03012.

[56] R. Abbasi et al. "The IceCube Data Acquisition System: Signal Capture, Digitization, and Timestamping". In: *Nucl. Instrum. Meth. A* 601 (2009), pp. 294–316. DOI: 10.1016/j.nima.2009.01.001. arXiv: 0810.4930 [physics.ins-det].

[57] B. Nilsson and A. Brahme. "9.01 - Interaction of Ionizing Radiation with Matter". In: *Comprehensive Biomedical Physics*. Ed. by Anders Brahme. Oxford: Elsevier, 2014, pp. 1–36. ISBN: 978-0-444-53633-4. DOI: https://doi.org/10.1016/B978-0-444-53632-7.00920-5. URL: https://www.sciencedirect.com/science/article/pii/B9780444536327009205.

[58] P.A. Cherenkov. "Visible emission of clean liquids by action of γ radiation". In: 93 (1934). ref Archived October 22, 2007, at the Wayback Machine, p. 385.

[59] "South Pole glacial climate reconstruction from multi-borehole laser particulate stratigraphy". In: *Journal of Glaciology* 59.218 (2013), 1117–1128. DOI: 10.3189/2013JoG13J068.

[60] R. Abbasi et al. "In-situ estimation of ice crystal properties at the South Pole using LED calibration data from the IceCube Neutrino Observatory". In: *The Cryosphere Discussions* 2022 (2022), pp. 1–48. DOI: 10.5194/tc-2022-174. URL: https://tc.copernicus.org/preprints/tc-2022-174/.

[61] M. Rongen. "Measuring the optical properties of IceCube drill holes". en. In: *EPJ Web of Conferences*. Vol. 116. EDP Sciences, 2016, pp. 06011,

[62] A. Karle. "Entwicklung eines neuartigen atmosph¨arischen Tscherenkovdetektors und Messungen an hochenergetischer Kosmischer Strahlung zwischen 15 und 1000 TeV". PhD dissertation. Munchen Univ., 1994.

[63] M. G. Aartsen et al. "Measurement of Atmospheric Neutrino Oscillations at 6-56 GeV with IceCube DeepCore". In: *Phys. Rev. Lett.* 120.7 (2018), p. 071801. DOI: 10.1103/PhysRevLett.120.071801. arXiv: 1707.07081 [hep-ex].

[64] Sebastian Fiedlschuster. "The Effect of Hole Ice on the Propagation and Detection of Light in IceCube". In: (Apr. 2019). arXiv: 1904.08422 [physics.ins-det].

[65] M. Ackermann et al. "Optical properties of deep glacial ice at the South Pole". In: *Journal of Geophysical Research: Atmospheres* 111.D13 (2006). DOI: https://doi.org/10.1029/2005JD006687. eprint: https://agupubs.onlinelibrary.wiley.com/doi/pdf/10.1029/2005JD006687. URL: https://agupubs.onlinelibrary.wiley.com/doi/abs/10.1029/2005JD006687.

[66] Dmitry Chirkin. "Study of South Pole ice transparency with IceCube flashers". In: *32nd International Cosmic Ray Conference*. Vol. 4. 2011, p. 161. DOI: 10.7529/ICRC2011/V04/0333.

[67] M. G. Aartsen et al. "Measurement of South Pole ice transparency with the IceCube LED calibration system". In: *Nuclear Instruments and Methods in Physics Research, Section A: Accelerators, Spectrometers, Detectors and Associated Equipment* 711 (2013), pp. 73–89. ISSN: 0168-9002. DOI: 10.1016/j.nima.2013.01.054.

[68] M. G. Aartsen et al. "Searching for eV-scale sterile neutrinos with eight years of atmospheric neutrinos at the IceCube Neutrino Telescope". In: *Phys. Rev. D* 102.5 (2020), p. 052009. DOI: 10.1103/PhysRevD.102.052009. arXiv: 2005.12943 [hep-ex].

[69] M. G. Aartsen et al. "eV-Scale Sterile Neutrino Search Using Eight Years of Atmospheric Muon Neutrino Data from the IceCube Neutrino Observatory". In: *Phys. Rev. Lett.* 125.14 (2020), p. 141801. DOI: 10.1103/PhysRevLett.125.141801. arXiv: 2005.12942 [hep-ex].

[70] R. Abbasi et al. "LeptonInjector and LeptonWeighter: A neutrino event generator and weighter for neutrino observatories". In: *Comput. Phys. Commun.* 266 (2021), p. 108018. DOI: 10.1016/j.cpc.2021.108018. arXiv: 2012.10449 [physics.comp-ph].

[71] J.-H. Koehne et al. "PROPOSAL: A tool for propagation of charged leptons". In: *Comput. Phys. Commun.* 184.9 (2013), pp. 2070–2090. ISSN: 0010-4655. DOI: 10.1016/j.cpc.2013.04.001. URL: https://www.sciencedirect.com/science/article/pii/S0010465513001355.

[72] C. Kopper. *CLSim*. 2019. URL: http://code.icecube.wisc.edu/svn/projects/clsim/,.

[73] M. G. Aartsen et al. "Efficient propagation of systematic uncertainties from calibration to analysis with the SnowStorm method in IceCube". In: *J. Cosmol. Astropart. P.* 10 (2019), p. 048. DOI: 10.1088/1475-7516/2019/10/048. arXiv: 1909.01530 [hep-ex].

[74] N. Whitehorn et al. *Wavedeform*. 2019. URL: http://code.icecube.wisc.edu/svn/projects/wavedeform/.

[75] Anatoli Fedynitch, Julia Becker Tjus, and Paolo Desiati. "Influence of hadronic interaction models and the cosmic ray spectrum on the high energy atmospheric muon and neutrino flux". In: *Phys. Rev. D* 86.11 (Dec. 2012). ISSN: 1550-2368. DOI: 10.1103/physrevd.86.114024. arXiv: 1206.6710 [hep-ph]. URL: http://dx.doi.org/10.1103/PhysRevD.86.114024.

[76] Anatoli Fedynitch et al. "Calculation of conventional and prompt lepton fluxes at very high energy". In: *EPJ Web Conf.* 99 (2015). Ed. by D. Berge et al., p. 08001. DOI: 10.1051/epjconf/20159908001. arXiv: 1503.00544 [hep-ph].

[77] C. A. Argüelles, J. Salvado, and C. N. Weaver. "nuSQuIDS". In: (2015). URL: https://github.com/Arguelles/nuSQuIDS.

[78] Carlos A. Argüelles, Jordi Salvado, and Christopher N. Weaver. *nuSQuIDS: A toolbox for neutrino propagation*. 2021. arXiv: 2112.13804 [hep-ph].

[79] L. Wolfenstein. "Neutrino oscillations in matter". In: *Phys. Rev. D* 17 (9 May 1978), pp. 2369–2374. DOI: 10.1103/PhysRevD.17.2369. URL: https://link.aps.org/doi/10.1103/PhysRevD.17.2369.

[80] L. Wolfenstein. "Neutrino oscillations and stellar collapse". In: *Phys. Rev. D* 20 (10 Nov. 1979), pp. 2634–2635. DOI: 10.1103/PhysRevD.20.2634. URL: https://link.aps.org/doi/10.1103/PhysRevD.20.2634.

[81] M. M. Guzzo, A. Masiero, and S. T. Petcov. "On the MSW effect with massless neutrinos and no mixing in the vacuum". In: *Phys. Lett. B* 260 (1991), pp. 154–160. DOI: 10.1016/0370-2693(91)90984-X.

[82] Bhupal Dev et al. "Neutrino non-standard interactions: A status report". In: *SciPost Phys. Proc.* 2 (Dec. 2019). ISSN: 2666-4003. DOI: 10.21468/scipostphysproc.2.001. arXiv: 1907.00991 [hep-ph]. URL: http://dx.doi.org/10.21468/SciPostPhysProc.2.001.

[83] Y. Farzan and M. Tortola. "Neutrino oscillations and Non-Standard Interactions". In: *Front. in Phys.* 6 (2018), p. 10. DOI: 10.3389/fphy.2018.00010. arXiv: 1710.09360 [hep-ph].

[84] O G Miranda and H Nunokawa. "Non standard neutrino interactions: current status and future prospects". In: *New Journal of Physics* 17.9

(Sept. 2015), p. 095002. DOI: 10.1088/1367-2630/17/9/095002. URL: https://dx.doi.org/10.1088/1367-2630/17/9/095002.

[85] Pilar Coloma et al. "Curtailing the Dark Side in Non-Standard Neutrino Interactions". In: *JHEP* 04 (2017), p. 116. DOI: 10.1007/JHEP04(2017)116. arXiv: 1701.04828 [hep-ph].

[86] Pilar Coloma et al. "COHERENT Enlightenment of the Neutrino Dark Side". In: *Phys. Rev. D* 96.11 (2017), p. 115007. DOI: 10.1103/PhysRevD.96.115007. arXiv: 1708.02899 [hep-ph].

[87] Jiajun Liao and Danny Marfatia. "COHERENT constraints on nonstandard neutrino interactions". In: *Phys. Lett. B* 775 (2017), pp. 54–57. DOI: 10.1016/j.physletb.2017.10.046. arXiv: 1708.04255 [hep-ph].

[88] Peter B. Denton, Yasaman Farzan, and Ian M. Shoemaker. "Testing large non-standard neutrino interactions with arbitrary mediator mass after COHERENT data". In: *JHEP* 07 (2018), p. 037. DOI: 10.1007/JHEP07(2018)037. arXiv: 1804.03660 [hep-ph].

[89] James B. Dent et al. "Accelerator and reactor complementarity in coherent neutrino-nucleus scattering". In: *Phys. Rev. D* 97.3 (2018), p. 035009. DOI: 10.1103/PhysRevD.97.035009. arXiv: 1711.03521 [hep-ph].

[90] Julien Billard, Joseph Johnston, and Bradley J. Kavanagh. "Prospects for exploring New Physics in Coherent Elastic Neutrino-Nucleus Scattering". In: *JCAP* 11 (2018), p. 016. DOI: 10.1088/1475-7516/2018/11/016. arXiv: 1805.01798 [hep-ph].

[91] Manfred Lindner, Werner Rodejohann, and Xun-Jie Xu. "Coherent Neutrino-Nucleus Scattering and new Neutrino Interactions". In: *JHEP* 03 (2017), p. 097. DOI: 10.1007/JHEP03(2017)097. arXiv: 1612.04150 [hep-ph].

[92] Yasaman Farzan et al. "Probing neutrino coupling to a light scalar with coherent neutrino scattering". In: *JHEP* 05 (2018), p. 066. DOI: 10.1007/JHEP05(2018)066. arXiv: 1802.05171 [hep-ph].

[93] Vedran Brdar, Werner Rodejohann, and Xun-Jie Xu. "Producing a new Fermion in Coherent Elastic Neutrino-Nucleus Scattering: from Neutrino Mass to Dark Matter". In: *JHEP* 12 (2018), p. 024. DOI: 10.1007/JHEP12(2018)024. arXiv: 1810.03626 [hep-ph].

[94] Francesco Capozzi, Ian M. Shoemaker, and Luca Vecchi. "Solar Neutrinos as a Probe of Dark Matter-Neutrino Interactions". In: *JCAP* 07 (2017), p. 021. DOI: 10.1088/1475-7516/2017/07/021. arXiv: 1702.08464 [hep-ph].

[95] Francesco Capozzi, Ian M. Shoemaker, and Luca Vecchi. "Neutrino Oscillations in Dark Backgrounds". In: *JCAP* 07 (2018), p. 004. DOI: 10.1088/1475-7516/2018/07/004. arXiv: 1804.05117 [hep-ph].

[96] M. C. Gonzalez-Garcia et al. "Neutrino Discovery Limit of Dark Matter Direct Detection Experiments in the Presence of Non-Standard Interactions". In: *JHEP* 07 (2018), p. 019. DOI: 10.1007/JHEP07(2018)019. arXiv: 1803.03650 [hep-ph].

[97] O. G. Miranda, M. A. Tortola, and J. W. F. Valle. "Are solar neutrino oscillations robust?" In: *JHEP* 10 (2006), p. 008. DOI: 10.1088/1126-6708/2006/10/008. arXiv: hep-ph/0406280.

[98] F. J. Escrihuela et al. "Constraining nonstandard neutrino-quark interactions with solar, reactor and accelerator data". In: *Phys. Rev. D* 80 (2009). [Erratum: Phys.Rev.D 80, 129908 (2009)], p. 105009. DOI: 10.1103/PhysRevD.80.129908. arXiv: 0907.2630 [hep-ph].

[99] M. C. Gonzalez-Garcia and Michele Maltoni. "Determination of matter potential from global analysis of neutrino oscillation data". In: *JHEP*

09 (2013), p. 152. DOI: 10.1007/JHEP09(2013)152. arXiv: 1307.3092 [hep-ph].

[100] Sanjib Kumar Agarwalla et al. "Probing Non-Standard Interactions at Daya Bay". In: *JHEP* 07 (2015), p. 060. DOI: 10.1007/JHEP07(2015)060. arXiv: 1412.1064 [hep-ph].

[101] I. Girardi, D. Meloni, and S. T. Petcov. "The Daya Bay and T2K results on $\sin^2 2\theta_{13}$ and Non-Standard Neutrino Interactions". In: *Nucl. Phys. B* 886 (2014), pp. 31–42. DOI: 10.1016/j.nuclphysb.2014.06.014. arXiv: 1405.0416 [hep-ph].

[102] L. J. Flores, E. A. Garcés, and O. G. Miranda. "Exploring NSI degeneracies in long-baseline experiments". In: *Phys. Rev. D* 98.3 (2018), p. 035030. DOI: 10.1103/PhysRevD.98.035030. arXiv: 1806.07951 [hep-ph].

[103] Jiajun Liao, Danny Marfatia, and Kerry Whisnant. "Degeneracies in long-baseline neutrino experiments from nonstandard interactions". In: *Phys. Rev. D* 93.9 (2016), p. 093016. DOI: 10.1103/PhysRevD.93.093016. arXiv: 1601.00927 [hep-ph].

[104] K. N. Deepthi, Srubabati Goswami, and Newton Nath. "Can nonstandard interactions jeopardize the hierarchy sensitivity of DUNE?" In: *Phys. Rev. D* 96.7 (2017), p. 075023. DOI: 10.1103/PhysRevD.96.075023. arXiv: 1612.00784 [hep-ph].

[105] Sanjib Kumar Agarwalla, Sabya Sachi Chatterjee, and Antonio Palazzo. "Degeneracy between θ_{23} octant and neutrino non-standard interactions at DUNE". In: *Phys. Lett. B* 762 (2016), pp. 64–71. DOI: 10.1016/j.physletb.2016.09.020. arXiv: 1607.01745 [hep-ph].

[106] Tommy Ohlsson, He Zhang, and Shun Zhou. "Nonstandard interaction effects on neutrino parameters at medium-baseline reactor antineutrino

experiments". In: *Phys. Lett. B* 728 (2014), pp. 148–155. DOI: 10.1016/j.physletb.2013.11.052. arXiv: 1310.5917 [hep-ph].

[107] Yu-Feng Li and Ye-Ling Zhou. "Shifts of neutrino oscillation parameters in reactor antineutrino experiments with non-standard interactions". In: *Nucl. Phys. B* 888 (2014), pp. 137–153. DOI: 10.1016/j.nuclphysb.2014.09.013. arXiv: 1408.6301 [hep-ph].

[108] Suppanat Supanyo, Monsit Tanasittikosol, and Sikarin Yoo-Kong. "Natural TeV cutoff of the Higgs field from a multiplicative Lagrangian". In: *Phys. Rev. D* 106.3 (2022), p. 035020. DOI: 10.1103/PhysRevD.106.035020. arXiv: 2205.06687 [hep-th].

[109] Steven Weinberg. "Baryon- and Lepton-Nonconserving Processes". In: *Phys. Rev. Lett.* 43 (21 Nov. 1979), pp. 1566–1570. DOI: 10.1103/PhysRevLett.43.1566. URL: https://link.aps.org/doi/10.1103/PhysRevLett.43.1566.

[110] Benjamin Fuks et al. "Probing the Weinberg operator at colliders". In: *Phys. Rev. D* 103.11 (2021), p. 115014. DOI: 10.1103/PhysRevD.103.115014. arXiv: 2012.09882 [hep-ph].

[111] Peter Minkowski. "$\mu \to e\gamma$ at a Rate of One Out of 10^9 Muon Decays?" In: *Phys. Lett. B* 67 (1977), pp. 421–428. DOI: 10.1016/0370-2693(77)90435-X.

[112] Rabindra N. Mohapatra. "Neutrino masses and mixings in gauge models with spontaneous parity violation". In: *Phys. Rev. D* 23 (1 Jan. 1981), pp. 165–180. DOI: 10.1103/PhysRevD.23.165. URL: https://link.aps.org/doi/10.1103/PhysRevD.23.165.

[113] Robert Foot et al. "Seesaw Neutrino Masses Induced by a Triplet of Leptons". In: *Z. Phys. C* 44 (1 Jan. 1989), p. 441. DOI: 10.1007/BF01415558. URL: https://link.aps.org/doi/10.1103/PhysRevD.23.165.

[114] Benjamin Fuks et al. "Probing the Weinberg operator at colliders". In: *Phys. Rev. D* 103.11 (1 Jan. 2021), p. 115014. DOI: 10.1103/PhysRevD.103.115014. arXiv: 2012.09882 [hep-ph]. URL: https://link.aps.org/doi/10.1103/PhysRevD.23.165.

[115] Rabindra N. Mohapatra. "Probing heavy Majorana neutrinos and the Weinberg operator through vector boson fusion processes in proton-proton collisions at $\sqrt{s} = 13$ TeV". In: *Phys. Rev. D* 23 (1 June 2022), pp. 165–180. DOI: 10.1103/PhysRevD.23.165. arXiv: 2206.08956 [hep-ex]. URL: https://link.aps.org/doi/10.1103/PhysRevD.23.165.

[116] Jordi Salvado et al. "Non-standard interactions with high-energy atmospheric neutrinos at IceCube". In: *J. High Energy Phys.* 01 (1 June 2017), p. 141. DOI: 10.1007/JHEP01(2017)141. arXiv: 1609.03450 [hep-ph]. URL: https://link.aps.org/doi/10.1103/PhysRevD.23.165.

[117] Carla Biggio, Mattias Blennow, and Enrique Fernandez-Martinez. "General bounds on non-standard neutrino interactions". In: *JHEP* 08 (1 June 2009), p. 090. DOI: 10.1088/1126-6708/2009/08/090. arXiv: 0907.0097 [hep-ph]. URL: https://link.aps.org/doi/10.1103/PhysRevD.23.165.

[118] Tommy Ohlsson. "Status of non-standard neutrino interactions". In: *Rept. Prog. Phys.* 76 (1 June 2013), p. 044201. DOI: 10.1088/0034-4885/76/4/044201. arXiv: 1209.2710 [hep-ph]. URL: https://link.aps.org/doi/10.1103/PhysRevD.23.165.

[119] Ivan Esteban et al. "Updated constraints on non-standard interactions from global analysis of oscillation data". In: *JHEP* 08 (1 June 2018). [Addendum: JHEP 12, 152 (2020)], p. 180. DOI: 10.1007/JHEP08(2018)180. arXiv: 1805.04530 [hep-ph]. URL: https://link.aps.org/doi/10.1103/PhysRevD.23.165.

[120] Pilar Coloma and Thomas Schwetz. "Generalized mass ordering degeneracy in neutrino oscillation experiments". In: *Phys. Rev. D* 94.5 (1 June 2016). [Erratum: Phys.Rev.D 95, 079903 (2017)], p. 055005. DOI: 10.1103/PhysRevD.94.055005. arXiv: 1604.05772 [hep-ph]. URL: https://link.aps.org/doi/10.1103/PhysRevD.23.165.

[121] R. Abbasi et al. "All-flavor constraints on nonstandard neutrino interactions and generalized matter potential with three years of IceCube DeepCore data". In: *Phys. Rev. D* 104 (7 Oct. 2021), p. 072006. DOI: 10.1103/PhysRevD.104.072006. arXiv: 2106.07755 [hep-ph]. URL: https://link.aps.org/doi/10.1103/PhysRevD.104.072006.

[122] M. G. Aartsen et al. "Search for Nonstandard Neutrino Interactions with IceCube DeepCore". In: *Phys. Rev. D* 97.7 (1 June 2018), p. 072009. DOI: 10.1103/PhysRevD.97.072009. arXiv: 1709.07079 [hep-ex]. URL: https://link.aps.org/doi/10.1103/PhysRevD.23.165.

[123] G. Mitsuka et al. "Study of Non-Standard Neutrino Interactions with Atmospheric Neutrino Data in Super-Kamiokande I and II". In: *Phys. Rev. D* 84 (1 June 2011), p. 113008. DOI: 10.1103/PhysRevD.84.113008. arXiv: 1109.1889 [hep-ex]. URL: https://link.aps.org/doi/10.1103/PhysRevD.23.165.

[124] S. V. Demidov. "Bounds on non-standard interactions of neutrinos from IceCube DeepCore data". In: *JHEP* 03 (1 June 2020), p. 105. DOI: 10.1007/JHEP03(2020)105. arXiv: 1912.04149 [hep-ph]. URL: https://link.aps.org/doi/10.1103/PhysRevD.23.165.

[125] P. Adamson et al. "Search for flavor-changing non-standard neutrino interactions by MINOS". In: *Phys. Rev. D* 88 (7 June 2013), p. 072011. DOI: 10.1103/PhysRevD.88.072011. arXiv: 2206.08956 [hep-ex]. URL: https://link.aps.org/doi/10.1103/PhysRevD.88.072011.

[126] Peter Denton, Yasaman Farzan, and Ian Shoemaker. "Testing large non-standard neutrino interactions with arbitrary mediator mass after COHERENT data". In: *Journal of High Energy Physics* 2018 (1 July 2018), pp. 165–180. DOI: 10.1007/JHEP07(2018)037. arXiv: 2206.08956 [hep-ex]. URL: https://link.aps.org/doi/10.1103/PhysRevD.23.165.

[127] Ivan Esteban et al. "Updated fit to three neutrino mixing: exploring the accelerator-reactor complementarity". In: *JHEP* 01 (1 June 2017), p. 087. DOI: 10.1007/JHEP01(2017)087. arXiv: 1611.01514 [hep-ph]. URL: https://link.aps.org/doi/10.1103/PhysRevD.23.165.

[128] Pablo F. de Salas et al. "Neutrino Mass Ordering from Oscillations and Beyond: 2018 Status and Future Prospects". In: *Front. Astrono. Sp. S.* 5 (1 June 2018), p. 36. ISSN: 2296-987X. DOI: 10.3389/fspas.2018.00036. arXiv: 1806.11051 [hep-ph]. URL: https://www.frontiersin.org/article/10.3389/fspas.2018.00036.

[129] M. G. Aartsen et al. "Evidence for Astrophysical Muon Neutrinos from the Northern Sky with IceCube". In: *Phys. Rev. Lett.* 115 (8 June 2015), p. 081102. DOI: 10.1103/PhysRevLett.115.081102. arXiv: 2206.08956 [hep-ex]. URL: https://link.aps.org/doi/10.1103/PhysRevLett.115.081102.

[130] Ivan Esteban et al. "Global analysis of three-flavour neutrino oscillations: synergies and tensions in the determination of θ_{23}, δ_{CP}, and the mass ordering". In: *J. High Energy Phys.* 01 (1 June 2019), p. 10. DOI: 10.1007/JHEP01(2019)106. arXiv: 1811.05487 [hep-ph]. URL: https://link.aps.org/doi/10.1103/PhysRevD.23.165.

[131] A. Albert et al. "Search for non-standard neutrino interactions with 10 years of ANTARES data". In: *Phys. Rev. D* 23 (1 Dec. 2021), pp. 165–

180. DOI: 10.1103/PhysRevD.23.165. arXiv: 2112.14517 [hep-ex]. URL: https://link.aps.org/doi/10.1103/PhysRevD.23.165.

[132] Thomas Gaisser. "Spectrum of cosmic-ray nucleons, kaon production, and the atmospheric muon charge ratio". In: *Astroparticle Physics* 35 (1 July 2012), 801–806. DOI: 10.1016/j.astropartphys.2012.02.010. arXiv: 2206.08956 [hep-ex]. URL: https://link.aps.org/doi/10.1103/PhysRevD.23.165.

[133] Felix Riehn et al. "The hadronic interaction model Sibyll 2.3c and Feynman scaling". In: *Proc. S.* ICRC2017 (1 June 2017), p. 301. DOI: 10.22323/1.301.0301. arXiv: 1709.07227 [hep-ph]. URL: https://link.aps.org/doi/10.1103/PhysRevD.23.165.

[134] Atri Bhattacharya et al. "Perturbative charm production and the prompt atmospheric neutrino flux in light of RHIC and LHC". In: *Journal of High Energy Physics* 2015 (1 Feb. 2015), pp. 165–180. DOI: 10.1007/JHEP06(2015)110. arXiv: 2206.08956 [hep-ex]. URL: https://link.aps.org/doi/10.1103/PhysRevD.23.165.

[135] Jet Propulsion Laboratory. "AIRS/AMSU/HSB Version 6 Level 3 Product User Guide". In: *Phys. Rev. D* 6 (2 Nov. 2017), pp. 165–180. DOI: 10.1109/TGRS.2002.808236. arXiv: 2206.08956 [hep-ex]. URL: https://docserver.gesdisc.eosdis.nasa.gov/repository/Mission/AIRS/3.3_ScienceDataProductDocumentation/3.3.4_ProductGenerationAlgorithms/V6_L2_Product_User_Guide.pdf.

[136] A. Cooper-Sarkar, P. Mertsch, and S. Sarkar. "The high energy neutrino cross-section in the Standard Model and its uncertainty". en. In: *Journal of High Energy Physics* 23.8 (1 June 2011), pp. 42, DOI: 10.1103/PhysRevD.23.165. arXiv: 2206.08956 [hep-ex]. URL: https://link.aps.org/doi/10.1103/PhysRevD.23.165.

[137] Adam M. Dziewonski and Don L. Anderson. "Preliminary reference Earth model". In: *Physics of the Earth and Planetary Interiors* 25.4 (1 June 1981), pp. 297–356. ISSN: 0031-9201. DOI: https://doi.org/10.1016/0031-9201(81)90046-7. arXiv: 2206.08956 [hep-ex]. URL: https://www.sciencedirect.com/science/article/pii/0031920181900467.

[138] S. Axani. *SPE Templates Technote: Extracting and fitting procedure*. June 2019. DOI: 10.1103/PhysRevD.23.165. arXiv: 2206.08956 [hep-ex]. URL: https://docushare.wipac.wisc.edu/dsweb/Get/Document-85572/SPE_Templates_Technote_v2.pdf,.

[139] M. G. Aartsen et al. "In-situ calibration of the single-photoelectron charge response of the IceCube photomultiplier tubes". In: *JINST* 15.06 (1 June 2020), P06032. DOI: 10.1088/1748-0221/15/06/P06032. arXiv: 2002.00997 [physics.ins-det]. URL: https://link.aps.org/doi/10.1103/PhysRevD.23.165.

[140] J. Ahrens et al. "Muon track reconstruction and data selection techniques in AMANDA". In: *Nuclear Instruments and Methods in Physics Research, Section A: Accelerators, Spectrometers, Detectors and Associated Equipment* 524.1-3 (1 May 2004), pp. 169–194. ISSN: 0168-9002. DOI: 10.1016/j.nima.2004.01.065. arXiv: 2206.08956 [hep-ex]. URL: https://link.aps.org/doi/10.1103/PhysRevD.23.165.

[141] M. G. Aartsen et al. "Energy Reconstruction Methods in the IceCube Neutrino Telescope". In: *JINST* 9 (1 June 2014), P03009. DOI: 10.1088/1748-0221/9/03/P03009. arXiv: 1311.4767 [physics.ins-det]. URL: https://link.aps.org/doi/10.1103/PhysRevD.23.165.

[142] C. Argüelles. *GolemFit*. June 2019. DOI: 10.1103/PhysRevD.23.165. arXiv: 2206.08956 [hep-ex]. URL: https://github.com/IceCubeOpenSource/GolemFit/tree/SterilizeSuperOptimized,.

[143] S. S. Wilks. "The Large-Sample Distribution of the Likelihood Ratio for Testing Composite Hypotheses". In: *Ann. Math. Stat.* 9.1 (1 June 1938), pp. 60 –62. DOI: 10.1214/aoms/1177732360. arXiv: 2206.08956 [hep-ex]. URL: https://doi.org/10.1214/aoms/1177732360.

[144] Sara Algeri et al. "Searching for new physics with profile likelihoods: Wilks and beyond". In: *Phys. Rev. D* 23 (1 Nov. 2019), pp. 165–180. DOI: 10.1103/PhysRevD.23.165. arXiv: 1911.10237 [physics.data-an]. URL: https://link.aps.org/doi/10.1103/PhysRevD.23.165.

[145] B. J. Jones. "Sterile neutrinos in cold climates". PhD dissertation. Massachusetts Institute of Technology, June 2015, pp. 165–180. DOI: 10.1103/PhysRevD.23.165. arXiv: 2206.08956 [hep-ex]. URL: https://dspace.mit.edu/handle/1721.1/101327.

[146] M. Honda et al. "Calculation of atmospheric neutrino flux using the interaction model calibrated with atmospheric muon data". In: *Phys. Rev. D* 75 (4 Feb. 2007), p. 043006. DOI: 10.1103/PhysRevD.75.043006. arXiv: 2206.08956 [hep-ex]. URL: https://link.aps.org/doi/10.1103/PhysRevD.75.043006.

[147] Anatoli Fedynitch, Julia Becker Tjus, and Paolo Desiati. "Influence of hadronic interaction models and the cosmic ray spectrum on the high energy atmospheric muon and neutrino flux". In: *Phys. Rev. D* 86 (11 Dec. 2012), p. 114024. DOI: 10.1103/PhysRevD.86.114024. arXiv: 2206.08956 [hep-ex]. URL: https://link.aps.org/doi/10.1103/PhysRevD.86.114024.

[148] A. V. Karelin et al. "The Proton and Helium cosmic ray spectra from 50 GeV to 15 TeV". In: *Astrophys. Space Sci. Transac.* 7.2 (1 June 2011), pp. 235–238. DOI: 10.5194/astra-7-235-2011. arXiv: 2206.08956 [hep-ex]. URL: http://www.astrophys-space-sci-trans.net/7/235/2011/.

[149] R. Alfaro et al. "All-particle cosmic ray energy spectrum measured by the HAWC experiment from 10 to 500 TeV". In: *Phys. Rev. D* 96 (12 Dec. 2017), p. 122001. DOI: 10.1103/PhysRevD.96.122001. arXiv: 1710.00890 [astro-ph.HE]. URL: https://link.aps.org/doi/10.1103/PhysRevD.96.122001.

[150] Y. S. Yoon et al. "Proton and Helium Spectra from the CREAM-III Flight". In: *Astrophys. J.* 839.1 (1 June 2017), p. 5. DOI: 10.3847/1538-4357/aa68e4. arXiv: 1704.02512 [astro-ph.HE]. URL: https://link.aps.org/doi/10.1103/PhysRevD.23.165.

[151] B. Bartoli et al. "Cosmic ray proton plus helium energy spectrum measured by the ARGO-YBJ experiment in the energy range 3-300 TeV". In: *Phys. Rev. D* 91.11 (1 June 2015), p. 112017. DOI: 10.1103/PhysRevD.91.112017. arXiv: 1503.07136 [hep-ex]. URL: https://link.aps.org/doi/10.1103/PhysRevD.23.165.

[152] G. D. Barr et al. "Uncertainties in atmospheric neutrino fluxes". In: *Phys. Rev. D* 74 (9 Nov. 2006), p. 094009. DOI: 10.1103/PhysRevD.74.094009. arXiv: 0611266 [astro-ph]. URL: https://link.aps.org/doi/10.1103/PhysRevD.74.094009.

[153] Patrick Heix et al. "Seasonal Variation of Atmospheric Neutrinos in IceCube". In: *PoS* ICRC2019 (1 June 2020), p. 465. DOI: 10.22323/1.358.0465. arXiv: 1909.02036 [astro-ph.HE]. URL: https://link.aps.org/doi/10.1103/PhysRevD.23.165.

[154] M. G. Aartsen et al. "Observation and characterization of a cosmic muon neutrino flux from the northern hemisphere using six years of Icecube data". In: *Phys. Rev. D* 833.1 (1 Dec. 2016), p. 3. DOI: 10.3847/0004-637x/833/1/3. arXiv: 1607.08006 [astro-ph.HE]. URL: https://doi.org/10.3847/0004-637x/833/1/3.

[155] Austin Schneider. "Characterization of the Astrophysical Diffuse Neutrino Flux with IceCube High-Energy Starting Events". In: *Proc. S.* ICRC2019 (1 June 2020), p. 1004. DOI: 10.22323/1.358.1004. arXiv: 1907.11266 [astro-ph.HE]. URL: https://link.aps.org/doi/10.1103/PhysRevD.23.165.

[156] M. G. Aartsen et al. "Evidence for High-Energy Extraterrestrial Neutrinos at the IceCube Detector". In: *Science* 342.6161 (1 June 2013), p. 1242856. DOI: 10.1126/science.1242856. arXiv: 1311.5238 [astro-ph.HE]. URL: https://www.science.org/doi/abs/10.1126/science.1242856.

[157] M. G. Aartsen et al. "Observation of High-Energy Astrophysical Neutrinos in Three Years of IceCube Data". In: *Phys. Rev. Lett.* 113 (1 June 2014), p. 101101. DOI: 10.1103/PhysRevLett.113.101101. arXiv: 1405.5303 [astro-ph.HE]. URL: https://link.aps.org/doi/10.1103/PhysRevD.23.165.

[158] M. G. Aartsen et al. "Measurements using the inelasticity distribution of multi-TeV neutrino interactions in IceCube". In: *Phys. Rev. D* 99 (3 Feb. 2019), p. 032004. DOI: 10.1103/PhysRevD.99.032004. arXiv: 1808.07629 [astro-ph.HE]. URL: https://link.aps.org/doi/10.1103/PhysRevD.99.032004.

[159] M. G. Aartsen et al. "Characteristics of the diffuse astrophysical electron and tau neutrino flux with six years of IceCube high energy cascade data". In: *Phys. Rev. Lett.* 125.12 (1 June 2020), p. 121104. DOI: 10.1103/PhysRevLett.125.121104. arXiv: 2001.09520 [astro-ph.HE]. URL: https://link.aps.org/doi/10.1103/PhysRevD.23.165.

[160] Per Askebjer et al. "Optical properties of deep ice at the South Pole: absorption". In: *Appl. Opt.* 36.18 (1 June 1997), pp. 4168–4180. DOI:

10.1364/AO.36.004168. arXiv: 9701025 [physics]. URL: http://www.osapublishing.org/ao/abstract.cfm?URI=ao-36-18-4168.

[161] Raj Gandhi et al. "Ultrahigh-energy neutrino interactions". In: *Astropart. Phys.* 5 (1 June 1996), pp. 81–110. DOI: 10.1016/0927-6505(96)00008-4. arXiv: 9512364 [hep-ph]. URL: https://link.aps.org/doi/10.1103/PhysRevD.23.165.

[162] Aaron C. Vincent, Carlos A. Argüelles, and Ali Kheirandish. "High-energy neutrino attenuation in the Earth and its associated uncertainties". In: *J. Cosmol. Astropart. P.* 11 (1 June 2017), p. 012. DOI: 10.1088/1475-7516/2017/11/012. arXiv: 1706.09895 [hep-ph]. URL: https://link.aps.org/doi/10.1103/PhysRevD.23.165.

[163] Amy Connolly, Robert S. Thorne, and David Waters. "Calculation of high energy neutrino-nucleon cross sections and uncertainties using the Martin-Stirling-Thorne-Watt parton distribution functions and implications for future experiments". In: *Phys. Rev. D* 83 (11 June 2011), p. 113009. DOI: 10.1103/PhysRevD.83.113009. arXiv: 1102.0691 [hep-ph]. URL: https://link.aps.org/doi/10.1103/PhysRevD.83.113009.

[164] Amanda Cooper-Sarkar, Philipp Mertsch, and Subir Sarkar. "The high energy neutrino cross-section in the Standard Model and its uncertainty". In: *J. High Energy Phys.* 2011.8 (1 Aug. 2011), p. 42. ISSN: 1029-8479. DOI: 10.1007/JHEP08(2011)042. arXiv: 1106.3723 [hep-ph]. URL: https://doi.org/10.1007/JHEP08(2011)042.

[165] C. A. Argüelles. "New physics with atmospheric neutrinos". PhD thesis. The University of Wisconsin-Madison, June 2015, pp. 165–180. DOI: 10.1103/PhysRevD.23.165. arXiv: 2206.08956 [hep-ex]. URL: https://ui.adsabs.harvard.edu/abs/2015PhDT.....94D.

[166] Glen Cowan et al. "Asymptotic formulae for likelihood-based tests of new physics". In: *Eur. Phys. J. C* 71 (1 June 2011). [Erratum: Eur.Phys.J.C 73, 2501 (2013)], p. 1554. DOI: 10.1140/epjc/s10052-011-1554-0. arXiv: 1007.1727 [physics.data-an]. URL: https://link.aps.org/doi/10.1103/PhysRevD.23.165.

[167] R. Abbasi et al. "Strong Constraints on Neutrino Nonstandard Interactions from TeV-Scale ν_u Disappearance at IceCube". In: *Phys. Rev. Lett.* 129.1 (1 June 2022), p. 011804. DOI: 10.1103/PhysRevLett.129.011804. arXiv: 2201.03566 [hep-ex]. URL: https://link.aps.org/doi/10.1103/PhysRevD.23.165.

[168] Gary J. Feldman and Robert D. Cousins. "Unified approach to the classical statistical analysis of small signals". In: *Phys. Rev. D* 57.7 (1 Apr. 1998), 3873–3889. ISSN: 1089-4918. DOI: 10.1103/physrevd.57.3873. arXiv: 9711021 [physics]. URL: http://dx.doi.org/10.1103/PhysRevD.57.3873.

[169] W. Heisenberg. "Über den anschaulichen Inhalt der quantentheoretischen Kinematik und Mechanik". In: *Zeitschrift fur Physik* 43.3-4 (1 Mar. 1927), pp. 172–198. DOI: 10.1007/BF01397280. arXiv: 2206.08956 [hep-ex]. URL: https://link.aps.org/doi/10.1103/PhysRevD.23.165.

[170] E. Schrodinger. "About Heisenberg uncertainty relation". In: *Sitzungsber. Preuss. Akad. Wiss. Berlin (Math. Phys.)* 19 (1 June 1930), pp. 296–303. DOI: 10.1103/PhysRevD.23.165. arXiv: quant-ph/9903100 [hep-ex]. URL: https://link.aps.org/doi/10.1103/PhysRevD.23.165.

[171] H. P. Robertson. "The Uncertainty Principle". In: *Physical Review* 34.1 (1 July 1929), pp. 163–164. DOI: 10.1103/PhysRev.34.163. arXiv: 2206.08956 [hep-ex]. URL: https://link.aps.org/doi/10.1103/PhysRevD.23.165.

[172] C. Alden Mead. "Possible Connection Between Gravitation and Fundamental Length". In: *Phys. Rev.* 135 (3B Aug. 1964), B849–B862. DOI: 10.1103/PhysRev.135.B849. arXiv: 2206.08956 [hep-ex]. URL: https://link.aps.org/doi/10.1103/PhysRev.135.B849.

[173] C. Alden Mead. "Observable Consequences of Fundamental-Length Hypotheses". In: *Phys. Rev.* 143 (4 Mar. 1966), pp. 990–1005. DOI: 10.1103/PhysRev.143.990. arXiv: 2206.08956 [hep-ex]. URL: https://link.aps.org/doi/10.1103/PhysRev.143.990.

[174] T Padmanabhan. "Limitations on the operational definition of spacetime events and quantum gravity". In: *Classical and Quantum Gravity* 4.4 (1 July 1987), p. L107. DOI: 10.1088/0264-9381/4/4/007. arXiv: 2206.08956 [hep-ex]. URL: https://dx.doi.org/10.1088/0264-9381/4/4/007.

[175] Y. JACK NG and H. VAN DAM. "LIMIT TO SPACE-TIME MEASUREMENT". In: *Modern Physics Letters A* 09.04 (1 June 1994), pp. 335–340. DOI: 10.1142/S0217732394000356. arXiv: https://doi.org/10.1142/S0217732394000356 [hep-ex]. URL: https://doi.org/10.1142/S0217732394000356.

[176] Michele Maggiore. "A generalized uncertainty principle in quantum gravity". In: *Physics Letters B* 304.1 (1 June 1993), pp. 65–69. ISSN: 0370-2693. DOI: https://doi.org/10.1016/0370-2693(93)91401-8. arXiv: 2206.08956 [hep-ex]. URL: https://www.sciencedirect.com/science/article/pii/0370269393914018.

[177] G. Amelino-Camelia. "Limits on the measurability of space-time distances in the semiclassical approximation of quantum gravity". In: *Mod. Phys. Lett. A* 9 (1 June 1994), pp. 3415–3422. DOI: 10.1142/S0217732394003245. arXiv: gr-qc/9603014 [hep-ex]. URL: https://link.aps.org/doi/10.1103/PhysRevD.23.165.

[178] Luis J. Garay. "Quantum gravity and minimum length". In: *Int. J. Mod. Phys. A* 10 (1 June 1995), pp. 145–166. DOI: 10.1142/S0217751X95000085. arXiv: gr-qc/9403008 [hep-ex]. URL: https://link.aps.org/doi/10.1103/PhysRevD.23.165.

[179] Ronald J. Adler and David I. Santiago. "On gravity and the uncertainty principle". In: *Mod. Phys. Lett. A* 14 (1 June 1999), p. 1371. DOI: 10.1142/S0217732399001462. arXiv: gr-qc/9904026 [hep-ex]. URL: https://link.aps.org/doi/10.1103/PhysRevD.23.165.

[180] Fabio Scardigli. "Generalized uncertainty principle in quantum gravity from micro - black hole Gedanken experiment". In: *Phys. Lett. B* 452 (1 June 1999), pp. 39–44. DOI: 10.1016/S0370-2693(99)00167-7. arXiv: hep-th/9904025 [hep-ex]. URL: https://link.aps.org/doi/10.1103/PhysRevD.23.165.

[181] S. Capozziello, G. Lambiase, and G. Scarpetta. "Generalized uncertainty principle from quantum geometry". In: *Int. J. Theor. Phys.* 39 (1 June 2000), pp. 15–22. DOI: 10.1023/A:1003634814685. arXiv: gr-qc/9910017 [hep-ex]. URL: https://link.aps.org/doi/10.1103/PhysRevD.23.165.

[182] Abel Camacho. "Generalized uncertainty principle and deformed dispersion relation induced by nonconformal metric fluctuations". In: *Gen. Rel. Grav.* 34 (1 June 2002), pp. 1839–1845. DOI: 10.1023/A:1020712007452. arXiv: gr-qc/0206006 [hep-ex]. URL: https://link.aps.org/doi/10.1103/PhysRevD.23.165.

[183] Xavier Calmet, Michael Graesser, and Stephen D. H Hsu. "Minimum Length from Quantum Mechanics and Classical General Relativity". In: *Phys. Rev. Lett.* 93 (21 Nov. 2004), p. 211101. DOI: 10.1103/PhysRevLett.93.211101. arXiv: 2206.08956 [hep-ex]. URL: https://link.aps.org/doi/10.1103/PhysRevLett.93.211101.

[184] S. W. Hawking. "The Unpredictability of Quantum Gravity". In: *Commun. Math. Phys.* 87 (1 June 1982), pp. 395–415. DOI: 10.1007/BF01206031. arXiv: 2206.08956 [hep-ex]. URL: https://link.aps.org/doi/10.1103/PhysRevD.23.165.

[185] John Archibald Wheeler. "Geons". In: *Phys. Rev.* 97 (2 Jan. 1955), pp. 511–536. DOI: 10.1103/PhysRev.97.511. arXiv: 2206.08956 [hep-ex]. URL: https://link.aps.org/doi/10.1103/PhysRev.97.511.

[186] Vittorio Gorini et al. "Properties of quantum Markovian master equations". In: *Reports on Mathematical Physics* 13.2 (1 June 1978), pp. 149–173. ISSN: 0034-4877. DOI: https://doi.org/10.1016/0034-4877(78)90050-2. arXiv: 2206.08956 [hep-ex]. URL: https://www.sciencedirect.com/science/article/pii/0034487778900502.

[187] Goran Lindblad. "On the Generators of Quantum Dynamical Semigroups". In: *Commun. Math. Phys.* 48 (1 June 1976), p. 119. DOI: 10.1007/BF01608499. arXiv: 2206.08956 [hep-ex]. URL: https://link.aps.org/doi/10.1103/PhysRevD.23.165.

[188] D.A. Lidar, A. Shabani, and R. Alicki. "Conditions for strictly purity-decreasing quantum Markovian dynamics". In: *Chemical Physics* 322.1-2 (1 Mar. 2006), pp. 82–86. DOI: 10.1016/j.chemphys.2005.06.038. arXiv: 2206.08956 [hep-ex]. URL: https://doi.org/10.1016\%2Fj.chemphys.2005.06.038.

[189] A. M. Gago et al. "A Study on quantum decoherence phenomena with three generations of neutrinos". In: *Phys. Rev. D* 23 (1 Aug. 2002), pp. 165–180. DOI: 10.1103/PhysRevD.23.165. arXiv: hep-ph/0208166 [hep-ex]. URL: https://link.aps.org/doi/10.1103/PhysRevD.23.165.

[190] Fabio Benatti and Roberto Floreanini. "Open system approach to neutrino oscillations". In: *Journal of High Energy Physics* 2000.02 (1 Feb.

2000), pp. 032–032. DOI: 10.1088/1126-6708/2000/02/032. arXiv: 2206.08956 [hep-ex]. URL: https://doi.org/10.1088/1126-6708/2000/02/032.

[191] F. Benatti and R. Floreanini. "Massless neutrino oscillations". In: *Phys. Rev. D* 64 (8 Sept. 2001), p. 085015. DOI: 10.1103/PhysRevD.64.085015. arXiv: 2206.08956 [hep-ex]. URL: https://link.aps.org/doi/10.1103/PhysRevD.64.085015.

[192] F. Benatti and R. Floreanini. "Non-standard Neutral Kaon Dynamics from Infinite Statistics". In: *Annals of Physics* 273.1 (1 June 1999), pp. 58–71. ISSN: 0003-4916. DOI: https://doi.org/10.1006/aphy.1998.5896. arXiv: 2206.08956 [hep-ex]. URL: https://www.sciencedirect.com/science/article/pii/S0003491698958961.

[193] Thomas Stuttard and Mikkel Jensen. "Neutrino decoherence from quantum gravitational stochastic perturbations". In: *Phys. Rev. D* 102.11 (1 June 2020), p. 115003. DOI: 10.1103/PhysRevD.102.115003. arXiv: 2007.00068 [hep-ph]. URL: https://link.aps.org/doi/10.1103/PhysRevD.23.165.

[194] E. Lisi, A. Marrone, and D. Montanino. "Probing Possible Decoherence Effects in Atmospheric Neutrino Oscillations". In: *Phys. Rev. Lett.* 85 (6 Aug. 2000), pp. 1166–1169. DOI: 10.1103/PhysRevLett.85.1166. arXiv: 2206.08956 [hep-ex]. URL: https://link.aps.org/doi/10.1103/PhysRevLett.85.1166.

[195] J. C. Carrasco, F. N. Díaz, and A. M. Gago. "Probing CPT breaking induced by quantum decoherence at DUNE". In: *Phys. Rev. D* 99 (7 Apr. 2019), p. 075022. DOI: 10.1103/PhysRevD.99.075022. arXiv: 2206.08956 [hep-ex]. URL: https://link.aps.org/doi/10.1103/PhysRevD.99.075022.

[196] S. W. Hawking. "Virtual black holes". In: *Phys. Rev. D* 53 (1 June 1996), pp. 3099–3107. DOI: 10.1103/PhysRevD.53.3099. arXiv: hep-th/9510029 [hep-ex]. URL: https://link.aps.org/doi/10.1103/PhysRevD.23.165.

[197] G T Horowitz. "Topology change in classical and quantum gravity". In: *Classical and Quantum Gravity* 8.4 (1 Apr. 1991), p. 587. DOI: 10.1088/0264-9381/8/4/007. arXiv: 2206.08956 [hep-ex]. URL: https://dx.doi.org/10.1088/0264-9381/8/4/007.

[198] S. Carlip. "Spacetime foam: a review". In: *Phys. Rev. D* 23 (1 Sept. 2022), pp. 165–180. DOI: 10.1103/PhysRevD.23.165. arXiv: 2209.14282 [gr-qc]. URL: https://link.aps.org/doi/10.1103/PhysRevD.23.165.

[199] Carl H. Brans and Duane Randall. "Exotic differentiable structures and general relativity". In: *Gen. Rel. Grav.* 25 (1 June 1993), p. 205. DOI: 10.1007/BF00758828. arXiv: gr-qc/9212003 [hep-ex]. URL: https://link.aps.org/doi/10.1103/PhysRevD.23.165.

[200] Torsten Asselmeyer-Maluga. "Exotic Smoothness and Quantum Gravity". In: *Class. Quant. Grav.* 27 (1 June 2010), p. 165002. DOI: 10.1088/0264-9381/27/16/165002. arXiv: 1003.5506 [gr-qc]. URL: https://link.aps.org/doi/10.1103/PhysRevD.23.165.

[201] Christopher Duston. "Exotic Smoothness in Four Dimensions and Euclidean Quantum Gravity". In: *Int. J. Geom. Meth. Mod. Phys.* 8 (1 June 2011), pp. 459–484. DOI: 10.1142/S0219887811005233. arXiv: 0911.4068 [gr-qc]. URL: https://link.aps.org/doi/10.1103/PhysRevD.23.165.

[202] Robbert Dijkgraaf et al. "A Black hole Farey tail". In: *Phys. Rev. D* 23 (1 May 2000), pp. 165–180. DOI: 10.1103/PhysRevD.23.165. arXiv:

hep-th/0005003 [hep-ex]. URL: https://link.aps.org/doi/10.1103/PhysRevD.23.165.

[203] Edward Witten. "A note on boundary conditions in Euclidean gravity". In: *Rev. Math. Phys.* 33.10 (1 June 2021), p. 2140004. DOI: 10.1142/S0129055X21400043. arXiv: 1805.11559 [hep-th]. URL: https://link.aps.org/doi/10.1103/PhysRevD.23.165.

[204] R. Loll, W. Westra, and S. Zohren. "Taming the cosmological constant in 2-D causal quantum gravity with topology change". In: *Nucl. Phys. B* 751 (1 June 2006), pp. 419–435. DOI: 10.1016/j.nuclphysb.2006.06.033. arXiv: hep-th/0507012 [hep-ex]. URL: https://link.aps.org/doi/10.1103/PhysRevD.23.165.

[205] Jan Ambjorn and R. Loll. "Nonperturbative Lorentzian quantum gravity, causality and topology change". In: *Nucl. Phys. B* 536 (1 June 1998), pp. 407–434. DOI: 10.1016/S0550-3213(98)00692-0. arXiv: hep-th/9805108 [hep-ex]. URL: https://link.aps.org/doi/10.1103/PhysRevD.23.165.

[206] Abhay Ashtekar et al. "Constructing Hamiltonian quantum theories from path integrals in a diffeomorphism-invariant context". In: *Class. Quant. Grav.* 17 (1 June 2000), pp. 4919–4940. DOI: 10.1088/0264-9381/17/23/310. arXiv: quant-ph/9904094 [hep-ex]. URL: https://link.aps.org/doi/10.1103/PhysRevD.23.165.

[207] Kristin Schleich and Donald M. Witt. "Generalized sums over histories for quantum gravity. 1. Smooth conifolds". In: *Nucl. Phys. B* 402 (1 June 1993), pp. 411–468. DOI: 10.1016/0550-3213(93)90649-A. arXiv: gr-qc/9307015 [hep-ex]. URL: https://link.aps.org/doi/10.1103/PhysRevD.23.165.

[208] Kristin Schleich and Donald M. Witt. "Generalized sums over histories for quantum gravity. 2. Simplicial conifolds". In: *Nucl. Phys. B* 402 (1

June 1993), pp. 469–530. DOI: 10.1016/0550-3213(93)90650-E. arXiv: gr-qc/9307019 [hep-ex]. URL: https://link.aps.org/doi/10.1103/PhysRevD.23.165.

[209] J. B. Hartle. "UNRULY TOPOLOGIES IN TWO-DIMENSIONAL QUANTUM GRAVITY". In: *Class. Quant. Grav.* 2 (1 June 1985), pp. 707–720. DOI: 10.1088/0264-9381/2/5/013. arXiv: 2206.08956 [hep-ex]. URL: https://link.aps.org/doi/10.1103/PhysRevD.23.165.

[210] Gerard 't Hooft. "Virtual Black Holes and Space–Time Structure". In: *Found. Phys.* 48.10 (1 June 2018), pp. 1134–1149. DOI: 10.1007/s10701-017-0133-0. arXiv: 2206.08956 [hep-ex]. URL: https://link.aps.org/doi/10.1103/PhysRevD.23.165.

[211] M. L. Ravn. "A search for quantum gravity motivated decoherence in atmospheric neutrinos using IceCube DeepCore". MsC dissertation. Niels Bohr Institute, June 2022, pp. 165–180. DOI: 10.1103/PhysRevD.23.165. arXiv: 2206.08956 [hep-ex]. URL: https://link.aps.org/doi/10.1103/PhysRevD.23.165.

[212] Luis A. Anchordoqui et al. "Probing Planck scale physics with IceCube". In: *Phys. Rev. D* 72 (1 June 2005), p. 065019. DOI: 10.1103/PhysRevD.72.065019. arXiv: hep-ph/0506168 [hep-ex]. URL: https://link.aps.org/doi/10.1103/PhysRevD.23.165.

[213] T. Stuttardd. *Decoherence SQuIDS branch*. June 2022. DOI: 10.1103/PhysRevD.23.165. arXiv: 2206.08956 [hep-ex]. URL: https://github.com/ts4051/SQuIDS/tree/decoherence_py3.

[214] T. Stuttardd. *Decoherence nuSQuIDS branch*. June 2022. DOI: 10.1103/PhysRevD.23.165. arXiv: 2206.08956 [hep-ex]. URL: https://github.com/ts4051/nuSQuIDS/tree/decoherence_py3.

[215] Edgar Bugaev et al. "Propagation of tau neutrinos and tau leptons through the earth and their detection in underwater / ice neutrino telescopes". In: *Astropart. Phys.* 21 (1 June 2004), pp. 491–509. DOI: 10.1016/j.astropartphys.2004.03.002. arXiv: hep-ph/0312295 [hep-ex]. URL: https://link.aps.org/doi/10.1103/PhysRevD.23.165.

[216] T. Stuttard. *Decoherence Matrix Oscillations Solver*. June 2021. DOI: 10.1103/PhysRevD.23.165. arXiv: 2206.08956 [hep-ex]. URL: https://github.com/icecube/wg-oscillations-fridge/tree/master/analysis/oscNext_decoherence/theory/density_matrix_osc_solver.

[217] Manasse Mbonye and Fred C. Adams. "Possible limits on photon propagation from quantum gravity and space - time foam". In: *Phys. Lett. B* 585 (1 June 2004), pp. 1–5. DOI: 10.1016/j.physletb.2004.01.075. arXiv: astro-ph/0402570 [hep-ex]. URL: https://link.aps.org/doi/10.1103/PhysRevD.23.165.

[218] Wayne A. Christiansen et al. "Limits on Spacetime Foam". In: *Phys. Rev. D* 83 (1 June 2011), p. 084003. DOI: 10.1103/PhysRevD.83.084003. arXiv: 0912.0535 [astro-ph.CO]. URL: https://link.aps.org/doi/10.1103/PhysRevD.23.165.